Graphite nodules and local residual stresses in ductile iron: Thermo-mechanical modelingand experimental validation

Andriollo, Tito; Hattel, Jesper Henri; Thorborg, Jesper; Tiedje, Niels Skat

Publication date:
2017

Document Version
Publisher's PDF, also known as Version of record

Graphite nodules and local residual stresses in ductile iron: Thermo-mechanical modeling and experimental validation

PhD Thesis

$$(EIv'')'' = q - \rho A\ddot{v}$$

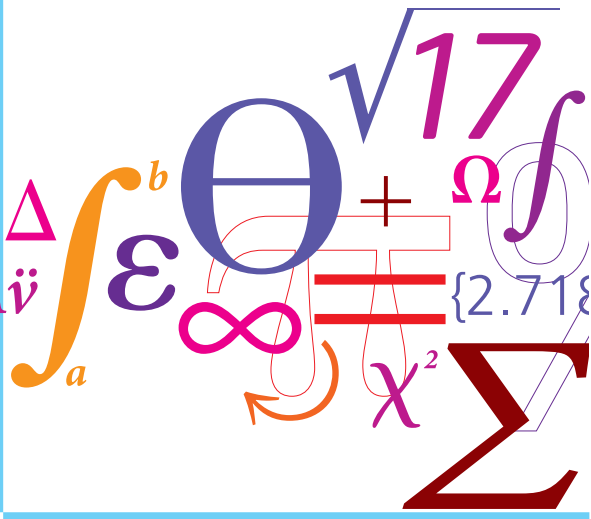

Tito Andriollo
October 2016

DTU Mechanical Engineering
Department of Mechanical Engineering

Graphite nodules and local residual stresses in ductile iron: Thermo-mechanical modeling and experimental validation

Tito Andriollo
Department of Mechanical Engineering
Technical University of Denmark

A thesis submitted for the degree of
Doctor of Philosophy
October 2016

Title of the thesis:
Graphite nodules and local residual stresses in ductile iron: Thermo-mechanical modeling and experimental validation

Ph.D. Student:
Tito Andriollo
E-mail: titoan@mek.dtu.dk

Main Supervisor:
Jesper Henri Hattel
Technical University of Denmark
E-mail: jhat@mek.dtu.dk

Co-supervisors:
Jesper Thorborg
Magma GmbH
Technical University of Denmark
E-mail: jest@mek.dtu.dk
Niels Skat Tiedje
Technical University of Denmark
E-mail: nsti@mek.dtu.dk

DTU Mechanical Engineering
Section of Manufacturing Engineering
Technical University of Denmark
Produktionstorvet, Bld. 427S
DK-2800 Kgs. Lyngby
Denmark
Phone (+45) 4525 4763
Fax (+45) 4593 0190
www.mek.dtu.dk

ISBN: 978-87-7475-476-3

To my father,
who never allowed the plumber
to replace the old ductile iron pipes
with new polymeric ones...
I wish he could know
where research has taken me!

Preface

The present thesis, to be submitted in partial fulfillment of the requirement for the Doctor of Philosophy degree, relates to the work carried out at the Department of Mechanical Engineering (MEK) of the Technical University of Denmark (DTU) from 01.09.2013 to 03.10.2016. This period includes a 5-week leave of absence for family care.

The majority of the work was funded internally by DTU MEK and was supervised by Professor Jesper H. Hattel, with Associate Professor Niels S. Tiedje and Doctor Jesper Thorborg acting as co-supervisors. The experimental activities received the additional financial support of the Strategic Research Center 'REWIND-Knowledge based engineering for improved reliability of critical wind turbine components', Danish Research Council for Strategic Research, under Grant No. 10-093966 and of the U. S. Department of Energy, Office of Science, Office of Basic Energy Sciences, under Contract No. DE-AC02-06CH11357.

First and foremost, as author of this thesis I express my sincere gratitude to all Danish taxpayers. My hope is that the money taken from their pockets has been used in a way that justifies, at least to some extent, the trust they put in scientific research. However, as money is not the only thing that matters in a PhD student's life, I want to give special thanks to my main supervisor Jesper too. Above all, for his exceptional human side, which I infinitely appreciated during the less happy days I had to get through at some point. I am also indebted to my co-supervisors: to Jesper, for his capacity of being always a solid point of reference, and to Niels, for introducing me to the great world of ductile iron. In addition, particular gratitude goes to Søren, who was the first to believe in the possibility of measuring the residual stress locally, and to Yubin and Rosa, who gave a fundamental contribution in putting the idea into practice. Mads and Nikolaj deserve a special mention as well, as they have provided me support with the Gleeble and with many other technical issues. Finally, I want to thank all the members of the process modeling group for creating a very special working atmosphere: in a certain sense, I can say I have been working at home every day of my PhD.

Tito Andriollo

Kgs. Lyngby,
September 2016

Abstract

Ductile iron is nowadays widely used in key industrial sectors like off-shore, transport and energy production, accounting for as much as 25 % of the total casting production in the world. It is well known that ductile iron parts, depending on their size, may contain residual stresses developing over distances of a few millimeters or more, which arise due to the presence of constraints that hinder the free thermal contraction of the material during cooling. Fortunately, dedicated studies performed in the last few decades have provided a detailed understanding of the phenomenon, and today reliable tools exist that allow predicting and coping with the problem in almost all practical cases.

On the other hand, the intrinsic composite nature of ductile iron suggests the possible formation of another type of residual stresses, at much shorter length scales, associated with the thermal contraction mismatch between the two main metallurgical phases forming the material microstructure: the graphite nodules and the metallic matrix. Surprisingly, the subject has not received much consideration in the past, probably due the common belief that the graphite particles are very soft and unable to withstand any kind of loading. As a matter of fact, however, experimental evidence exists for their mechanical importance, especially at relatively high temperature and under compressive loadings, indicating that ductile iron might not be considered as a merely "voided material" in all situations.

Taking this as point of departure, the present work initially focuses on finding a satisfactory description of the nodules' thermo-elastic behavior, which is shown to be missing in the published literature, by means of micro-mechanical homogenization analyses based on a representative unit cell. These, combined with the application of elastic bound theory for polycrystalline materials, lead to the conclusion that the nodules cannot be considered as homogeneous and isotropic at the microstructural scale. Consequently, a novel strategy to simulate their elastic response is proposed, which consists in modeling their characteristic internal structure, composed of graphite platelets arranged into conical sectors, in an explicit manner. The resulting anisotropic model turns out to provide homogenized values for the ductile iron thermo-elastic properties at the macro-scale in excellent agreement with the experiments. In addition, it also indicates that the average thermal contraction of the nodules is likely 3 to 4 times smaller compared to that of the surrounding matrix, hence confirming the existence of a driving force for the formation of stresses at the local scale.

In order to investigate this last aspect, the final stages of the manufacturing process are simulated numerically, accounting for the different thermal expansion of the nodules and of the matrix during both the eutectoid transformation and the subsequent cooling to room temperature. The results show the formation of significant residual stresses in the matrix region close to the nodules, which are mainly deviatoric and strongly affected by the number of conical sectors forming the graphite particles.

To support the numerical findings, whose relevance calls for an adequate experimental validation, two techniques are employed. The Oliver-Pharr nano-indentation method is considered first, with

the aim of obtaining some direct information concerning the constitutive behavior of the individual graphite particles. Unfortunately, the technique turns out to feature a number of assumptions that pose strong limitations to its applicability to brittle, inhomogeneous and anisotropic structures like the nodules. Interestingly, one of them is related to a concealed way of accounting for the particular contact condition arising between the indenter and the sample during the test, which is revealed in detail in this work for the first time in literature.

The second technique considered is a novel 3D X-ray diffraction method based on synchrotron radiation. This time, the experiments are successful and lead to the determination of the residual stress state around a single nodule lying beneath the material surface. The results are the first ever produced, and confirm the theoretical predictions that local stresses up to approximately half the macroscopic yield strength may remain in the ductile iron microstructure after manufacturing.

Needless to say, this new type of residual stresses is expected to play an important role in determining the properties of ductile iron. Knowledge of the factors controlling it will pave the way for further optimization of the material performance under in-service loading.

Resumé

Duktilt støbejern er i dag meget udbredt i væsentlige industrielle sektorer som offshore, transport og energiproduktion, og som tegner sig for op til 25 % af den samlede støbeproduktion på globalt plan. Det er velkendt, at emner af duktilt støbejern, afhængigt af størrelse, kan indeholde restspændinger der udvikles over afstande på få millimeter eller mere og som opstår på grund af begrænsninger, som forhindrer den frie termiske kontraktion af materialet under afkøling. Heldigvis har dedikerede studier, som er gennemført inden for de sidste årtier, sørget for en detaljeret forståelse af fænomenet og i dag findes der pålidelige værktøjer, som kan forudsige og håndtere problemer i næsten ethvert praktisk tilfælde.

På den anden side, den indre komposit natur af duktilt støbejern tyder på en mulig formation af en anden type restspænding ved meget kortere længdeskalaer, og som er associeret med misforholdet mellem den termiske kontraktion af to primære metallurgiske faser, der danner mikrostrukturen af materialet: grafit kugler (noduler) og den metalliske matrix. Overraskende, så har emnet ikke fået meget opmærksomhed tidligere, muligvis på grund af den gængse forestilling om, at grafit partikler er meget bløde og ikke er i stand til at modstå nogen form for belastning. Faktisk findes der eksperimentelt bevis for deres mekaniske betydning, specielt ved relativt høje temperaturer og ved tryk-belastninger, som indikerer at duktilt støbejern muligvis ikke blot kan betragtes som ”ikke-eksisterende materiale” i alle situationer.

Med det som udgangspunkt, fokuserer det aktuelle arbejde på at finde en tilfredsstillende beskrivelse af nodulernes termo-elastiske adfærd, som vises at være fraværende fra det publicerede litteratur, ved hjælp af mikromekanisk homogeniserings analyse baseret på en repræsentativ enhedscelle. Dette, kombineret med anvendelse af elastisk nedre-og øvre-værditeori for polykrystalline materialer, fører til den konklusion, at nodulerne ikke kan opfattes som homogene og isotropiske på den mikrostrukturelle skala. Derfor foreslås en ny strategi til at simulere nodulernes elastiske opførsel, og som består af modellering af dets karakteristiske interne struktur, som består af grafit plateller arrangeret i koniske sektorer i en eksplicit måde. Det resulterende anistropiske model viser sig at give homogeniserede værdier for det duktile støbejerns termoelastiske egenskaber på den makroskopiske skala, og som er i fremragende overensstemmelse med eksperimenter. Ydermere, indikerer det også at den gennemsnitlige termiske kontraktion af nodulerne sandsynligvis er 3 til 4 gange mindre i forhold til den omkringliggende matrix, og dermed bekræfter den forekommende drivkraft for formation af spændinger på den lokale skala.

For at undersøge det sidste aspekt, er de afsluttende stadier i fremstillingsprocessen simuleret numerisk ved at tage højde for de forskellige termiske udvidelser af nodulerne og af matricen, både under den eutektoide transformation og den efterfølgende afkøling til stuetemperatur. Resultaterne viser formationen af betydelige restspændinger i matrix regionen tæt på nodulerne, som primært er deviatoriske og stærkt påvirket af antallet af koniske sektorer, som danner grafit partiklerne.

For at understøtte de numeriske resultater, hvor det giver mening at udføre passende eksperimentel validering, er der gjort brug af to metoder. Oliver-Pharr nano-indhak metoden er først taget i betragtning, med det formål om at opnå noget direkte viden om den konstitutive opførsel af de individuelle grafit partikler. Desværre viser det sig, at metoden involverer et antal antagelser, som udgør en kraftig begrænsning til dets brug til skøre, inhomogene og anistrope strukturer som i nodulerne. Interessant nok, er en af antagelserne relateret til en skjult måde at gøre rede for den specifikke kontakt-tilstand der forekommer mellem indenteren og prøven under forsøget, og som for første gang i litteraturen er afsløret i detaljer i dette arbejde.

Den anden metode er en ny 3D X-ray diffraktionsmetode baseret på synkrotron stråling. Denne gang er eksperimenterne vellykkede og fører til bestemmelse af restspændings tilstanden omkring en enkel nodul, som ligger under materiale overfladen. Resultaterne er de første produceret nogensinde og bekræfter de teoretiske forudsigelser, at lokale spændinger op til omkring det halve af den makroskopiske flydestyrke, forbliver i det duktile støbejerns mikrostruktur efter fremstillingen.

Den nye type restspænding forventes at spille en afgørende rolle ved bestemmelse af duktilt støbejerns egenskaber. Viden om de faktorer der styrer egenskaberne vil give mulighed for yderligere optimering af materialets ydeevne ved belastninger under brug.

List of appended publications

The following journal publications are part of the present thesis:

PAPER I T. Andriollo, J. Thorborg, and J. Hattel, "Analytical solution to the 1D Lemaitre's isotropic damage model and plane stress projected implicit integration procedure", *Applied Mathematical Modelling*, vol. 40, no. 11–12, pp. 5759–5774, 2016.

PAPER II T. Andriollo and J. Hattel, "On the isotropic elastic constants of graphite nodules in ductile cast iron: analytical and numerical micromechanical investigations", *Mechanics of Materials*, vol. 96, pp. 138–150, 2016.

PAPER III T. Andriollo, J. Thorborg, and J. Hattel, "Modeling the elastic behavior of ductile cast iron including anisotropy in the graphite nodules", *International Journal of Solids and Structures*, vol. 100-101, pp. 523–535, 2016.

PAPER IV T. Andriollo, J. Thorborg, N. Tiedje, and J. Hattel, "A micro-mechanical analysis of thermo-elastic properties and local residual stresses in ductile iron based on a new anisotropic model for the graphite nodules", *Modelling and Simulation in Materials Science and Engineering*, vol. 24, no. 5, p. 055012(19pp), 2016.

PAPER V T. Andriollo, J. Thorborg, and J. Hattel, "Analysis of the equivalent indenter concept used to extract Young's modulus from a nano-indentation test: Some new insights into the Oliver-Pharr method", *Modelling and Simulation in Materials Science and Engineering* [under review]

PAPER VI Y. Zhang, T. Andriollo, S. Fæster, W. Liu, J. Hattel, and R. Barabash, "Three-dimensional local residual stress and orientation gradients near graphite nodules in ductile cast iron", *Acta Materialia,* vol. 121, pp. 173–180, 2016.

Contents

Chapter 1
Introduction

This introductory chapter is meant to provide the reader with sufficient background to understand the aim and motivation of the scientific work presented in the thesis, as well as in the appended articles.

1.1 An unexplored aspect of the interplay structure-process-properties-performance in ductile iron

The discovery of ductile iron dates back to 1943, when Keith D. Millis of the International Nickel Company Research Laboratory found out that a small addition of magnesium to gray cast iron resulted in the formation of spherical graphite particles [1]. Since then, the material has experienced an enormous and constantly growing development, until becoming in 1998 the only ferrous casting alloy with a positive growth rate on the market [2]. Today, its high technological importance is reflected by the fact that as much as 25 % of the castings produced worldwide are made of ductile iron [3]. The main reason behind this phenomenal success is the unique combination of castability, high ductility and strength such material can offer, along with lower prices compared to traditional low carbon steels [4]. Examples of typical products are small and medium sized heavily loaded parts with high demands for consistent quality for the automotive industry and very large industrial components with extreme demands for mechanical properties, particularly fatigue strength and fracture toughness [5].
Over the years, a great deal of effort has been put to understand the science and engineering of ductile iron. Nevertheless, despite extensive experimental and theoretical studies, there are still some aspects which remain unclear. The primary reason is the complex set of interactions arising between material structure, manufacturing process and final mechanical properties, whose understanding may not be considered as fully achieved yet [6]. Among all these interactions, there is one in particular that has probably received much less consideration than necessary in the past: the possible formation of local residual stresses at the micro-structural level. This will be presented in details in the next paragraphs, on the basis of the direct application of the well-established structure-process-properties-performance paradigm [7] illustrated in figure 1.1.

1.1.1 Ductile iron as a natural composite

From a metallurgical standpoint, ductile iron may be classified as a ternary Fe-C-Si alloy where iron represents the main element by mass. The carbon and silicon content is normally adjusted so as to obtain eutectic or near-eutectic compositions according to the ternary equilibrium phase diagram. These are characterized by values of the carbon equivalent, defined as the sum wt% C + 1/3 wt% Si,

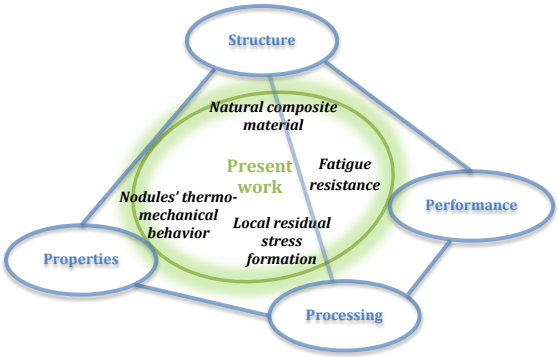

Figure 1.1 – The particular type of interaction between structure, processing, properties and performance of ductile iron considered in the present work.

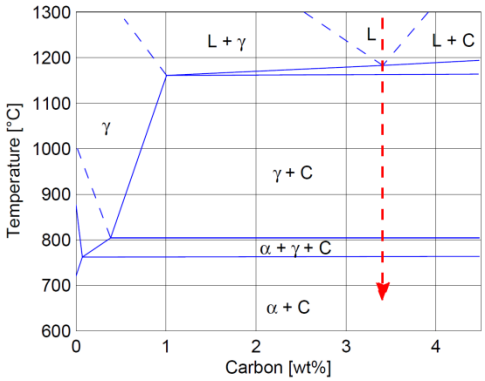

Figure 1.2 – Schematic slice of the ternary Fe-C-Si phase diagram for a silicon concentration of 2.4 wt%. Data taken from [11].

close to 4.3 wt%. Larger or smaller values lead to the so-called hyper-eutectic or hypo-eutectic grades respectively.

With reference to figure 1.2, solidification of eutectic ductile iron begins with the independent nucleation of graphite and austenite from a properly inoculated melt [8]. The characteristic spherical shape of the graphitic phase is obtained by adding Mg and, in some cases, rare earth elements such as Ce and La to the base liquid metal, which give rise to a melt with low content of S and O [5]. As solidification proceeds, the graphite particles, often called *spheroids* or *nodules*, become enveloped by the austenite dendrites, and their further growth becomes controlled by carbon diffusion from the liquid through the austenite. Eventually, the liquid remaining in between the different dendrites or in between the secondary arms of the same dendrite solidifies, generating the so-called last-to-freeze zones [8]. During the subsequent solid-state-cooling, marked with the red arrow in figure 1.2, the nodules keep growing, due to the reduced carbon solubility in the surrounding austenite. When the eutectoid interval is reached, austenite decomposition takes place. Slow cooling rate and high Si content favor the formation of ferrite, whereas high cooling rate and small amounts of elements like Mn, Cr or Cu promote the pearlitic transformation.

From the optical micrographs shown in figure 1.3, it is clear that the final ductile iron microstructure may be naturally considered as composite [9][10], consisting of graphite particles embedded in a continuous matrix. The very high degree of nodularity of the former has justified the alternative designation of spheroidal graphite iron (SGI) or nodular cast iron (NCI), to emphasize the difference with other members of the cast iron family where the graphite is present in more irregular forms.

1.1.2 Local residual stresses arising during manufacturing

It is common knowledge that ductile iron components may be affected by the presence of residual stresses. This issue is normally more critical for parts used in the as-cast state, whereas it is

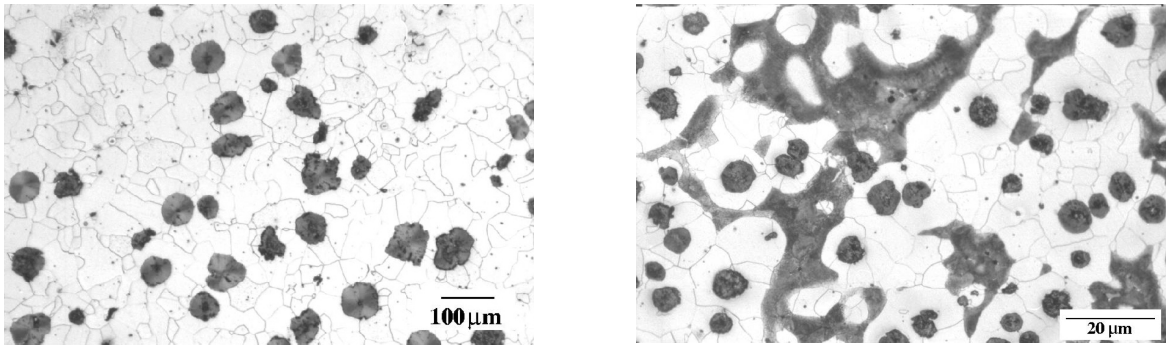

Figure 1.3 – Examples of **(a)** fully ferritic and **(b)** ferritic-pearlitic ductile iron microstructures. Reproduced from [13].

relatively less important for components which are subjected to further heat treatment. Formally, residual stresses in a body are defined as those stresses which are not necessary to maintain equilibrium with the surrounding environment. Equivalently, they can also be described as the stresses which are not generated by the action of external forces, but rather by the volumetric misfit among different parts of the same component [12].

In casting processes, residual stresses normally arise due to hindered thermal contraction. This simply means that they are associated with the presence of constraints that prevents the natural, free volumetric variation of the material upon cooling. As shown in figure 1.4, it is custom to distinguish between external and internal constraints [14]. The first type refers to the action of the mold, which, if stiff and strong, can effectively oppose the thermal contraction of the casting. The second type instead, indicates the constraint exerted on a particular region by the surrounding material which undergoes a different level of contraction. This implies the presence of an uneven volumetric variation within the casting itself, which, neglecting phase transformations, can originate from

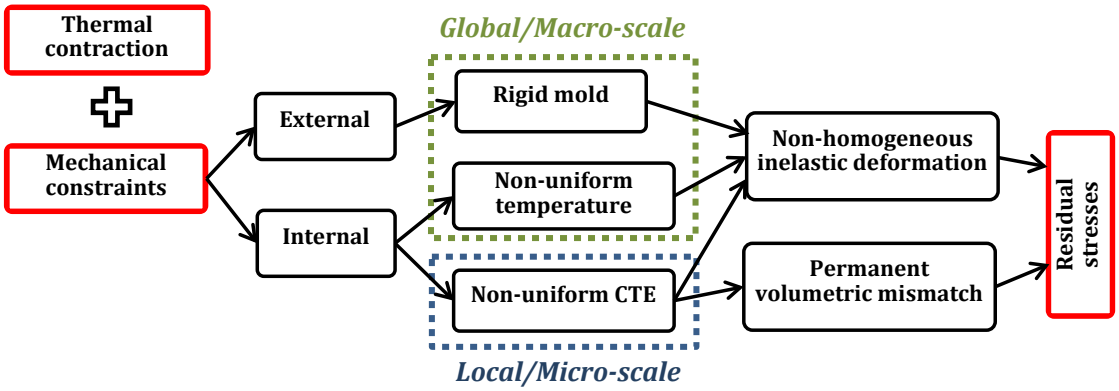

Figure 1.4 – Schematic of the formation of residual stresses in a casting process, with indication of which driving mechanisms are active either at the global or at the local scale.

either a non-uniform temperature distribution, or from non-homogeneous material properties, i.e. different values of the coefficient of thermal expansion (CTE).
From the reasoning above, one might think that mold constraints and temperature gradients could be responsible for the formation of transient stresses only. In fact, once the mold is removed and the casting has cooled down completely, no volumetric misfits should remain, either internal or external. Unfortunately, this is not true, as the transient stresses can promote non-homogeneous inelastic deformation during cooling, which in turn translates into a permanent, residual stress state in the final component.
The two constraints just discussed drive residual stresses whose characteristic length scale normally coincides with the full size of the component. For this reason, they are normally referred to as *global* or *macroscopic* stresses. It is important to remark that, in the context of the present work, the characteristic length scale is defined as the distance over which the stresses self-equilibrate. Conversely, the residual stresses arising from variations in CTE are more likely to promote *local* or *microscopic* stresses, as they are frequently associated with the presence of two or more microstructural phases of different chemical nature.
Concerning ductile iron, most of the past scientific and technological efforts have been addressed towards understanding and minimizing residual stresses occurring at the macroscopic level. However, the intrinsic composite structure visible in figure 1.3 suggests that local stresses might form too, as a consequence of the thermal expansion mismatch between the nodules and the surrounding matrix. To better appreciate this point, let us consider the specific case of ferritic ductile iron. The CTE of the matrix at room temperature can be assumed to be $\alpha_m = 12 \times 10^{-6}$ °C^{-1} [15][16]. Regarding the nodules, dedicated CTE measurements do not seem to be available in the literature. Nevertheless, extensive experimental studies performed in the '70s on polycrystalline graphite for nuclear applications have reported values in the range of $\alpha_g \approx 3 \div 4 \times 10^{-6}$ °C^{-1} [17]. By multiplying the difference in the CTEs by a hypothetic temperature jump of 700 °C, roughly coinciding with the cooling from the end of the eutectoid transformation, which marks the point where the nodules have attained their final size [18], one obtains a differential thermal strain of $5 \div 6 \times 10^{-3}$. This is as much as three times the permanent plastic deformation which conventionally defines the proof stress of a material.
It has to be emphasized that the large difference between α_m and α_g is quite realistic. Indeed, it is an empirical fact that all crystalline solids expand by about 2 % on heating from absolute zero to their melting point [19]. This means that an estimate of the average CTE can be calculated as $\alpha = 0.02/T$, where T is the melting temperature in Kelvin. For the ferritic matrix, the latter can be assumed to be 1800 K. Graphite instead does not possess a real melting point at atmospheric pressure, as its triple point lies at several MPa [20]. However, by considering the temperature of the triple point itself (≈ 4600 K [20]), it is possible to calculate an approximation to the ratio of the respective CTEs as

$$\frac{\alpha_m}{\alpha_g} = \frac{T_g}{T_m} = \frac{4600}{1800} \approx 2.6 \tag{1.1}$$

which justifies the large difference between the experimental values previously mentioned.
On the basis of the present argument, it seems logical to expect a significant level of local residual stresses in the final ductile iron microstructure. In fact, this type of residual stresses has been known

to develop in traditional metal-matrix composites for long [21]. On the contrary, to the author's best knowledge, the very first paper which analyzes quantitatively the formation of local residual stresses in ductile iron was published only in 2005 [16]. A natural question then arises as to why this subject has been overlooked for such a long time. In the author's opinion, the primary reason has been the very limited knowledge of the thermo-mechanical behavior of the nodules, which have been traditionally considered as very soft and unable to withstand any kind of loading. This issue is examined in depth in the next section.

1.1.3 Properties of the graphite nodules

While the properties of the ductile iron matrix seem to be quite established, a detailed literature survey has shown that the thermo-mechanical role of the nodules is still, after 70 years, an open issue. On the one hand, contrary to common beliefs, experimental evidence exists for their importance during macroscopic material deformation. On the other hand, as a matter of fact, reliable information regarding their constitutive behavior is not available yet.

1.1.3.1 Micro-structural importance: Experimental evidence

As stated previously, the nodules have often been considered to have negligible influence on the mechanical properties of ductile iron. Especially in micro-mechanical analyses focusing on simulating uniaxial tensile tests, several authors simply neglected their presence, indeed regarding the material as porous [22][23][24]. This was justified mainly on the basis of microscopy observations, which had reported early debonding for spheroids sitting on the surface of the tensile test specimen [25]. However, as correctly pointed out in [26], the stress state around nodules located in the bulk is likely to be different, due to the material inhomogeneity, therefore it seems not possible to conclude that debonding always occurs, independently of the real local loading conditions. In addition, it is a fact that the tensile stress-strain curves for ductile iron are never perfectly linear, even at very low stress levels, due to the almost immediate onset of plasticity [27][28][29]. This can hardly be explained with a simple porous model, as finite element calculations for the stress concentration factor corresponding to cavities of the shapes typical of real nodules have provided the maximum value of 5.39 [30].

Apart from this, the voided-material assumption might still be reasonable at high values of the triaxiality ratio, at least in those circumstances where complete debonding from the matrix will certainly take place. But it is more difficult to rationalize in more complex situations, like cyclic loading or when the hydrostatic part of the stress tensor becomes negative. Clear facts point in this direction.

First of all, the low-cycle fatigue behavior of ductile iron with stress ratio equal to -1 is better reproduced by models where nodules are treated as rigid spheres instead of voids [31]. At the same time, it has been proved that fatigue crack propagation cannot be modeled within the classic linear elastic fracture mechanics framework [32]. This might be related to the fact that, according to the imposed stress intensity factor, different competing damage mechanisms are active in the matrix and / or in the nodules [18]. Secondly, examinations of the cross-section of cylindrical samples heavily deformed (90 %) in compression at different temperatures have shown that, when the testing temperature is close to the eutectoid transformation, the nodules do not deform at all. That

is, they maintain their spherical shape whereas all the surrounding ferrite grains flatten out [33]. This is perhaps the most striking evidence of the fact that the nodules do have some load carrying capacity, at least under compressive forces.
The last observation is particularly important in the context of the present work. In fact, it leads to the conclusion that local residual stresses are, in principle, to be expected during manufacturing, as the nodules can oppose, to a certain extent, the free contraction of the matrix.

1.1.3.2 Mechanical behavior: Modeling uncertainty

Having clarified the non-negligible role of the nodules from a mechanical standpoint, it would be useful to gain more knowledge concerning their individual constitutive behavior. In this way, a more quantitative interpretation of the results discussed in the previous section could be achieved. Unfortunately, this task is complicated by the much reduced size of the particles, which has always challenged any experimental characterization based on direct techniques. Apparently, the only simple method to test their mechanical properties is nano-indentation, which has provided values for the Young's modulus in the range 15 ÷ 28 GPa [34][35][36]. Nevertheless, the validity of such measurements is quite disputable, as the nodules are highly anisotropic at the nanoscale [37], meaning that the concept of nano-indentation based Young's modulus loses its significance. In addition, it has been argued [16] that the sharp Berkovich indenter usually employed could simply separate the graphite layers, without creating any elastic deformation at all.
The difficulties in performing reliable measurements have contributed to create a large uncertainty concerning the real mechanical properties of the nodules. For instance, most of the authors who have tried to consider the spheroids in their analyses have assumed that they behave as isotropic linear elastic particles. However, as may be seen in table 1, there is no agreement whatsoever regarding values for their elastic constants. The spread is so large that it seems that all options, from a void up to a rigid body, are possible.
The indetermination on the nodules' mechanical properties carry over to uncertainty on the magnitude of the local residual stresses. In reference [16], compressive values of about 500 MPa for

Table 1 – Micromechanical modeling of ductile iron elastic response: Assumed values for the nodules' isotropic elastic constants.

Year	Authors	Young's modulus (GPa)	Poisson's ratio
1980	Speich et al. [38]	8.5	0.29
1992	Era et al. [39]	303	Not specified
1997	Boccaccini, R. [40]	8.5	0.2
1998	Pundale et al. [41]	0 (void)	0 (void)
2002	Cooper et al. [42]	8.5	0.2
2003	Gaudig et al. [43]	4.17	0.2225
2004	Sjögren & Svensson [10]	*	Not available
2005	Collini & Nicoletto [44]	15	0.3
2005	Bonora & Ruggiero [16]	300-375	Not specified
2006	Nicoletto et al. [45]	15	0.3
2014	Carazo et al. [46]	*	0.2225
2015	Fernandino et al. [36]	15	0.28

* = $0.173 \cdot Nodularity + 18.9 \rightarrow 36.2$ GPa for 100 % nodularity

the stress component normal to the nodule-matrix interface were proposed. Nevertheless, these were primarily a consequence of 1) the very high Young's modulus, of about 300-375 GPa, and 2) the perfectly elastic behavior assumed for the graphite particles.
The impossibility to verify these two major assumptions, combined with the technical problems of performing direct local residual stress measurements, were probably at the basis of the absence of any follow-up investigation. As of 2016, to the author's best knowledge, ref. [16] remains the only systematic work on local residual stresses in ductile iron ever published in literature.

1.1.4 Influence on the material performance

The absence of a reliable quantification of the local residual stress state in ductile iron can potentially constitute a severe limitation towards optimizing the material performance. In fact, despite having a different origin, residual stresses at the micro-structural level can be at least as detrimental as those occurring at the macro-scale. According to the discussion reported in [21][47] for the general case of metal-matrix composites, stresses arising from a mismatch in the thermal expansion during manufacturing may compromise the material properties in several different ways. For instance, they can be responsible for reduced elastic response of the material, damage amplification, accelerated stress corrosion, reduced toughness and fatigue resistance, etc.
All these aspects are particularly relevant for ductile iron, since the material is typically used in applications which strongly require such characteristics. Examples include automotive steering knuckles, control arms, brake calipers and wind turbine rotor hubs, just to mention a few. Therefore, from an engineering perspective, proper quantitative knowledge about local residual stresses seems essential to improve the in-service behavior of ductile iron even further.
At the same time, from a more scientific standpoint, a detailed description of the thermo-mechanical interactions developing between the nodules and the surrounding matrix might also contribute to shed light on some phenomena which are still poorly understood. Figure 1.5 shows an example of crack propagation under cyclic loading, which still represents an open field of research.

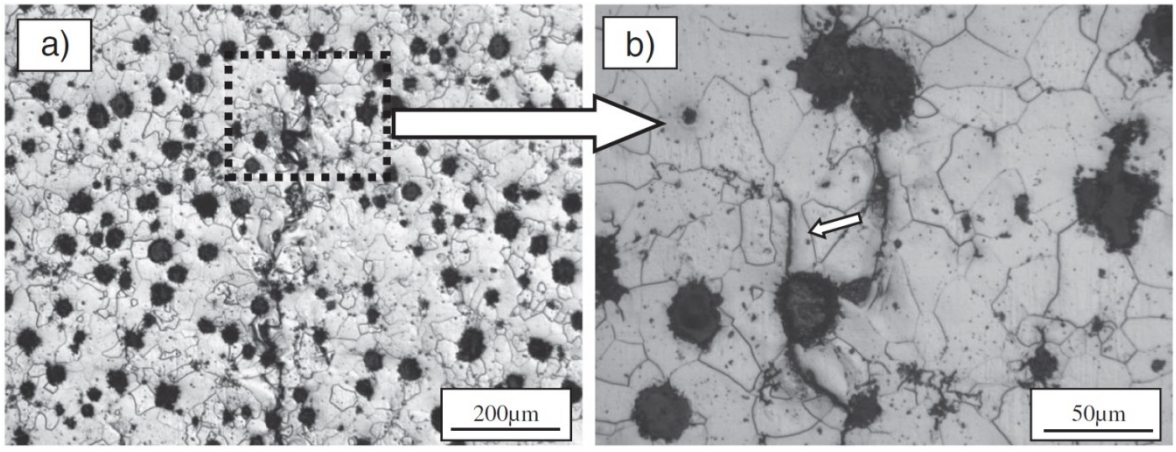

Figure 1.5 – Fatigue crack propagation in ferritic ductile iron. Reprinted from [48] with permission of John Wiley and Sons.

1.2 Objectives of the thesis

From the arguments just presented, it is clear that the intrinsic composite nature of ductile iron may lead to the formation of significant local residual stresses during manufacturing. Unfortunately, any sound estimate of their magnitude is made impossible by the lack of reliable data concerning the thermo-mechanical properties of the graphite nodules. However, as local residual stresses could seriously prevent achieving the maximum material performance during in-service loading, additional investigations in this area are highly necessary.
Within this framework, the present thesis aims at:

1. Obtaining a more precise knowledge of the nodules' thermo-mechanical behavior. This is the very first step needed to describe the interaction between the graphite particles and the surrounding matrix in more quantitative terms. In order to achieve this, a theoretical model is to be devised which allows determining the mechanical response of the nodules to a much higher degree of accuracy compared to what is possible at present. In this respect, the data presented in table 1 should be taken as reference.
2. Investigating the formation of local residual stresses in ferritic ductile iron by means of the model developed in the previous point. In particular, it is extremely important to come up with a reliable approximation of their magnitude to assess the impact they could have on the material properties. That is, the question of whether or not local residual stresses are negligible has to be answered properly.
3. Performing a thorough experimental validation of both the proposed theoretical model for the nodules and the local residual stress predictions. Concerning this, direct techniques are to be preferred over indirect ones, as the latter are normally characterized by much larger uncertainties.

In plain words, whereas the previous sections discussed *where?*, *when?* and *why?* local residual stresses form, the remainder of this work will focus on *how much?* residual stress can be realistically expected in the final ductile iron microstructure.

1.3 Structure of the thesis

The thesis is composed by 7 chapters and 6 appended journal articles. To facilitate reading, a short description of each chapter is given in the following, where special emphasis is placed on clarifying the connections with the papers in appendix.

Chapter 1 – Introduction
This introductory chapter provides the reader with sufficient background to understand the overall aim and motivation of the present scientific work. The basic problem is exposed within the framework of the well-known structure-process-properties-performance paradigm, and the primary investigation objectives are defined. Section 1.1 in particular can be seen as a stand-alone, preparatory discussion for **PAPER II** to **VI**.

Chapter 2 − Modeling framework

This chapter describes the methodology used to model the formation of local residual stresses in ferritic ductile iron. A proper micro-mechanical framework is presented, and the primary homogenization procedures are outlined. Special consideration is given to the selection of a periodic unit cell approach and the related implementation of appropriate periodic boundary conditions in the finite element software ABAQUS, as discussed in **PAPER III**.

Chapter 3 – Ferrite matrix behavior

The mechanical behavior of the ferritic matrix of the ductile iron grade GJS-400 is analyzed in detail in this chapter, considering both experimental and modeling aspects. Concerning this last point, a parameter identification strategy for Lemaitre's damage model based on an analytical solution developed by the author in **PAPER I** is illustrated, accompanied by the description of a new 2D plane-stress implicit integration algorithm.

Chapter 4 – Thermo-mechanics of the nodules

Here the main results obtained regarding thermo-mechanical modeling of the graphite nodules are presented. Initially, some preliminary findings are briefly outlined which extend previous investigations by other authors. After that, the inadequacy of the assumption of isotropy and homogeneity of the nodules at the micro-scale is discussed, according to the analysis of **PAPER II**. Finally, a new, anisotropic model is presented, which is based on transmission electron microscopy (TEM) observations of the real internal structure of the graphite particles. This last part of the exposition reflects primarily the content of **PAPER IV** and, partly, of **PAPER III**.

Chapter 5 – Local residual stresses

This chapter, entirely based on **PAPER IV**, explores the formation of local residual stresses during manufacturing by means of numerical simulations. The starting point is the anisotropic formulation of the nodules presented in the previous chapter. Several considerations are also made concerning the relation between the residual stress pattern in the nodules and their internal structure and failure mode.

Chapter 6 – Experimental validation via direct techniques

Experimental validation via direct methods of the two main theoretical results achieved, i.e. the anisotropic model for the nodules and the local residual stress prediction around them, is addressed here. First, the Oliver-Pharr nano-indentation method is discussed, highlighting the hidden assumptions of the procedure (**PAPER V)** and their consequences when probing the nodules' elastic properties. After that, the novel differential aperture X-ray microscopy (DAXM) synchrotron technique is shortly described, which allows measuring the residual elastic strain in the ferrite matrix with a spatial resolution of 1 micron. Results of measurements conducted at Argonne National Laboratory are finally presented and compared with theoretical predictions (**PAPER VI**).

Chapter 7 – Concluding remarks

This chapter summarizes the main conclusions of the thesis in relation to the objectives set in the introduction. New questions stemming from the presented results are put forth and used to outline future research paths.

Chapter 2
Modeling framework

This chapter describes the basics of the methodology adopted to model the formation of local residual stresses in ductile iron.

2.1 Micro-mechanical approach

The intrinsic composite nature of ductile iron described in section 1.1.1 suggests adopting a micro-mechanical approach for the problem at hand. This means that the individual constituents, i.e. the nodules and the matrix, are each treated as continua via continuum mechanics, with their individual representative properties and arrangement defining the overall material behavior [49].
As explained in [50], the first step in performing a micro-mechanical analysis is the identification of the relevant length scales involved. What should normally be defined is 1) the *micro-scale*, as the scale at which the material is heterogeneous, 2) the *meso-scale*, which is the smallest scale at which the material may be considered as homogeneous, and finally 3) the *macro-scale*, where traditional engineering methods apply. Micro-mechanical techniques are subsequently used to determine the properties of the material at the meso-scale, given the characteristics of the constituents at the micro-scale. This process is known as *homogenization*, and the resulting *effective* properties provide the input needed for static or dynamic analyses of the entire component or structure. The inverse process is called *localization* instead, and consists in finding the behavior of the micro-structural constituents for a prescribed overall material response.
In the context of the present work, two main types of micro-mechanical analyses are performed:

1. Homogenization studies, to assess the admissibility of a certain set of thermo-mechanical properties for the nodules via comparison with properties for ductile iron measured at the macro-scale.
2. Localization analyses, to calculate the local residual stresses arising at the interface between the nodules and the ferrite matrix for prescribed global temperature variations and boundary conditions.

As said previously, these types of investigations require the preliminary definition of suitable length scales. The identification of the micro- and macro-scale for ferritic ductile iron is straightforward, as the first one coincides with the size of the micro-structure seen in figure 1.3, and the second one is simply the size of the component under examination. In contrast, the definition of the most appropriate meso-scale calls for a more thorough discussion, which is presented in detail in the next section.

2.2 Periodic unit cell

Today, micro-mechanical techniques extensively rely on the concept of representative volume element (RVE) [51], which is intuitively defined as the minimum volume whose constitutive behavior is equivalent to that of a homogeneous fictitious material. According to this definition, the meso-scale turns out to be determined by the dimension of the RVE.
In ductile iron, the non-uniform size and distribution of the nodules imply that a RVE should include a considerable number of particles in order to be realistic. For instance, in [36] it was recommended to consider a minimum of 56 nodules for 2D problems, meaning that a corresponding 3D RVE should contain, to a first approximation, at least $56^{3/2} \approx 420$ graphite particles. This number, in itself, would not be prohibitive. Unfortunately, as will be explained in the next chapter, the mechanical behavior of the nodules can only be simulated by explicitly taking into account their internal structure. From a computational point of view, it is clear that the discretization of so many particles, each one featuring complex internal geometry, would be cumbersome.
As a consequence, a less demanding periodic unit cell approach [52] is deemed more appropriate for the present analyses. The method assumes the ductile iron microstructure to be periodic and generated by the spatial repetition of the same elementary unit, reported in figure 2.1. As can be noted, the latter is composed of a cube with a single, spherical nodule in the center, whose relative size is adjusted to give the 11.5 % volumetric graphite concentration typical of the GJS-400 ferritic grade [53]. An example of unit cell mesh discretization in the finite element (FE) software ABAQUS, which is the modeling software primarily used in the present investigations in combination with the codes developed by the author in C-language, is given in figure 2.2.
It is important to remark that, in spite of their simplicity, many unit cell models have been successfully applied to ductile iron in the past, e.g. [16][22][24][45][54][55]. On the other hand, it should be clear that some material features, like non-uniform nodule shape, size and distribution, cannot be captured with such periodic approach.

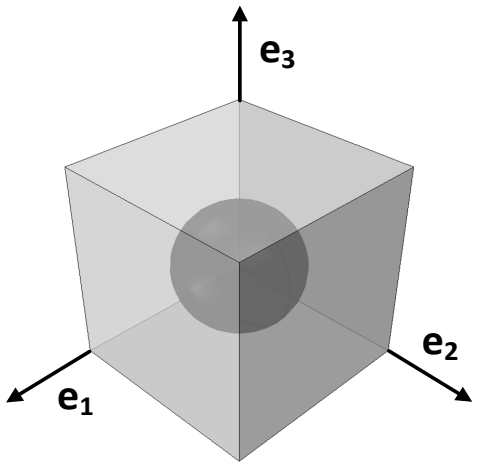

Figure 2.1 – 3D periodic unit cell representing the micro-structure of ferritic ductile iron.

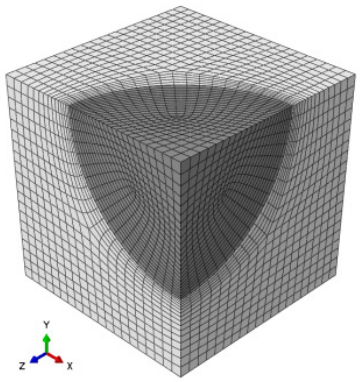

Figure 2.2 – Example of mesh used in ABAQUS. Only 1/8 of the periodic unit cell is shown.

2.3 Periodic boundary conditions

2.3.1 Definition

The periodicity assumption implies that, upon loading, the continuity of the displacements and of the surface tractions with the adjacent unit cells must be satisfied at any time. This requirement can be fulfilled a priori by the application of special periodic boundary conditions, as thoroughly discussed in [52]. Considering any two equivalent points $\boldsymbol{x}$ and $\boldsymbol{x}+\boldsymbol{d}$ lying on opposite faces of the unit cell and separated by the characteristic periodic length $\boldsymbol{d}$, the following constraints must be imposed:

$$\begin{aligned} \boldsymbol{u}(\boldsymbol{x}+\boldsymbol{d}) &= \boldsymbol{u}(\boldsymbol{x}) + \bar{\boldsymbol{\varepsilon}} \cdot \boldsymbol{d} \\ \boldsymbol{t}(\boldsymbol{x}+\boldsymbol{d}) &= -\boldsymbol{t}(\boldsymbol{x}) \end{aligned} \tag{2.1}$$

where $\boldsymbol{u}$ and $\boldsymbol{t}$ denote displacement and surface traction. The 2[nd] order tensor $\bar{\boldsymbol{\varepsilon}}$ represents the average of the infinitesimal strain over the entire unit cell volume, and it is normally an externally imposed quantity in homogenization analyses.

2.3.2 ABAQUS implementation

The implementation of the periodic boundary conditions (2.1) in ABAQUS deserves a special comment. This issue was examined in a recent article [56], where the authors claimed that the constraint on the boundary traction was unnecessary within the context of a displacement-based FE analysis [57]. However, as shown in **PAPER III**, this implies that the associated FE system of equations becomes undetermined, unless further, subjective assumptions are made on the nature of the external nodal forces. Therefore, to obtain unique results, both displacement and traction conditions must be imposed simultaneously.

In ABAQUS, a natural method to enforce (2.1) is to use the "Linear constraint equations" command [58], which allows imposing a scalar linear constraint of the type

$$a_1 u_1 + a_2 u_2 + \cdots + a_k u_k = 0 \tag{2.2}$$

where $u_j, j = 1{:}\,k$ are generic displacement degree of freedoms (dofs) and $a_j, j = 1{:}\,k$ are real coefficients. Nevertheless, this approach has two limitations. First of all, the first dof appearing in an equation is automatically eliminated and cannot be used in any subsequent relation. Secondly, equations can only be formulated in terms of displacement dofs, hence imposition of the traction part of (2.1) is in principle not trivial. To overcome these issues, a general method is proposed in **PAPER III,** which is illustrated in figure 2.3. It can been seen that, in order to impose the periodic traction condition, entries of the FE global stiffness matrix related to the boundary nodal forces are extracted by means of the MATRIX GENERATE command [59]. Moreover, repetition of dofs already set as first dofs in previous equations is avoided by prior reduction to echelon form via Gauss-Jordan pivoting of the matrix associated with the set of linear constraints.

Another critical aspect of the FE implementation relates to the choice of the boundaries over which the periodic conditions (2.1) have to be imposed. In fact, it is of utmost importance to avoid generating a number of linear independent constraints greater than the number of dofs associated

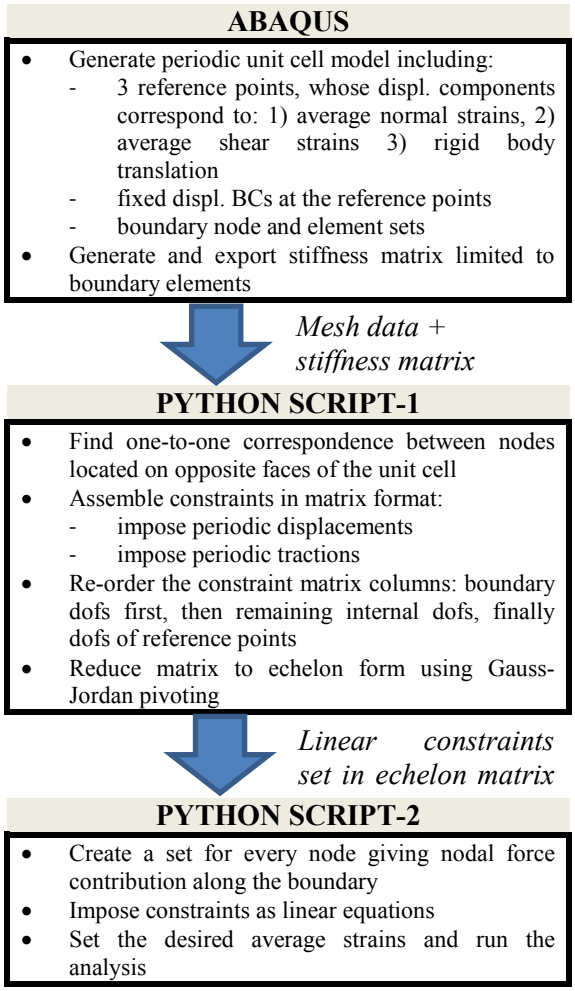

Figure 2.3 – Procedure for setting up periodic displacement and traction boundary conditions in ABAQUS.

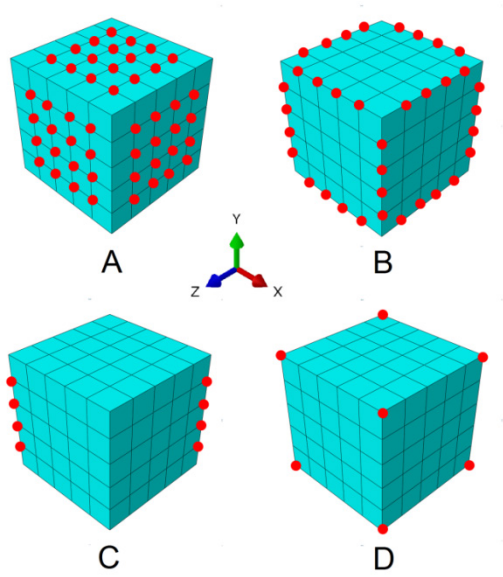

Figure 2.4 – Definition of useful node sets on the unit cell mesh: (a) face internal nodes, (b) edge internal nodes, (c) pair of opposite parallel edges along y-direction, (d) corner nodes.

with the boundary nodes of the model: if that happened, spurious deformation would occur in the unit cell, adversely affecting the quality of the analysis.

A simple strategy to deal with this last issue is presented in **PAPER III** as well. With reference to the 3D unit cell mesh of figure 2.4, the following quantities are introduced:

- n_f: number of face internal nodes
- n_e: number of edge internal nodes
- n_c: number of corner nodes
- $n_b = n_f + n_e + n_c$: number of total boundary nodes

Periodic displacement boundary conditions are applied considering all n_b nodes. Constraints are set between all possible pairs of equivalent nodes, meaning that a single corner node will be subjected

to 3 linear constraints of the vector type (2.1)(a), an edge node to two, and a face node to one only. The total number of linear independent equations C_d generated in this way may be determined as

$$C_d = 3\left(\frac{1}{2}n_f + \frac{3}{4}n_e + (n_c - 1)\right) \tag{2.3}$$

Conversely, periodic traction boundary conditions are imposed considering the face internal nodes only, plus the internal nodes lying on 3 pairs of opposite parallel edges as shown in figure 2.4 (c), one pair for each Cartesian direction. Consequently, the number of independent traction constraints C_t created is given by

$$C_t = 3\left(\frac{1}{2}n_f + \frac{1}{4}n_e\right) \tag{2.4}$$

The overall number of linear independent equations C_{tot} is then

$$C_{tot} = C_d + C_t + 3 \tag{2.5}$$

where the last term relates to the prescribed motion of a single selected node, necessary to avoid rigid body translation. By inserting expressions (2.3) and (2.4) into (2.5), it can be easily verified that $C_{tot} = 3n_b$, i.e. the number of independent constraints is exactly equal to the number of boundary dofs.

2.4 Homogenization methods

As stated in section 2.1, homogenization analyses are employed here to assess the admissibility of a certain set of thermo-mechanical parameters for the nodules via comparison with effective properties measured at the macro-scale. In this respect, two procedures which allow calculating effective properties for the unit cell of figure 2.1, to be compared with experimental values for ductile iron, are presented in the following.

2.4.1 Linear elastic case

Under the assumption of linear elastic behavior of all material constituents, a linear relation between volume averages of the stress and strain field over the whole unit cell is sought in the form

$$\bar{\boldsymbol{\sigma}} = \bar{\mathbb{C}} : \bar{\boldsymbol{\varepsilon}} \tag{2.6}$$

where $\bar{\mathbb{C}}$ is the 4th order effective stiffness tensor.
It is important to say that small deformations are always assumed in the present work, so that $\boldsymbol{\sigma}$ is the usual Cauchy stress tensor and the strain $\boldsymbol{\varepsilon}$ is defined as

$$\boldsymbol{\varepsilon} = \frac{1}{2}\left(\boldsymbol{\nabla u} + (\boldsymbol{\nabla u})^{\boldsymbol{T}}\right) \tag{2.7}$$

with respect to the displacement field $\boldsymbol{u}$. The symbols $\boldsymbol{\nabla}()$ and $()^T$ appearing in the last equation denote the gradient and transposition operator respectively.
In the most general anisotropic case, the tensor $\bar{\mathbb{C}}$ possesses 21 independent components. Similarly to what is done in [60] for the case of a RVE, they can be determined by prescribing in sequence six independent loadings in the form $\bar{\boldsymbol{\varepsilon}}^{(1)}, \dots, \bar{\boldsymbol{\varepsilon}}^{(6)}$ to the unit cell according to equation (2.1). The

corresponding average stresses $\bar{\boldsymbol{\sigma}}^{(1)}, \dots, \bar{\boldsymbol{\sigma}}^{(6)}$ may then be used to set up a linear system of equations for the effective elastic constants.
The calculated effective stiffness tensor can be decomposed into an isotropic and an anisotropic part as follows:

$$\bar{\mathbb{C}} = \bar{\mathbb{C}}^{\text{iso}} + \bar{\mathbb{C}}^{\text{ani}} \tag{2.8}$$

The former can be further written as

$$\bar{\mathbb{C}}^{\text{iso}} = 3\bar{k}\mathbb{S} + 2\bar{\mu}\mathbb{D} \tag{2.9}$$

where $\mathbb{S}$ and $\mathbb{D}$ are the spherical and deviatoric projection tensors [61], which form an orthogonal basis for isotropic 4th order tensors. The quantities $\bar{k}$ and $\bar{\mu}$ represent the effective bulk and shear modulus respectively and may be calculated as

$$\bar{k} = \frac{1}{3}\frac{\langle \bar{\mathbb{C}} | \mathbb{S} \rangle}{\langle \mathbb{S} | \mathbb{S} \rangle}, \qquad \bar{\mu} = \frac{1}{2}\frac{\langle \bar{\mathbb{C}} | \mathbb{D} \rangle}{\langle \mathbb{D} | \mathbb{D} \rangle} \tag{2.10}$$

where $\langle \cdot \mid \cdot \rangle$ indicates the scalar product between 4th order tensors. Conversion to effective Young's modulus and Poisson's ratio is performed via the basic relations

$$\bar{E} = \frac{9\bar{k}\bar{\mu}}{3\bar{k} + \bar{\mu}}, \quad \bar{\nu} = \frac{3\bar{k} - 2\bar{\mu}}{2(3\bar{k} + \bar{\mu})} \tag{2.11}$$

The last two quantities can be naturally compared to experimental values for ductile iron available in the literature.
Finally, an anisotropy index may be obtained as [36]

$$I_a = \left(\frac{\left\langle \bar{\mathbb{C}} - \bar{\mathbb{C}}^{\text{iso}} \middle| \bar{\mathbb{C}} - \bar{\mathbb{C}}^{\text{iso}} \right\rangle}{\langle \bar{\mathbb{C}} | \bar{\mathbb{C}} \rangle} \right)^{1/2} \tag{2.12}$$

The latter parameter provides an indication of the degree of anisotropy of the unit cell. Therefore, it is particularly useful to discuss the validity of the periodic approach for modeling the ductile iron mechanical response, which is known to be isotropic at the macro-scale.

2.4.2 Inelastic case

It must be emphasized that the homogenization analysis presented in the previous section is valid provided that the entire unit cell behaves elastically. And correspondingly, only effective elastic properties can be determined. On the other hand, it is sometimes very useful to be able to calculate a few effective non-linear parameters as well, like the proof stress or the maximum tensile strength during tensile testing. In order to achieve this, a different type of homogenization technique may be adopted, based on the application of the plane-remain-plane constraint widely used in other studies on ductile iron, e.g. [16][44][53]. Essentially, tensile testing along one of the three unit cell principal axes (shown in figure 2.1) can be simulated by increasing the distance between two opposite faces by a prescribed amount, at the same time enforcing all six faces to remain plane and to conserve the same orientation. This means that all points on a given face will experience the same displacement in the direction perpendicular to the face itself. The magnitude of such displacement is set arbitrarily on the two faces orthogonal to the assumed loading axis, whereas on

the remaining four it is determined by imposition of an average stress-free condition. At each time during “uniaxial” loading, the effective stress and strain can then be calculated by averaging the corresponding microscopic quantities over the entire unit cell volume. From the tensile stress-strain curve obtained in this way, other useful effective properties, like those mentioned before, can be easily estimated.

Chapter 3
Ferrite matrix behavior

This chapter is dedicated to the analysis of the constitutive behavior of the matrix of ductile iron. Specifically, the grade GJS-400 according to UNI-EN 1563 is considered throughout the analysis. This choice is motivated by the relevance of this material to the industrial community, particularly to the wind energy sector, and by its relatively homogeneous ferrite matrix, which considerably simplifies the theoretical treatment of the problem.

3.1 Thermo-mechanical data

3.1.1 Isotropy assumption

Following the authors listed in table 1, who have all modeled ductile iron using micro-mechanical approaches, the constitutive behavior of the ferrite matrix at the micro-scale is assumed to be isotropic. One should bear in mind, however, that the size of the matrix grains is usually comparable with the size of the graphite particles, as figure 1.3 indicates. Therefore, any calculation of the local residual stress field around the nodules should, in principle, consider the anisotropy of the single ferrite crystals. On the other hand, the bcc lattice of the ferrite exhibits only a moderate anisotropy, with the apparent Young's modulus changing between 130 and 280 GPa according to the direction considered (**PAPER III**). In addition, from a practical point of view, by taking the grain anisotropy into account one would obtain results which depend on the local grain orientation. In contrast, the present work aims at determining only an approximate average value for the residual stress around the nodules, indeed independent of the particular local crystallography.

3.1.2 Experimental observations

On the basis of the isotropy assumption just discussed, the mechanical behavior of the ferritic ductile iron matrix can be studied by creating a polycrystalline material with similar metallurgical features and testing it at the macro-scale [62]. Uniaxial tensile curves at room temperature obtained in this way for the GJS-400 matrix show the typical ductile response of low carbon steel [24]. Initially, a linear elastic stage is seen, followed by yielding at approximately 300 MPa and subsequent hardening up to about 440 MPa. This ductile behavior finds direct confirmation in in-situ observations of plastic deformation and damage evolution in ductile iron samples strained in tension [26].
Concerning the matrix properties at higher temperature, which are crucial for the accurate calculation of the residual stresses developing during manufacturing, very little information can be

found in the literature. In [16] an indication of the variation of Young's modulus, CTE and initial yield stress up to 1000 °C is given. Unfortunately, this data is not sufficient to fully characterize the non-linear constitutive response of the ferrite above room temperature, which is expected to show some kind of time-dependent behavior in analogy with steels of similar composition [63]. In order to gain a deeper insight into this unexplored topic, an experimental campaign was carried out, as described in the following.

Steel with 0.036 wt% C, 1.99 wt% Si and 0.1 wt% Mn was cast in Y-blocks as shown in figure 3.1 (a). From the bottom part of each block, cylindrical specimens with gauge length 28 mm and gauge diameter 5 mm were machined (figure 3.1 (b)) and tested in tension at different temperatures and different strain rates using the Gleeble 1500 [64] thermo-mechanical simulator, see figure 3.1 (c). The obtained results, which are preliminary and have not been published yet, are reported in figure 3.2. Unfortunately, the average grain size of the tested material is in the order of 1 mm, therefore much larger compared to that of real GJS-400 castings. As a consequence, according to the Hall-Petch equation, the stress required to promote inelastic deformation is likely under-estimated. However, the curves of are still very valuable, as they indicate that already at 350 °C some strain-rate sensitivity starts to be present, which becomes very pronounced at 700 °C.

The reason for the abnormal grain size is probably the particular chemical composition adopted. Silicon and carbon are known to be ferrite- and austenite-stabilizing elements respectively [65]. The high concentration of the former combined with the unusually low amount of the latter gives rise to an alloy whose ferritic field stretches from liquidus all the way down to room temperature. The lack

(a)

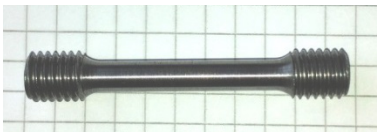

(b)

(c)

Figure 3.1 – Ductile iron matrix mechanical testing. **(a)** Cast Y-blocks, with composition similar to the GJS-400 ferrite matrix but different grain size. **(b)** Cylindrical specimen machined from the bottom of the Y-block. **(c)** Setup for high-temperature tensile testing using the Gleeble 1500 simulator.

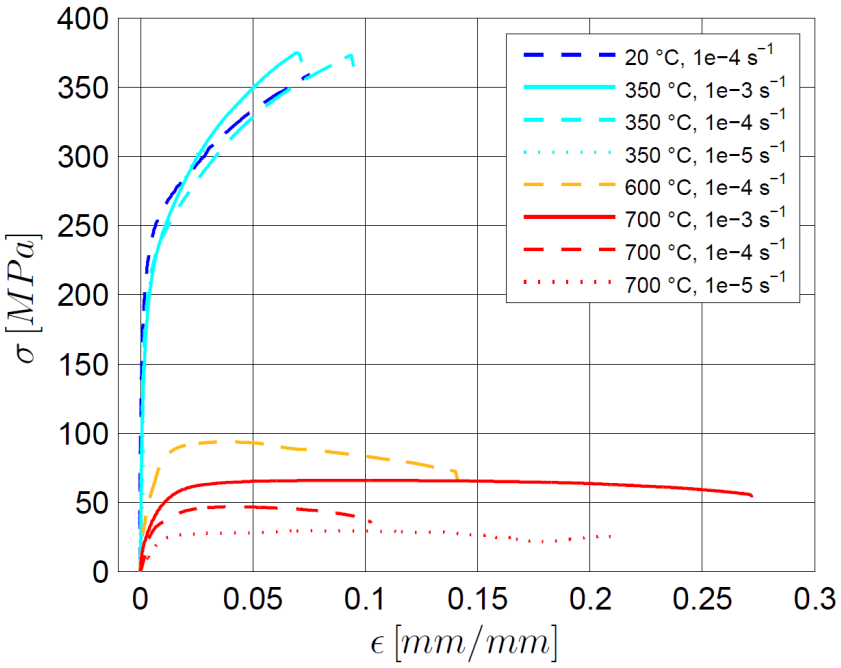

Figure 3.2 – Experimental engineering stress-strain tensile curves at different temperatures and different strain rates for the ferrite matrix material.

of any eutectoid transformation, with associated nucleation of newer, smaller crystals, can partly explain the very coarse grains observed in the final microstructure.

It has to be mentioned that this issue seems to be well-known in electrical steels, which are a class of metallic materials with composition similar to the one investigated here [66][67]. Their microstructure is normally refined by hot-rolling until the desired grain size is eventually obtained. However, in the present case hot-rolling does not seem to provide indisputable advantages. Indeed, if on the one hand it would refine the grains, on the other it would destroy the as-cast microstructure completely, closing the porosity, redistributing the segregation, etc. As a consequence, grain refinement via increased cooling rate during solidification might be, in the author's opinion, a better option. Unfortunately, this strategy could not be tested in the context of the present work due to time and budget constraints.

3.2 Constitutive models

The experimental findings presented in the previous section clearly show that ductile damage is important during loading at room temperature, whereas time-dependent inelastic deformation seems to be the most relevant phenomenon at intermediate temperatures.

3.2.1 Ductile damage at room temperature: Lemaitre's model

A simple way to model the observed ductile behavior of the ferrite matrix at room temperature is by using continuum damage models, like those developed by Lemaitre [68] and Bonora [69]. In the present work, the isotropic version of the former is adopted, whose constitutive equations may be summarized as follows:

- additive strain decomposition:

$$\boldsymbol{\varepsilon}^{tot} = \boldsymbol{\varepsilon}^{el} + \boldsymbol{\varepsilon}^{pl} + \mathbf{I}\alpha\Delta T \tag{3.1}$$

- elastic constitutive law:

$$\widetilde{\boldsymbol{\sigma}} = \mathbb{C}^{el} : \boldsymbol{\varepsilon}^{el}, \qquad \widetilde{\boldsymbol{\sigma}} = \boldsymbol{\sigma}/(1-D) \tag{3.2}$$

- yield function:

$$f = \frac{\sigma_e}{1-D} - \sigma_y(r) \leq 0, \qquad \sigma_e = \left(\frac{3}{2}\mathbf{s} : \mathbf{s}\right)^{1/2}, \qquad \mathbf{s} = \boldsymbol{\sigma} - \mathbf{I}\frac{tr(\boldsymbol{\sigma})}{3} \tag{3.3}$$

- flow rule:

$$\dot{\boldsymbol{\varepsilon}}^{pl} = \frac{\partial f}{\partial \boldsymbol{\sigma}}\dot{\lambda} \tag{3.4}$$

- isotropic hardening rule:

$$\sigma_y = k(r + r_0)^n, \qquad r_0 = \left(\frac{\sigma_y^0}{k}\right)^{1/n} \tag{3.5}$$

- effective plastic strain increment and hardening parameter increment:

$$\dot{p} = \frac{\dot{r}}{1-D}, \qquad \dot{r} = \dot{\lambda} \tag{3.6}$$

- damage evolution law:

$$\dot{D} = \left(\frac{Y}{S}\right)^s \dot{p}, \qquad if\ p > p_{crit} \tag{3.7}$$

- energy release rate:

$$Y = \frac{\sigma_e^2 R_v}{2E(1-D)^2}, \qquad R_v = \frac{2}{3}(1+\nu) + 3(1-2\nu)\left(\frac{tr(\boldsymbol{\sigma})}{3\sigma_e}\right)^2 \tag{3.8}$$

- consistency condition:

$$f \leq 0, \qquad \dot{\lambda} \geq 0, \qquad f\dot{\lambda} = 0 \tag{3.9}$$

where the meaning of the different symbols is explained in table 2. It may be noticed that 9 material parameters are required: 3 thermo-elastic (E, ν, α), 3 related to plastic flow (σ_y^0, k, n) and finally 3 related to damage (p_{crit}, S, s). In principle, an additional parameter specifying the conditions at which crack nucleation occurs would be necessary: however, in the present investigations damage never exceeds 0.1, which is well below the critical fracture initiation threshold for common metals and alloys [70].

Table 2 – Symbols used in the definition of Lemaitre's damage model.

$\boldsymbol{\varepsilon}^{tot}, \boldsymbol{\varepsilon}^{el}, \boldsymbol{\varepsilon}^{pl}$	Total, elastic, plastic strain tensor	R_v	Triaxiality function
$\mathbb{C}^{el}$	4th order elastic stiffness tensor	f	Yield function
$\mathbf{I}$	2nd order identity tensor	D	Damage variable
$\boldsymbol{\sigma}$	Stress tensor	$S,\ s$	Lemaitre's damage evolution parameters
$\tilde{\boldsymbol{\sigma}}$	Effective stress tensor	Y	Energy release rate
$\mathbf{s}$	Stress deviator	$k,\ n$	Isotropic hardening parameters
σ_e	Equivalent von Mises stress	p	Equivalent plastic strain
$\sigma_y,\ \sigma_y^0$	Actual, initial yield stress	p_{crit}	Critical effective plastic strain for damage evolution
E	Young's modulus		
ν	Poisson's ratio	r	Hardening variable
α	Thermal expansion coefficient	λ	Plastic multiplier
ΔT	Temperature variation		

3.2.1.1 Parameter identification via 1D analytical solution

The parameters entering Lemaitre's model are usually determined from knowledge of the damage evolution history in loaded specimens, obtainable by means of well-established experimental methods [71]. Nevertheless, often such information is either not available or too expensive to obtain for the specific material at hand. Under these circumstances, it is common practice to identify the material constants on the basis of an optimization analysis aiming at minimizing the error between the predicted numerical results and a reference uniaxial tensile curve [70]. However, the use of such procedure in combination with a numerical resolution of the mathematical model exhibits three main disadvantages. First of all, it requires the use of an optimization algorithm coupled with a numerical tool for solving the system of differential equations (3.1) – (3.9), which makes the method elaborate and time-consuming. Secondly, the numerical solution procedure in itself is complicated by the "softening" behavior of the damaged material at sufficiently large strains. Thirdly, the produced values for the material parameters are affected, in addition to the experimental & optimization uncertainty, by the error associated with the numerical discretization adopted.

With the aim of overcoming all the above-mentioned aspects, an analytical solution to the isotropic Lemaitre's model for the specific case of uniaxial tensile testing is presented in **PAPER I**. The key-point in the derivation is the choice of the hardening law (3.5), which allows obtaining an integral relationship between total strain and effective stress. By means of the generalized binomial theorem [72], it is proved that the relation between the former quantities after damage initiation can be expressed as

$$\varepsilon^{tot}(\tilde{\sigma}) = \bar{\varepsilon}^{tot} + \frac{\tilde{\sigma} - \bar{\sigma}}{E} + \\ +2B \sum_{m=0}^{+\infty} \frac{(-1)^m}{2m+1} \binom{\beta}{m} \left[\left(1 - \frac{\tilde{\sigma}^{z+1}}{\tilde{\sigma}_{lim}^{z+1}} \right)^{m+1/2} - \left(1 - \frac{\bar{\sigma}^{z+1}}{\tilde{\sigma}_{lim}^{z+1}} \right)^{m+1/2} \right] \tag{3.10}$$

in which $\tilde{\sigma}_{lim}$, $\bar{\varepsilon}^{tot}$, $\bar{\sigma}$, B, m, β, z simply denote combinations of the basic nine parameters entering the constitutive equations of the model. As discussed in **PAPER I**, expression (3.10) can be used in combination with a Matlab script for fast identification of the material parameters for the ferrite ductile iron matrix, on the basis of the uniaxial tensile curve reported in [24].

3.2.1.2 Numerical implementation for the plane-stress case

In the context of the present work, some preliminary investigations were carried out using a 2D periodic plane-stress model instead of the full 3D unit cell of figure 2.1. The reason was to enable a direct comparison with in-situ microscopy observations taken on the surface of tensile test specimens, where the stress state is biaxial in nature.

Whereas the 3D numerical implementation of the Lemaitre's isotropic model may be performed relatively easily following the implicit discretization scheme suggested in [73], the corresponding 2D plane-stress formulation presents more challenges. Indeed, if a traditional displacement-based implicit finite element code is used, a natural complication arises in ensuring the out-of-plane components of the stress tensor to be zero at the end of each load increment. This is due to the fact that the solution procedure is strain-driven, and the stress components are treated as dependent variables. To cope with the problem, three different strategies can be used, as discussed in [74]: A) direct inclusion of the plane-stress constraint at the Gauss point level, B) addition of a plane-stress constraint at the global structural level, C) use of plane-stress projected constitutive equations at the Gauss point level. The first two solutions are usually easier to implement, but at the price of higher computational time. As a consequence, approach C) is to be preferred whenever possible, as it leads to more efficient computational procedures due to the fact that only the relevant in-plane stress and strain components are considered [75]. Quite surprisingly, in spite of this important advantage, no scientific works concerning the plane-stress projected implementation of Lemaitre's model had been published in literature before 2016.

To fill the gap, a new, fully implicit integration procedure is presented in the second part of **PAPER I**. Due to space limitation, the associated mathematical expressions, which are quite lengthy, are not reported here. However, it is emphasized that the entire system of discretized equations is reduced to a single, scalar, non-linear equation, which may be easily solved using a standard Newton's method. Furthermore, in order to ensure achieving maximum convergence rate at the global finite element level, a suitable expression for consistent tangent modulus is also derived.

3.2.2 Visco-plastic flow at intermediate temperatures: Peric's model

The tensile stress-strain curves of figure 3.2 indicate that between room temperature and the temperature of the eutectoid transformation, the mechanical response of the ferrite matrix is affected by the time-scale of the experiment. Therefore, its behavior should be described by a model capable of taking the strain-rate sensitivity into account. A possible option is the model proposed by Peric [76], which is defined by the same additive strain decomposition, elastic law, yield function and flow rule stated in expressions (3.1) – (3.4) (where the damage variable is set to zero), with the addition of the following equation

$$\dot{\lambda} = \begin{cases} \frac{1}{\mu}\left[\left(\frac{\sigma_e}{\sigma_y}\right)^{1/m} - 1\right] & \text{if } f(\boldsymbol{\sigma}, \sigma_y) > 0 \\ 0 & \text{if } f(\boldsymbol{\sigma}, \sigma_y) \leq 0 \end{cases} \tag{3.11}$$

which replaces the consistency condition (3.9) in dictating the magnitude of the inelastic deformation. The material constants μ and m denote the viscosity-related parameter and the rate-sensitivity parameter respectively. It may be noticed that Peric's model is, after all, very similar to the well-known Perzyna's model [77]. Its advantage is that in the limit $\epsilon \to 0$ the classic time-independent von Mises formulation with yield stress σ_y is recovered exactly, whereas the Perzyna's model shows a limiting time-independent yield stress of twice σ_y [74].

Chapter 4
Thermo-mechanics of the nodules

This chapter summarizes the main results concerning modeling the thermo-mechanical behavior of the graphite nodules. Conceptually, it is divided into two parts. In the first one, the so-called phenomenological approach is discussed, which has been the traditional choice for modeling the nodules in the past. Basically, this methodology rests on postulating a certain type of behavior a priori, e.g. isotropic linear elastic, and on determining the associated constitutive parameters via direct or indirect measurements. The second part of the chapter presents instead an innovative micro-mechanical approach, where the internal structure of the nodules is modeled explicitly. The advantage is that the mechanical properties of the single building blocks forming the graphite particles are known to a higher level of accuracy, so that the overall uncertainty on the nodules' behavior may be reduced significantly.

4.1 Phenomenological approach

4.1.1 Early results: Extension of previous authors' findings

The vast majority of authors who have tried to model the nodules in the past have assumed that they behave as isotropic linear elastic particles. However, as already explained in section 1.1.3.2, the main complication with this choice is the difficulty of selecting suitable values for the corresponding elastic constants, i.e. Young's modulus and Poisson's ratio. In an effort to solve this issue, some initial investigations by the author, published in a series of two conference papers [78][79], were dedicated to find the nodules' best approximation in terms of a homogeneous isotropic material, on the basis of the response generated at the macro-scale.

The new analyses were inspired by the investigations of Bonora & Ruggiero [16], which represented the state-of-the-art in the field at the time, and focused on modeling the early deformation stage of GJS-400 during tensile testing. To make the results comparable with those of the previous authors, a periodic unit cell approach was adopted and the formation of local residual stresses was modelled by simulating a uniform temperature decrease from a temperature of 1000 °C, neglecting any phase transformation. Poisson's ratio and CTE of the nodules were taken equal to those of common grades of isotropic polycrystalline graphite, whereas Young's modulus was varied systematically to generate a range of effective properties, to be compared against experimental values for GJS-400. Furthermore, the nodule-matrix interface was modeled as a frictionless contact interface and ductile damage occurring in the ferrite was simulated using Lemaitre's model.

Most importantly, three additional aspects, overlooked in reference [16], were also taken into account. First of all, the loading conditions for nodules located on the surface as well as in the bulk of the material were recreated, by employing both 2D plane-stress and full 3D periodic unit cells. Secondly, a maximum load carrying capacity for the graphite was set, according to a simple elastic-perfectly plastic formulation based on the J2-flow theory of plasticity. Thirdly, the effective Poisson's ratio, in addition to the effective Young's modulus, was calculated according to the homogenization procedure described in section 2.4.2 and compared with experimental data.
The results of the analyses showed that, when inelastic deformation of the graphite is neglected, the effective properties are controlled by the twofold effect played by the nodules' elastic stiffness. On the one hand, larger values of the nodules' Young's modulus make the entire unit cell stiffer, as the nodule offers greater resistance to being deformed to an "oval" shape by the surrounding matrix during tensile loading. On the other hand, they drive higher residual stresses at the end of the manufacturing stage, increasing the risk of promoting plastic deformation in the matrix, with consequent loss of stiffness at the macro-scale. The interaction between these two factors generates the 3-stage behavior visible in figure 4.1 (a) and (b), whose nature is explained in detail in [78][79]. It has to be mentioned that the vertical shift of the 2D plane-stress curve is simply a consequence of how the volumetric concentration of graphite is defined in either a 2D or 3D model.
The results for the 3D formulation do not change significantly if a yield threshold is set for the nodules according to typical values for isotropic polycrystalline graphite [17]. In fact, during the manufacturing process the stress field developing in the nodule is mainly hydrostatic. Therefore, no yielding can occur according to the J2-flow theory of plasticity. During subsequent loading, deviatoric stress components build up, but they are not sufficient to cause an appreciable amount of yielding, at least within the small deformation range investigated (up to 0.5 % strain). It should be kept in mind, however, that the choice of adopting the J2-flow formulation for the graphite was

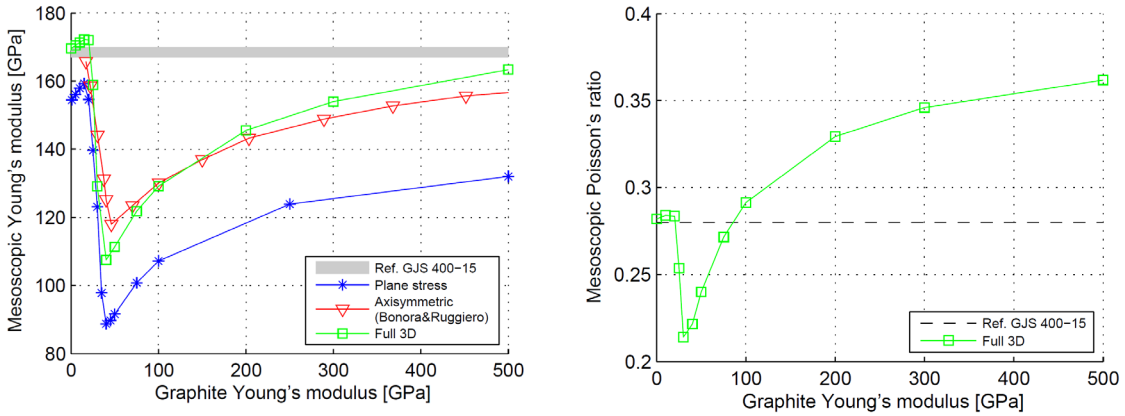

(a) **(b)**

Figure 4.1 – Predicted effective **(a)** Young's modulus and **(b)** Poisson's ratio as a function of the graphite particles' Young modulus, for different unit cell geometries. The nodules are assumed to behave as isotropic linear elastic particles, with Poisson's ratio and CTE equal to those of common grades of isotropic polycrystalline graphite.

dictated by the necessity of setting, in the simplest way, a maximum load carrying capacity for the nodules. There are no solid grounds to sustain that such theory really reflects the physical behavior of the graphite particles.
Despite simplistic and affected by large uncertainties on several important parameters, these initial investigations allowed drawing a fundamental conclusion: the combined stiffness and strength of the nodules cannot be sufficient to give rise to yielding in the matrix at the end of the manufacturing process. Indeed, if that happened, the matrix would remain in the plastic state upon subsequent tensile loading, causing a too low effective Young's modulus and a too high effective Poisson's ratio compared to the measured values for ductile iron, the last effect due to plastic incompressibility of the ferrite.

4.1.2 Inadequacy of the assumption of isotropy and homogeneity

The analyses presented in the previous section attempted to identify suitable values for the nodules' isotropic elastic constants without making any initial assumptions on their admissible range. That is, no value for the nodules' Young modulus was discarded a priori, mainly as a consequence of the large spread of seemingly possible choices documented in table 1. On the other hand, it is clear that having an indication of where the elastic constants should approximately lie would simplify the problem considerably.
This idea is at the basis of the analysis presented in **PAPER II**, which rests on three fundamental assumptions:

1. The nodules can be considered as mechanically isotropic;
2. Their behavior can be described by a linear elastic model;
3. Their basic building blocks are graphite platelets with hexagonal symmetry.

The last point is justified by TEM observations of the nodules' internal structure, which will be described in detail in the next section.
It follows from assumption 1 that the building blocks, which are strongly anisotropic, must then be arranged in a statistically homogeneous way throughout each nodule to provide overall isotropic elastic properties. This observation is crucial, as it allows establishing a domain of physically admissible values for the nodules' isotropic moduli. Indeed, according to the discussion on the statistical order of polycrystalline materials reported in [80], assuming that nodules are statistically homogeneous and isotropic polycrystalline aggregates consisting of many single anisotropic graphite crystals, then 1st order upper and lower bounds on the isotropic elastic constants can be derived, corresponding to Voigt and Reuss bounds. Moreover, if the distribution of the local elastic moduli is not correlated with the crystal shape and size (for instance, it is excluded that, on average, lengthy platelets are stiffer in one direction than compact platelets), then tighter 2nd order bounds can be established, corresponding to Hashin-Shtrikman bounds [81]. Finally, if no particular crystal shape and size is distinguishable, implying that many platelet shapes and sizes exist in an irregular composition, even tighter 3rd order bounds can be derived.
Explicit analytical expressions for the 1st, 2nd and 3rd order bounds in the case of crystals with hexagonal symmetry may be found in [9], [82] and [83] respectively. By using the former in combination with the anisotropic elastic constants of a single graphite crystal, reported in table 3,

Table 3 – Elastic constants of a single graphite crystal with hexagonal symmetry [84]. Entries are in GPa.

C11	C44	C12	C13	C33
1107	4.4	175	-2.5	29

bounds on the isotropic bulk and shear moduli of the polycrystalline aggregate may be determined. These can be subsequently converted into bounds on Young's modulus and Poisson's ratio, following the procedure outlined in **PAPER II**.

The calculated bounds may be used to define admissible domains for the isotropic constants, which are reported graphically in figure 4.2. At first glance, it may be seen that an increase in the homogeneity requirement leads to a contraction of the corresponding admissible domain. This is particularly evident for the maximum admissible value of the Young's modulus, which drops from the value of 521.3 GPa obtained by applying 1st order bounds to 272.2 GPa for 3rd order bounds; conversely, the minimum value increases from 1.3 GPa to 4.2 GPa. It is worth remarking that within each domain, intermediate Young's modulus values are characterized by a very large variation in Poisson's ratio, which may actually become negative. In principle, this possibility should not be excluded a priori, both theoretically and physically, as there is experimental evidence of polycrystalline materials whose cross-section expands when stretched under uniaxial tension [85]. It is also interesting to observe that most of the authors listed in table 1 have assumed values for Young's modulus and Poisson's ratio in the range 4 ÷ 36 GPa and 0.2 ÷ 0.3 respectively, which lie outside any domain.

As said previously, the isotropy assumption on the nodules' mechanical behavior holds only if the graphite platelets are arranged in a statistically homogeneous way throughout the nodules themselves. Consequently, their isotropic moduli must lie at least within the 1st order domain indicated in figure 4.2, henceforth simply denoted as admissible domain. This motivates a new type of inverse analyses, similar to the ones presented in the previous section, where, in addition to allow

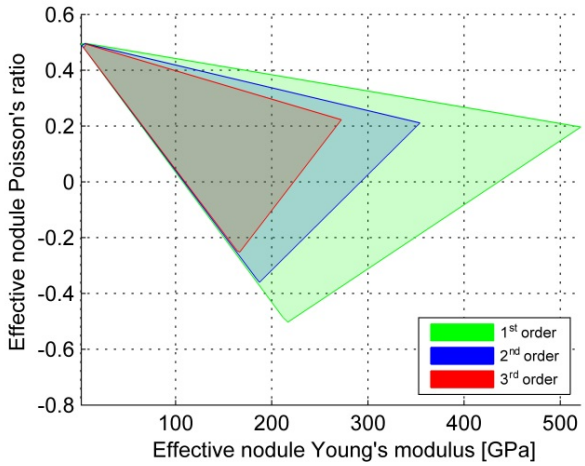

Figure 4.2 – Admissible domains for the nodules' isotropic elastic moduli, according to different levels of statistical order assumed for the graphite crystals.

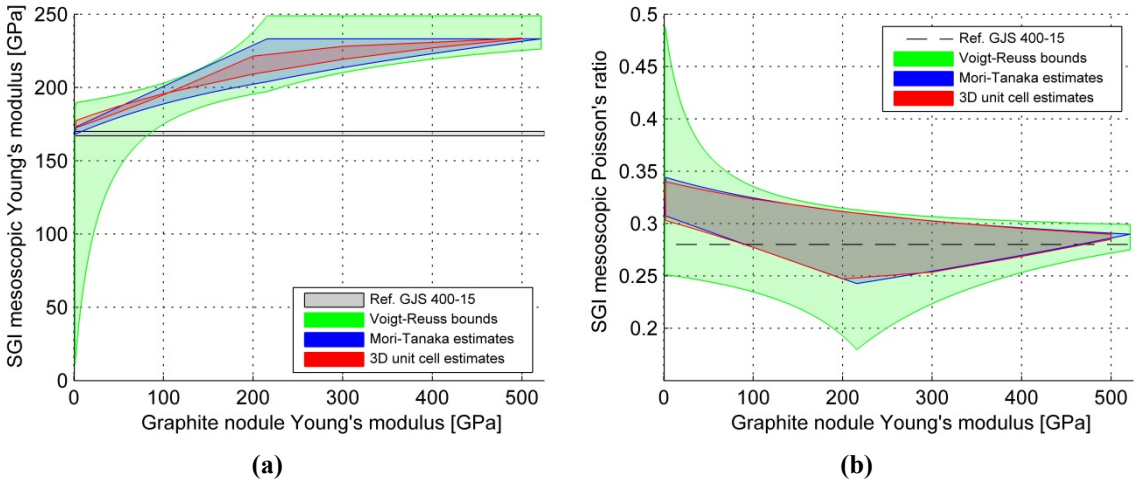

Figure 4.3 – Effect of statistically admissible nodules' constants on the effective **(a)** Young's modulus and **(b)** Poisson's ratio of ductile iron. For a given value of the nodules' Young's modulus, bounds and estimates are derived considering the full range of values for Poisson's ratio indicated by the 1st order domain of figure 4.2.

matching the effective elastic properties of ductile iron, the best set of nodules' elastic constants is also required to belong to such domain. The main results of these new investigations are concisely presented in the following paragraphs, whereas the full details are available in **PAPER II**.

Figure 4.3 shows the effects of choosing values for the nodules' elastic constants which belong to the admissible domain, under the assumptions of linear elastic behavior of the ferrite matrix and perfect bonding with the graphite. In both figure 4.3 (a) and (b) three contours are plotted in addition to the reference literature values for the GJS-400 elastic constants. The first one indicates the extension of the well-known Voigt-Reuss bounds for a two-phase composite: for each value of the nodules' Young's modulus, when the Poisson's ratio is varied within the corresponding admissible domain, the ductile iron elastic response is bounded by the green area. The second and third contours, instead, represent estimates for the effective elastic properties obtained via the analytical Mori-Tanaka approach [49] and via the numerical 3D unit cell model described in section 2.2.

From an analysis of figure 4.3 (a) it may be concluded that values for the nodules' Young's modulus above approximately 100 GPa must be rejected, as the horizontal band indicating experimental measurements lies well outside the Voigt-Reuss bounds in that range. Conversely, with focus on the data of figure 4.3 (b), no values can be excluded on the basis of the same principle, because the reference Poisson's ratio always falls in between the bounds. Nevertheless, analytical and numerical estimates clearly indicate that the experimental value of GJS-400 can only be matched by assuming the nodules' Young's modulus to be above 100 GPa. Therefore, there is an evident contradiction between values which allow matching the effective Young's modulus of ductile iron and those which are necessary for matching the effective Poisson's ratio.

It should be emphasized, however, that the last consideration is based on a series of analyses where two important factors are ignored: the possibility of having a weak nodule-matrix interface and/or matrix plastification induced by the formation of local residual stresses during manufacturing.

Concerning this, further investigations presented in **PAPER II** demonstrate that for a wide range of admissible nodule's elastic parameters, the experimental Young's modulus of ductile iron can be actually matched by inducing a controlled amount of plastic deformation in the matrix during manufacturing. In fact, as explained in the previous section, the initial yielding of the ferrite strongly affects the effective stiffness of the unit cell upon subsequent loading. Therefore, the former can be artificially tuned by varying the magnitude of the residual stress field via selecting a convenient stress-free temperature in the range 0 ÷ 750 °C, i.e. the temperature from which the residual stresses are assumed to build up. On the other hand, it is also shown in **PAPER II** that yielding of the matrix drives unrealistically high values of the effective Poisson's ratio, together with an asymmetry of the tension-compression response which does not find confirmation in experimental findings [86][87]. Inclusion of a yield threshold for the nodules according to the von Mises criterion does not sort any effect on the results, for the reasons discussed earlier.
In summary, it does not seem possible to find values for the nodule's isotropic elastic constants which belong to the admissible domain of figure 4.2 and, at the same time, allow recovering the effective elastic properties of ductile iron measured at the macro-scale. The reason is probably that the nodules cannot be assumed homogeneous and isotropic at a micro-scale, at least from a micromechanical viewpoint. In other words, they cannot be considered as constituted of graphite platelets which are arranged in a statistically homogeneous way. This means that a satisfactory elastic constitutive description should take into consideration the intrinsic inhomogeneity and anisotropy of the nodules as well.
It has to be remarked that it might still be possible to find values for the nodules' Young's modulus and Poisson's ratio which allow a good match with the ductile iron response recorded during uniaxial testing. After all, this is what many of the authors listed in table 1 have done. However, it is difficult to justify such isotropic parameters on the basis of physical grounds and, in addition, there is no guarantee that they will work for different loading conditions. Moreover, even if they provide good results when used as input for homogenization procedures, the description they offer in terms of stress & strain fields in and around the nodules is quite disputable. Obviously, this point is of utmost importance in the context of the present thesis, whose ultimate aim (see section 1.2) is precisely the accurate description of the local residual stress state developing at the micro-scale.

4.2 Nano-structure-based modeling

From the arguments adduced so far, it may be concluded that the phenomenological approach is likely inappropriate for the present purposes. A viable alternative, presented in **PAPER III** and **PAPER IV**, consists in modeling the intrinsic structure of the graphite nodules explicitly. In this way, their mechanical behavior turns out to be defined by properties and spatial arrangement of the elementary units they are made of. In this respect, it has to be mentioned that a few pioneering works along this line were done already in the late '80s [88][39]. Nevertheless, the scarce experimental knowledge available at the time, combined with the limitations of the analytical approach adopted, prevented devising models consistent with the elastic properties of ductile iron measured at the macro-scale.

4.2.1 The nodules' internal structure from recent experimental investigations

Figure 4.4 (a) shows the microstructure of a typical grade of ferritic ductile iron. From a chemical perspective, each nodule is made of a small nucleus containing complex oxides and sulfides, which served as nucleation site during solidification [89], and a much thicker outer shell of graphitic nature, which represents the major part of the nodule by volume. As shown by electron microscopy investigations [90], the latter one may be subdivided into two parts, according to the schematic of figure 4.4 (b): a bulk region, constituted by oriented graphite crystals arranged into conical sectors radiating from the nodule center to the outer periphery, and a superficial graphite layer, characterized by smaller grains with high misorientation.

It seems to be well established now that the basic building blocks forming the conical sectors in the internal region are graphite platelets consisting of graphene layers piled up with only few crystallographic defects [37][91]. These structural units have thicknesses in the sub-micrometer range and appear to be elongated along the graphene planes. From a continuum point of view, they can be described on the basis of the hexagonal unit cell reported in figure 4.4 (c) [29], where the c-direction is orthogonal to the graphene layers. Within a sector, the platelets are stacked on each other, with the c-direction constant and oriented approximately radially. Nevertheless, the stacking is not perfect, and rotations about the c-axis occur on an almost regular basis, defining domains of similar orientation [92].

In contrast, only a few investigations have been reported in literature so far regarding the nature of the superficial structure of the nodules. Monchoux *et al.* [90] described a microcrystalline, highly disorientated layer approximately 1.5 micrometer thick over an overall diameter of approximately 30-40 microns, giving a powder-like diffraction diagram; later, the presence of microcrystalline areas at the extreme outer periphery of the nodules was also observed by Theuwissen *et al.* [93][94]. According to the former authors, the existence of this surface layer would be connected to the amount of graphite which precipitates during solid state cooling, due to the reduced carbon

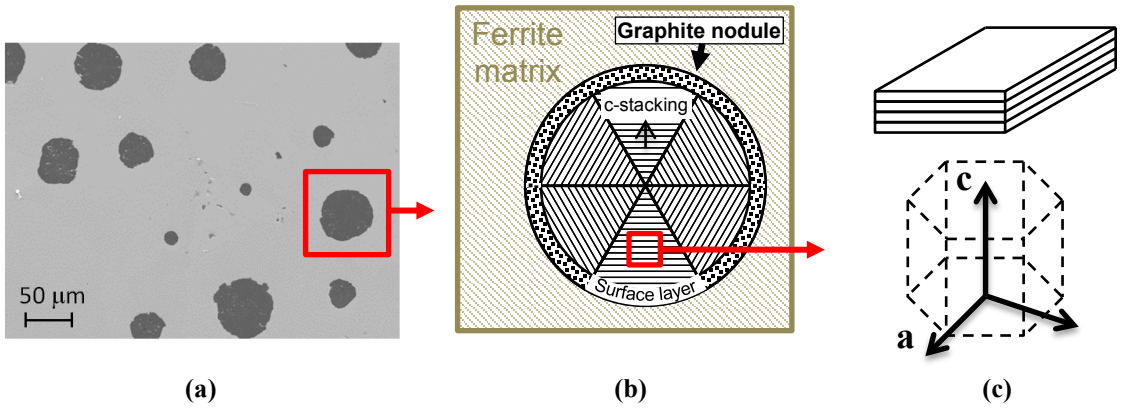

Figure 4.4 – Nodules' structure at different scales. **(a)** Micrograph of ferritic ductile iron. **(b)** Schematic of the division of a nodule into an oriented internal bulk region and an external surface layer. **(c)** Platelets arrangement within a single sector and hexagonal graphite unit cell.

solubility in the metallic matrix. This hypothesis is also supported by the extensive work of Di Cocco *et al.* [18][95][96], who, in order to justify some experimental results, speculated on the existence of a gradient of mechanical properties within the nodules connected to the different stages of growth during solidification. On the basis of thermodynamic calculations, they suggested a value for the thickness of the layer associated with solid state cooling of 10 % the final nodule radius, which is in very good agreement with Monchoux *et al.* findings. However, the reason for the different structure of the graphite crystals in this region compared to the bulk of the nodule remains unclear.

4.2.2 A new thermo-elastic anisotropic model for the nodules

On the basis of the experimental studies presented in the previous section, a new anisotropic micromechanical model for the nodules is proposed, which is physically consistent with their intrinsic structure. Each graphite particle is assimilated to a sphere composed of two concentric regions: an internal core and an external shell with thickness equal to 10 % the radius. The former is additionally subdivided into a progressive number of conical sectors by means of sectioning with orthogonal planes passing through the sphere center. In this way, internal regions with 8, 48 and 80 partitions are obtained, as shown in figure 4.5, which qualitatively cover the range of values suggested by the experimental investigations.
The sectors are assigned the thermo-elastic properties characteristic of unidirectional graphite, reported in table 3 and in figure 4.5. For the sake of clarity, it is recalled at this point that the general thermo-elastic relation for a material exhibiting hexagonal symmetry takes the form [97]

$$\begin{Bmatrix}\sigma_{11}\\ \sigma_{22}\\ \sigma_{33}\\ \sigma_{13}\\ \sigma_{23}\\ \sigma_{12}\end{Bmatrix} = \begin{bmatrix} c_{11} & c_{12} & c_{13} & 0 & 0 & 0 \\ c_{12} & c_{11} & c_{13} & 0 & 0 & 0 \\ c_{13} & c_{13} & c_{33} & 0 & 0 & 0 \\ 0 & 0 & 0 & c_{44} & 0 & 0 \\ 0 & 0 & 0 & 0 & c_{44} & 0 \\ 0 & 0 & 0 & 0 & 0 & (c_{11}-c_{12})/2 \end{bmatrix} \cdot \begin{Bmatrix} \varepsilon_{11}-\alpha_1\Delta T \\ \varepsilon_{22}-\alpha_1\Delta T \\ \varepsilon_{33}-\alpha_3\Delta T \\ 2\varepsilon_{13} \\ 2\varepsilon_{23} \\ 2\varepsilon_{12} \end{Bmatrix} \tag{4.1}$$

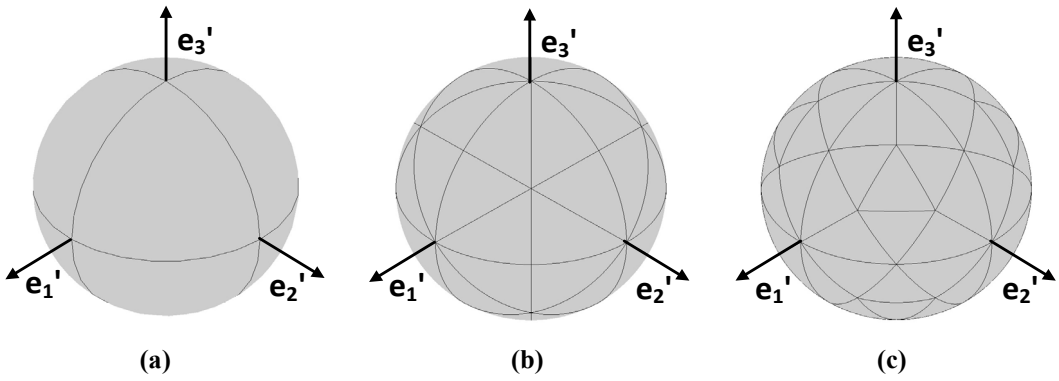

Figure 4.5 – Modeling the graphite nodules according to their real internal structure. Subdivision of the internal nodule core region into **(a)** 8 **(b)** 48 and **(c)** 80 sectors respectively.

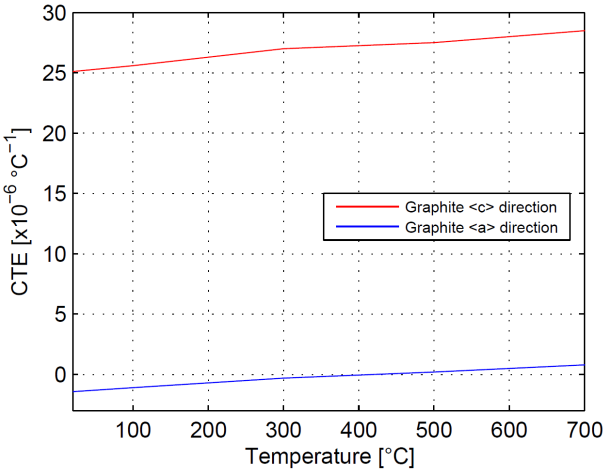

Figure 4.6 – Anisotropic CTE along the principal directions of a unidirectional graphite crystal [98].

where the index 3 denotes the c-direction as defined in figure 4.4 (c). In the model such direction is identified, within each conical partition, by the axis connecting the center of the sphere to the centroid of the related spherical triangle, which is formally defined as the element of the spherical surface identified by a given sector. As a body exhibiting hexagonal symmetry is transversely isotropic with respect to the basal plane (i.e. the graphene layers in this case), the other two principal material directions can be set arbitrarily without affecting the analysis. It has to be remarked that if the c-direction is prescribed parallel to the radius pointwise throughout the entire nodule core, a spherically anisotropic description is obtained, which is essentially equivalent to assuming an infinite number of conical sectors.

For the external shell instead, which is supposed to be representative of the superficial layer of the nodule, a linear elastic isotropic behavior is assumed. This is motivated by the much smaller size of the crystallites in that region and their high degree of misorientation. As a consequence, the elastic properties are assumed to be equal to those of commercial grades of fine grain isotropic graphite, reported in table 4. In particular, a variation of Young's modulus between 9.7 and 10.9 GPa is considered, associated with the uncertainty on the real size of the crystallites. Regarding Poisson's ratio, a sharp value of 0.2 can be chosen instead, which is quite standard for polycrystalline graphite. Finally, the CTE can be assumed equal, to a first approximation, to the average of the CTEs along the principal graphite crystallographic directions, given in figure 4.6.

Table 4 – Physical properties of commercial grades of fine grain isotropic graphite produced by Asbury Carbons [99].

Type	Fine Grain	Super Fine Grain	Ultra Fine Grain
Grade	IPG	IPG15	IPG19
Average grain size (micron)	25	8	4
Young's modulus (GPa)	9.7	10.1	10.9
Compressive strength (MPa)	79	106	135

4.2.3 Predictions of effective thermo-elastic properties

The model proposed in the previous section may be used for modeling the behavior of the single nodule contained in the 3D unit cell of figure 2.1. Accordingly, the associated thermo-elastic effective properties, obtainable by means of the general homogenization technique described in section 2.4.1, provide a simple, indirect method of validation. Indeed, if they do not agree with experimental values for ductile iron measured at the macro-scale, the model has to be inevitably rejected.

Before presenting the results of the homogenization procedure as reported in **PAPER IV**, a few important aspects have to be discussed. First of all, it has to be recalled that such mathematical procedure assumes elastic behavior of all micro-structural constituents, meaning that possible inelastic deformation in the matrix cannot be taken into account. Secondly, the anisotropy of the model representing the nodule implies that the orientation of its main axes with respect to the unit cell could potentially play an important role. This issue is analyzed in depth in **PAPER III** for a model very similar to the one proposed in the previous section. It is shown that variations of only less than 1 % on the effective elastic quantities are recorded by changing the relative orientation between the nodule and the unit cell, meaning that this parameter can be reasonably neglected in the analyses. Finally, it has to be remarked that the anisotropy of the nodule could make the entire unit cell anisotropic, to a certain extent. This would be in contrast to the observed behavior of ductile iron at the macro-scale, which is undoubtedly isotropic. Fortunately, this inconsistency is not supported by the values of the anisotropy index, equation (2.12), which remain below 1.5 % throughout all calculations.

Having clarified these points, the focus is now turned to the outcome of the elastic homogenization procedure. As visible in figure 4.7 (a) and (b), the effective values for Young's modulus at room temperature and average CTE in the interval 700 ÷ 20 °C are in excellent agreement with experiments, according to the assumed range 9.7 to 10.9 GPa for the nodule surface layer stiffness. Within this range, it may also be seen from the error bars that a variation in the number of conical sectors from a minimum of 8 up to plus infinite produces a change in the effective Young's modulus of 2-3 GPa. This is related to the increment in the nodule core stiffness associated with the tendency of the graphite platelets to form a rigid shell as the number of sectors increases, as thoroughly explained in **PAPER IV**. Regarding the third and last effective isotropic thermo-elastic quantity, namely Poisson's ratio, calculated values turn out to be in the range of 0.278 to 0.280. Again, there is a very good match with experimental measurements, which have been reported between 0.275 and 0.280 according to different sources [4][86]. Finally, figure 4.7 (c) and (d) provide an indication of the sensitivity of the predicted effective elastic properties to variations of the surface layer thickness, for the particular choice made of the other model parameters. It is seen that in order to match the experimental Young's modulus, the former quantity has to have a value of approximately 10 % the nodule radius, which is in agreement with the TEM observations and thermodynamic calculations discussed in the last paragraph of section 4.2.1.

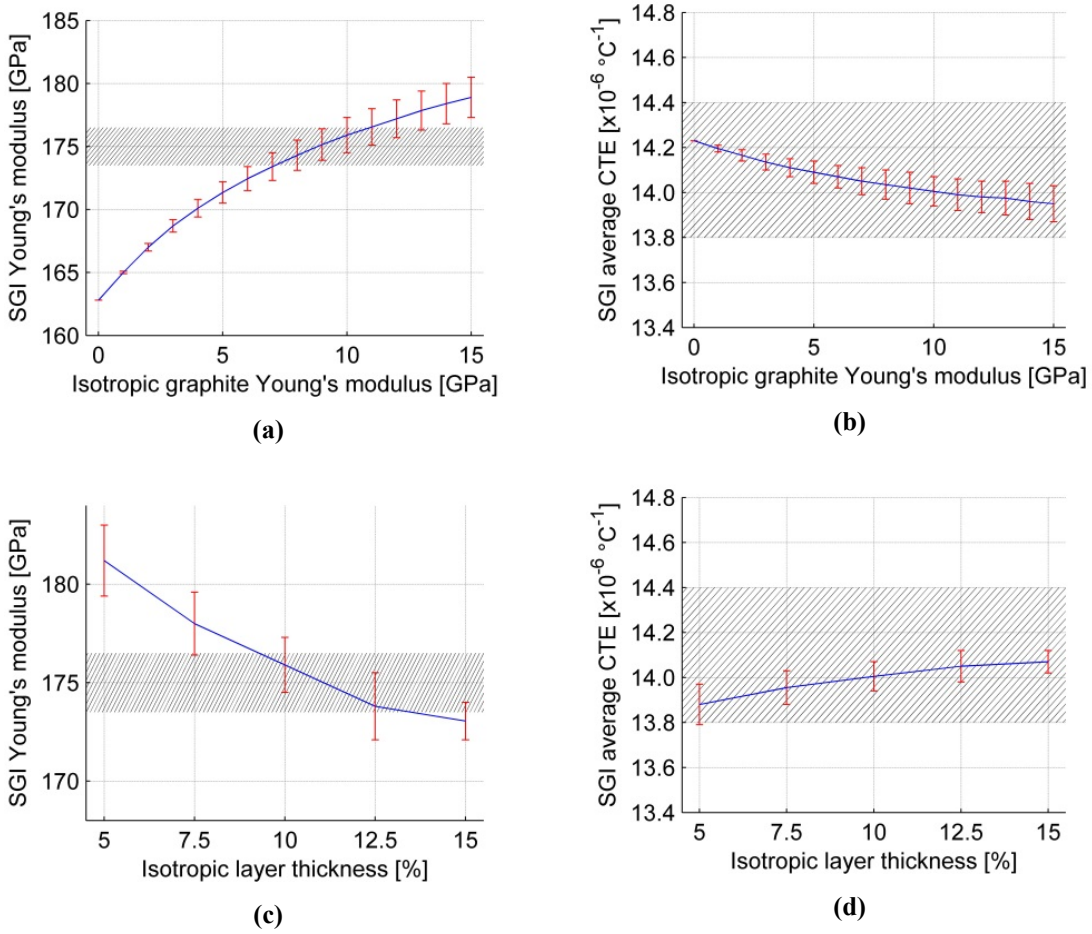

Figure 4.7 – Predicted effective thermo-elastic properties as a function of the superficial nodule layer Young's modulus **(a,b)** and thickness **(c,d)**. In (a,b) the thickness is fixed at 10 % of the nodule radius, whereas in (c,d) the Young's modulus is set at 10 GPa. In all plots the error bars denote the spread due the variation in the number of conical sectors contained in the nodule core region. The hatched intervals indicate reference experimental values for GJS-400 ductile iron.

Chapter 5
Local residual stresses

The anisotropic model for the graphite nodules presented in the previous chapter enables studying the interaction with the surrounding matrix in a novel, quantitative fashion. The following sections describe how this can be exploited to investigate the magnitude of the local residual stresses which develop in the ductile iron micro-structure during manufacturing.

5.1 Micro-structural volumetric variations during manufacturing

The accurate numerical prediction of the local residual stresses arising in ductile iron requires a preliminary, careful examination of all the different stages of the manufacturing process. To some extent, this task is simplified by the fact that the GJS-400 grade is normally used in the as-cast state, without any additional heat-treatments, implying that only solidification and solid-state cooling need to be taken into consideration. These two steps were already described in detail in section 1.1.1 for an alloy of nearly-eutectic composition, under the assumption of thermo-dynamic equilibrium. Here, however, a different type of analysis is performed, which focuses on identifying the volumetric variations experienced by the different microstructural phases over time. Indeed, as explained in the introduction, these represent the driving force behind the formation of local stresses in the material.

With reference to the slice of the Fe-C-Si phase diagram shown in figure 1.2, it may be assumed that, upon cooling, ductile iron follows the path indicated by the red dashed arrow. During solidification, the mushy consistence of the material implies that only hydrostatic stresses can, to a certain extent, develop in addition to the basic metallostatic pressure. In principle, these might be promoted by the well-known graphitic expansion associated with the eutectic reaction. Thermo-dynamic arguments suggest, in fact, that during this stage the radius of the nodules grows up to approximately 90 % of its final value [18]. However, this expansion is fully compensated by the shrinkage connected to the liquid-to-solid transition of the matrix, and as a matter of fact, the overall macroscopic effect is a slight contraction of the material.

Upon completion of the eutectic transformation, solid-state cooling in the austenitic field begins. During this stage, the nodules expand another 5 %, while the surrounding metallic phase undergoes thermal contraction. Nevertheless, it seems reasonable to assume that the volume mismatch between the two is compensated by plastic flow of the soft austenitic matrix, and any tension is released almost instantaneously due to its very low flow stress, probably in the order of a few MPa [63].

As explained in **PAPER IV**, the situation becomes more complicated when the eutectoid interval is reached, as on the one hand the matrix transforms into ferrite, hence increasing in volume and creating more space for the graphite particles, but on the other hand the nodules expand too, due to

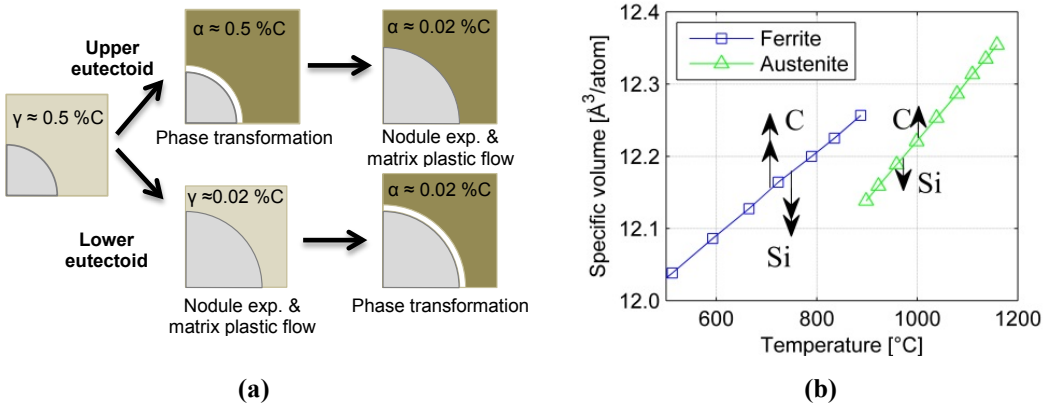

Figure 5.1 – **(a)** Schematic of the volume variations occurring during the eutectoid transformation. **(b)** Specific volume as a function of temperature for pure iron [100], with indication of the effects of C and Si. Double arrows indicate a stronger effect compared to single arrows.

carbon migration from the metallic phase. It is clear that the complex thermo-mechanical interactions between all phases involved could only be fully understood by simulating the nucleation and growth of the single ferritic grains. Nevertheless, as the interest here is only in capturing the global effect, a simplified analysis is performed, as schematically shown in figure 5.1 (a). The starting point is to assume that the eutectoid reaction takes place simultaneously throughout the matrix at a fixed temperature, which may correspond to either the upper T_U or the lower T_L eutectoid temperature.

In the first case, the austenite containing 0.5 wt% carbon transforms into supersaturated ferrite at T_U, with a resulting volume expansion ΔV. Subsequently, the ferrite gradually releases the excess of carbon until the equilibrium concentration of 0.02 % is achieved at T_L. Meanwhile, the nodule radius increases approximately 5 %, which is far more than the ΔV associated with the austenite-ferrite transformation. Therefore, no "clearance" between the nodule and the matrix remains at the end of the process.

Conversely, in the second case the austenite cools down without transforming from T_U to T_L, gradually loosing carbon. During this stage, the nodule expands to almost its final size, promoting plastic deformation in the matrix. This should not look unrealistic, as at temperatures close to the eutectoid transformation the compressive strength of the graphite particles is much larger compared to the flow stress of the matrix, as already emphasized in section 1.1.3.1. Subsequently, the low-carbon austenite transforms into ferrite at T_L with an associated ΔV.

The main difference between the two scenarios just described is that in the first one no differential expansion between the nodules and the matrix remains, whereas in the second one a differential volume change is produced. This is equal to the ΔV of the austenite-ferrite transformation, which, for pure iron, is of approximately 1 % at 910 °C [101]. The main ductile iron allying elements, namely C and Si, affect this volume variation in two ways: by increasing/decreasing the transformation temperature and by changing the lattice parameter to a different extent in the ferrite and in the austenite. As explained by Cockett and Davis [102], silicon increases the transformation temperature, therefore reducing the associated "jump" between the specific volume curves shown in

figure 5.1 (b). At the same time, it also promotes a larger lattice contraction in ferrite than in austenite: both factors contribute to reduce ΔV. Carbon instead generates exactly the opposite effect. Cockett and Davis measured ΔV for an iron alloy with 0.005 wt% C and increasing Si content, concluding that the primary variable controlling ΔV was the transformation temperature. For instance, with 1.45 wt% Si, the phase change occurred at 1020 °C with a ΔV of 0.79 %, which is approximately the value that may be calculated from the curves for pure iron of figure 5.1 (b) assuming the transformation to take place at the same temperature. Hence, assuming T_L to be equal to 700 °C for the ductile iron at hand, ΔV may be reasonably estimated from figure 5.1 (b) as 1.4 %.
In conclusion, according to the first hypothesis no differential expansion would take place during the eutectoid transformation, whereas according to the second one the matrix would expand locally 1.4 % more than the nodules in volume. As what happens in reality is probably something in between the two extremes, an average value of 0.7 % is considered in the present work.
Finally, from T_L down to room temperature the carbon mass contained in the nodules remains approximately constant. On the other hand, thermomechanical interactions with the matrix still arise from the mismatch in the CTE values, as discussed in section 1.1.2.

5.2 Numerical predictions

5.2.1 Model setup

In light of the arguments put forth in the previous section, it seems unlikely that thermo-mechanical interactions of significant magnitude develop in the microstructure before the eutectoid transformation. Therefore, the formation of local residual stresses may be reasonably simulated by subjecting the 3D unit cell of figure 2.1 to cooling starting from the eutectoid transformation down to room temperature, accounting for the different thermal expansion of the nodule and the matrix. To a sufficient degree of approximation, the temperature variation may be assumed uniform over the entire unit cell volume. This is justified by the reduced size of the latter compared to the length-scale over which temperature gradients normally arise in real casting processes.
Concerning the properties of the unit cell constituents, the thermo-elastic anisotropic model proposed in section 4.2.2 can be naturally adopted to describe the mechanical behavior of the graphite nodule. Regarding the matrix instead, an obvious choice would be the model due to Peric (see section 3.2.2), which may effectively account for possible visco-plastic deformation in the ferrite. Unfortunately, any reliable identification of the associated material parameters is prevented by the uncertainty on the experimental data available, which is limited to the curves of figure 3.2. As a consequence, within the context of the present work, a simple linear elastic relation is considered. Clearly, this choice is valid provided that the magnitude of the local stresses remains significantly below the yield stress of the ferrite over the entire temperature interval considered.

5.2.2 Equivalent CTE of the nodules

As stated in section 1.1.2, direct CTE measurements for the nodules are not available in the published literature. However, on the basis of the newly-developed anisotropic model, numerical estimates may be obtained by performing a series of finite element simulations considering one

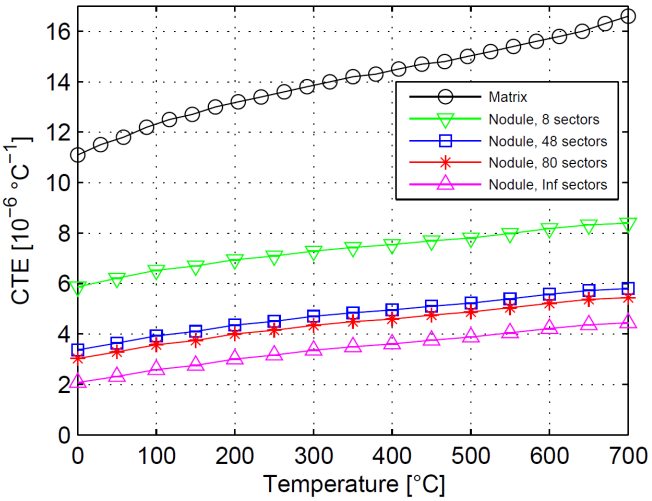

Figure 5.2 – Nodule equivalent CTE for different numbers of conical sectors in the internal core, compared to the CTE of the ferrite matrix.

nodule alone, without the presence of the surrounding matrix, and recording its average contraction during cooling. An equivalent CTE may then be defined as

$$CTE_{eq} = \frac{1}{3V}\frac{dV}{dT} \tag{5.1}$$

where V denotes the nodule volume.

Figure 5.2 compares the calculated values for CTE_{eq}, taken from **PAPER IV**, with the CTE of the ferrite matrix. It may be noted that the predicted average thermal contraction of the nodule is always smaller than that of the matrix over the entire temperature range examined, independently of the number of sectors the nodule core is made of. This confirms the speculations of section 1.1.2 about the existence of a driving force for the formation of local residual stresses in ductile iron, as the free shrinkage of the ferrite during cooling is hindered by the presence of the embedded graphite particles.

In addition, figure 5.2 shows that the larger the number of conical sectors, the smaller the corresponding equivalent CTE. This is because the graphite in the core region contracts almost only in the c-direction, which is oriented approximately radially according to the schematic of figure 4.4 (b) and (c). However, the contraction towards the nodule center is opposed by the high in-plane stiffness of the graphite platelets with different orientation located in the neighboring sectors. Obviously, this effect becomes more pronounced when the distance between adjacent partitions is decreased, or, equivalently, the number of sectors is increased. When this number tends to infinity, the nodule core behaves as a sort of shell with high circumferential stiffness, subjected to a negative internal pressure which builds up progressively as the temperature diminishes. In section 5.3.1, the consequence of this particular loading configuration will be discussed more thoroughly in relation to some experimental findings.

5.2.3 Residual stresses in and around the nodules

A comprehensive set of finite element simulations of the residual stress state in and around the graphite particles in ductile iron were carried out on the basis of the model described in section 5.2.1. The results, which are documented in detail in **PAPER IV,** show that very large hoop stresses are generated during cooling at the extreme outer periphery of the nodule core, as visible in figure 5.3. This is primarily due to the high in-plane stiffness of the graphite platelets in that region, which strongly opposes the compressive action generated by the greater thermal contraction of the matrix. In particular, extremely high compressive stresses, above 1 GPa, are recorded at the points of contact between two or more conical sectors. These values are probably unrealistic, as local buckling and/or fracture of the single platelets are likely to occur. Nevertheless, as inelastic deformation is not considered in the model, the stresses arising at these concentration points propagate through the nodule surface layer into the matrix. In order to diminish their unphysical impact on the overall analysis, it is convenient to present results for the residual stresses in the matrix not in terms of the maximum stress recorded, but by using an average criterion. More specifically, two average values are considered: one related to a fictitious shell enveloping the nodule and another one associated with the external boundary layer of the unit cell depicted in figure 2.1, both having a thickness of 10 % the nodule radius. They are assumed to be representative of the overall stress state in the matrix regions closest to and most distant from the nodule respectively. In this way, a global indication of the residual stress gradient existing in the ferrite matrix can be obtained.

From an analysis of the related data reported in figure 5.4 (a) and (b), two major observations can be made. First of all, the mean von Mises stress is approximately one order of magnitude larger close to the nodule than at the unit cell boundary, but, at the same time, the mean hydrostatic stress shows almost negligible variations between these two different locations. The reason is that near the interface the matrix is compressed along the nodule radial direction, whereas it is stretched circumferentially, hence generating stress components which are primarily deviatoric. Accordingly, a steep gradient in the von Mises stress is recorded. In addition, a strong influence of the nodule core partitioning is observed: it appears that by varying the number of conical sectors from 8 to 48,

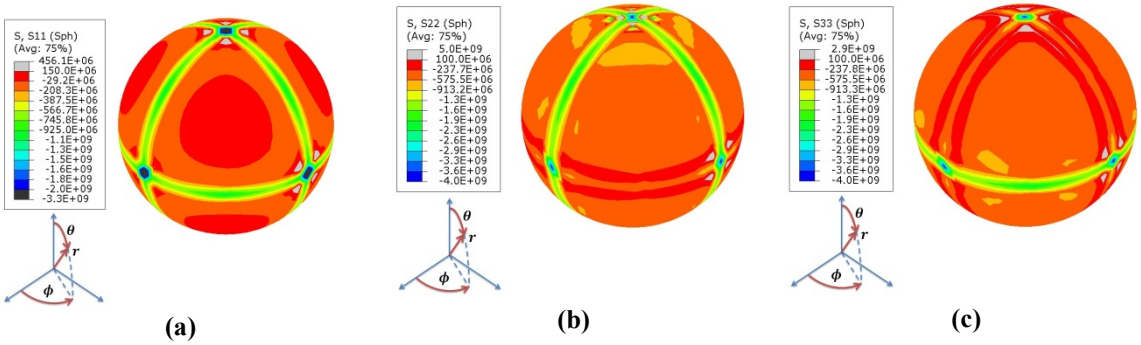

Figure 5.3 – **(a)** Radial, **(b)** circumferential and **(c)** meridional residual stress components on the outer part of a nodule core with 8 internal sectors. The spherical coordinate system used has the origin in the nodule center and the zenith direction points upward. Units are Pa. The upper contour limits have been artificially reduced to avoid the spurious influence of a few elements close to the contact points between 4 sectors.

a 50 % increment in the values of both deviatoric and hydrostatic mean stresses is obtained, followed by another 50 % increase when their number tends to infinite. This effect is simply due to the increased CTE mismatch between the matrix and the nodule which arises from the reduced thermal contraction of the latter one, already pointed out in connection with figure 5.2.
Finally, figure 5.4 (c) and (d) show how the mean local residual stresses in the matrix are affected by a variation of the graphite volume fraction within the range 7.0 to 13.0 %. This interval is representative of values found in typical grades of ductile iron, obtained by minor changes in the composition, solidification parameters, etc. Not surprisingly, it is seen that by increasing the nodule relative volume, the surrounding stress field increases accordingly. Nevertheless, while the other mean stress quantities almost double throughout the considered interval, the mean von Mises stress around the nodule, which is by far the most critical in terms of absolute values, exhibits only a modest 3 % variation.

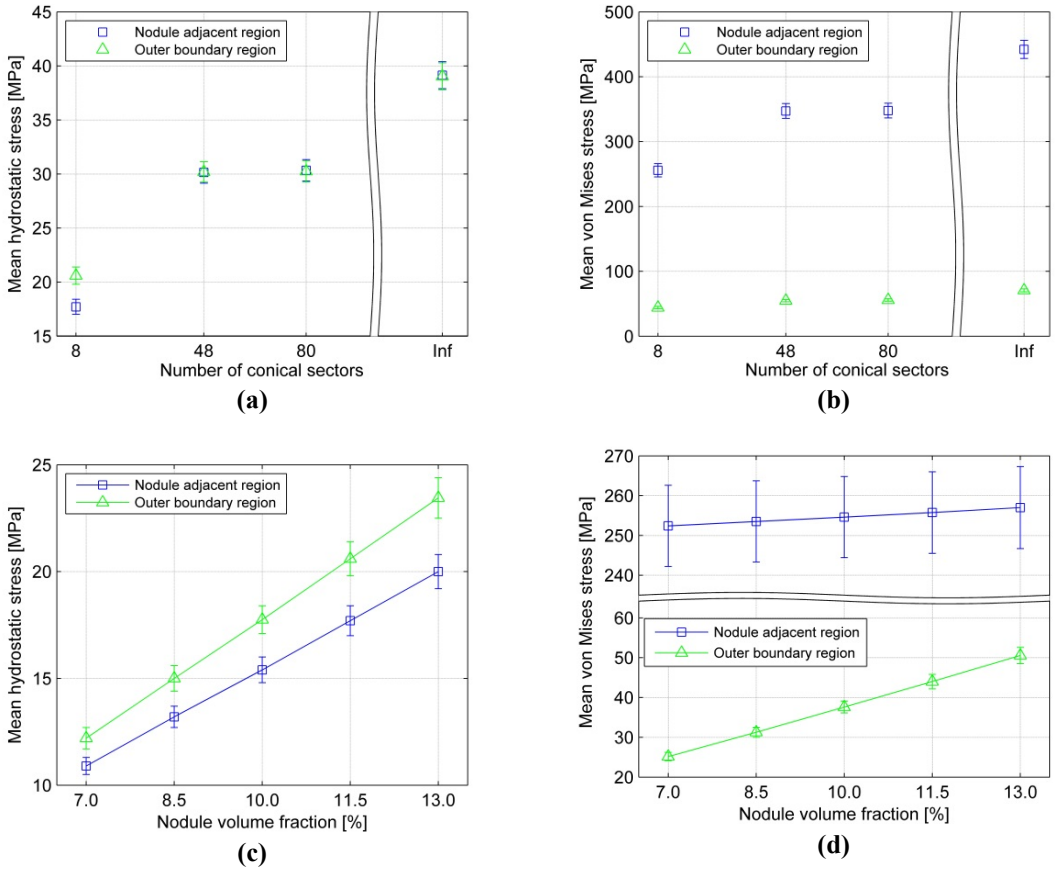

Figure 5.4 – Mean hydrostatic and von Mises local residual stresses in the matrix as a function of the number of conical sectors in the nodule core **(a, b)** and the graphite particles volume fraction **(c, d)**. In (a, b) the volume fraction is 11.5 %, whereas in (c, d) the number of sectors is 8. The nodule-adjacent region is identified as the matrix shell enveloping the nodule with a thickness of 10 % its radius. Similarly, the outer boundary region corresponds to the 10 % thick unit cell boundary layer. All error bars indicate the spread due the variation in the nodule surface layer Young's modulus between 9.7 and 10.9 GPa.

5.3 Link to experimental findings

5.3.1 The nodules' failure mode

While investigating the ferritic ductile iron behavior under loading, Di Cocco *et al.* [96] reported the presence of an internal form of damage in some nodules sitting on the sample surface, which was referred to as "disgregation". It was characterized by the formation of cracks originating from the center of the particles and propagating radially. The fact that this type of failure was detected during both tensile and fatigue testing suggests that it is, to a certain extent, independent of the specific loading condition applied. Rather, it might be related to the presence of a specific residual stress state in the nodules, representing the main driving force for fracture.

More specifically, it was observed during tensile testing of ductile iron that the nodules tend to separate from the matrix [25], hence becoming mechanically "isolated". Nevertheless, a non-negligible stress field probably still exists inside them, associated with the anisotropic thermal deformation of the graphite occurring during manufacturing. As explained in the last paragraph of section 5.2.2, the free contraction in the c-direction of the platelets located in a given sector is hindered by the presence of the adjacent partitions with different orientations. This implies that during cooling tensile stresses locally develop perpendicularly to the graphite platelets, as shown in figure 5.5 (a). The predicted stresses are particularly high in the center of the nodule and along the interfaces between different sectors, where, additionally, a weaker mechanical bonding probably exists. It is not difficult to realize that the local change in orientation of these tensile forces could have a "tearing" action in the latter regions, at the same time promoting the formation of a "void" in the center of the particle. As long as a nodule remains fully embedded in the ferrite, the superposed compressive action of the matrix probably prevents any crack opening, but when debonding begins, the probability of having this "disgregation" mechanism increases. By comparing figure 5.5 (b), which schematically shows the expected failure mode for a debonded particle, with figure 5.5 (c), taken from the work of Di Cocco *et al.,* support for the argument is found.

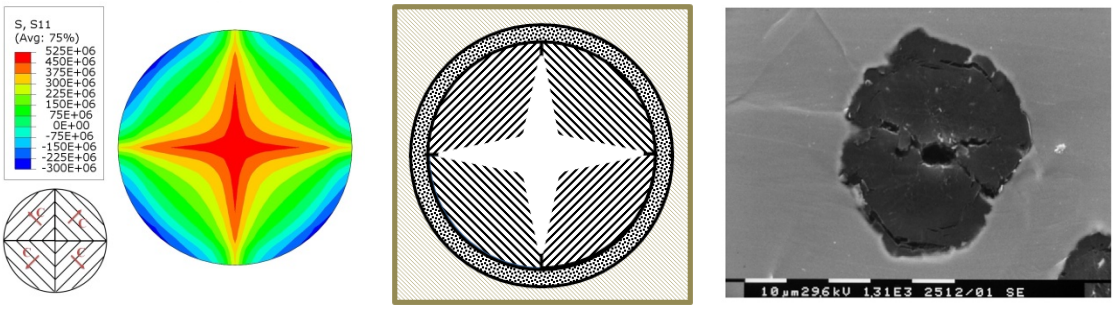

(a) **(b)** **(c)**

Figure 5.5 – "Disgregation" mechanism in the bulk of a nodule. **(a)** Stress component locally orthogonal to the graphite platelets, over the middle section of a nodule core with 8 sectors, in Pa, after cooling neglecting the presence of the matrix. **(b)** Schematic of the expected failure mode. **(c)** Scanning electron microscope image of the lateral surface of a mini tensile specimen at 13 % engineering strain, reprinted from [96] with permission of Elsevier. Radial cracks propagating from the center of the partially debonded nodule are visible.

5.3.2 The nodules' internal structure

The present findings indicate that the nodules are potentially subjected to significant compressive forces during cooling. This suggests a simple explanation for the variation in the graphite crystal structure between the surface and the bulk of the nodules, which, as stated in section 4.2.1, is still a source of debate. In fact, Oku *et al.* [103] investigated the effects of compressive pre-stresses on fine-grain isotropic graphite, and found that upon subsequent compression the material Young's modulus was reduced, whereas its strength was increased. The changes were more pronounced at high temperatures and were connected to rotation and cracking of the single graphite crystallites, which tended to assume a low-energy configuration with the stiff basal planes oriented perpendicularly to the applied stress. It is not unrealistic then to hypothesize that something similar could happen during the manufacturing process of ductile iron. As long as the nodules are not subjected to significant external pressure, i.e. until the end of solidification, graphite keeps growing in conical sectors. However, when compressive hoop stresses start building up in the outer nodule layers due to contraction of the surrounding solid matrix, this growing condition is no longer energetically favorable. As a consequence, smaller crystallites with different orientation form, hence generating the surface layer observed by the authors cited in section 4.2.1.

5.3.3 The nodules' size effect

According to figure 5.4 (a) and (b), the graphite particles drive the formation of high deviatoric residual stresses in the surrounding matrix which strongly increase in magnitude as the number of conical sectors grows. Considering the model overestimation due to the linear elastic assumption, which will be discussed in detail in the next chapter, a variation of at least 50 MPa in the stress magnitude close to the nodule is still expected when the number of core partitions is varied from 8 to 48. This is approximately 1/3 of the maximum stress amplitude that can be applied to the GJS-400 grade in order to achieve a target fatigue life of 2.5 million cycles under axial loading [104]. An obvious question then arises with regard to the factors controlling such number. Intuitively, one would expect that larger nodules contain a higher number of partitions. This seems to find confirmation in several experimental works on the subject [91][92][93][105], where some sectors appear to branch at a certain distance from the nodule center, even though this could be an artificial effect due to sectioning of a 3D geometry with a plane. However, if confirmed, it would suggest the presence of a material size-effect, i.e. a non-scaling relation between particle size and magnitude of the surrounding residual stresses, which could provide additional justification for the observed link between ductile iron fatigue resistance and dimensions of the nodules [106][107]. Dedicated experimental investigations would be useful to verify this potential connection and its relative importance compared to other factors.

Chapter 6
Experimental validation via direct techniques

As explained in the introduction, the past uncertainty on the nodules' properties and on the local residual stress magnitude, perfectly exemplified by table 1, was primarily associated with difficulties in performing direct measurements of any kind. While the nodules' mechanical response could still, to a certain extent, be probed using indentation instruments, no technique was available to characterize the residual stress state around nodules fully embedded in the ductile iron matrix. Today, however, with the advent of new, powerful X-ray diffraction techniques based on synchrotron radiation, the possibilities offered by materials characterization have improved dramatically compared to those available at the time when most of the studies reported in table 1 were carried out.
In this context, this chapter reviews first the traditional nano-indentation technique, highlighting its limitations when applied to testing the nodules' properties. After that, it presents the successful application of one of these novel X-ray diffraction methods to measure the residual stress distribution around a single graphite nodule lying beneath the material surface. Needless to say, such data form an ideal basis to validate the numerical model developed in chapter 5.

6.1 Nano-indentation

6.1.1 Introduction to the technique

Instrumented nano-indentation is a well-established technique which is widely used for probing mechanical properties of materials at length scales in the sub-micrometer range. Its high scientific relevance combined with a relatively simple experimental setup have attracted the attention of many researchers in the last decades, and several dedicated review papers exist which offer extensive accounts of the subject, e.g. [108][109][110].
In essence, a nano-indentation test consists in pressing a 3-sided pyramidal Berkovich indenter onto the surface of the sample under investigation and recording the resulting applied force vs penetration curve (figure 6.1 (a)). The main difference compared to traditional indentation techniques performed at the micron or millimeter scale is that the area of the residual impression left on the material is normally not measured, due to its much reduced size. For this reason, mechanical properties are usually estimated on the basis of the loading and unloading characteristics alone. Concerning this, a number of methods have been proposed so far which allow deriving parameters related to elastic and plastic material behavior, fracture toughness, creep,

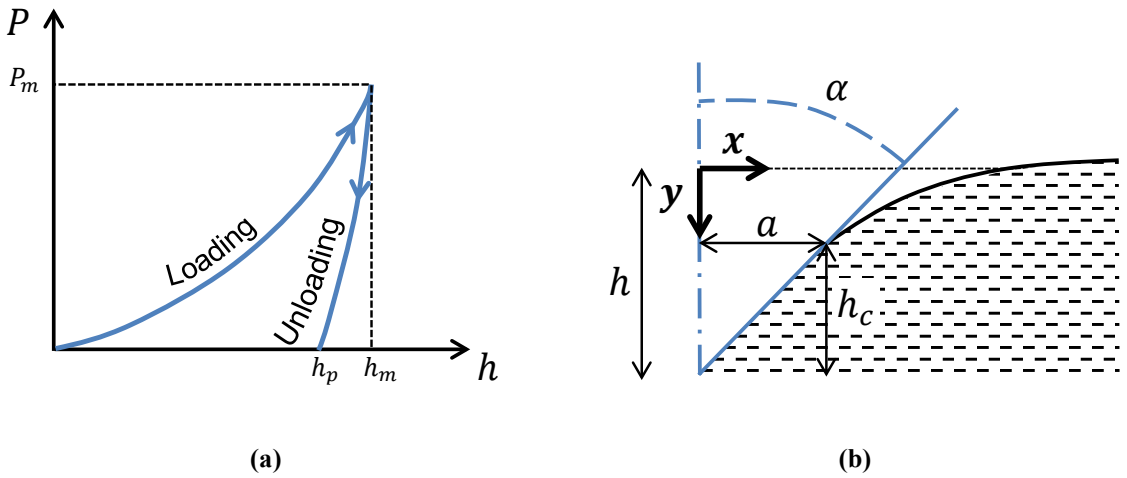

(a) **(b)**

Figure 6.1 – Nano-indentation test. **(a)** Recorded load vs penetration curve. **(b)** Definition of the main geometrical quantities and of the coordinate axes.

impact resistance, etc., a full list of which has recently been given in a comprehensive monograph [111].

Focusing in particular on the determination of the isotropic elastic constants from nano-indentation data, the main analysis procedures available at the present time can be roughly classified into three distinct categories. The first one comprises methods which make use of additional experimental quantities, for instance measurements of the residual surface profile using the atomic force microscope [112][113] or of the contact area at maximum load using electrical resistance techniques [114]. Despite delivering very precise results, the application of these procedures has been limited somehow by the much higher degree of experimental complexity they involve, which seems in contrast to the conceptual simplicity of a nano-indentation test. In order to keep the experimental burden to a minimum, a second group of methods has been devised which only require knowledge of the force-penetration curve. The latter is analyzed on the basis of a set of dimensionless functions which are constructed from a large number of finite element simulations of the indentation process, as done in e.g. [115][116][117]. An intrinsic limitation in this case is the range of validity of the derived dimensionless relations, which are typically obtained under specific assumptions for the material inelastic behavior during loading. As a consequence, they should be used with caution for materials whose constitutive response is either completely unknown or remarkably different from the one employed in the numerical simulations. Finally, the third category refers to methodologies which rely on exact analytical solutions to the so-called Boussinesq's problem of indentation into an elastic half-space [118]. The well-known technique proposed by Doerner and Nix [119] and later extended and improved by Oliver and Pharr [120] belongs to this group, and it is nowadays widely adopted in the scientific community for its simplicity combined with relatively good accuracy.

6.1.2 The Oliver-Pharr method of analysis

6.1.2.1 Assumptions and apparent inconsistencies

As just mentioned, the Oliver-Pharr method is likely the most popular technique for extracting the isotropic elastic constants of a material from nano-indentation data. However, it features a number of built-in assumptions which have to be taken into proper consideration when assessing the reliability of the obtained results.

First of all, it should be clear that the method works provided that the material can be considered as isotropic at the indentation scale, which is typically in the range of 1 micron or less. For metals, for instance, this implies that either the grain size has to be in the order of nano-meters, or that the anisotropy of the single crystals has to be negligible, to a certain extent.

Secondly, only the value of a particular combination of the isotropic elastic constants, called the reduced Young's modulus E^*, can be univocally determined. Formally, this is defined as

$$E^* = E/(1-\nu^2) \tag{6.1}$$

where E and ν denote the standard Young's modulus and Poisson's ratio respectively. Accordingly, some a priori knowledge of one of these two parameters is required in order to identify the other. If this information is missing, the method becomes ineffective.

A third important aspect is that the entire procedure is based on purely elastic solutions developed for axisymmetric indenters [121][122][123][124][125]. How these can effectively be used to analyze nano-indentation data, which is normally affected by an appreciable amount of inelastic deformation produced by the pyramidal indenter, is a matter which needs a special comment. The very first point to note is that the Oliver-Pharr method considers only the unloading part of a nano-indentation test, which is assumed to be an entirely elastic process. Furthermore, the force-penetration curve obtained using the 3-sided Berkovich indenter is supposed to be the same as that generated by a conical indenter with the same area-to-depth ratio. Despite apparently questionable, extensive finite element calculations and experimental investigations have confirmed that these two assumptions are either fully satisfied, or lead to negligible errors in almost all practical cases [115][126][114][127].

Finally, there is still another critical point to discuss, which relates to the applicability of the above-mentioned elastic solutions, obtained for indentation into a perfectly flat half-plane, to the description of the unloading stage, which involves contact with a surface containing a residual impression. The key-point is that this particular contact condition can arguably be described by the equivalent indenter concept [128], whose profile is determined pointwise by the vertical distance between the real indenter and the profile of the sample surface after unloading, as schematically shown in figure 6.2. In principle, the Oliver-Pharr method takes this geometrical effect into account via a correction parameter ϵ appearing in the formula for the calculation of the contact depth h_c [129][130][126], whose geometrical definition is given in figure 6.1 (b). The particular expression used is

$$h_c = h - \epsilon\frac{P}{P'} \tag{6.2}$$

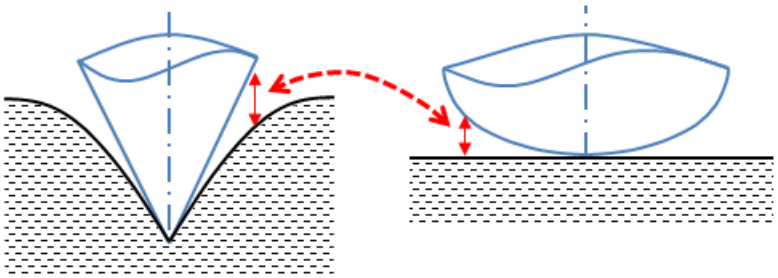

Figure 6.2 – Geometrical definition of the equivalent indenter concept.

where P is the applied load, h is the total downward displacement of the indenter tip relative to the undeformed sample surface and P' is the slope of the unloading curve. Nevertheless, it is the present author's opinion that a consistent application of the equivalent indenter concept should also entail other modifications, in addition to the inclusion of the ϵ parameter. Indeed, according to the standard Oliver-Pharr procedure, the reduced Young's modulus is calculated by means of the formula

$$E^* = \frac{\sqrt{\pi}}{2\beta}\frac{P'}{\sqrt{\mathrm{A}}} \tag{6.3}$$

where β is a small correction factor, which normally takes the value of ≈ 1.05 [109], and A is the projected contact area, equal to πa^2 in figure 6.1 (b). This last quantity is estimated from the contact depth h_c on the basis of the geometrical relation $A = A_r(h_c)$ characteristic of the *real* indenter. In the eyes of the author, this is inconsistent, as one would expect that it is the function $A = A_{eq}(h_c)$ associated with the *equivalent* indenter that should be used instead. Furthermore, h_c is obtained from expression (6.9) assuming h to represent the *total* downward displacement of the indenter tip. In principle, given the elastic nature of the previous relation, only the *recoverable* part of the penetration, i.e. the total minus the residual, should be considered. Else, when the indenter separates from the sample at the end of the unloading stage, meaning that $h_c = 0$, h would be equal to the residual penetration h_p indicated in figure 6.1 (a). But this would imply that, to satisfy equation (6.9), some load $P \neq 0$ should still be transmitted across the contact surface, which is non-sense of course.

However, as a matter of fact, the Oliver-Pharr method has repeatedly proved to provide good accuracy even when the residual impression left on the material is actually not negligible in comparison to the maximum indentation depth. This is somewhat surprising, given the apparent inconsistencies just discussed. A possible explanation, which was actually missing in the published literature, is put forth in the following section, on the basis of the findings of **PAPER V**.

6.1.2.2 A new interpretation based on the equivalent indenter concept

The starting point of the analysis presented in **PAPER V** is to hypothesize that the equivalent indenter concept can effectively account for a surface containing a residual impression, provided

that the function describing its equivalent shape, and not the one of the real indenter, is used in the associated contact equations.

To verify this, a two-step procedure is followed. First, dimensional analysis is used to prove that the axisymmetric shape of the equivalent indenter can be regarded as a material property, assuming that size-effects are negligible. This means that it can be described with respect to the x-y coordinate system of figure 6.1 (b) by the function

$$\bar{y} = \bar{f}(\bar{x}, E, \nu, p_1, p_2, \dots) \tag{6.4}$$

where $p_1, p_2, \dots$ denote generic inelastic material parameters and the symbol $(\bar{\ })$ indicates normalization with respect to an arbitrary length l.

Subsequently, nano-indentation tests on different materials are simulated via finite element modeling, each time recording the equivalent indenter shape $\bar{f}(\bar{x})$ associated with the residual impression left on the sample. In all cases, it is found that the unloading stage is well described by the elastic functions [125]

$$\bar{h} = \int_0^{\bar{a}} \frac{\bar{f}'(\bar{x})}{\sqrt{1-(\bar{x}/\bar{a})^2}} d\bar{x}\,, \qquad P = 2E^* l^2 \int_0^{\bar{a}} \frac{\bar{x}^2 \bar{f}'(\bar{x})}{\sqrt{\bar{a}^2 - \bar{x}^2}} d\bar{x} \tag{6.5}$$

where $\bar{f}'$ is simply the derivative of the function $\bar{f}(\bar{x})$ extracted from the model. The fact that the last two expressions were derived analytically assuming a perfectly flat contact surface, leads to the conclusion that the equivalent indenter is indeed a viable concept.

Unfortunately, in most real cases the shape of the equivalent indenter is unknown, as it would call for local profilometry which is normally not feasible. As a consequence, the possibility of formulating the problem of extracting the reduced Young's modulus from the unloading curve as an optimization problem, where both E^* and $\bar{f}(\bar{x})$ are to be determined at the same time, is additionally investigated in **PAPER V**. However, the related analysis demonstrates that the problem cannot be solved unambiguously, due to the particular mathematical structure of the relations (6.9), unless additional constraints are introduced to set restrictions on the admissible functions among which the solution $\bar{f}(\bar{x})$ is to be sought.

Interestingly, it turns out that the Oliver-Pharr method intrinsically embeds one of these constraints. In fact, by manipulating the apparently inconsistent equation (6.2), it is possible to show that it implies a relation between contact depth and elastic penetration which is the same as the one valid for a conical indenter. Moreover, the semi-apical angle of the latter can be calculated as

$$\alpha_{eq} = \pi/2 - \operatorname{atan}\left[\frac{2\cot(\alpha)}{\pi}\left(\frac{h_p/h_m}{1-h_p/h_m} + \frac{2-\epsilon}{2}\right)^{-1}\right] \tag{6.6}$$

where α denotes the semi-apical angle of the real indenter used in the test. The dependency of α_{eq} on the quantity h_p/h_m, which represents the ratio between permanent and maximum indenter penetration, is visualized in figure 6.3. Two different values for the constant ϵ are considered: 0.72, which is typical of a conical indenter, and 0.75, which relates to a paraboloid but is often used in practice as it seems to provide better results [109]. It can be noted that when the material is perfectly elastic, i.e. $h_p/h_m = 0$, α_{eq} reduces to $\alpha = 70.3^0$, the semi-apical angle assumed for the real indenter. This happens exactly for $\epsilon = 0.72$, whereas a small deviation is seen for $\epsilon = 0.75$.

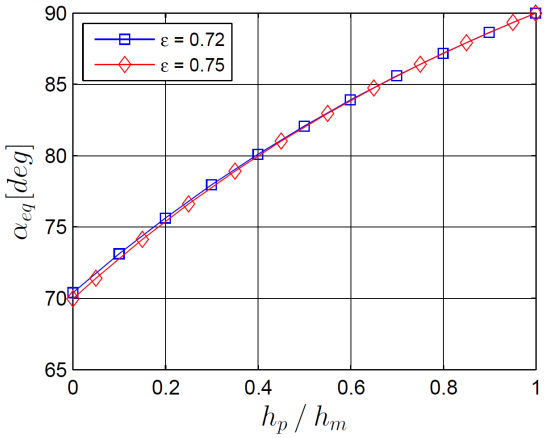

Figure 6.3 – Semi-apical angle of the equivalent conical indenter implicitly assumed by the Oliver-Pharr method, as a function of the ratio between residual and maximum penetration.

Conversely, when the material exhibits extensive plastic deformation and h_p/h_m tends to one, α_{eq} approaches 90 degrees, independently of the ϵ value. This is sensible, as during loading the material conforms perfectly to the real indenter shape, which is retained during subsequent unloading due to negligible elastic recovery.
In conclusion, it seems that the apparent inconsistencies in the Oliver-Pharr method are in reality associated with a concealed, convenient choice of the equivalent indenter profile. This might explain the good accuracy provided by the method even in presence of significant residual impression on the sample.

6.1.3 Applicability limits for nodules' testing

To the author's best knowledge, all the nano-indentation tests on graphite nodules reported in the literature so far are based on the Oliver-Pharr method. Unfortunately, the assumptions behind the technique suggest that the reliability of the measurements is, at the very least, disputable.
First of all, as explained in section 4.2.1, the nodules are inhomogeneous and strongly anisotropic at the local scale. This is undoubtedly in contrast with the isotropy assumption under which the analytical solutions which form the backbone of the method are derived. Moreover, even by assuming that the reduced Young's modulus is still somehow indicative of the local stiffness, it is clear that its determination would be affected by the different orientations of the conical sectors the nodule core is made of. This effect is captured in figure 6.4, which reports the results of nano-indentation tests conducted along a line crossing a nodule of diameter ≈ 150 μm, using 1 μm as maximum indentation depth. It may be seen that the reduced Young's modulus varies by as much as a factor 3 to 4 throughout the particle.
Another issue is that even with a meaningful value for the reduced Young's modulus on hand, the quantification of the standard isotropic elastic constants would be problematic. In fact, as mentioned in section 4.1.2, graphitic materials are characterized by a very large spread in Poisson's ratio. So it is not possible to assume a value for the latter a priori and then use it in combination with the definition (6.1) to calculate the Young's modulus, as often done for metals.

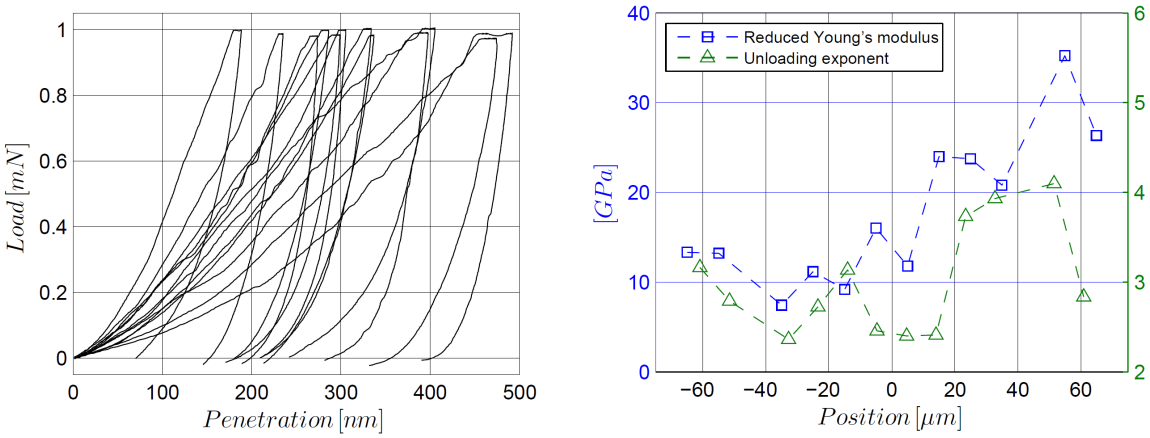

(a) **(b)**

Figure 6.4 – Nano-indentation testing of a graphite nodule. **(a)** Load-penetration curves obtained by indenting the nodule at several positions along its main diameter. Courtesy of Dr. Techn. Grethe Winther, DTU Mechanical Engineering, and Dr. Søren Fæster, DTU Wind Energy. **(b)** Reduced Young's modulus and exponent associated with fitting the first 40 % of the unloading curve, calculated by applying the standard Oliver-Pharr method to the data in (a).

Finally, the intrinsic shape of the equivalent indenter associated with the Oliver-Pharr method has proved to work very well for materials which deform plastically. On the other hand, brittle materials like graphite behave in a totally different manner during the loading stage, meaning that an alternative type of analysis is probably needed to achieve the same level of accuracy [131].

It has to be remarked that the Oliver-Pharr method is not the only possibility. Other techniques exist which allow analyzing the nano-indentation curves, as explained in section 6.1.1. Nevertheless, they imply the use of either advanced characterization instruments, which complicate the measurements considerably, or of dimensionless relations obtained from a large number of finite element simulations, which can only be obtained provided that the material inelastic behavior is known, to some extent. These reasons have probably discouraged the application of these alternative techniques to the present case.

In conclusion, standard nano-indentation does not seem to be appropriate for testing the elastic properties of the nodules contained in ductile iron. As a consequence, it is the author's opinion that previous values reported in the literature should be taken with care, as there are no solid grounds to sustain that they reflect the real particles' behavior.

6.2 3D differential aperture X-ray microscopy

6.2.1 Overview of the technique

Differential aperture X-ray microscopy (DAXM) is a recently developed non-destructive technique based on synchrotron radiation, which provides crystallographic orientation and local elastic strain with submicron spatial resolution in three dimensions [132][133][134]. It is applicable to single-crystal, polycrystals, composites and functionally graded materials and represents a unique way of performing quantitative microstructural characterization on mesoscopic length scales.

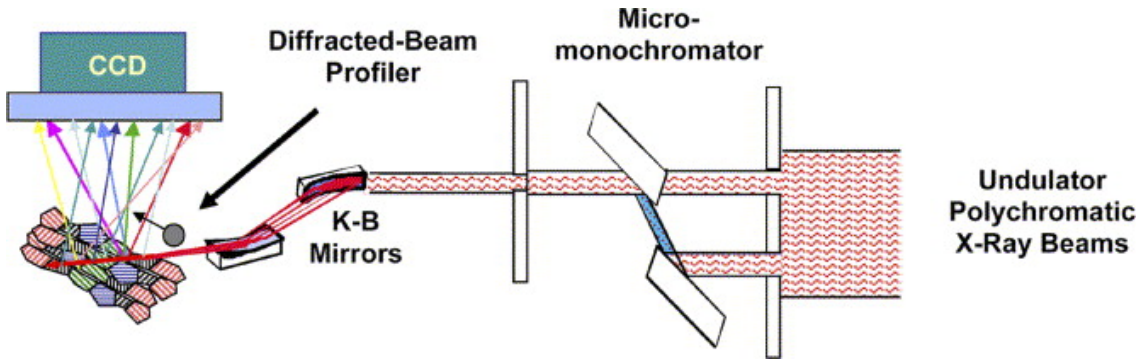

Figure 6.5 – Schematic depiction of the DAXM layout. The removable/insertable micro-monochromator provides white or monochromatic beams; the elliptically figured Kirckpatrick–Baez (K-B) mirrors focus the incident beams to ~0.5 μm diameter at the sample position; a 50 μm diameter Pt wire is used as a diffracted beam profiler and a CCD area detector collects white beam Laue diffraction patterns. Reprinted from [133] with permission of Elsevier.

The experimental configuration for DAXM at beamline 34-ID-E at the Advanced Photon Source of Argonne National Laboratory (USA) is schematically reported in figure 6.5. A polychromatic X-ray beam generated by the synchrotron ondulator enters from the right hand side. The removable/insertable monochromator can be used to select either single or multiple wavelengths before the beam is focused on the target via two Kirckpatrick–Baez mirrors, designed for energies in the range 8 ÷ 25 keV. The focused beam with diameter ~0.5 μm hits the sample at an angle of 45°, generating diffraction patterns which are collected by a CCD detector. To separate the patterns associated with different positions along the penetration depth, which overlap on the detector, a differential aperture depth profiling method is adopted [132]. This consists in stepping a 50 μm diameter platinum wire along the sample surface and collecting CCD images at regular intervals. By subtracting CCD images taken before and after each step, it is possible to reconstruct the full diffraction pattern at all depths. From knowledge of this, local crystallographic orientations and elastic strains can eventually be calculated with a resolution of 0.1° and $1x10^{-4}$ mm/mm respectively by means of dedicated software.

6.2.2 Residual elastic strain around a fully embedded nodule

A comprehensive experimental campaign was carried out to investigate the local microstructure and the presence of residual elastic strain in the ferrite grains surrounding the nodules in ductile iron. The DAXM technique was selected for two reasons. Firstly, it provides sufficient resolution to identify gradients of strain and orientation near the particles. Secondly, it offers a penetration depth which enables studying the material state around nodules which are fully embedded in the ferrite. This is of fundamental importance, as the investigations showed that the residual strain around nodules exposed on the surface is remarkably different, likely due to some mechanical relaxation. It is emphasized that due to space limitations, only the main findings are discussed in the following sections. A complete description of the experiments may be found in **PAPER VI** and in the associated supplementary material available online.

6.2.2.1 Experimental setup

A ductile iron sample with the composition indicated in table 5 was chosen for the study. Its microstructure consisted of almost spherical graphite nodules surrounded by a relatively homogeneous matrix with very large ferrite fraction (~95%) and average grain size of ~30 µm. The mean size (equivalent circle diameter) and mean volume fraction of the nodules were ~30 µm and 11.5%, respectively. It should be noted that this last value coincides with the one chosen in section 2.2 to model the standard GJS-400 ferritic grade, which was subsequently taken as reference in the numerical calculations of chapter 4 and chapter 5.

To enable sub-surface DAXM investigations, the 3D distribution of the graphite nodules was characterized by X-ray tomography using a Zeiss Xradia 520 Versa micro-CT system. This allowed identifying nodules with three important requisites: very high spheroidicity, no close neighboring particles and distance from the surface not greater than approx. 70-80 µm. The first two conditions are important to facilitate the interpretation of the results and to make the comparison with the numerical model more realistic, whereas the third one ensures that the diffracted X-ray intensity is above the critical threshold needed for reliable measurements.

A nodule fulfilling all the previous requirements is the one indicated by the white arrow in figure 6.6 (a), which has a diameter of approximately 50 µm and it is located about 15 µm beneath the sample surface. The region around it was selected for DAXM analysis, which was carried out using two beam modes. First a polychromatic beam was employed to determine the crystallographic orientations on a slice crossing the nodule and perpendicular to the sketch of figure 6.6 (b). Then a

Table 5 – Average composition of the ductile iron sample used for the DAXM investigations (wt %).

C	Si	Mn	P	S	Cr	Ni	Co	Cu	Mg
3.68	2.30	0.22	0.015	0.011	0.027	0.048	0.024	0.016	0.11

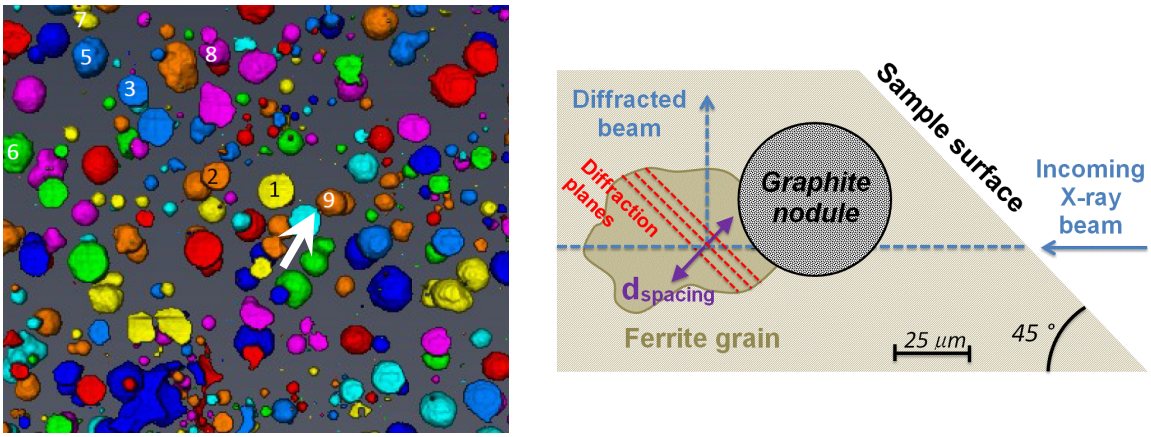

(a) **(b)**

Figure 6.6 – Experimental setup for DAXM of ductile iron. **(a)** X-ray computed tomography of the sample, with indication of the sub-surface nodule chosen for the analysis. **(b)** Schematic of the DAXM applied to a ferrite grain close the selected nodule, illustrating the crystallographic planes generating monochromatic diffraction and the corresponding interplanar spacing.

monochromatic beam was used for determining the interplanar spacing d associated with the atomic planes parallel to the sample surface and belonging to a ferrite grain located behind the nodule, as schematically shown in figure 6.6 (b). From knowledge of d, the normal elastic strain component in the direction perpendicular to the previous planes was estimated as

$$\varepsilon_n = (d - d_0)/d_0 \tag{6.7}$$

where d_0 denotes the value of the interplanar spacing for a reference unstrained crystal. This last quantity was calculated on the basis of the characteristic (h, k, l) indices by means of the expression

$$d_0 = a_0/\sqrt{h^2 + k^2 + l^2} \tag{6.8}$$

The parameter a_0 appearing in the last formula indicates the lattice constant of ferrite. For its determination, the following relation, which takes data from various publications into account, was used [135]

$$a_0 = a_{Fe} + \frac{10}{3a_{Fe}^2}[(a_{Fe} - 0.001297w_C)^2(a_{Fe} + 0.011606w_C) - a_{Fe}^3] - 0.0006w_{Si} + 0.0006w_{Mn} \tag{6.9}$$

where $a_{Fe} = 2.8664$ Å is the lattice parameter of pure ferrite and w_x is the weight percentage of the element x. For the present case, the Si and Mn contents listed in table 5 and a maximum solubility of 0.005 wt% of C in ferrite at room temperature were used as w_{Si}, w_{Mn} and w_C, respectively.

It has to be pointed out that given the high Si content, a large uncertainty on the coefficient multiplying w_{Si} in equation (6.9) might severely affect the accuracy of the calculated elastic strain (6.7). However, values close to 0.0006 have been confirmed by a number of authors. For instance, Polcarova *et al.* [136] measured 0.00069 on pure Fe-Si crystals, with negligible amount of carbon, whereas Cockett [102] proposed 0.00042, considering ferrite with 0.005 % carbon. The only exception is the work of Rubin *et al.* [137] where a much higher coefficient of 0.00185 was suggested. Nevertheless, their analyses were performed directly on ductile iron containing graphite particles, in which the elastic lattice distortion due to local residual stresses might lead to erroneous results. The scarce reliability seems supported by the fact that the 0.00185 coefficient was later found to generate unrealistic values for the carbon content in ferrite at room temperature determined via standard XRD measurements.

6.2.2.2 Measurements vs model predictions

The crystallographic orientations of the ferrite grains determined using the polychromatic beam mode for the 2D slice described previously are shown in figure 6.7 (a). A critical misorientation angle of ~0.1° is used for revealing the detailed dislocation boundary structure, whereas a critical angle of 3° is used for defining individual grains. It is evident that only a few relatively small grains are nearly dislocation free, whereas most of the others are plastically deformed, containing dislocation boundaries with misorientation angles below 1°. Clearly, this represents a clue of the existence of local stresses greater than the ferrite flow stress at some point during the processing history of the sample.

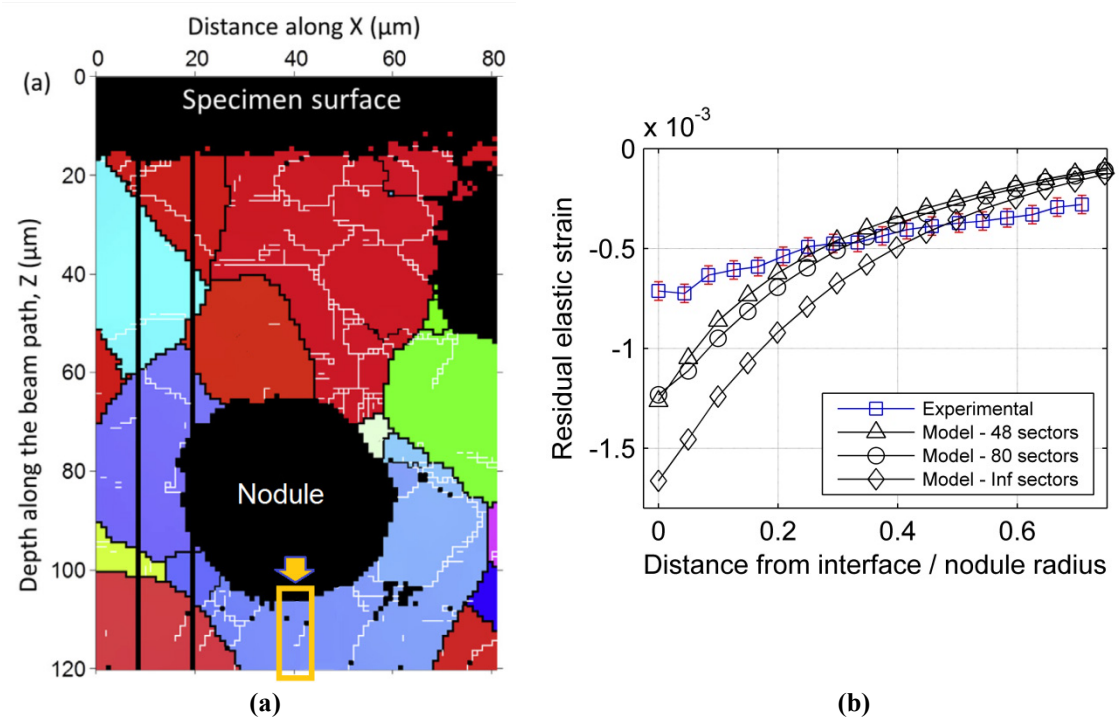

(a) **(b)**

Figure 6.7 – Results of the DAXM analysis. **(a)** Crystallographic orientations for the 2D slice whose trace is indicated by the horizontal blue dashed line in figure 6.6 (b). Dislocation boundaries with misorientation angles in the range of 0.1-1°, 1-3°, and >3° are shown in thin white, thin black and thick black lines, respectively. **(b)** Elastic strain in the direction perpendicular to the sample surface, and approximately normal to the nodule-matrix interface, relative to the region indicated by the yellow box at the bottom of the crystallographic map in (a). The error bars refer to 10 % uncertainty on the local chemical composition. For comparison, the elastic strain predicted by the numerical model developed in chapter 5 is also reported.

Figure 6.7 (b) reports instead the residual elastic strain measured with monochromatic beam in the region indicated by the yellow box at the bottom of the figure 6.7 (a), as a function of the normalized distance from the nodule-matrix interface. As may be deduced from the schematic of figure 6.6 (b), the specific vertical location selected for creating the 2D slice implies that the strain refers to a direction which is approximately radial with respect to the nodule. Therefore, the compressive values seen close to the latter, which gradually decrease in magnitude moving further into the ferrite, are physically consistent with the type of thermo-mechanical interaction hypothesized in the introductory chapter: that is, during manufacturing the matrix shrinks more that the nodule, hence generating normal compressive forces at the interface between the two.

It is important to clarify that the observed values cannot be ascribed to gradients in chemical composition. In fact, one might speculate that local segregation of elements like Si and Mn could drive changes in the ferrite lattice parameter according to expression (6.9). As these are not taken into account via a corresponding variation of the d_0 parameter in equation (6.7), an artificial strain gradient might arise. However, the Si + Mn segregation that would be required to generate the strain gradient visible in figure 6.7 (b) would be 2.5÷3.0 wt%, which is almost more than the average content present in the material. A 10 % variation, which is more realistic as discussed in **PAPER VI**, changes the strain only by the small amount indicated by the error bars. Furthermore, a similar

gradient is also observed in the deviatoric strains, which can be calculated from the orientation map of figure 6.7 (a). As these do not depend on the choice of the lattice parameter, the compressive strain variation may be considered as real.

Concerning the comparison with the predictions of the model introduced in section 5.2.1, which are also shown in figure 6.7, it may be noted that the experimentally recorded strain pattern is reproduced quite well, even though the simulated gradients and absolute values seemed somewhat overestimated by a factor 2. Considering the thermo-elastic nature of the model and the limited mechanical data available, which makes any inelastic description out of reach, the relatively good agreement between theoretical predictions and measurements is surprisingly good.

A possible explanation is that inelastic deformation does take place in the outer part of the nodule core during solid-state cooling, as hypothesized in section 5.2.3, but it somehow remains localized to a region of limited thickness, without propagating to the entire graphite particle. In this way, the pressure exerted by the surrounding matrix is partially relieved, and the residual gradients smoothed out, but at the same time the overall material elastic stiffness remains almost unaffected. This hypothesis could justify the over prediction of the residual elastic strains, while at the same time explaining the excellent agreement of figure 4.7 obtained in terms of simulated macroscopic elastic properties.

With regard to the discrepancy that still exists between numerical predictions and measurements, it has to be admitted that it was rather expected. In fact, a quite rough approximation of the eutectoid transformation is considered in the analysis, and any kind of high-temperature creep mechanism in the matrix, which could partly relieve the elastic strain, is ignored. In this respect, the plastic deformation observed in the grains of figure 6.7 (b) clearly indicates that some non-linear phenomena occur in the ferrite at some point, meaning that the linear elastic assumption is likely too simplistic. Moreover, the anisotropy of the single ferritic grains is also neglected in the model. Given the microscopic scale considered, including in the simulation some crystallographic information of the region around the nodule would probably improve the results. Finally, the periodic unit cell approach and the perfect spheroidal geometry assumed for the nodule also constitute a limitation, whose effect is however difficult to quantify.

Chapter 7
Concluding remarks

7.1 Conclusions

The present findings demonstrate unequivocally that the load carrying capacity of the nodules must be taken into account when analyzing the mechanical behavior of ductile iron at the micro-structural scale. In other words, the old belief that the presence of the graphite particles can be neglected a priori in light of their presumed soft nature and marginal strength is to be categorically rejected. The key point is that their strongly inhomogeneous and anisotropic character implies that the response they offer is very much dependent on the loading scenario: in some circumstances, they show minor stiffness, while in others they may closely resemble rigid bodies.

In this respect, the availability of TEM studies of their internal structure has turned out to be of utmost importance to unveil their real elastic behavior. First of all, it has allowed, via elastic bound theory analysis, to rule out the hypothesis that they could be modeled as homogeneous and isotropic. A direct implication of this is that it is not possible to justify any of the isotropic parameters reported in table 1 on the basis of physical grounds. Even if some of them provide a good match with the ductile iron response at the macro-scale recorded during uniaxial testing, there is no guarantee that they work for different loading conditions, nor that the description they offer in terms of stress & strain fields in and around the nodules is accurate. This conclusion is expected to have significant consequences on the way local phenomena in ductile iron will be addressed in the future, e.g. crack propagation, as most of the past studies were based on considering the graphite particles as isotropic.

Knowledge of the real nodules' structure has also helped bring to light the scarce reliability of the nano-indentation tests performed according to the Oliver-Pharr method, which were apparently suggesting values for the Young's modulus in the range 15 ÷ 28 GPa. Indeed, the real anisotropic, inhomogeneous and brittle nature of the graphite particles is simply too far from the implicit assumptions of isotropy, homogeneity, and somewhat uniform plastic deformation the technique rests on. Concerning this, it has to be emphasized that the condition of uniform plastic flow is required to justify the particular shape of the equivalent indenter associated with the method, which has been revealed by the present investigations for the first time in literature.

Finally, the numerical reconstruction of the nodules' internal morphology has led to the development of a new micro-mechanical model, which performs excellently when used to predict the ductile iron thermo-elastic behavior at the macroscopic scale. Moreover, the model turns out to be characterized by an average thermal contraction which is 3 to 4 times smaller compared to that of the ferrite matrix, hence confirming the hypothesis of a pronounced CTE mismatch that was initially supported by materials science speculations only.

In relation to this last aspect, the present PhD work has demonstrated from a theoretical and experimental viewpoint that significant local residual stresses may form during the manufacturing process. This is certainly a breakthrough compared to the past, when only macroscopic residual stresses were assumed to exist in ductile iron castings. Thanks to the new model for the nodules and the advanced DAXM synchrotron technique, the nodule-matrix interaction has been studied in an unprecedented manner, leading to the conclusion that deviatoric stresses of up to approximately 150 MPa may be present in the ferrite region in the vicinity of the graphite particles. The former value is meant to be indicative only, but it is reported to emphasize that the local residual stresses may be of the same order of magnitude of the macroscopic ductile iron yield strength, at least for low-alloyed ferritic grades.
The existence of non-negligible stresses at the micro-scale opens up for a totally new way of looking at the structure and properties of ductile iron. For instance, the presence of the graphite layer with different structure on the surface of the nodules may be explained, in this new framework, by cracking and rotation of the single crystallites upon formation of localized compressive forces in that region. Similarly, the connection between magnitude of the local residual stresses and number of the nodules' internal subdivisions provides an additional ingredient to understand the link between fatigue resistance and size of the graphite particles.

7.2 Future work

The description of the local residual stresses obtained so far cannot be considered as fully comprehensive. Both the theoretical and the experimental analyses presented in the previous chapters feature simplifying assumptions which leave room for improvement. Concerning modeling, given the difficulties with extending the nodules' model to the inelastic regime, the priority is a reliable time-dependent description of the ferrite behavior, together with a more realistic representation of the eutectoid transformation. Moreover, in order to analyze general micro-structures which are not limited to the case of a spherical graphite particle isolated from the others, the unit cell should be replaced with a RVE which embeds statistical data regarding the nodules' size, shape and spatial distribution. With respect to the experimental technique instead, only monochromatic diffraction measurements from a single Laue spot have been carried out up to now, which provide knowledge of one strain component only. In principle, by combining diffraction data coming from three widely separated spots the full elastic strain tensor, and therefore the stress tensor too, can be reconstructed [138]. This would allow for a much deeper understanding of the local thermo-mechanical conditions experienced by the material, in addition to enable better validation of the theoretical models.
Apart from these very technical considerations, it has to be emphasized that the present PhD work has covered only the first three points of the structure-process-properties-performance diagram of figure 1.1. Performance aspects have been just shortly touched upon, despite being probably the most relevant from a technological perspective, as key industrial sectors like off-shore, transport and energy production are constantly pushing for lighter and more reliable ductile iron components. As mentioned in the previous section, the presence of local residual stresses constitutes an element that may actually be used to shed further light on why the material performs in a certain way under

certain conditions. For instance, by studying how the process parameters affect the local residual stress state, and how this in turn affects the e.g. fatigue resistance, useful indications may be obtained on how to manufacture critical parts with longer service life. The unexplored field of local residual stresses can then potentially represent the key to optimize the ductile iron performance even further, contributing to ensure a bright future for this evergreen material.

References

[1] C. R. Loper Jr., "The origin of ductile iron - part I," *Foundry Manag. Technol.*, vol. 122, no. 11, 1994.

[2] C. Labrecque and M. Gagne, "Review ductile iron: 50 years of continuous development," *Can. Metall. Q.*, vol. 37, pp. 343–378, 1998.

[3] "47th Census of World Casting Production," Dec. 2013.

[4] Ductile Iron Society, "Ductile Iron data for design engineers," 2013. [Online]. Available: http://www.ductile.org/ductile-iron-data/. [Accessed: 10-Oct-2015].

[5] N. S. Tiedje, "Solidification, processing and properties of ductile cast iron," *Mater. Sci. Technol.*, vol. 26, no. 5, pp. 505–514, May 2010.

[6] G. Hütter, L. Zybell, and M. Kuna, "Micromechanisms of fracture in nodular cast iron: From experimental findings towards modeling strategies – A review," *Eng. Fract. Mech.*, vol. 144, pp. 118–141, Aug. 2015.

[7] P. Yang and J.-M. Tarascon, "Towards systems materials engineering," *Nat. Mater.*, vol. 11, no. 7, pp. 560–563, 2012.

[8] G. Rivera, R. Boeri, and J. Sikora, "Revealing and characterising solidification structure of ductile cast iron," *Mater. Sci. Technol.*, vol. 18, no. 6, pp. 691–697, 2002.

[9] G. Grimvall, "Cast Iron as a Composite: Conductivities and Elastic Properties," *Adv. Mater. Res.*, vol. 4–5, no. 4–5, pp. 31–46, 1997.

[10] T. Sjögren and I. L. Svensson, "Modelling the effect of graphite morphology on the modulus of elasticity in cast irons," *Int. J. Cast Met. Res.*, vol. 17, no. 5, pp. 271–279, Oct. 2004.

[11] C. Vogel, C. Juhl, and E. Maahn, *Metallurgi for ingeniører*, 9th ed. Polyteknisk Forlag, 2001.

[12] P. J. Withers and H. K. D. H. Bhadeshia, "Residual stress. Part 1 – Measurement techniques," *Mater. Sci. Technol.*, vol. 17, no. 4, pp. 355–365, Apr. 2001.

[13] M. A. Yescas-Gonzalez and H. K. D. H. Bhadeshia, "Cast Irons," *University of Cambridge*, 2001. [Online]. Available: http://www.msm.cam.ac.uk/phase-trans/2001/adi/cast.iron.html. [Accessed: 29-Jun-2016].

[14] J. Campbell, *Castings*, 2nd ed. Oxford: Butterworth-Heinemann, 2003.

[15] "Grain-oriented electrical steel - Technical data sheet," 2015. [Online]. Available: www.atimetals.com. [Accessed: 07-Dec-2015].

[16] N. Bonora and A. Ruggiero, "Micromechanical modeling of ductile cast iron incorporating damage. Part I: Ferritic ductile cast iron," *Int. J. Solids Struct.*, vol. 42, no. 5–6, pp. 1401–1424, Mar. 2005.

[17] R. Taylor, R. G. Brown, K. Gilchrist, E. Hall, A. T. Hodds, B. T. Kelly, and F. Morris, "Mechanical properties of reactor graphite," *Carbon N. Y.*, vol. 5, no. 5, pp. 519–531, 1967.

[18] V. Di Cocco, F. Iacoviello, a. Rossi, M. Cavallini, and S. Natali, "Graphite nodules and fatigue crack propagation micromechanisms in a ferritic ductile cast iron," *Fatigue Fract. Eng. Mater. Struct.*, vol. 36, no. 9, pp. 893–902, Sep. 2013.

[19] M. Ashby, H. Shercliff, and D. Cebon, *Materials : engineering, science, processing and design*. Elsevier Butterworth-Heinemann, 2010.

[20] A. I. Savvatimskiy, "Measurements of the melting point of graphite and the properties of

liquid carbon (a review for 1963-2003)," *Carbon N. Y.*, vol. 43, no. 6, pp. 1115–1142, 2005.
[21] S. Ho and E. J. Lavernia, "Thermal residual stresses in metal matrix composites: A review," *Appl. Compos. Mater.*, vol. 2, no. 1, pp. 1–30, 1995.
[22] M. Kuna and D. Z. Sun, "Three-dimensional cell model analyses of void growth in ductile materials," *Int. J. Fract.*, vol. 81, no. 3, pp. 235–258, 1996.
[23] W. Brocks, S. Hao, and D. Steglich, "Micromechanical modelling of the damage and toughness behaviour of nodular cast iron materials," *J. Phys. IV*, vol. 6, no. 6, pp. 43–52, 1996.
[24] K. S. Zhang, J. B. Bai, and D. François, "Ductile fracture of materials with high void volume fraction," *Int. J. Solids Struct.*, vol. 36, no. 23, pp. 3407–3425, Aug. 1999.
[25] M. J. Dong, B. Tie, A. S. Béranger, C. Prioul, and D. François, "Damage Effect on the Fracture Toughness of Nodular Cast Iron," *Adv. Mater. Res.*, vol. 4–5, pp. 181–188, 1997.
[26] J. H. Liu, X. Y. Hao, G. L. Li, and G. S. Liu, "Microvoid evaluation of ferrite ductile iron under strain," *Mater. Lett.*, vol. 56, no. 5, pp. 748–755, 2002.
[27] T. Sjögren and I. L. Svensson, "Studying elastic deformation behaviour of cast irons by acoustic emission," *Int. J. Cast Met. Res.*, vol. 18, no. 4, pp. 249–256, 2005.
[28] J. Kohout, "A simple relation for deviation of grey and nodular cast irons from Hooke's law," *Mater. Sci. Eng. a*, vol. A313, no. 1–2, pp. 16–23, 2001.
[29] T. Sjogren, "Influences of the graphite phase on elastic and plastic deformation behaviour of cast irons - PhD Thesis," Linköping University, 2007.
[30] E. Dorazil, *High strength austempered ductile cast iron*. Horwood, 1991.
[31] F. Rabold and M. Kuna, "Cell model simulation of void growth in nodular cast iron under cyclic loading," *Comput. Mater. Sci.*, vol. 32, no. 3–4, pp. 489–497, Mar. 2005.
[32] C. Berdin, M. J. Dong, and C. Prioul, "Local approach of damage and fracture toughness for nodular cast iron," *Eng. Fract. Mech.*, vol. 68, no. 9, pp. 1107–1117, 2001.
[33] I. Hervas, M. B. Bettaieb, and E. Hug, "Damage mechanisms evolution of ductile cast irons under thermomechanical loadings," *Int. J. Mater. Prod. Technol.*, vol. 47, no. 1/2/3/4, p. 23, 2013.
[34] P. Dierickx, C. Verdu, A. Reynaud, and R. Fougeres, "A study of physico-chemical mechanisms responsible for damage of heat treated and as-cast ferritic spheroïdal graphite cast irons," *Scr. Mater.*, vol. 34, no. 2, pp. 261–268, Jan. 1996.
[35] S. K. Pradhan, B. B. Nayak, S. S. Sahay, and B. K. Mishra, "Mechanical properties of graphite flakes and spherulites measured by nanoindentation," *Carbon N. Y.*, vol. 47, no. 9, pp. 2290–2292, Aug. 2009.
[36] D. O. Fernandino, A. P. Cisilino, and R. E. Boeri, "Determination of effective elastic properties of ferritic ductile cast iron by computational homogenization, micrographs and microindentation tests," *Mech. Mater.*, vol. 83, pp. 110–121, Apr. 2015.
[37] B. Miao, K. Fang, W. Bian, and G. Liu, "On the microstructure of graphite spherulites in cast irons by TEM and HREM," *Acta Metall. Mater.*, vol. 38, no. 11, pp. 2167–2174, Nov. 1990.
[38] G. R. Speich, A. J. Schwoeble, and B. M. Kapadia, "Elastic moduli of gray and nodular cast iron," *Trans. ASME. J. Appl. Mech.*, vol. 47, no. 4, pp. 821–826, 1980.
[39] H. Era, K. Kishitake, K. Nagai, and Z. Z. Zhang, "Elastic modulus and continuous yielding behaviour of ferritic spheroidal graphite cast iron," *Mater. Sci. Technol.*, vol. 8, no. 3, pp. 257–261, Jul. 1992.
[40] A. R. Boccaccini, "Young's modulus of cast-iron as a function of volume content, shape and orientation of graphite inclusions," *Zeitschrift Fuer Met. Res. Adv. Tech.*, vol. 88, no. 1, pp. 23–26, 1997.
[41] S. H. Pundale, R. J. Rogers, and G. R. Nadkarni, "Finite element modeling of elastic

modulus in ductile irons: Effect of graphite morphology," *Trans. Am. Foundrymen's Soc.*, vol. 106, pp. 99–105, 1998.

[42] C. A. Cooper, R. Elliott, and R. J. Young, "Investigation of elastic property relationships for flake and spheroidal cast irons using Raman spectroscopy," *Acta Mater.*, vol. 50, no. 16, pp. 4037–4046, Sep. 2002.

[43] W. Gaudig, R. Mellert, U. Weber, and S. Schmauder, "Self-consistent one-particle 3D unit cell model for simulation of the effect of graphite aspect ratio on Young's modulus of cast-iron," *Comput. Mater. Sci.*, vol. 28, no. 3–4, pp. 654–662, Nov. 2003.

[44] L. Collini and G. Nicoletto, "Determination of the relationship between microstructure and constitutive behaviour of nodular cast iron with a unit cell model," *J. Strain Anal. Eng. Des.*, vol. 40, no. 2, pp. 107–116, Jan. 2005.

[45] G. Nicoletto, L. Collini, R. Konečná, and E. Riva, "Analysis of Nodular Cast Iron Microstructures for Micromechanical Model Development," *Strain*, vol. 42, no. 2, pp. 89–96, May 2006.

[46] F. D. Carazo, S. M. Giusti, A. D. Boccardo, and L. A. Godoy, "Effective properties of nodular cast-iron: A multi-scale computational approach," *Comput. Mater. Sci.*, vol. 82, pp. 378–390, Feb. 2014.

[47] W. . Clegg, "A stress analysis of the tensile deformation of metal-matrix composites," *Acta Metall.*, vol. 36, no. 8, pp. 2141–2149, 1988.

[48] D. O. Fernandino and R. Boeri, "Study of the fracture of ferritic ductile cast iron under different loading conditions," *Fatigue Fract. Eng. Mater. Struct.*, vol. 38, no. 5, pp. 610–620, May 2015.

[49] J. Aboudi, S. Arnold, and B. Bednarcyk, *Micromechanics of Composite Materials: a Generalized Multiscale Analysis Approach*. Butterworth-Heinemann, 2012.

[50] H. Stang, "Elastic Properties of Materials with a Microstructure," in *Lecture notes for the course Mechanical Modeling of Materials in Civil Engineering*, 2014, p. 38.

[51] M. G. D. Geers, V. G. Kouznetsova, and W. A. M. Brekelmans, "Multi-scale computational homogenization: Trends and challenges," *J. Comput. Appl. Math.*, vol. 234, no. 7, pp. 2175–2182, Aug. 2010.

[52] A. Drago and M. Pindera, "Micro-macromechanical analysis of heterogeneous materials: Macroscopically homogeneous vs periodic microstructures," *Compos. Sci. Technol.*, vol. 67, no. 6, pp. 1243–1263, May 2007.

[53] D. Steglich and W. Brocks, "Micromechanical modeling of damage and fracture of ductile materials," *Fatigue Fract. Eng. Mater. Struct.*, vol. 21, no. 10, pp. 1175–1188, Jan. 1998.

[54] L. Collini, "Micromechanical modeling of the elasto-plastic behavior of heterogeneous nodular cast iron," Universita' degli Studi di Parma, 2004.

[55] D. Steglich and W. Brocks, "Micromechanical modelling of the behaviour of ductile materials including particles," *Comput. Mater. Sci.*, vol. 9, no. 1–2, pp. 7–17, Dec. 1997.

[56] L. Qi, W. Tian, and J. Zhou, "Numerical evaluation of effective elastic properties of composites reinforced by spatially randomly distributed short fibers with certain aspect ratio," *Compos. Struct.*, vol. 131, pp. 843–851, Nov. 2015.

[57] Z. Xia, C. Zhou, Q. Yong, and X. Wang, "On selection of repeated unit cell model and application of unified periodic boundary conditions in micro-mechanical analysis of composites," *Int. J. Solids Struct.*, vol. 43, no. 2, pp. 266–278, Jan. 2006.

[58] Dassault Systèmes Simulia Corp., "Abaqus 6.13, Abaqus Analysis User's Guide section 35.2.1." 2013.

[59] Dassault Systèmes Simulia Corp., "Abaqus 6.13, Abaqus Analysis User's Guide section 10.3.1." 2013.

[60] P. Wriggers, *Introduction to Computational Micromechanics*. Springer, 2005.

[61] M. Itskov, *Tensor Algebra and Tensor Analysis for Engineers*. Berlin, Heidelberg: Springer Berlin Heidelberg, 2007.
[62] W. Baer, D. Steglich, W. Brocks, G. Pusch, and J. Petit, "Experimental determination and micromechanical modelling of damage in nodular cast iron," *Proc. 11th Eur. Conf. Fract. (ECF 11)*, 1996.
[63] R. Kaibyshev and I. Kazakulov, "Deformation Behavior of Fe-3%Si Steel at High Temperatures," *Key Eng. Mater.*, vol. 171–174, no. 171–174, pp. 213–218, 2000.
[64] D. S. Inc., "Gleeble® 1500 Thermal-Mechanical Simulator," 2015. [Online]. Available: http://www.gleeble.com/products/gleeble-1500.html. [Accessed: 02-Aug-2015].
[65] G. M. Paolucci, *Lezioni di metallurgia per laurea in ingegneria meccanica: 2*, 2nd ed. Padova: Edizioni Libreria Progetto, 2002.
[66] F. Malagari, "Silicon steels and their applications," *Met. Eng. Q.*, vol. 13, no. 1, pp. 14–18, 1973.
[67] Moses, "Electrical steels: past, present and future developments," *Phys. Sci. Meas. Instrumentation, Manag. Educ. IEE Proc. a*, vol. 137, no. 5, pp. 233–245, 1990.
[68] J. Lemaitre, "A continuous damage mechanics model for ductile fracture," *J. Eng. Mater. Technol. ASME*, vol. 107, no. 1, pp. 83–89, 1985.
[69] N. Bonora, "A nonlinear CDM model for ductile failure," *Eng. Fract. Mech.*, vol. 58, no. 1–2, pp. 11–28, Sep. 1997.
[70] J. Lemaitre and R. Desmorat, *Engineering damage mechanics : ductile, creep, fatigue and brittle failures*. Springer, 2005.
[71] J. Lemaitre and J. Dufailly, "Damage measurements," *Eng. Fract. Mech.*, vol. 28, no. 5–6, pp. 643–661, 1987.
[72] H.-J. Weber and G. B. Arfken, *Essential mathematical methods for physicists*. Academic Press, 2004.
[73] E. de Souza Neto, "A fast, one-equation integration algorithm for the Lemaitre ductile damage model," *Commun. Numer. Methods Eng.*, vol. 18, no. 8, pp. 541–554, May 2002.
[74] E. de Souza Neto, D. Peric, and D. R. J. Owens, *Computational methods for plasticity : theory and applications*. Wiley, 2008.
[75] J. C. Simo, "A return mapping algorithm for plane stress elastoplasticity," *Int. J. Numer. Methods Eng.*, vol. 22, no. 3, pp. 649–670, 1986.
[76] D. Peric, "On a class of constitutive equations in viscoplasticity: formulation and computational issues," *Int. J. Numer. Methods Eng.*, vol. 36, no. 8, 1993.
[77] Perzyna, "The constitutive equations for rate sensitive plastic materials," *Q. Appl. Math.*, vol. 20, no. 4, 1963.
[78] T. Andriollo, J. Thorborg, N. Tiedje, and J. Hattel, "Modeling of damage in ductile cast iron - The effect of including plasticity in the graphite nodules," *IOP Conf. Ser. Mater. Sci. Eng.*, vol. 84, no. 1, 2015.
[79] T. Andriollo, J. Thorborg, and J. Hattel, "The influence of the graphite mechanical properties on the constitutive response of a ferritic ductile cast iron – A micromechanical FE analysis," in *Proceedings of the XIII International Conference on Computational Plasticity, Fundamentals and Applications*, 2015, pp. 632–641.
[80] H. H. Wawra, B. K. D. Gairola, and E. Kroner, "Comparison between experimental values and theoretical bounds for the elastic constants E, G, K, and μ of aggregates of noncubic crystallites," *Zeitschrift Fur Met.*, vol. 73, no. 2, pp. 69–71, 1982.
[81] Z. Hashin and S. Shtrikman, "A variational approach to the theory of the elastic behaviour of polycrystals," *J. Mech. Phys. Solids*, vol. 10, pp. 343–352, 1962.
[82] J. P. Watt and L. Peselnick, "Clarification of the Hashin-Shtrikman bounds on the effective elastic moduli of polycrystals with hexagonal, trigonal, and tetragonal symmetries," *J. Appl.*

Phys., vol. 51, no. 3, p. 1525, 1980.
[83] E. Kroner, "Bounds for effective elastic moduli of disordered materials," *J. Mech. Phys. Solids*, vol. 25, no. 2, pp. 137–155, 1977.
[84] G. Savini, Y. J. Dappe, S. Öberg, J. C. Charlier, M. I. Katsnelson, and A. Fasolino, "Bending modes, elastic constants and mechanical stability of graphitic systems," *Carbon N. Y.*, vol. 49, no. 1, pp. 62–69, Jan. 2011.
[85] R. Lakes, "Advances in negative Poisson's ratio materials," *Adv. Mater.*, vol. 5, no. 4, pp. 293–296, 1993.
[86] American Foundrymen's Society, *Ductile iron handbook*. Schaumburg, Illinois, United States: American Foundrymen's Society, 1992.
[87] G. N. J. Gilbert, "Stress/strain properties of nodular cast irons in tension and compression," *BCIRA J.*, vol. 12, no. 2, pp. 170–193, 1964.
[88] J. R. Dryden and G. R. Purdy, "The effect of graphite on the mechanical properties of cast irons," *Acta Metall.*, vol. 37, no. 7, pp. 1999–2006, Jul. 1989.
[89] D. M. Stefanescu, "Cast Iron," in *Metals Handbook 9th Edition*, ASM International, 1989, pp. 168–181.
[90] J. P. Monchoux, C. Verdu, G. Thollet, R. Fougères, and A. Reynaud, "Morphological changes of graphite spheroids during heat treatment of ductile cast irons," *Acta Mater.*, vol. 49, no. 20, pp. 4355–4362, Dec. 2001.
[91] B. Miao, D. O. North Wood, W. Bian, K. Fang, and M. H. Fan, "Structure and growth of platelets in graphite spherulites in cast iron," *J. Mater. Sci.*, vol. 29, no. 1, pp. 255–261, 1994.
[92] K. Theuwissen, J. Lacaze, M. Véron, and L. Laffont, "Nano-scale orientation mapping of graphite in cast irons," *Mater. Charact.*, vol. 95, pp. 187–191, Sep. 2014.
[93] K. Theuwissen, M.-C. Lafont, L. Laffont, B. Viguier, and J. Lacaze, "Microstructural Characterization of Graphite Spheroids in Ductile Iron," *Trans. Indian Inst. Met.*, vol. 65, no. 6, pp. 627–631, Sep. 2012.
[94] K. Theuwissen, J. Lacaze, and L. Laffont, "Structure of graphite precipitates in cast iron," *Carbon N. Y.*, vol. 96, pp. 1120–1128, Jan. 2016.
[95] V. Di Cocco, F. Iacoviello, and M. Cavallini, "Damaging micromechanisms characterization of a ferritic ductile cast iron," *Eng. Fract. Mech.*, vol. 77, no. 11, pp. 2016–2023, Jul. 2010.
[96] V. Di Cocco, F. Iacoviello, A. Rossi, and D. Iacoviello, "Macro and microscopical approach to the damaging micromechanisms analysis in a ferritic ductile cast iron," *Theor. Appl. Fract. Mech.*, vol. 69, pp. 26–33, Feb. 2014.
[97] D. Tromans, "Elastic anisotropy of hcp metal crystals and polycrystals," *Int. J. Res. Rev. Appl. Sci.*, vol. 6, no. 4, 2011.
[98] E. G. Steward, B. P. Cook, and E. A. Kellet, "Dependence on temperature of the interlayer spacing in carbons of different graphitic perfection," *Nature*, vol. 187, no. 4742, pp. 1015–1016, 1960.
[99] Asbury Carbons, "Isotropic graphite for high strength applications," 2015. [Online]. Available: http://asbury.com. [Accessed: 06-Dec-2015].
[100] G. H. Cockett and C. D. Davis, "The lattice expansion of Fe-Si alloys and the volume change at the A3 point," *J. Iron Steel Inst.*, vol. 201, no. 2, pp. 110–115, 1963.
[101] T. Lyman, H. E. Boyer, P. M. Unterweiser, J. E. Foster, J. P. Hontas, and H. Lawton, Eds., *Metals Handbook, Vol. 1: Properties and Selection of Metals*, 8th ed. American Society for Metals, 1961.
[102] G. H. Cockett, "Lattice expansion of Fe-Si alloys and volume change at A3 point," *Iron Steel Inst. -- J.*, vol. 201, pp. 110–115, 1963.
[103] T. Oku, A. Kurumada, Y. Imamura, K. Kawamata, and M. Shiraishi, "Effects of prestresses

on mechanical properties of isotropic graphite materials," *J. Nucl. Mater.*, vol. 258–263, pp. 814–820, 1998.
[104] M. Shirani and G. Härkegård, "Large scale axial fatigue testing of ductile cast iron for heavy section wind turbine components," *Eng. Fail. Anal.*, vol. 18, no. 6, pp. 1496–1510, Sep. 2011.
[105] T. Hara, T. Kitagawa, K. Kuroki, S. Saikawa, K. Terayama, S. Ikeno, and K. Matsuda, "Morphologies of Some Graphites in Ductile Cast Irons," *Mater. Trans.*, vol. 55, no. 9, pp. 1500–1505, 2014.
[106] M. Caldera, M. Chapetti, J. M. Massone, and J. A. Sikora, "Influence of nodule count on fatigue properties of ferritic thin wall ductile iron," *Mater. Sci. Technol.*, vol. 23, no. 8, pp. 1000–1004, Aug. 2007.
[107] A. Vaško, "Fatigue Properties of Synthetic Nodular Cast Irons," *Key Eng. Mater.*, vol. 635, pp. 5–8, Dec. 2014.
[108] A. C. Fischer-Cripps, "Critical review of analysis and interpretation of nanoindentation test data," *Surf. Coatings Technol.*, vol. 200, no. 14–15, pp. 4153–4165, Apr. 2006.
[109] W. C. Oliver and G. M. Pharr, "Measurement of hardness and elastic modulus by instrumented indentation: Advances in understanding and refinements to methodology," *J. Mater. Res.*, vol. 19, no. 1, pp. 3–20, 2004.
[110] Y.-T. Cheng and C.-M. Cheng, "Scaling, dimensional analysis, and indentation measurements," *Mater. Sci. Eng. R Reports*, vol. 44, no. 4–5, pp. 91–149, Aug. 2004.
[111] A. C. Fischer-Cripps, *Nanoindentation*. Springer, 2011.
[112] Z. Li, Y.-T. Cheng, H. T. Yang, and S. Chandrasekar, "On two indentation hardness definitions," *Surf. Coatings Technol.*, vol. 154, no. 2–3, pp. 124–130, May 2002.
[113] M. Mata and J. Alcala, "Mechanical property evaluation through sharp indentations in elastoplastic and fully plastic contact regimes," *J. Mater. Res.*, vol. 18, no. 7, pp. 1705–1709, 2003.
[114] B. Poon, D. Rittel, and G. Ravichandran, "An analysis of nanoindentation in elasto-plastic solids," *Int. J. Solids Struct.*, vol. 45, no. 25–26, pp. 6399–6415, Dec. 2008.
[115] M. Dao, N. Chollacoop, K. J. Van Vliet, T. A. Venkatesh, and S. Suresh, "Computational modeling of the forward and reverse problems in instrumented sharp indentation," *Acta Mater.*, vol. 49, no. 19, pp. 3899–3918, Nov. 2001.
[116] Y.-T. Cheng and C.-M. Cheng, "Relationships between hardness, elastic modulus, and the work of indentation," *Appl. Phys. Lett.*, vol. 73, no. 5, p. 614, 1998.
[117] Y.-T. Cheng, Z. Li, and C.-M. Cheng, "Scaling relationships for indentation measurements," *Philos. Mag. A*, vol. 82, no. 10, pp. 1821–1829, Jul. 2002.
[118] J. Boussinesq, "Applications des potentiels a l'etude de equilibre et du mouvement des solides elastiques," Paris, 1885.
[119] M. F. Doerner and W. D. Nix, "A method for interpreting the data from depth-sensing indentation instruments," *J. Mater. Res.*, vol. 1, no. 4, pp. 601–609, Jan. 1986.
[120] W. C. Oliver and G. M. Pharr, "An improved technique for determining hardness and elastic modulus using load and displacement sensing indentation experiments," *J. Mater. Res.*, vol. 7, no. 6, pp. 1564–1580, 1992.
[121] A. E. H. Love, "Bousinnesq's problem for a rigid cone," *Q. J. Math.*, vol. os-10, no. 1, pp. 161–175, 1939.
[122] J. W. Harding and I. N. Sneddon, "The elastic stresses produced by the indentation of the plane surface of a semi-infinite elastic solid by a rigid punch," *Proc. Camb. Philol. Soc.*, vol. 41, no. 1, pp. 16–26, 1945.
[123] Sneddon, "Boussinesq's problem for a rigid cone," *Proc. Camb. Philol. Soc.*, vol. 44, pp. 492–507, 1948.

[124] C. M. Segedin, “The relation between load and penetration for a spherical punch,” *Mathematika*, vol. 4, no. 2, p. 156, Feb. 1957.
[125] I. N. Sneddon, “The relation between load and penetration in the axisymmetric boussinesq problem for a punch of arbitrary profile,” *Int. J. Eng. Sci.*, vol. 3, no. 1, pp. 47–57, May 1965.
[126] G. M. Pharr and A. Bolshakov, “Understanding nanoindentation unloading curves,” *J. Mater. Res.*, vol. 17, no. 10, pp. 2660–2671, 2002.
[127] N. A. Sakharova, J. V. Fernandes, J. M. Antunes, and M. C. Oliveira, “Comparison between Berkovich, Vickers and conical indentation tests: A three-dimensional numerical simulation study,” *Int. J. Solids Struct.*, vol. 46, no. 5, pp. 1095–1104, Mar. 2009.
[128] A. Bolshakov, W. C. Oliver, and G. M. Pharr, “An explanation for the shape of nanoindentation unloading curves based on finite element simulation,” *Mater. Res. Soc. Symp. Proc.*, vol. 356, pp. 675–680, 1995.
[129] J. Woirgard and J. C. Dargenton, “An alternative method for penetration depth determination in nanoindentation measurements,” *J. Mater. Res.*, vol. 12, no. 9, pp. 2455–2458, 1997.
[130] J. Woirgard, J.-C. Dargenton, C. Tromas, and V. Audurier, “A new technology for nanohardness measurements: principle and applications,” *Surf. Coatings Technol.*, vol. 100–101, no. 1–3, pp. 103–109, Mar. 1998.
[131] J. Gong, H. Miao, and Z. Peng, “Analysis of the nanoindentation data measured with a Berkovich indenter for brittle materials: effect of the residual contact stress,” *Acta Mater.*, vol. 52, no. 3, pp. 785–793, Feb. 2004.
[132] W. Yang, G. E. Ice, J. D. Budai, J. Z. Tischler, and B. C. Larson, “Three-dimensional X-ray structural microscopy with submicrometre resolution,” *Nature*, vol. 415, no. 6874, pp. 887–890, 2002.
[133] W. Yang, B. C. Larson, J. Z. Tischler, G. E. Ice, J. D. Budai, and W. Liu, “Differential-aperture X-ray structural microscopy: a submicron-resolution three-dimensional probe of local microstructure and strain,” *Micron*, vol. 35, no. 6, pp. 431–439, Aug. 2004.
[134] B. C. Larson and L. E. Levine, “Submicrometre-resolution polychromatic three-dimensional X-ray microscopy,” *J. Appl. Crystallogr.*, vol. 46, no. 1, pp. 153–164, 2013.
[135] H. K. D. H. Bhadeshia, S. A. David, J. M. Vitek, and R. W. Reed, “Stress induced transformation to bainite in Fe–Cr–Mo–C pressure vessel steel,” *Mater. Sci. Technol.*, vol. 7, no. 8, pp. 686–698, Aug. 1991.
[136] M. Polcarova, K. Godwod, J. Bak-Misiuk, S. Kadeckova, and J. Bradler, “Lattice parameters of Fe-Si alloy single crystals,” *Phys. Status Solidi a*, vol. 106, no. 1, pp. 17–23, 1988.
[137] P. Rubin, F. Huyan, P. Hedstrom, and R. Larker, “Effect of Solute Silicon on the Lattice Parameter of Ferrite in Ductile Irons,” *Isij Int.*, vol. 54, no. 1, pp. 248–250, 2014.
[138] L. E. Levine, C. Okoro, and R. Xu, “Full elastic strain and stress tensor measurements from individual dislocation cells in copper through-Si vias,” *IUCrJ*, vol. 2, no. 6, pp. 635–642, 2015.

Appendix A
PAPER I

Applied Mathematical Modelling 40 (2016) 5759–5774

Contents lists available at ScienceDirect

Applied Mathematical Modelling

journal homepage: www.elsevier.com/locate/apm

Analytical solution to the 1D Lemaitre's isotropic damage model and plane stress projected implicit integration procedure

T Andriollo [a,*], J Thorborg [a,b], J Hattel [a]

[a] Department of Mechanical Engineering, Technical University of Denmark, DK-2800 Kgs. Lyngby, Denmark
[b] MAGMA GmbH, D-52072 Aachen, Germany

ARTICLE INFO

Article history:
Received 7 January 2015
Revised 4 December 2015
Accepted 13 January 2016
Available online 25 January 2016

Keywords:
Damage
Lemaitre model
Analytical solution
Plane stress
Implicit integration

ABSTRACT

In the present paper, for the first time in literature an exact analytical solution to Lemaitre's isotropic damage model is developed for the special case of uniaxial tensile testing. This is achieved by taking advantage of a convenient formulation of the isotropic hardening function, which allows obtaining an integral relationship between total strain and effective stress. By means of the generalized binomial theorem, an expression in terms of infinite series is subsequently derived. The solution is found to simplify considerably existing techniques for material parameters identification based on optimization, as all issues associated with classical numerical solution procedures of the constitutive equations are eliminated. In addition, an implicit implementation of the plane stress projected version of Lemaitre's model is discussed, showing that the resulting algebraic system can be reduced to a single non-linear equation. The accuracy of the proposed integration scheme is then verified by means of the presented 1D analytical solution. Finally, a closed-form expression for the consistent tangent modulus taking damage evolution into account is given, and its impact on the convergence rate is analyzed.

1. Introduction

Lemaitre's model [1] is today one of the most widely used techniques for modeling damage evolution in ductile materials. Despite several improvements have been proposed in order to account for additional effects like micro-cracks closure under compressive stresses [2] and anisotropy [3,4], the original isotropic formulation limited to isotropic hardening is still often employed due to its simplicity and the relatively low number of material parameters involved. The latter can be easily determined from knowledge of the damage evolution history in loaded specimens, obtainable by means of well-established experimental methods [5]. Nevertheless, it might be that such information is either not available or too expensive to obtain for the specific material at hand. Under these circumstances, it is common practice to identify the material constants on the basis of an optimization analysis aiming at minimizing the error between the predicted numerical results and a reference uniaxial tensile curve [6]. More recently, methodologies which offer improved accuracy by combining the classical experimental stress–strain relationship with other observables have also been proposed [7,8]. However, the use of all such procedures in combination with a numerical resolution of the mathematical model exhibits three main disadvantages. First

* Corresponding author. Tel.: +45 45 25 47 22.
E-mail address: titoan@mek.dtu.dk (T. Andriollo).

http://dx.doi.org/10.1016/j.apm.2016.01.024
S0307-904X(16)30012-9/

Nomenclature

s_{ij}	Deviatoric part of the stress tensor
δ_{ij}	Kronecker delta
ε_{ij}^{tot}, ε_{ij}^{e}, ε_{ij}^{p}	Total/elastic/plastic strain tensor
σ_{ij}	Stress tensor
$\tilde{\sigma}_{ij}$	Effective stress tensor
σ_e	Equivalent Von Mises stress
σ_y, σ_y^0	Actual/initial yield stress
E	Young's modulus
D	Damage variable
R_v	Triaxiality function
S, s	Lemaitre's damage evolution parameters
Y	Energy release rate
Φ	Yield function
k, n	Isotropic hardening parameters
p	Equivalent Von Mises plastic strain
p_{crit}	Critical effective plastic strain for damage evolution
r	Hardening variable
λ	Plastic multiplier
ν	Poisson's ratio
$(\cdot)$	Increment operator
$\Delta()$	Finite variation operator

of all, it requires the use of an optimization algorithm coupled with a numerical tool for solving the underlying system of differential equations. Secondly, the numerical solution procedure in itself is complicated by the "softening" behavior of the damaged material at sufficiently large strains. Thirdly, the produced values for the material parameters are affected, in addition to the experimental & optimization uncertainty, by the error associated with the numerical discretization adopted. With the aim of overcoming all the above-mentioned aspects, an analytical solution to the isotropic Lemaitre's model for the specific case of uniaxial tensile testing is developed in the present paper. Quite surprisingly, no previous works on the subject appear to have been published in literature, despite the intrinsic value that analytical solutions possess, especially in relation to numerical implementations assessment.

Lemaitre's model has also proved effective in predicting damage evolution in situations of plane stress, as recently confirmed by geometric transferability investigations carried out on flat specimens of Ti-6Al-4 V alloy [9]. These characteristic loading conditions are frequently encountered in industrial processes where material degradation becomes a critical factor, as discussed in [10] for the case of sheet metal forming. If a traditional displacement-based implicit finite element code with global full Newton–Raphson iterations is used for the related numerical analysis, a natural complication arises in ensuring the out-of-plane components of the stress tensor to be zero at the end of each load increment. This issue is thoroughly discussed in the context of general elasto-plasticity in [11], where three different techniques are suggested to cope with the problem: (A) direct inclusion of the plane stress constraint at the Gauss point level, (B) addition of a plane stress constraint at the global structural level, (C) use of plane stress projected constitutive equations at the Gauss point level. The first two solutions are usually easier to implement, but at the price of higher computational time; an example of implicit constitutive discretization of Lemaitre's model with kinematic hardening using approach (A) is given in [12]. As a consequence, approach (C) is to be preferred whenever possible, as it leads to more efficient computational procedures due to the fact that only the relevant in-plane stress and strain components are considered [13]. This is also the approach adopted in the second part of the present paper, where it is shown that implicit integration of the plane stress projected Lemaitre's model with isotropic hardening using the elastic predictor-return mapping scheme can be reduced to a single non-linear equation. Furthermore, a closed-form expression for the related consistent tangent modulus is proposed, which is found to improve significantly the convergence rate.

2. Lemaitre's isotropic damage model with isotropic hardening

The fundamental equations characterizing Lemaitre's isotropic damage model with isotropic hardening are reported here in Cartesian components [6]:

(a) additive strain decomposition:

$$\varepsilon_{ij}^{tot} = \varepsilon_{ij}^{e} + \varepsilon_{ij}^{p}, \tag{1}$$

(b) elastic constitutive law:

$$\frac{\sigma_{ij}}{1-D} = \frac{E}{1+\nu}\left[\varepsilon^e_{ij} + \frac{\nu}{1-2\nu}\delta_{ij}\varepsilon^e_{kk}\right], \tag{2}$$

(c) flow rule:

$$\dot{\varepsilon}^p_{ij} = \frac{3s_{ij}}{2\sigma_e}\frac{\dot{\lambda}}{1-D}, \tag{3}$$

(d) yield function:

$$\Phi = \frac{\sigma_e}{1-D} - \sigma_y(r) \leq 0, \;\; \sigma_e = \left(\frac{3}{2s_{ij}s_{ij}}\right)^{\frac{1}{2}}, \tag{4}$$

(e) isotropic hardening rule:

$$\sigma_y = f(r), \tag{5}$$

(f) hardening parameter increment:

$$\dot{r} = (1-D)\dot{p}, \;\; \dot{p} = \left(\frac{2}{3}\dot{\varepsilon}^p_{ij}\dot{\varepsilon}^p_{ij}\right)^{\frac{1}{2}}, \tag{6}$$

(g) damage evolution law:

$$\dot{D} = \left(\frac{Y}{S}\right)^s \dot{p}, \;\; if \;\; p > p_{crit}, \tag{7}$$

(h) energy release rate:

$$Y = \frac{\sigma_e^2 R_v}{2E(1-D)^2}, \;\; R_v = \frac{2}{3}(1+\nu) + 3(1-2\nu)\left(\frac{\sigma_{kk}}{3\sigma_e}\right)^2, \tag{8}$$

(i) consistency condition:

$$\Phi \leq 0, \;\; \dot{\lambda} \geq 0, \;\; \Phi\dot{\lambda} = 0. \tag{9}$$

It may be easily demonstrated that the flow rule (3) together with (6) imply the equality $\dot{r} = \dot{\lambda}$. The derivation is reported in [14].

With regards to the isotropic hardening function appearing in Eq. (5), it is often assumed to have the exponential form:

$$\sigma_y = \sigma_y^0 + R^\infty \;(1 - \exp(-br)), \tag{10}$$

where b is a material parameter and R^∞ represents a saturation value corresponding to $r \to +\infty$. In the context of the present work, the following power-law hardening rule is chosen instead:

$$\sigma_y = k(r + r_0)^n, \;\; r_0 = \left(\frac{\sigma_y^0}{k}\right)^{1/n}, \tag{11}$$

in which k denotes the hardening factor, n the hardening exponent and r_0 is simply a constant whose value is adjusted to ensure $\sigma_y = \sigma_y^0$ for $r = 0$: from a physical point of view, it could be thought of as a parameter associated with the hardening induced by the initial amount of dislocations present in the virgin material. The reason for adopting formulation (11) over (10) is the lower degree of complexity it entails in developing an analytical solution, as explained in the next section.

3. Analytical solution for uniaxial tensile test

The tensor equations presented above may be recast in the corresponding 1D form as follows:

$$\varepsilon^{tot} = \varepsilon^e + \varepsilon^p, \tag{12}$$

$$\sigma = (1-D)E\varepsilon^e, \tag{13}$$

$$\dot{r} = (1-D)\dot{\varepsilon}^p, \tag{14}$$

$$\Phi = \frac{\sigma}{1-D} - \sigma_y(r) \leq 0, \tag{15}$$

$$\sigma_y = k(r + r_0)^n, \tag{16}$$

$$\dot{D} = \left(\frac{Y}{S}\right)^s \dot{\varepsilon}^p \;\; if \;\; \varepsilon^p > p_{crit}, \tag{17}$$

$$Y = \frac{\sigma^2}{2E(1-D)^2}, \tag{18}$$

$$\Phi \leq 0, \;\; \dot{r} \geq 0, \;\; \Phi \dot{r} = 0, \tag{19}$$

where use has been made of the standard equalities $\sigma_e = \sigma_{11} = \sigma$ and $p = \varepsilon^p_{11} = \varepsilon^p$, which are valid in the uniaxial case.

In the next paragraphs, an integral solution in the form $\sigma = f(\varepsilon^{tot})$ to the set of Eqs. (12)–(19) is sought, assuming monotonic growth of the applied total strain, which is taken to be the independent variable for the problem at hand. The two differential relations (14) and (17) are assumed to be complemented by the initial conditions $r = D = 0$ for $\varepsilon^{tot} = 0$. The analysis is split into two parts: the first one corresponds to the pure elasto-plastic regime ($\varepsilon^p \leq p_{crit} \Rightarrow D \equiv 0$), whereas the second one considers damage evolution in addition to plastic flow ($\varepsilon^p > p_{crit} \Rightarrow D > 0$).

3.1. Elasto-plastic regime

For values of the externally imposed total strain which are sufficiently small, the stress state remains inside the yield surface and the material behaves elastically. This means that $\Phi < 0 \Rightarrow \dot{r} = 0 \Rightarrow \dot{\varepsilon}^p = 0 \Rightarrow \varepsilon^{tot} = \varepsilon^e$ and the entire system of Eqs. (12)–(19) reduces to the simple Hooke's law:

$$\sigma = E\varepsilon^{tot}. \tag{20}$$

When the applied strain exceeds the critical threshold $\varepsilon^{tot} = \sigma_y^0/E$, plastic flow takes place, implying $\dot{r} > 0 \Rightarrow \Phi = 0$. However, as long as $\varepsilon^p \leq p_{crit}$, no damage occurs in the material, therefore Eq. (14) dictates $\dot{\varepsilon}^p = \dot{r}$ and consequently $\varepsilon^p = r$ as both variables are assumed to have the same initial value at the beginning of the test. Using the last expression in Eq. (16) gives $\sigma_y = k(\varepsilon^p + r_0)^n$; then, by combining this result with Eqs. (12), (13), (15) one obtains the implicit expression relating stress and total strain as:

$$\sigma = k\left(\varepsilon^{tot} - \frac{\sigma}{E} + r_0\right)^n. \tag{21}$$

The critical stress value $\bar{\sigma}$ at which damage evolution starts during uniaxial straining can be easily found by setting $\varepsilon^{tot} = \varepsilon^e + \varepsilon^p = \bar{\sigma}/E + p_{crit}$ in the last equation, obtaining:

$$\bar{\sigma} = k(p_{crit} + r_0)^n \tag{22}$$

and the corresponding critical total strain is found as:

$$\bar{\varepsilon}^{tot} = p_{crit} + \frac{\bar{\sigma}}{E}. \tag{23}$$

3.2. Damage regime

Once the externally applied strain grows beyond the critical value $\bar{\varepsilon}^{tot}$ calculated according to Eq. (23), damage evolution occurs in addition to plastic flow. In order to simplify the calculations, it is convenient to introduce the effective stress $\tilde{\sigma}$ as [14]:

$$\tilde{\sigma} = \frac{\sigma}{1-D}. \tag{24}$$

By using the above definition together with the consistency condition $\Phi = 0$, the number of equations appearing in the system (12)–(19) can be reduced by 3, and the following 5 relations are obtained:

$$\varepsilon^{tot} = \varepsilon^e + \varepsilon^p, \tag{25}$$

$$\tilde{\sigma} = E\varepsilon^e, \tag{26}$$

$$\dot{r} = (1-D)\dot{\varepsilon}^p \tag{27}$$

$$\tilde{\sigma} = k(r + r_0)^n \tag{28}$$

$$\dot{D} = \left(\frac{\tilde{\sigma}^2}{2ES}\right)^s \dot{\varepsilon}^p, \tag{29}$$

which need to be further combined together and then integrated to find a suitable solution in the form $\tilde{\sigma} = f(\varepsilon^{tot})$.

The starting point is to invert and subsequently differentiate Eq. (28) to get:

$$r = \left(\frac{\tilde{\sigma}}{k}\right)^{1/n} - r_0 \;\; \Rightarrow \;\; \dot{r} = \frac{\tilde{\sigma}^{\frac{1}{n}-1}}{nk^{1/n}}\dot{\tilde{\sigma}}. \tag{30}$$

It is worth noticing in the last expression that as $\dot{r}$ is required to be positive, the effective stress variable $\tilde{\sigma}$ grows monotonically during the test. Combination of Eq. (30) with Eq. (27) yields:

$$\dot{\varepsilon}^p(1-D) = \frac{\tilde{\sigma}^{\frac{1}{n}-1}}{nk^{1/n}}\dot{\tilde{\sigma}}. \tag{31}$$

Finally, the plastic strain increment $\dot{\varepsilon}^p$ appearing in the last relation can be expressed in terms of $\tilde{\sigma}$ and $\dot{D}$ by use of the damage evolution law (29), leading to:

$$\left(\frac{\tilde{\sigma}^2}{2ES}\right)^{-s}(1-D)\dot{D} = \frac{\tilde{\sigma}^{\frac{1}{n}-1}}{nk^{1/n}}\dot{\tilde{\sigma}}. \tag{32}$$

Simple algebraic manipulation allows the equivalent form:

$$(1-D)\dot{D} = A\tilde{\sigma}^{\alpha}\dot{\tilde{\sigma}}, \tag{33}$$

where the following constants have been defined:

$$A = \left(nk^{\frac{1}{n}}(2ES)^s\right)^{-1},\ \alpha = 2s + \frac{1}{n} - 1. \tag{34}$$

The differential Eq. (33) is in separable form and can be integrated from the state $(0, \bar{\sigma})$ to $(D, \tilde{\sigma})$, providing the following direct relation between the effective stress and the damage variable:

$$D - \frac{D^2}{2} = \frac{A}{\alpha+1}\left(\tilde{\sigma}^{\alpha+1} - \bar{\sigma}^{\alpha+1}\right). \tag{35}$$

It is important to point out that the last integral expression has been obtained in closed-form taking advantage of very basic functions of D and $\tilde{\sigma}$ that appear at both sides of (33). In particular, the simple power-law dependence on $\tilde{\sigma}$ is a direct consequence of the specific hardening rule adopted. It may be demonstrated that if the exponential expression (10) were chosen instead of (11), a relation of the type $\tilde{\sigma}^{2s}/(R^{\infty} + \sigma_y^0 - \tilde{\sigma})$ would appear at the right-hand side of Eq. (33), which could not be integrated analytically using conventional techniques.

For a given value of $\tilde{\sigma}$, expression (35) represents a 2nd order polynomial in D. Remembering that the damage variable must be confined to the interval [0, 1], only one root can be accepted (the other being greater than one); its value may be calculated using a standard algebraic formula as:

$$D(\tilde{\sigma}) = 1 - \sqrt{1 - \frac{2A}{\alpha+1}\left(\tilde{\sigma}^{\alpha+1} - \bar{\sigma}^{\alpha+1}\right)}. \tag{36}$$

It is important to observe that the latter relation poses a limitation on the maximum accepted value of $\tilde{\sigma}$, as the argument of the square root must remain positive. From a physical point of view, such limit value $\tilde{\sigma}_{lim}$ corresponds to the point at which damage equals one, meaning that the material stops having any load carrying capacity. In light of these considerations, the following inequality holds:

$$\tilde{\sigma} \le \tilde{\sigma}_{lim} = \left(\frac{\alpha+1}{2A} + \bar{\sigma}^{\alpha+1}\right)^{\frac{1}{\alpha+1}}. \tag{37}$$

Having clarified the range of validity of expression (36), Eqs. (25) and (26) may be differentiated and combined together to express the plastic strain increment in terms of total strain increment and effective stress increment as:

$$\dot{\varepsilon}^p = \dot{\varepsilon}^{tot} - \dot{\tilde{\sigma}}/E. \tag{38}$$

Then, (38) can be inserted into Eq. (31) to obtain, after simple manipulations, the following expression:

$$\dot{\varepsilon}^{tot} = \left(\frac{1}{E} + \frac{\tilde{\sigma}^{\frac{1}{n}-1}}{(1-D)nk^{1/n}}\right)\dot{\tilde{\sigma}}. \tag{39}$$

Relation (39) represents again a differential equation in separable form, where the function $D(\tilde{\sigma})$ is defined according to Eq. (36). Integration from the state $(\bar{\varepsilon}^{tot}, \bar{\sigma})$ to $(\varepsilon^{tot}, \tilde{\sigma})$ yields:

$$\varepsilon^{tot}(\tilde{\sigma}) = \bar{\varepsilon}^{tot} + \frac{\tilde{\sigma} - \bar{\sigma}}{E} + I(\tilde{\sigma}). \tag{40}$$

The function $I(\tilde{\sigma})$ appearing in the last expression corresponds to:

$$I(\tilde{\sigma}) = z\int_{\bar{\sigma}}^{\tilde{\sigma}} \frac{\tilde{\sigma}^{\alpha-2s}}{\sqrt{\tilde{\sigma}_{lim}^{\alpha+1} - \tilde{\sigma}^{\alpha+1}}}d\tilde{\sigma}, \tag{41}$$

where $\tilde{\sigma}_{lim}$is defined according to (37) and the constant z denotes the following combination of material parameters:

$$z = \frac{1}{nk^{\frac{1}{n}}}\sqrt{\frac{\alpha+1}{2A}} \tag{42}$$

It is worth noticing that as the hardening exponent n is usually smaller than unity, the definition (34) implies that the following inequality is satisfied:

$$\frac{1}{n} - 1 = \alpha - 2s > 0. \tag{43}$$

As s is a positive parameter, it follows that α is greater than zero as well. Consequently, both z and $\tilde{\sigma}_{lim}$ turn out to be strictly positive, as inspection of Eqs. (37) and (42) reveals.

Unluckily, the integral in Eq. (41) cannot be computed in a straightforward manner; however, an exact solution in terms of infinite series is presented in the next section.

3.3. Exact integral solution in terms of infinite series

The first step to arrive to an analytical expression for the integral (41) is to make the following variable change:

$$\frac{\tilde{\sigma}_{lim}^{\alpha+1} - \tilde{\sigma}^{\alpha+1}}{\tilde{\sigma}_{lim}^{\alpha+1}} = x \;\Leftrightarrow\; \tilde{\sigma} = \tilde{\sigma}_{lim}(1-x)^{\frac{1}{\alpha+1}}, \tag{44}$$

in order to obtain:

$$I(x) = B \int_{\bar{x}}^{x} \frac{(1-x)^{\beta}}{\sqrt{x}} dx, \tag{45}$$

where the following constants have been introduced:

$$B = -\frac{z}{\alpha+1}(\tilde{\sigma}_{lim})^{\frac{\alpha-4s+1}{2}}, \quad \beta = \frac{-2s}{\alpha+1}. \tag{46}$$

Expression (37) states that $\tilde{\sigma}$ can never grow beyond the value $\tilde{\sigma}_{lim}$at which damage equals unity. Consequently, the definition (44) implies x to be positive and less than one. Under these conditions, the numerator of the integrand in expression (45) can be represented in terms of an infinite series by means of the binomial theorem generalized to real powers [15]:

$$(1+x)^{\beta} = \sum_{m=0}^{+\infty} \binom{\beta}{m} x^m, \quad \binom{\beta}{m} = \frac{\beta(\beta-1)(\beta-2)\ldots(\beta-m+1)}{m!}, \tag{47}$$

where convergence is guaranteed for $|x| < 1$. By using the latter result in Eq. (45) one obtains:

$$I(x) = B \int_{\bar{x}}^{x} \left(\sum_{m=0}^{+\infty} (-1)^m \binom{\beta}{m} x^{m-1/2} \right) dx, \tag{48}$$

and straightforward integration provides:

$$I(x) = 2B \sum_{m=0}^{+\infty} \frac{(-1)^m}{2m+1} \binom{\beta}{m} \left[x^{m+1/2} - \bar{x}^{m+1/2} \right]. \tag{49}$$

The last expression represents a closed-form solution to the integral reported in Eq. (41); therefore, it allows relation (40) between the effective stress and the total strain to be defined in the following exact analytical form:

$$\varepsilon^{tot}(\tilde{\sigma}) = \bar{\varepsilon}^{tot} + \frac{\tilde{\sigma} - \bar{\sigma}}{E} + 2B \sum_{m=0}^{+\infty} \frac{(-1)^m}{2m+1} \binom{\beta}{m} \left[\left(1 - \frac{\tilde{\sigma}^{\alpha+1}}{\tilde{\sigma}_{lim}^{\alpha+1}} \right)^{m+1/2} - \left(1 - \frac{\bar{\sigma}^{\alpha+1}}{\tilde{\sigma}_{lim}^{\alpha+1}} \right)^{m+1/2} \right]. \tag{50}$$

An appealing feature of the above solution is that the first 10 terms of the expansion are already sufficient to achieve an accuracy of approximately 0.3 % on the calculated total strain, as Fig. 1 shows.

4. Application to damage parameters identification

The analytical solution developed in the previous sections can be effectively used in all material parameters identification procedures which involve fitting of one or more experimentally measured uniaxial stress–strain curves. As data are usually provided as a set of $(\varepsilon_i^{tot},\ \sigma_i^{exp})$ values, a natural measure of the deviation of the model predictions from measurements is:

$$\mathcal{L}(\mathcal{A}) = \frac{1}{n_e} \sum_{n=1}^{n_e} \left[\sigma\left(\varepsilon_i^{tot}, \mathcal{A}\right) - \sigma_i^{exp} \right]^2, \tag{51}$$

where n_e indicates the total number of experimental points and $\mathcal{A}$ denotes a certain set of material parameters:

$$\mathcal{A} = \left[E, \sigma_y^0, k, n, p_{crit}, S, s \right] \tag{52}$$

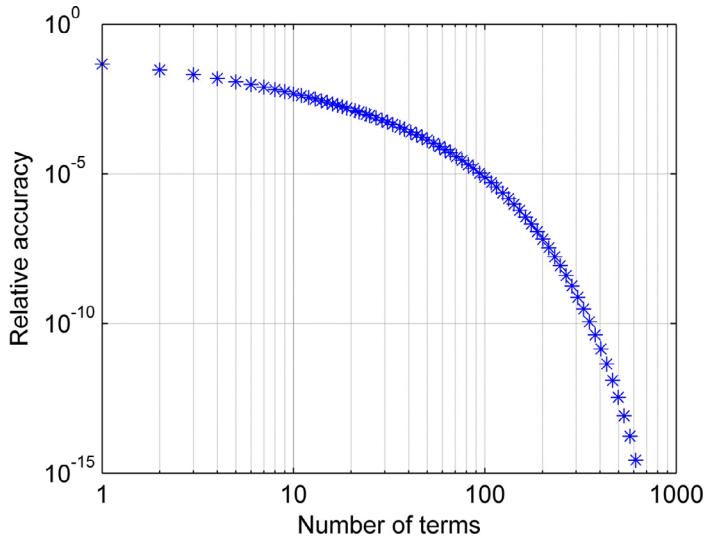

Fig. 1. Relative accuracy of the computed solution as a function of the number of terms included in the series expansion of Eq. (50). Values are obtained using an effective stress of 600 MPa, corresponding to a total strain of approximately 0.3, and the material parameters of Table 1. The accuracy is related to a reference solution with 10,000 terms.

The best set of parameters can be determined by minimizing expression (51) with respect to $\mathcal{A}$. A discussion on the numerical procedures currently available for such optimization problem may be found, for instance, in [6] or [16], where the specific issue of damage parameter identification is addressed. Usually, values for E and σ_y^0 can be directly read off the uniaxial tensile curve, so that the number of unknown parameters in (51) reduces to five. Moreover, if the critical strain $\bar{\varepsilon}^{tot}$ at which damage evolution begins can be experimentally determined (normally, it can be roughly identified with the peak point of the curve [6], i.e. the ultimate stress), the optimization can be performed into two distinct stages. In the first one, all experimental points with $\varepsilon_i^{tot} > \bar{\varepsilon}^{tot}$ are neglected, and the two plastic flow parameters k and n are calculated; then, a new minimization analysis including the entire data set is run for determining the remaining damage parameters S and s. It has to be emphasized that with this kind of approach, the final damage threshold D_c at which crack initiation occurs turns out to be implicitly defined by the point of maximum total strain. An additional algebraic constraint could be used during optimization to set D_c to a specific level or to keep it within a prescribed range.

4.1. Obtaining the solution for a fixed total strain value

In Eq. (51), for a given $\mathcal{A}$ and a given total strain ε_i^{tot}, the corresponding stress value $\sigma(\varepsilon_i^{tot}, \mathcal{A})$ predicted by the isotropic Lemaitre's damage model can be calculated as follows:

- the constants $A,\ \alpha, \tilde{\sigma}_{lim}, z, B, \beta$ are determined according to (34), (37), (42), (46);
- the critical total strain $\bar{\varepsilon}^{tot}$ and stress $\bar{\sigma}$ for damage initiation are computed using (22) and (23);
- the total strain value is checked:
- $\varepsilon_i^{tot} \leq \sigma_y^0/E$: stress is calculated using (20);
- $\sigma_y^0/E < \varepsilon_i^{tot} \leq \bar{\varepsilon}^{tot}$: stress is calculated using (21);
- $\varepsilon_i^{tot} > \bar{\varepsilon}^{tot}$: the effective stress is calculated first by solving the algebraic Eq. (50).
  Then, the corresponding damage value is obtained from (36) and finally the stress is determined via (24).

It is worth noticing that Eq. (50) still requires a numerical algorithm to be solved for a prescribed value of the total strain. However, the advantage is that it is not the common stress which appears in the expression, but the effective stress. This quantity grows monotonically during tensile testing, as explained in Section 3.2. Therefore, its dependence on the total strain turns out to be monotonic as well, as confirmed by Eq. (39), which may be rewritten for convenience in the following form:

$$\frac{d\varepsilon^{tot}}{d\tilde{\sigma}} = \frac{1}{E} + \frac{\tilde{\sigma}^{\frac{1}{n}-1}}{(1-D)nk^{1/n}}. \tag{53}$$

Further differentiation provides:

$$\frac{d^2\varepsilon^{tot}}{d\tilde{\sigma}^2} = \frac{(1-n)\tilde{\sigma}^{\frac{1}{n}-2}}{(1-D)n^2k^{1/n}} + \frac{\tilde{\sigma}^{\frac{1}{n}-1}}{(1-D)^2nk^{1/n}}\frac{dD}{d\tilde{\sigma}}. \tag{54}$$

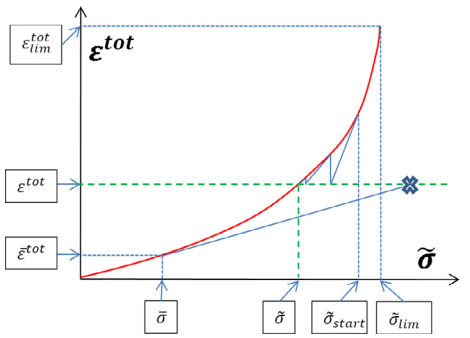

Fig. 2. Qualitative representation of the function $\varepsilon^{tot}(\tilde{\sigma})$ defined by Eq. (50) and influence of the starting point on the subsequent Newton–Raphson iterations.

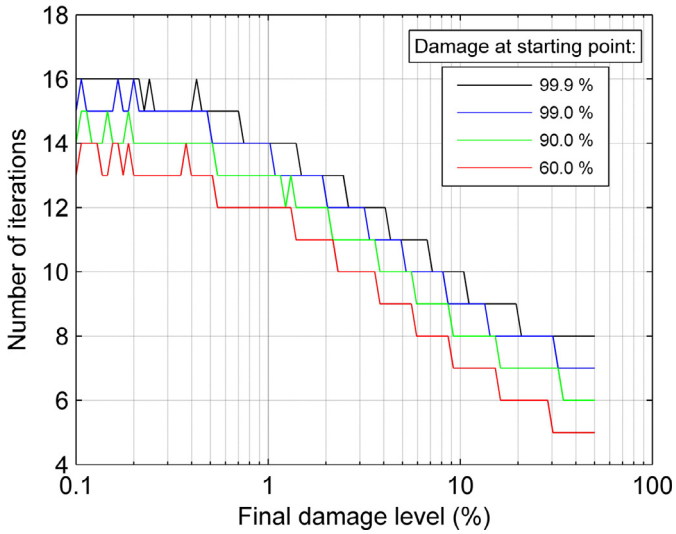

Fig. 3. Number of Newton–Raphson iterations required to achieve machine precision while solving Eq. (50) for the effective stress. Curves are parametric in the choice of the initial starting point.

As damage can never decrease, $dD/d\tilde{\sigma}$ is always positive in the latter expression. As a consequence, both the first and the second derivative of the function $\varepsilon^{\mathrm{tot}}(\tilde{\sigma})$ are always greater than zero. This means that ideal conditions for application of the Newton–Raphson algorithm exist, as the function is smooth, monotonic and with constant convexity. This is of course in sharp contrast with the behavior of the stress-total strain relationship, which inevitably exhibits softening at a certain stage, compromising the stability of finite element codes based on the Newton–Raphson method.

Within the present context, the choice of the starting point for the numerical iterations deserves a special comment. With reference to Fig. 2, for a given total strain ε^{tot} it is important to choose an initial value $\tilde{\sigma}_{start}$ which is larger than the effective stress $\tilde{\sigma}$ which represents the final solution. This ensures a fast convergence of the Newton–Raphson method. Conversely, if a smaller value is adopted, the updated value for the effective stress might be larger than the limit value $\tilde{\sigma}_{lim}$ defined in expression (37). In such a case, it is necessary to set as the new value a point between $\tilde{\sigma}_{start}$ and $\tilde{\sigma}_{lim}$, whose choice is somehow arbitrary.

In situations of practical interest, a good strategy is to select as starting point an effective stress value which corresponds to a very high damage level, according to Eq. (35). The reason is that in common materials damage values close to unity are usually never achieved, as cracks nucleate when the critical damage threshold $D_c < 1$ is exceeded. Fig. 3 shows the number of Newton–Raphson iterations required to solve Eq. (50) for a range of total strains corresponding to damage levels between 0.1 and 50%, using the parameters of Table 1. As one would expect, the closer the initial and final states, the lower the number of iterations required to achieve machine precision. However, by choosing as starting point a damage level of 60 %, only 2–3 iterations are saved compared to selecting a starting point with 99.9 % damage. Therefore, effective stresses corresponding to damage values close to unity should be preferred when it comes to select a suitable starting point, as they allow solving the function $\varepsilon^{\mathrm{tot}}(\tilde{\sigma})$ over almost the entire admissible range of total strain, at the same time maintaining the computational cost reasonable.

Table 1
Admissible range used in the constrained optimization analysis and computed value for each material parameter of the ferritic matrix of GJS 400-18 ductile iron.

	k (MPa)	n	p_{crit} (%)	S (MPa)	s
Admissible range	500 ÷ 1000	0.100 ÷ 0.300	0 ÷ 10.000	0.100 ÷ 10.000	0.100 ÷ 5.000
Calculated value	818	0.245	0.533	0.357	0.167

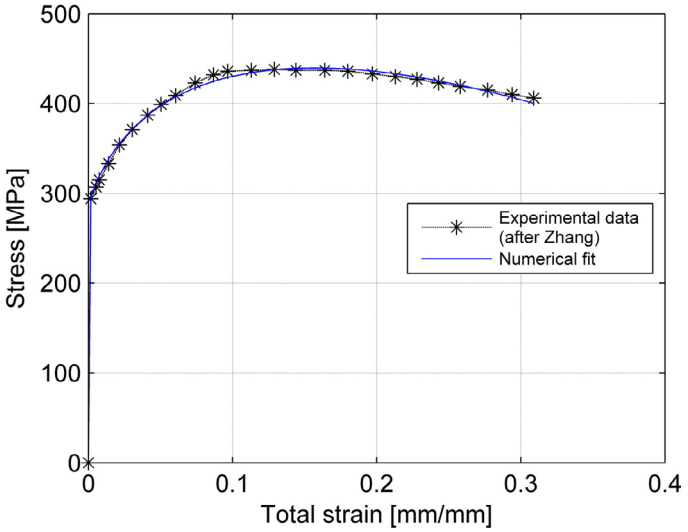

Fig. 4. Lemaitre's damage parameters identification for the ferritic matrix of GJS 400-18 ductile cast iron. The experimental uniaxial tensile curve is taken from [17].

4.2. Damage parameters for the GJS 400-18 ductile iron matrix

In order to give an example of the applicability of the proposed analytical solution in the context of the simple identification procedure described above, material parameters have been determined on the basis of the uniaxial tensile curve for the ferritic matrix of GJS 400-18 (according to EN1563) ductile cast iron reported in [17]. Such material is known to be very ductile and characterized by values of Young's modulus and initial yield strength of $E=210$ GPa and $\sigma_y^0=295$ MPa respectively. As the curve was provided as true stress vs true strain, conversion to "engineering" quantities has been necessary.

Minimization of Eq. (51) has been carried out using the standard genetic algorithm available in the Matlab Global Optimization Toolbox. In a first step, an admissible range for the hardening quantities k and n have been determined by taking into account only the increasing part of the uniaxial curve. Then, in a second stage, the damage parameters have also been included in the analysis, this time considering the entire dataset. The optimization algorithm has been run setting maximum and minimum constraints on S and s according to realistic values for metals and alloys on the basis of the data reported in [6]. Moreover, admissible values for the critical plastic strain have been limited to 10%, which is approximately the deformation corresponding to the point of initial softening in the uniaxial tensile curve. An additional non-linear constraint which ensures that $\varepsilon^{\mathrm{tot}}(\tilde{\sigma}_{lim})$ be greater than the maximum total strain experimentally recorded has also been enforced.

A summary of the imposed limit constraints together with the calculated values of all material parameters is reported in Table 1. It is worth saying that the computed values are of the same order of magnitude of those tabulated in [6], except for the damage exponent s, which is usually greater than or equal to one. A qualitative comparison between the experimental data and the stress–strain curve predicted using the calculated parameters is given in Fig. 4.

5. Implicit algorithm for the plane stress case

In this section, a plane-stress projected version of Lemaitre's isotropic model is first derived and then discretized using the implicit (backward-Euler) method. Furthermore, it is shown that the resulting algebraic system can be reduced to a single non-linear equation, similar to what done in [18] for the general 3D case. The notation adopted closely follows that employed in [11] for deriving the implicit plane stress projected version of the classical von-Mises plasticity model; in particular, boldface capital letters are used for matrices, and boldface lowercase letters for vectors.

To simplify the derivation, it is convenient to replace the yield function (4) with the equivalent form:

$$\Phi=\frac{\sigma_e^2}{(1-D)^2}-\sigma_y^2(r)\le 0,\quad \sigma_e=\left[\left(\frac{3}{2}\right)s_{ij}s_{ij}\right]^{\frac{1}{2}}. \tag{55}$$

As a consequence, the flow rule (3) becomes:

$$\dot{\varepsilon}^p_{ij} = \frac{3s_{ij}}{(1-D)^2}\dot{\lambda} \tag{56}$$

Furthermore, it could be shown that (6) combined with (56) leads to the following relation:

$$\dot{r} = (1-D)\dot{p} = \dot{\lambda}\left[\frac{6s_{ij}s_{ij}}{(1-D)^2}\right]^{1/2}. \tag{57}$$

By using the last 3 formulas and the definition of the effective stress (24), the 2D plane-stress projected Lemaitre's model can now be written in terms of the in-plane stress and strain components only as follows:

$$\boldsymbol{\varepsilon}^{tot} = \boldsymbol{\varepsilon}^{e} + \boldsymbol{\varepsilon}^{p}, \tag{58}$$

$$\tilde{\boldsymbol{\sigma}} = \mathbf{D}\boldsymbol{\varepsilon}^{e}, \tag{59}$$

$$\Phi = \frac{3}{2}\tilde{\boldsymbol{\sigma}}^{T}\mathbf{P}\tilde{\boldsymbol{\sigma}} - \sigma_y^2(r) \le 0, \tag{60}$$

$$\dot{\boldsymbol{\varepsilon}}^{p} = \frac{3\dot{\lambda}}{1-D}\mathbf{P}\tilde{\boldsymbol{\sigma}}, \tag{61}$$

$$\dot{r} = (1-D)\dot{p} = \dot{\lambda}\sqrt{6\tilde{\boldsymbol{\sigma}}^{T}\mathbf{P}\tilde{\boldsymbol{\sigma}}}, \tag{62}$$

$$\dot{D} = \left(\frac{Y}{S}\right)^{s}\dot{p}\ \ if\ \ p > p_{crit}, \tag{63}$$

$$Y = \frac{1}{2}\tilde{\boldsymbol{\sigma}}^{T}\mathbf{D}^{-1}\tilde{\boldsymbol{\sigma}}, \tag{64}$$

$$\Phi \le 0,\ \ \dot{\lambda} \ge 0,\ \ \Phi\dot{\lambda} = 0, \tag{65}$$

where:

- the effective stress vector $\tilde{\boldsymbol{\sigma}}$ and the generic strain vector ε are defined as:

$$\tilde{\boldsymbol{\sigma}} = \frac{1}{1-D}\begin{bmatrix}\sigma_{11} & \sigma_{22} & \sigma_{12}\end{bmatrix}^{T},\ \ \boldsymbol{\varepsilon} = \begin{bmatrix}\varepsilon_{11} & \varepsilon_{22} & 2\varepsilon_{12}\end{bmatrix}^{T} \tag{66}$$

- the plane stress isotropic elasticity matrix **D** and the "deviatoric" matrix **P** are given by:

$$\mathbf{D} = \frac{E}{1-\nu^2}\begin{bmatrix}1 & \nu & 0\\ \nu & 1 & 0\\ 0 & 0 & \frac{1-\nu}{2}\end{bmatrix},\ \ \mathbf{P} = \frac{1}{3}\begin{bmatrix}2 & -1 & 0\\ -1 & 2 & 0\\ 0 & 0 & 6\end{bmatrix}. \tag{67}$$

It is worth observing that expression (64) for the energy release rate has been obtained on the basis of its formal definition, reported in [6]. Moreover, for deriving Eqs. (60) and (62) the well-known identity $s_{ij}s_{ij} = \sigma_{ij}s_{ij}$ has been used.

At this point, the system of differential Eqs. (58)–(65) is implicitly discretized, i.e. all differentials are replaced by the corresponding finite variation in the pseudo-time step $t_n \to t_{n+1}$ and the other variables are evaluated at t_{n+1}:

$$\boldsymbol{\varepsilon}^{tot}_{n+1} = \boldsymbol{\varepsilon}^{e}_{n+1} + \boldsymbol{\varepsilon}^{p}_{n+1}\ , \tag{68}$$

$$\tilde{\boldsymbol{\sigma}}_{n+1} = \mathbf{D}\boldsymbol{\varepsilon}^{e}_{n+1}, \tag{69}$$

$$\Phi_{n+1} = \frac{3}{2}\tilde{\boldsymbol{\sigma}}^{T}_{n+1}\mathbf{P}\tilde{\boldsymbol{\sigma}}_{n+1} - \sigma_y^2(r_{n+1}) \le 0, \tag{70}$$

$$\Delta\boldsymbol{\varepsilon}^{p} = \frac{3\Delta\lambda}{1-D_{n+1}}\mathbf{P}\tilde{\boldsymbol{\sigma}}_{n+1}, \tag{71}$$

$$\Delta r = (1-D_{n+1})\Delta p = \Delta\lambda\sqrt{6\tilde{\boldsymbol{\sigma}}^{T}_{n+1}\mathbf{P}\tilde{\boldsymbol{\sigma}}_{n+1}}, \tag{72}$$

$$\Delta D = \left(\frac{Y_{n+1}}{S}\right)^{s}\Delta p\ \ if\ \ p_{n+1} > p_{crit}, \tag{73}$$

$$Y_{n+1} = \frac{1}{2}\tilde{\boldsymbol{\sigma}}^{T}_{n+1}\mathbf{D}^{-1}\tilde{\boldsymbol{\sigma}}_{n+1}, \tag{74}$$

$$\Phi_{n+1} \le 0,\ \ \Delta\lambda \ge 0,\ \ \Phi_{n+1}\Delta\lambda = 0. \tag{75}$$

The solution of the above system of non-linear equations is assumed to be performed according to an elastic predictor – return mapping scheme, which allows an efficient handling of the discrete condition (75). In the present paper, only the

return mapping stage ($\Delta\lambda > 0$) with $p_{n+1} > p_{crit}$ is discussed; the other two cases, elastic predictor ($\Delta\lambda = 0$) and return mapping ($\Delta\lambda > 0$) with $p_{n+1} < p_{crit}$ are basically identical to those described in details for the von-Mises plasticity model in [11]. In order to be consistent with the framework adopted by the latter authors, the total strain at the new time level, which is the main independent variable of the problem, is substituted by the elastic trial strain:

$$\boldsymbol{\varepsilon}^{e}_{\boldsymbol{trial}} = \boldsymbol{\varepsilon}^{e}_{\boldsymbol{n}} + \Delta\boldsymbol{\varepsilon}^{\boldsymbol{tot}} \;\Rightarrow\; \boldsymbol{\varepsilon}^{\boldsymbol{tot}}_{\boldsymbol{n+1}} = \boldsymbol{\varepsilon}^{e}_{\boldsymbol{trial}} - \boldsymbol{\varepsilon}^{e}_{\boldsymbol{n}} + \boldsymbol{\varepsilon}^{\boldsymbol{tot}}_{\boldsymbol{n}} = \boldsymbol{\varepsilon}^{e}_{\boldsymbol{trial}} + \boldsymbol{\varepsilon}^{p}_{\boldsymbol{n}}. \tag{76}$$

The last expression allows recasting (68) in the equivalent form:

$$\boldsymbol{\varepsilon}^{e}_{\boldsymbol{trial}} = \boldsymbol{\varepsilon}^{e}_{\boldsymbol{n+1}} + \Delta\boldsymbol{\varepsilon}^{\boldsymbol{p}}. \tag{77}$$

If the elastic law (69) and the flow rule (71) are inserted into (77) and the expressions for the hardening variable variation (72) and energy release rate (74) are used in (70) and (73), the discretized system for $\Delta\lambda \geq 0$ and $p_{n+1} > p_{crit}$ reduces to the following three algebraic equations:

$$\mathbf{D}^{-1}\tilde{\boldsymbol{\sigma}}_{\boldsymbol{trial}} = \mathbf{D}^{-1}\tilde{\boldsymbol{\sigma}}_{\boldsymbol{n+1}} + \frac{3\Delta\lambda}{1-D_{n+1}}\mathbf{P}\tilde{\boldsymbol{\sigma}}_{\boldsymbol{n+1}}, \tag{78}$$

$$\Phi_{n+1} = \frac{3}{2}\tilde{\boldsymbol{\sigma}}^{\boldsymbol{T}}_{\boldsymbol{n+1}}\mathbf{P}\tilde{\boldsymbol{\sigma}}_{\boldsymbol{n+1}} - \sigma_y^2\left(r_n + \Delta\lambda\sqrt{6\tilde{\boldsymbol{\sigma}}^{\boldsymbol{T}}_{\boldsymbol{n+1}}\mathbf{P}\tilde{\boldsymbol{\sigma}}_{\boldsymbol{n+1}}}\right) = 0, \tag{79}$$

$$D_{n+1} - D_n = \frac{\Delta\lambda}{1-D_{n+1}}\left(\frac{\tilde{\boldsymbol{\sigma}}^{\boldsymbol{T}}_{\boldsymbol{n+1}}\mathbf{D}^{-1}\tilde{\boldsymbol{\sigma}}_{\boldsymbol{n+1}}}{2S}\right)^{s}\sqrt{6\tilde{\boldsymbol{\sigma}}^{\boldsymbol{T}}_{\boldsymbol{n+1}}\mathbf{P}\tilde{\boldsymbol{\sigma}}_{\boldsymbol{n+1}}}, \tag{80}$$

in the three unknowns $\tilde{\boldsymbol{\sigma}}_{\mathbf{n}+1}$, $\Delta\lambda$ and D_{n+1}. To simplify things even further, similar to what is done in [13], the following orthogonal transformation $\mathbf{Q}$ is introduced:

$$\mathbf{Q} = \mathbf{Q}^{\mathbf{T}} = \mathbf{Q}^{-1} = \begin{bmatrix} 1/\sqrt{2} & 1/\sqrt{2} & 0 \\ 1/\sqrt{2} & -1/\sqrt{2} & 0 \\ 0 & 0 & 1 \end{bmatrix}, \tag{81}$$

and the matrix $\mathbf{D}^{-1}$ and $\mathbf{P}$ assume the corresponding diagonal form:

$$\mathbf{D}^{-1}_{\mathbf{Q}} = \mathbf{Q}^{\mathbf{T}}\mathbf{D}^{-1}\mathbf{Q} = \begin{bmatrix} \dfrac{1-\nu}{E} & 0 & 0 \\ 0 & \dfrac{1}{2G} & 0 \\ 0 & 0 & \dfrac{1}{G} \end{bmatrix}, \quad \mathbf{P}_{\mathbf{Q}} = \mathbf{Q}^{\mathbf{T}}\mathbf{P}\mathbf{Q} = \begin{bmatrix} 1/3 & 0 & 0 \\ 0 & 1 & 0 \\ 0 & 0 & 2 \end{bmatrix}. \tag{82}$$

Taking advantage of representation (82) which enables easier matrix multiplication and inversion, simple algebraic manipulations allow rewriting (78) in the new reference system as:

$$\tilde{\boldsymbol{\sigma}}_{\boldsymbol{Q,n+1}} = \mathbf{F}_{\mathbf{Q}}\tilde{\boldsymbol{\sigma}}_{\boldsymbol{Q,trial}}, \tag{83}$$

where matrix $\mathbf{F}_{\mathbf{Q}}$ is given by:

$$\mathbf{F}_{\mathbf{Q}} = \left(\mathbf{I} + 3\omega\mathbf{D}_{\mathbf{Q}}\mathbf{P}_{\mathbf{Q}}\right)^{-1} = \begin{bmatrix} \dfrac{1-\nu}{\omega E + 1 - \nu} & 0 & 0 \\ 0 & 1/(6\omega G + 1) & 0 \\ 0 & 0 & 1/(6\omega G + 1) \end{bmatrix}, \tag{84}$$

and the parameter ω has been introduced as:

$$\omega = \frac{\Delta\lambda}{\left(1 - D^{n+1}\right)}. \tag{85}$$

By inserting expression (83) into the scalar Eqs. (79) and (80) the following two relations are obtained:

$$\Phi_{n+1} = \frac{3}{2}\xi(\omega) - \sigma_y^2\left(r^n + \Delta\lambda\sqrt{6\xi(\omega)}\right) = 0, \tag{86}$$

$$D_{n+1} - D_n = \omega\left(\frac{\psi(\omega)}{2S}\right)^{s}\sqrt{6\xi(\omega)}, \tag{87}$$

in which the scalar functions ξ and ψ are given by:

$$\begin{aligned}\xi(\omega) &= \tilde{\boldsymbol{\sigma}}^{\boldsymbol{T}}_{\boldsymbol{Q,trial}}\mathbf{F}^{\mathbf{T}}_{\mathbf{Q}}\mathbf{P}_{\mathbf{Q}}\mathbf{F}_{\mathbf{Q}}\tilde{\boldsymbol{\sigma}}_{\boldsymbol{Q,trial}} = \\ &= \frac{1}{3}\left(\frac{1-\nu}{\omega E + 1 - \nu}\right)^2\left(\tilde{\sigma}_{11,trial}\right)^2 + \frac{1}{(6\omega G + 1)^2}\left(\tilde{\sigma}_{22,trial}\right)^2 + \frac{2}{(6\omega G + 1)^2}\left(\tilde{\sigma}_{12,trial}\right)^2,\end{aligned} \tag{88}$$

$$\psi(\omega) = \tilde{\boldsymbol{\sigma}}_{\boldsymbol{trial}}^{\boldsymbol{T}} \mathbf{F}_{\mathbf{Q}}^{\mathbf{T}} \mathbf{D}_{\mathbf{Q}}^{-1} \mathbf{F}_{\mathbf{Q}} \tilde{\boldsymbol{\sigma}}_{\boldsymbol{trial}} = \\ = \frac{1}{E} \frac{(1-\nu)^3}{(\omega E + 1 - \nu)^2} \left(\tilde{\sigma}_{11,trial}\right)^2 + \frac{1}{2G} \frac{1}{(6\omega G + 1)^2} \left(\tilde{\sigma}_{22,trial}\right)^2 + \frac{1}{G} \frac{1}{(6\omega G + 1)^2} \left(\tilde{\sigma}_{12,trial}\right)^2 . \tag{89}$$

It has to be remarked that the components of the trial effective stress entering the last two formulas are those of the transformed vector $\tilde{\boldsymbol{\sigma}}_{\mathbf{Q},\boldsymbol{trial}} = \mathbf{Q}\tilde{\boldsymbol{\sigma}}_{\boldsymbol{trial}}$.

Finally, by expressing D^{n+1} in terms of $\Delta\lambda$ and ω from Eq. (85) and inserting the result in (87) one gets after simple algebraic manipulations:

$$\Delta\lambda = \omega(1 - D_n) - \omega^2 \left(\frac{\psi(\omega)}{2S}\right)^s \sqrt{6\xi(\omega)}, \tag{90}$$

which provides the plastic multiplier as a function of the parameter ω only. Then, substitution of (90) into (86) yields:

$$\Phi_{n+1} = \frac{3}{2}\xi(\omega) - \sigma_y^2 \left(r^n + \omega(1 - D_n)\sqrt{6\xi(\omega)} - 6\omega^2 \left(\frac{\psi(\omega)}{2S}\right)^s \xi(\omega) \right) = 0. \tag{91}$$

The last expression represents fulfillment of the consistency condition at the new pseudo-time step t_{n+1} and contains the parameter ω as only unknown. With its solution at hand, obtained for instance using a simple Newton formula, the other variables are trivially updated as follows:

- calculate $\Delta\lambda$ from (90) and update damage as $D^{n+1} = 1 - \Delta\lambda/\omega$;
- update the hardening variable using $r^{n+1} = r^n + \Delta\gamma\sqrt{6\xi(\omega)}$;
- calculate the new effective stress $\tilde{\boldsymbol{\sigma}}_{\mathbf{Q},\boldsymbol{n+1}}$ in the diagonal reference system using (83);
- update the new elastic strain in the original reference system as $\boldsymbol{\varepsilon}_{\boldsymbol{n+1}}^{\boldsymbol{e}} = \mathbf{Q}\mathbf{D}_{\mathbf{Q}}^{-1}\tilde{\boldsymbol{\sigma}}_{\mathbf{Q},\boldsymbol{n+1}}$.

6. Closed-form expression for the consistent tangent modulus

The consistent tangent modulus represents the derivative of the stress $\boldsymbol{\sigma}_{\boldsymbol{n+1}}$ delivered by the integration algorithm with respect to the externally imposed total strain $\boldsymbol{\varepsilon}_{\boldsymbol{n+1}}^{\boldsymbol{tot}}$ and it plays a crucial role for attaining quadratic rate of asymptotic convergence in finite element implementations based on the full Newton–Raphson scheme [19]. In relation to the plane-stress projected Lemaitre's implicit integration procedure presented in the previous section, it is clear in the light of relation (76) that the derivative with respect to the total strain is equivalent to the derivative with respect to the trial elastic strain $\boldsymbol{\varepsilon}_{\boldsymbol{trial}}^{\boldsymbol{e}}$, which is in turn related to the derivative with respect to $\tilde{\boldsymbol{\sigma}}_{\boldsymbol{trial}}$ via the elasticity matrix $\mathbf{D}$.

With reference to the diagonal reference system defined by the transformation (81), the differential of the relation connecting stress and effective stress is given by:

$$d\boldsymbol{\sigma}_{\mathbf{Q},\boldsymbol{n+1}} = (1 - D_{n+1}) d\tilde{\boldsymbol{\sigma}}_{\mathbf{Q},\boldsymbol{n+1}} - \tilde{\boldsymbol{\sigma}}_{\mathbf{Q},\boldsymbol{n+1}} dD_{n+1}. \tag{92}$$

In what follows, suitable formulas for both differentials appearing on the right-hand side of the latter expression in terms of $d\tilde{\boldsymbol{\sigma}}_{\boldsymbol{trial}}$ will be developed.

Starting out with the differential of the effective stress, straightforward differentiation of (83) reads:

$$d\tilde{\boldsymbol{\sigma}}_{\mathbf{Q},\boldsymbol{n+1}} = \mathrm{d}\mathbf{F}_{\mathbf{Q}} \tilde{\boldsymbol{\sigma}}_{\mathbf{Q},\boldsymbol{trial}} + \mathbf{F}_{\mathbf{Q}} d\tilde{\boldsymbol{\sigma}}_{\mathbf{Q},\boldsymbol{trial}}. \tag{93}$$

By exploiting the property $\mathrm{d}\mathbf{F}_{\mathbf{Q}} = -\mathbf{F}_{\mathbf{Q}}\mathrm{d}\mathbf{F}_{\mathbf{Q}}^{-1}\mathbf{F}_{\mathbf{Q}}$ valid for invertible matrices together with Eq. (84) the following relation is promptly obtained:

$$\mathrm{d}\mathbf{F}_{\mathbf{Q}} = -3\mathbf{F}_{\mathbf{Q}}\mathbf{D}_{\mathbf{Q}}\mathbf{P}_{\mathbf{Q}}\mathbf{F}_{\mathbf{Q}} d\omega. \tag{94}$$

Then, by making use of the last relation and (83), Eq. (93) may be rewritten as:

$$d\tilde{\boldsymbol{\sigma}}_{\mathbf{Q},\boldsymbol{n+1}} = \mathbf{F}_{\mathbf{Q}} d\tilde{\boldsymbol{\sigma}}_{\mathbf{Q},\boldsymbol{trial}} - 3\mathbf{F}_{\mathbf{Q}}\mathbf{D}_{\mathbf{Q}}\mathbf{P}_{\mathbf{Q}}\tilde{\boldsymbol{\sigma}}_{\mathbf{Q},\boldsymbol{n+1}} d\omega. \tag{95}$$

The differential of the parameter ω can be put in relation with $d\tilde{\boldsymbol{\sigma}}_{\boldsymbol{trial}}$ by differentiating the consistency condition (91). Application of the chain rule provides:

$$\left.\frac{\partial\Phi_{n+1}}{\partial\omega}\right|_{\tilde{\boldsymbol{\sigma}}_{\mathbf{Q},\boldsymbol{trial}}} d\omega + \left.\frac{\partial\Phi_{n+1}}{\partial\tilde{\boldsymbol{\sigma}}_{\mathbf{Q},\boldsymbol{trial}}}\right|_{\omega} d\tilde{\boldsymbol{\sigma}}_{\mathbf{Q},\boldsymbol{trial}} = 0 \\ \Rightarrow \left(\frac{\partial\Phi_{n+1}}{\partial\omega} + \frac{\partial\Phi_{n+1}}{\partial\xi}\frac{\partial\xi}{\partial\omega} + \frac{\partial\Phi_{n+1}}{\partial\psi}\frac{\partial\psi}{\partial\omega}\right) d\omega + \left(\frac{\partial\Phi_{n+1}}{\partial\xi}\frac{\partial\xi}{\partial\tilde{\boldsymbol{\sigma}}_{\boldsymbol{trial}}} + \frac{\partial\Phi_{n+1}}{\partial\psi}\frac{\partial\psi}{\partial\tilde{\boldsymbol{\sigma}}_{\boldsymbol{trial}}}\right) d\tilde{\boldsymbol{\sigma}}_{\mathbf{Q},\boldsymbol{trial}} = 0. \tag{96}$$

Expressions for the partial derivatives appearing in (54) can be easily computed from (88) and (89); they are reported in the appendix at the end of the paper.

Then, by making use of (96) in Eq. (95) to eliminate $d\omega$, one gets:

$$d\tilde{\boldsymbol{\sigma}}_{\mathbf{Q},\boldsymbol{n+1}} = \left[\mathbf{F_Q} + 3\left(\frac{\partial \Phi_{n+1}}{\partial \omega}\right)^{-1} \mathbf{F_Q D_Q P_Q} \tilde{\boldsymbol{\sigma}}_{\mathbf{Q},\boldsymbol{n+1}} \otimes \frac{\partial \Phi_{n+1}}{\partial \tilde{\boldsymbol{\sigma}}_{\mathbf{Q},\boldsymbol{trial}}}\right] d\tilde{\boldsymbol{\sigma}}_{\mathbf{Q},\boldsymbol{trial}}. \tag{97}$$

The focus is now turned to the differential of the damage variable. By inverting (85) and taking its differential, one obtains:

$$dD^{n+1} = \frac{\Delta\lambda}{\omega^2} d\omega - \frac{d(\Delta\lambda)}{\omega}. \tag{98}$$

The differential of the plastic multiplier can be found by differentiating expression (90) by means of the usual chain rule:

$$\begin{aligned} d(\Delta\lambda) &= \left.\frac{\partial(\Delta\lambda)}{\partial\omega}\right|_{\tilde{\boldsymbol{\sigma}}_{\mathbf{Q},\boldsymbol{trial}}} d\omega + \left.\frac{\partial(\Delta\lambda)}{\partial\tilde{\boldsymbol{\sigma}}_{\mathbf{Q},\boldsymbol{trial}}}\right|_{\omega} d\tilde{\boldsymbol{\sigma}}_{\mathbf{Q},\boldsymbol{trial}} = \\ &= \left(\frac{\partial(\Delta\lambda)}{\partial\omega} + \frac{\partial(\Delta\lambda)}{\partial\xi}\frac{\partial\xi}{\partial\omega} + \frac{\partial(\Delta\lambda)}{\partial\psi}\frac{\partial\psi}{\partial\omega}\right) d\omega + \left(\frac{\partial(\Delta\lambda)}{\partial\xi}\frac{\partial\xi}{\partial\tilde{\boldsymbol{\sigma}}_{\boldsymbol{trial}}} + \frac{\partial(\Delta\lambda)}{\partial\psi}\frac{\partial\psi}{\partial\tilde{\boldsymbol{\sigma}}_{\boldsymbol{trial}}}\right) d\tilde{\boldsymbol{\sigma}}_{\mathbf{Q},\boldsymbol{trial}}. \end{aligned} \tag{99}$$

As before, expressions for the partial derivatives are reported in the appendix.

By first inserting (99) into (98) and then making use of (96) to express $d\omega$ in terms of $d\tilde{\boldsymbol{\sigma}}_{\mathbf{Q},\boldsymbol{trial}}$ one may find:

$$dD^{n+1} = \frac{1}{\omega}\left[\left(\frac{\partial \Phi_{n+1}}{\partial \omega}\right)^{-1}\left(\frac{\partial(\Delta\lambda)}{\partial\omega} - \frac{\Delta\lambda}{\omega}\right)\frac{\partial \Phi_{n+1}}{\partial \tilde{\boldsymbol{\sigma}}_{\mathbf{Q},\boldsymbol{trial}}} - \frac{\partial(\Delta\lambda)}{\partial\tilde{\boldsymbol{\sigma}}_{\mathbf{Q},\boldsymbol{trial}}}\right] d\tilde{\boldsymbol{\sigma}}_{\mathbf{Q},\boldsymbol{trial}}. \tag{100}$$

Now that the closed-form expressions (97) and (100) have been developed, they may be inserted into Eq. (92) to obtain a direct relation between the externally imposed variation in the trial effective stress $d\tilde{\boldsymbol{\sigma}}_{\mathbf{Q},\boldsymbol{trial}}$ and the corresponding variation of the stress $d\boldsymbol{\sigma}_{\mathbf{Q},\boldsymbol{n+1}}$ delivered by the integration algorithm. If the former is then written using the elastic law as $d\tilde{\boldsymbol{\sigma}}_{\mathbf{Q},\boldsymbol{trial}} = \mathbf{D_Q} d\boldsymbol{\varepsilon}^{\boldsymbol{e}}_{\mathbf{Q},\boldsymbol{trial}}$ and the inverse of the orthogonal transformation (81) is applied, the following relation may be obtained:

$$d\boldsymbol{\sigma}_{\boldsymbol{n+1}} = \mathbf{D^C} d\boldsymbol{\varepsilon}^{\boldsymbol{e}}_{\boldsymbol{trial}}, \tag{101}$$

where the consistent tangent modulus $\mathbf{D^C}$ turns out to be defined by:

$$\begin{aligned} \mathbf{D^C} = (1-D_{n+1})\mathbf{Q}\Bigg[&\mathbf{F_Q} + \frac{\tilde{\boldsymbol{\sigma}}_{\mathbf{Q},\boldsymbol{n+1}}}{\omega(1-D_{n+1})} \otimes \frac{\partial(\Delta\lambda)}{\partial\tilde{\boldsymbol{\sigma}}_{\mathbf{Q},\boldsymbol{trial}}} \\ &+ \left(\frac{\partial \Phi_{n+1}}{\partial \omega}\right)^{-1}\left(3\mathbf{F_Q D_Q P_Q} - \frac{\omega\partial(\Delta\lambda)/\partial\omega - \Delta\lambda}{\omega^2(1-D_{n+1})}\mathbf{I}\right)\tilde{\boldsymbol{\sigma}}_{\mathbf{Q},\boldsymbol{n+1}} \otimes \frac{\partial \Phi_{n+1}}{\partial \tilde{\boldsymbol{\sigma}}_{\mathbf{Q},\boldsymbol{trial}}}\Bigg]\mathbf{D_Q Q}. \end{aligned} \tag{102}$$

It is worth mentioning that despite the length of expression (102), almost all matrix–matrix products appearing have to be performed among matrices which are in diagonal form, thus maintaining the computational time at a reasonable level.

It is also interesting to observe that the consistent tangent modulus is not symmetric, as can be easily checked by substituting expressions reported in appendix for $\partial(\Delta\lambda)/\partial\tilde{\boldsymbol{\sigma}}_{\mathbf{Q},\boldsymbol{trial}}$ and $\partial\Phi_{n+1}/\partial\tilde{\boldsymbol{\sigma}}_{\mathbf{Q},\boldsymbol{trial}}$ into (102). Moreover, tedious but straightforward algebraic manipulations may show that when no damage evolution takes place, relation (102) simply reduces to the symmetric expression for the consistent tangent modulus reported in [11] for the implicit integration of the plane stress projected von Mises plasticity model.

7. Algorithm verification against 1D analytical solution

The plane stress projected implicit integration algorithm based on Eq. (91) and the corresponding consistent tangent modulus (102) have been implemented in an "in-house" developed finite element code based on a full Newton–Raphson scheme. A mesh composed by a single 2D isoparametric 4-node square element has been considered, as shown in Fig. 5, with material parameters taken from the GJS 400-18 ductile cast iron example of Table 1. Such element has been subjected to a uniaxial tensile test by imposing a total strain of 0.3 and the predicted stress compared with the 1D analytical solution presented in Section 3.

In Fig. 6 the relative accuracy of the numerical solution is plotted as a function of the number of increments used for achieving the final strain value, adopting a tolerance on the increment residual of 1×10^{-5}. In Fig. 7 instead, the number of increments is kept fixed at 10 and the number of total Newton–Raphson iterations needed to calculate the solution is reported as a function of the increment residual tolerance. It is seen that a great save in terms of iterations is achieved by using the consistent tangent modulus (102) compared to the corresponding plane stress projected implicit expression reported in [11], which is valid for the von-Mises plasticity model.

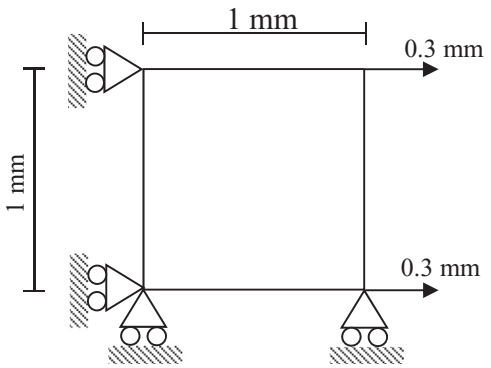

Fig. 5. Single 4-node square element subjected to a prescribed total strain of 0.3 in the horizontal direction.

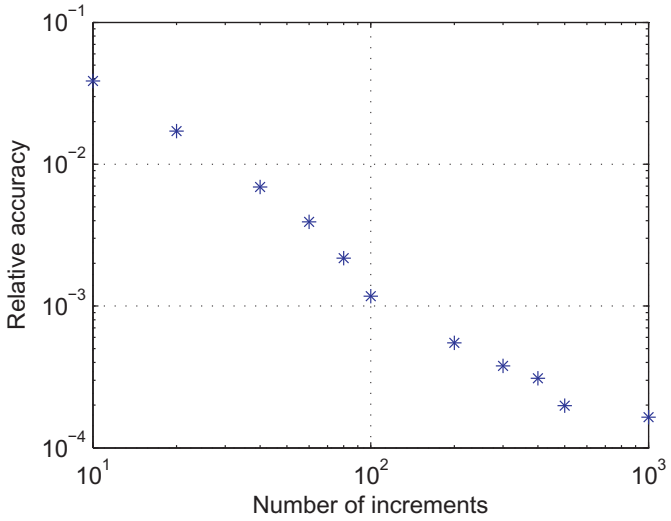

Fig. 6. Relative accuracy of the numerical stress solution as a function of the number of increments adopted, for a Newton–Raphson residual tolerance on each increment of $1x10^{-5}$.

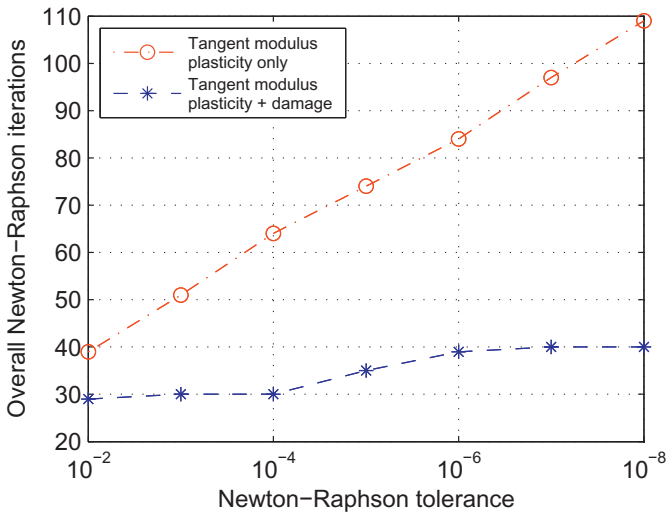

Fig. 7. Comparison of the number of total Newton–Raphson iterations needed to calculate the numerical solution with and without considering the influence of damage on the consistent tangent modulus.

8. Conclusions

By means of a smart choice of the isotropic hardening function, an analytical solution to Lemaitre's isotropic damage model in the form of an infinite expansion has been developed under the special conditions of uniaxial tensile testing. For a given value of the effective stress, the first 10 terms of the series already suffice to guarantee an accuracy of 0.3%. When the total strain is prescribed instead, the smooth and monotonic behavior of the corresponding implicit function guarantees that a very computationally efficient solution is obtainable using the Newton–Raphson method. This makes the analytical solution very attractive in the context of all material parameter identification procedures involving fitting of one or more experimentally measured uniaxial stress–strain curves, as it eliminates the need of using any numerical solver in combination with the optimization algorithm adopted.

The derived solution has also been used to verify a proposed implicit integration procedure restricted to the plane-stress version of Lemaitre's model. From a computational standpoint, the suggested numerical scheme is particularly advantageous as (a) only the relevant in-plane stress and strain components are considered and (b) the discretized system reduces to a single non-linear equation. A closed-form expression for the related consistent tangent modulus has also been provided, which is extremely valuable for increasing the convergence rate. This has been demonstrated for the simple 1D test case, where a substantial reduction in the number of required iterations is obtained when the effect of damage evolution on the global stiffness is taken into consideration, especially if high accuracy is needed. In summary, the proposed numerical scheme allows both a reduction in the computational complexity associated with the single iterations, as well as a decrease in their total number. As a final remark, it is worth mentioning that in absence of damage propagation, the entire numerical framework simply reduces to the implicit integration procedure for the plane-stress projected von Mises model reported in literature.

Appendix

Closed-from expressions for the partial derivatives appearing in Eqs. (96) and (99):

$$\frac{\partial \Phi_{n+1}}{\partial \omega} = -2\sigma_y H\left[(1-D^n)\sqrt{6\xi} - 12\omega\xi\frac{\psi^s}{(2S)^s}\right], \tag{A.1}$$

$$\frac{\partial \Phi_{n+1}}{\partial \xi} = \frac{3}{2} - 2\sigma_y H\left[\frac{3\omega}{\sqrt{6\xi}}(1-D^n) - 6\omega^2\frac{\psi^s}{(2S)^s}\right], \tag{A.2}$$

$$\frac{\partial \Phi_{n+1}}{\partial \psi} = 2\sigma_y H\left[6\omega^2\xi s\frac{\psi^{s-1}}{(2S)^s}\right], \tag{A.3}$$

$$\frac{\partial(\Delta\lambda)}{\partial \omega} = (1-D^n) - 2\omega\sqrt{6\xi}\left(\frac{\psi}{2S}\right)^s, \tag{A.4}$$

$$\frac{\partial(\Delta\lambda)}{\partial \xi} = -\frac{3\omega^2}{\sqrt{6\xi}}\left(\frac{\psi}{2S}\right)^s, \quad \frac{\partial(\Delta\lambda)}{\partial \psi} = -\omega^2\sqrt{6\xi}s\frac{\psi^{s-1}}{(2S)^s}, \tag{A.5}$$

$$\frac{\partial \xi}{\partial \omega} = -3\tilde{\boldsymbol{\sigma}}^{\boldsymbol{T}}_{\mathbf{Q},\boldsymbol{n}+1}\mathbf{P}_{\mathbf{Q}}\mathbf{F}_{\mathbf{Q}}\mathbf{D}_{\mathbf{Q}}\mathbf{P}_{\mathbf{Q}}\tilde{\boldsymbol{\sigma}}_{\mathbf{Q},\boldsymbol{n}+1}, \quad \frac{\partial \psi}{\partial \omega} = -3\tilde{\boldsymbol{\sigma}}^{\boldsymbol{T}}_{\mathbf{Q},n+1}\mathbf{D}_{\mathbf{Q}}^{-1}\mathbf{F}_{\mathbf{Q}}\mathbf{D}_{\mathbf{Q}}\mathbf{P}_{\mathbf{Q}}\tilde{\boldsymbol{\sigma}}_{\mathbf{Q},\boldsymbol{n}+1}, \tag{A.6}$$

$$\frac{\partial \xi}{\partial \tilde{\boldsymbol{\sigma}}_{\boldsymbol{trial}}} = \tilde{\boldsymbol{\sigma}}^{\boldsymbol{T}}_{\mathbf{Q},\boldsymbol{n}+1}\mathbf{P}_{\mathbf{Q}}\mathbf{F}_{\mathbf{Q}}, \quad \frac{\partial \psi}{\partial \tilde{\boldsymbol{\sigma}}_{\boldsymbol{trial}}} = \tilde{\boldsymbol{\sigma}}^{\boldsymbol{T}}_{\mathbf{Q},\boldsymbol{n}+1}\mathbf{D}_{\mathbf{Q}}^{-1}\mathbf{F}_{\mathbf{Q}}. \tag{A.7}$$

References

[1] J. Lemaitre, A continuous damage mechanics model for ductile fracture, J. Eng. Mater. Technol. ASME 107 (1985) 83–89.
[2] P. Ladevèze, J. Lemaitre, Damage effective stress in quasi unilateral conditions, in: 16th International Congress of Theoretical and Applied Mechanics, Lyngby , Denmark, 1984.
[3] J. Lemaitre, R. Desmorat, M. Sauzay, Anisotropic damage law of evolution, Eur. J. Mech. – A/Solids 19 (2000) 187–208, doi:10.1016/S0997-7538(00)00161-3.
[4] R. Desmorat, S. Cantournet, Modeling micro defects closure effect with isotropic/anisotropic damage, Int. J. Damage Mech. 17 (2007) 65–96, doi:10.1177/1056789507069541.
[5] J. Lemaitre, J. Dufailly, Damage measurements, Eng. Fract. Mech. 28 (1987) 643–661.
[6] J. Lemaitre, R. Desmorat, Engineering damage mechanics: ductile, creep, fatigue and brittle failures, Springer, 2005.
[7] E. Roux, M. Thonnerieux, P.O. Bouchard, Ductile damage material parameter identification: numerical investigation, Civil-Comp Proc. 93 (2010).
[8] P.-O. Bouchard, J.-M. Gachet, E. Roux, Ductile damage parameters identification for cold metal forming applications, in: AIP Conference Proceedings, 1353, 2011.
[9] N. Allahverdizadeh, A. Manes, M. Giglio, A. Gilioli, Geometry transferability of Lemaitre's continuum damage mechanics model in the plane stress specimens, Key Eng. Mater 592-593 (2013) 266–270, doi:10.4028/www.scientific.net/KEM.592-593.266.
[10] F.H. Aboutalebi, M. Nasresfahani, Numerical prediction of forming limit in hemispherical punch bulging by Lemaitre's ductile damage model, Appl. Mech. Mater. 110-116 (2012) 1437–1441.

[11] E. de Souza Neto, D. Peric, D.R.J. Owens, Computational methods for plasticity: theory and applications, Wiley, 2008.
[12] A.K. Singh, P.C. Pandey, An implicit integration algorithm for plane stress damage coupled elastoplasticity, Mech. Res. Commun. 26 (1999) 693–700, doi:10.1016/S0093-6413(99)00080-4.
[13] J.C. Simo, A return mapping algorithm for plane stress elastoplasticity, Int. J. Numer. Methods Eng. 22 (1986) 649–670.
[14] J. Lemaitre, A course on damage mechanics, Springer, 1996.
[15] H.-J. Weber, G.B. Arfken, Essential mathematical methods for physicists, Academic Press, 2004.
[16] B.M. Chaparro, S. Thuillier, L.F. Menezes, P.Y. Manach, J.V. Fernandes, Material parameters identification: gradient-based, genetic and hybrid optimization algorithms, Comput. Mater. Sci. 44 (2008) 339–346, doi:10.1016/j.commatsci.2008.03.028.
[17] K.S. Zhang, J.B. Bai, D. François, Ductile fracture of materials with high void volume fraction, Int. J. Solids Struct. 36 (1999) 3407–3425, doi:10.1016/S0020-7683(98)00157-7.
[18] E. de Souza Neto, A fast, one-equation integration algorithm for the Lemaitre ductile damage model, Commun. Numer. Methods Eng. 18 (2002) 541–554, doi:10.1002/cnm.511.
[19] J.C. Simo, Consistent tangent operators for rate-independent elastoplasticity, Comput. Methods Appl. Mech. Eng. 48 (1985) 101–118.

Appendix B
PAPER II

Mechanics of Materials 96 (2016) 138–150

Contents lists available at ScienceDirect

Mechanics of Materials

journal homepage: www.elsevier.com/locate/mechmat

On the isotropic elastic constants of graphite nodules in ductile cast iron: Analytical and numerical micromechanical investigations

Tito Andriollo*, Jesper Hattel

Department of Mechanical Engineering, Technical University of Denmark, DK-2800 Kgs., Lyngby, Denmark

ARTICLE INFO

Article history:
Received 29 June 2015
Revised 7 January 2016
Available online 23 February 2016

Keywords:
Micromechanics
Ductile cast iron
Spheroidal graphite iron
Graphite nodules
Isotropic effective elastic moduli

ABSTRACT

A comprehensive description of the mechanical behavior of nodules in ductile iron is still missing in the published literature. Nevertheless, experimental evidence exists for the importance of such graphite particles during macroscopic material deformation, especially under compressive loading. In the present paper, the nodules' elastic properties are thoroughly investigated by means of both analytical and numerical techniques. The analysis takes into account the influence of several non-linear phenomena, as local residual stresses arising during solid-state cooling, interface debonding and limited particle strength. It is shown that if the nodule internal structure is considered, the traditional isotropy assumption leads to the definition of a domain of admissible values for the effective elastic constants. However, micromechanical calculations indicate that values within the domain do not provide mesoscopic moduli in agreement with Young's modulus and Poisson's ratio recorded for common ferritic ductile iron grades. This suggests that graphite nodules may not be considered isotropic at the microscopic scale, at least from a mechanical viewpoint.

1. Introduction

Since its commercial introduction in 1948, ductile cast iron, also known as spheroidal graphite iron (SGI), has constantly found new fields of application, ranging from the automotive sector to the wind power industry. Nowadays, 25% of the castings produced worldwide are made of SGI (47th Census of World Casting Production, 2013). The main reason behind this enormous success is the unique combination of castability, high ductility and strength such material can offer, along with lower prices compared to traditional low carbon steels (Ductile Iron Society, 2013). Examples of typical modern SGI castings are small and medium sized heavily loaded parts with high demands for consistent quality for the automotive industry and very large industrial components with extreme demands for mechanical properties, particularly fatigue strength and fracture toughness (Tiedje, 2010).

From a metallurgical viewpoint, SGI is a ternary Fe-C-Si alloy whose properties to a large extent are controlled by chemical composition, cooling rate and heat treatment. The final microstructure may be naturally considered as composite (Grimvall, 1997), consisting of graphite nodules embedded in a continuous matrix which, in most engineering applications, may be either ferritic, pearlitic or a mixture of the two (American Foundrymen's Society, 1992). Extensive experimental investigations carried out in the last 60 years have provided qualitative knowledge of the effects of the most important microstructural parameters on the overall mechanical properties of SGI (Labrecque and Gagne, 1998). Nevertheless, a comprehensive quantitative description has always been challenged by the intrinsic material complexity, and much work remains to be done to cast light on

* Corresponding author. Tel.: +4545254722.
E-mail addresses: titoan@mek.dtu.dk (T. Andriollo), jhat@mek.dtu.dk (J. Hattel).

http://dx.doi.org/10.1016/j.mechmat.2016.02.007
0167-6636/

Nomenclature

E_{ij}	volume average of total strain tensor
Σ_{ij}	volume average of the stress tensor
ε_{ij}^{tot}, ε_{ij}^{e}, ε_{ij}^{p}	total, elastic, plastic strain tensor
σ_{ij}	stress tensor
s_{ij}	deviatoric part of the stress tensor
δ_{ij}	Kronecker delta
σ_e	equivalent Von Mises stress
σ_y, σ_y^0	Actual, initial yield stress
E	Young's modulus
ν	Poisson's ratio
K	bulk modulus
G	shear modulus
R_v	triaxiality function
f	yield function
D	Damage variable
S, s	Lemaitre's damage evolution parameters
Y	energy release rate
k, n	isotropic hardening parameters
p	equivalent Von Mises plastic strain
p_{crit}	critical effective plastic strain for damage evolution
r	hardening variable
α	thermal expansion coefficient
λ	plastic multiplier

the microscopic features which determine the mechanical constitutive behavior of SGI at the macroscopic scale.

In particular, the role of the individual graphite nodules is not fully understood yet. Probably, the main reason is that the only quantitative information available regarding their mechanical properties comes from nano-indentation tests performed according to the Oliver–Pharr method (Oliver and Pharr, 1992), which have provided values for the nodules Young's modulus in the range 15–28 GPa (Dierickx et al., 1996; Pradhan et al., 2009; Fernandino et al., 2015). The validity of such measurements is in any case disputable as (1) a priori values for Poisson's ratio must be assumed and (2) graphite nodules are not isotropic at all at the nanoscale (Miao et al., 1990; Miao et al., 1994), meaning that the concept of indentation Young's modulus loses its significance.

Often, in micromechanical analyses graphite nodules are simply regarded as voids in consideration of the above-mentioned presumed negligible stiffness and the weak bonding with the surrounding matrix. It must be emphasized that this last assumption is controversial too, as it is usually based on microscopy observations of early interface debonding for nodules sitting on the surface of tensile test specimens (Dong et al., 1997). As correctly pointed out in (Liu et al., 2002), the stress state around nodules located in the bulk is likely to be different, due to the material inhomogeneity, therefore it seems not possible to conclude that interface debonding always occurs, independently of the real local loading conditions.

Table 1
Micromechanical modeling of the SGI elastic response: assumed values for the nodules' isotropic elastic moduli.

Year	Authors	E_g (GPa)	ν_g
1980	Speich et al. (1980)	8.5	0.29
1992	Era et al. (1992)	303	Not specified
1997	Boccaccini (1997)	8.5	0.2
1998	Pundale et al. (1998)	0 (void)	0 (void)
2002	Cooper et al. (2002)	8.5	0.2
2003	Gaudig et al. (2003)	4.17	0.2225
2004	Sjögren and Svensson (2004)	*	Not available
2005	Bonora and Ruggiero (2005)	300-375	Not specified
2005	Collini and Nicoletto (2005)	15	0.3
2006	Nicoletto et al. (2006)	15	0.3
2014	Carazo et al. (2014)	*	0.2225
2015	Fernandino et al. (2015)	15	0.28

* $E_g = 0.173 \cdot Nodularity + 18.9 \rightarrow 36.2$ GPa for 100% nodularity.

As a matter of fact, there are clear indications pointing towards the mechanical importance of graphite nodules in SGI:

- First of all, low-cycle fatigue behavior with $R = -1$ is better reproduced by numerical models where nodules are treated as rigid spheres instead of voids (Rabold and Kuna, 2005). At the same time, it has been proved that fatigue crack propagation cannot be modeled within the classical linear elastic fracture mechanics framework (Berdin et al., 2001); this might be related to the fact that, according to the imposed stress intensity factor, different competing damage mechanisms are active in the matrix and / or in the nodules (Di Cocco et al., 2013).
- Secondly, tensile stress-strain curves for SGI are never linear, even at very low stress levels, due to immediate onset of plasticity (Sjögren and Svensson, 2005; Kohout, 2001). This can hardly be justified with a simple "voided matrix" model, as finite element calculations for the stress concentration factor corresponding to cavities of the shapes typical of real nodules have provided the maximum value of 5.39 (Dorazil, 1991).
- Thirdly, tensile and compression tests of SGI samples conducted at different temperatures (up to 800 °C) have highlighted large differences in the deformed nodule shapes (Hervas et al., 2013): if the graphite stiffness and strength were negligible compared to the matrix in the entire range of temperatures considered, the nodules should always deform in the same manner.

In light of these facts, it is clear that a thorough and complete understanding of the SGI mechanical behavior can only be achieved if accurate information on the nodules constitutive properties is available. This requirement is particularly important if non-linear phenomena like plastic deformation and fatigue are to be investigated, or the residual stresses arising during the manufacturing process are to be calculated. As previously mentioned, however, very little has been published in the literature concerning this issue, and even the basic elastic properties of the nodules are far from being firmly established. This uncertainty may be better appreciated by looking at Tables 1 and 2, which report the nodules' isotropic elastic constants

Table 2
Micromechanical modeling of the SGI elasto-plastic response: assumed nodules' mechanical behavior.

Year	Authors	Nodules considered as:
1996	Kuna and Sun (1996)	Voids
1996	Brocks et al. (1996)	Voids / rigid spheres
1998	Steglich and Brocks (1998)	Voids / rigid spheres
1999	Zhang et al. (1999)	Voids
2005	Bonora and Ruggiero (2005)	Isotropic linear elastic, $E_g = 300$–375 GPa
2011	Kosteski et al. (2011)	Isotropic linear elastic, $E_g = 15$ GPa, $\nu_g = 0.3$

assumed by researchers while modeling the micromechanical behavior of SGI in the elastic and elasto-plastic regime respectively. It may be seen that adopted values for Young's modulus span the range 4–375 GPa, with the "voids" and "rigid spheres" assumptions as lower and upper bounds. Certainly, more accuracy is needed if models capable of predicting the SGI mechanical performance are to be devised.

In this context, the present work aims at determining an effective elastic constitutive description of the graphite nodules based on physical grounds, which may be subsequently used for further investigations on the SGI mechanical properties. The analysis is carried out using both analytical and numerical micromechanical techniques and it is conceptually divided into two main parts. In the first one, a few assumptions regarding the nodules' internal structure and behavior are introduced, and it is shown that they lead to the definition of a domain of admissible values for the elastic moduli. In the second part, an inverse analysis is carried out to single out values within the admissible domain which allow matching the macroscopic Young's modulus and Poisson's ratio of a standard ferritic SGI grade. To make the inverse analysis more realistic, the influence of several factors, as interface debonding, plasticity and ductile damage in the matrix induced by residual stresses, as well as inelastic deformation of the nodules, is critically assessed by means of a 3D periodic unit cell model.

2. Materials

The object of the present analysis is the ferritic ductile iron GJS-400-15 according to the European Standard EN 1563, corresponding to the GGG-40 grade for the DIN 1693 Standard (Iron-foundry.com, n.d.). The reason for making a precise material selection is that Young's modulus variations of 5–10 GPa may be found among the different SGI grades available on the market. As the internal structure of the embedded graphite particles is the same, it is usually assumed that this spread in the elastic properties is primarily associated with a different volume fraction of the nodules, as well as with a different composition of the metallic matrix.

The GJS-400-15 is here considered as a 2-phase composite material constituted by spherical graphite particles regularly dispersed in a homogeneous ferritic matrix, with a volumetric graphite concentration of 12% (Steglich and Brocks, 1998); the constitutive behavior of each constituent is discussed in detail in the following.

2.1. Graphite nodules

In agreement with what implicitly done by the authors listed in Table 1, two fundamental assumptions are made regarding the graphite nodules:

1. they can be considered as mechanically isotropic;
2. their behavior can be described by a linear elastic model.

These assumptions have significant consequences. First of all, they imply the nodules' mechanical response to be completely determined in terms of two elastic constants, usually Young's modulus and Poisson's ratio. In addition, they have important implications on the description of the local stress and strain field in and around the nodules, e.g. the stress state in a nodule subjected to hydrostatic pressure is uniform, etc.

Furthermore, a third assumption, physically justified by TEM and micro-diffraction investigations of the nodules' internal structure (Miao et al., 1990, 1994), is introduced:

3. the basic nodule building blocks are graphite platelets with hexagonal structure.

It follows from assumption 1 that such building blocks, which are strongly anisotropic, must then be arranged in a "statistically homogeneous" way throughout each nodule to provide overall isotropic elastic properties. This observation is crucial for the development of the present analysis, as it allows establishing a domain of physically admissible values for the nodules' effective elastic moduli. The procedure is described in detail in Section 3.1.

As a concluding remark, it is worth saying that in the calculation of residual stresses arising during solid state cooling, the nodules' mechanical properties are assumed to be unaffected by temperature variations up to 750 °C and the thermal expansion coefficient is set to a constant value of 2.5×10^{-6} °C^{-1} (Bonora and Ruggiero, 2005).

2.2. Ferritic matrix

Ferrite is a metallic phase characterized by high ductility and moderate yield strength, especially in the vicinity of nodules due to migration of carbon atoms to the graphitic phase. Therefore, it seems appropriate to describe its constitutive response on the basis of Lemaitre's isotropic damage model (Lemaitre, 1985) with isotropic hardening, whose equations in Cartesian components are summarized as follows:

- additive strain decomposition:

$$\varepsilon_{ij}^{tot} = \varepsilon_{ij}^{e} + \varepsilon_{ij}^{p} + \delta_{ij}\alpha\Delta T \tag{1}$$

- elastic constitutive law:

$$\frac{\sigma_{ij}}{1-D} = \frac{E}{1+\nu}\left[\varepsilon_{ij}^{e} + \frac{\nu}{1-2\nu}\delta_{ij}\varepsilon_{kk}^{e}\right] \tag{2}$$

- flow rule:

$$\dot{\varepsilon}_{ij}^{p} = \frac{3s_{ij}}{2\sigma_e}\frac{\dot{\lambda}}{1-D} \tag{3}$$

Table 3
Material properties for ferritic matrix (after (Bonora and Ruggiero, 2005)).

Temperature (°C)	Young's modulus (GPa)	Thermal exp. coefficient (x10^{-5}°C^{-1})	Initial yield stress (MPa)
25	210.0	1.25	297
250	153.8	1.50	194
500	102.5	1.60	137
750	41.4	–	96
900	20.0	–	70
1000	0.1	2.40	60

Table 4
Plastic flow and damage evolution parameters for ferritic matrix.

Plastic flow factor k (MPa)	Plastic flow exponent n	Damage factor S (MPa)	Damage exponent s	Critical eff. plastic strain p_{crit} (mm/mm)
818.0	0.245	0.357	0.167	5.33×10^{-3}

- yield function:

$$f = \frac{\sigma_e}{1-D} - \sigma_y(r) \le 0,\ \ \sigma_e = \left(\frac{3}{2}s_{ij}s_{ij}\right)^{1/2} \tag{4}$$

- isotropic hardening rule:

$$\sigma_y = k(r+r_0)^n,\ \ r_0 = \left(\frac{\sigma_y^0}{k}\right)^{1/n} \tag{5}$$

- effective plastic strain increment and hardening parameter increment:

$$\dot{p} = \frac{\dot{r}}{1-D},\ \ \dot{r} = \dot{\lambda} \tag{6}$$

- damage evolution law:

$$\dot{D} = \left(\frac{Y}{S}\right)^s \dot{p},\ \ if\ \ p > p_{crit} \tag{7}$$

- energy release rate:

$$Y = \frac{\sigma_e^2 R_v}{2E(1-D)^2},\ \ R_v = \frac{2}{3}(1+\nu) + 3(1-2\nu)\left(\frac{\sigma_{kk}}{3\sigma_e}\right)^2 \tag{8}$$

- consistency condition:

$$f \le 0,\ \ \dot{\lambda} \ge 0,\ \ f\dot{\lambda} = 0 \tag{9}$$

It may be noticed that 9 material parameters are required: 3 thermo-elastic (E, ν, α), 3 related to plastic flow (σ_y^0, k, n) and finally 3 related to damage (p_{crit}, S, s). In principle, an additional parameter specifying the conditions at which crack nucleation occurs would be necessary: however, in the present investigations damage never exceeds 0.1, which is well below the critical fracture initiation threshold for common metals and alloys.

In Table 3 values for ferrite Young's modulus, thermal expansion coefficient and initial yield stress are reported over a wide range of temperatures, whereas Poisson's ratio is assumed to be constant and equal to 0.3. The initial yield strength at room temperature deserves a special comment, as it is considerably lower than that reported in (Baer et al., 1996) for a "manufactured" ferritic matrix, obtained by alloying mild steel Mk3Al with FeSi75 using fusion metallurgy. It has to be remarked, however, that the main conclusions of the present analysis are to a large extent unaffected by the specific choice of the initial yield stress value, and more in general of the other plastic and damage parameters.

The remaining five material quantities to be entered Lemaitre's model have been identified following a two-step procedure. Initially, an analytical solution to Eqs. (1)–(9) for uniaxial tensile loading has been calculated (Andriollo et al., 2016); it turns out that the relation between effective stress $\tilde{\sigma} = \sigma/(1-D)$ and total strain ε^{tot} may be expressed as:

$$\varepsilon^{tot}(\tilde{\sigma}) = \bar{\varepsilon}^{tot} + \frac{\tilde{\sigma}-\bar{\sigma}}{E} + 2B\sum_{m=0}^{+\infty}\frac{(-1)^m}{2m+1}\binom{\beta}{m} \times\left[\left(1-\frac{\tilde{\sigma}^{\alpha+1}}{\tilde{\sigma}_{lim}^{\alpha+1}}\right)^{m+1/2} - \left(1-\frac{\bar{\sigma}^{\alpha+1}}{\tilde{\sigma}_{lim}^{\alpha+1}}\right)^{m+1/2}\right] \tag{10}$$

where $\bar{\varepsilon}^{tot}$ and $\bar{\sigma}$ represent the critical total strain and stress at which damage evolution starts ($p = p_{crit}$) and the other quantities are defined as:

$$B = -\frac{z}{\alpha+1}(\tilde{\sigma}_{\lim})^{\frac{\alpha-4s+1}{2}},\quad \beta = \frac{-2s}{a+1}$$
$$z = \frac{1}{nk^{\frac{1}{n}}}\left(\frac{\alpha+1}{2A}\right)^{1/2},\quad \tilde{\sigma}_{\lim} = \left(\frac{\alpha+1}{2A} + \bar{\sigma}^{\alpha+1}\right)^{1/(\alpha+1)} \tag{11}$$
$$A = \left(nk^{\frac{1}{n}}(2ES)^s\right)^{-1},\quad a = 2s + \frac{1}{n} - 1$$

Then, by means of an inverse analysis performed using MATLAB, the best set of parameters has been selected according to a least square fitting of the experimental stress-strain curve at room temperature for ferrite given in (Zhang et al., 1999). Calculated values are reported in Table 4. As no information is available for the post-yielding behavior of the ferritic matrix at higher temperatures, plastic flow and damage evolution parameters are assumed to be constant, except for the temperature dependence of the initial yield stress previously mentioned. Time-dependent deformation mechanisms are also neglected.

3. Methods and theory

As already stated in the introduction, the aim of the present analysis is to determine values for the nodules' effective isotropic elastic moduli which on the one hand

Table 5
Elastic constants of a single graphite platelet. Entries are in GPa.

C11	C44	C12	C13	C33
1060	0.18	180	15	36.5

are admissible with respect to the physical assumptions of Section 2.1 and on the other hand allow matching the macroscopic Young's modulus and Poisson's ratio for GJS-400-15.

3.1. Bounds on the effective elastic constants of polycrystals with hexagonal symmetry

According to the discussion on the statistical order of polycrystalline material reported in (Wawra et al., 1982), assuming that nodules are statistically homogeneous and isotropic polycrystalline aggregates consisting of many single anisotropic graphite crystals, then 1st order upper and lower bounds on the effective isotropic elastic constants can be derived, corresponding to Voigt and Reuss bounds. Moreover, if the distribution of the local elastic moduli is not correlated with the crystal shape and size (for instance, it is excluded that, on average, lengthy platelets are stiffer in one direction than compact platelets), then tighter 2nd order bounds can be established, corresponding to Hashin–Shtrikman bounds. Finally, if no particular crystal shape and size is distinguishable, implying that many platelet shapes and sizes exist in an irregular composition, even tighter 3rd order bounds can be derived.

Explicit analytical expressions for the 1st, 2nd and 3rd order bounds in the case of crystals with hexagonal symmetry are quite lengthy and may be found in (Grimvall, 1997; Watt and Peselnick, 1980; Kroner, 1977), respectively. By using the former in combination with the anisotropic elastic constants of a single graphite crystal, bounds on the effective isotropic bulk and shear modulus of the polycrystalline aggregate may be determined. Values calculated in this way by Grimvall (1997) and Wawra et al. (1982) are reported in Table 6. It is worth noticing that the input values adopted by these authors, given in Table 5, are quite outdated. Nevertheless, calculations made by the present authors using more recent data (Savini et al., 2011) have shown only negligible variations in the results.

Bounds expressed in terms of bulk modulus K and shear modulus G can be converted to bounds on Young's modulus E and Poisson's ratio ν by means of the relations:

$$E = \frac{9KG}{3K+G}, \quad \nu = \frac{3K-2G}{2(3K+G)} \tag{12}$$

together with their inverse formulas:

$$K = \frac{E}{3(1-2\nu)}, \quad G = \frac{E}{2(1+\nu)} \tag{13}$$

It may be easily checked from the first of Eq. (12) that the maximum (minimum) value of E is achieved when both K and G are at their maximum (minimum). Bounds defined in this way are denoted by E^u and E^l respectively. Then, for each value of E in such interval, Eq. (13) may be employed to rewrite the constraints in terms of E and ν:

$$K^l < \frac{E}{3(1-2\nu)} < K^u$$
$$G^l < \frac{E}{2(1+\nu)} < G^u \tag{14}$$

where the superscripts "u" and "l" denote the bound type. Finally, after simple algebraic manipulations, the following expressions are obtained:

$$E^l < E < E^u \tag{15}$$

$$max\left\{\frac{1}{2}\left(1-\frac{E}{3K^l}\right),\ \frac{E}{2G^u}-1\right\} = \nu^l < \nu < \nu^u = min\left\{\frac{1}{2}\left(1-\frac{E}{3K^u}\right),\ \frac{E}{2G^l}-1\right\} \tag{16}$$

The last two relations, complemented by the data of Table 6, allow determining three different domains of admissible values for the effective Young's modulus and Poisson's ratio, according to the statistical order assumed (1st, 2nd or 3rd) for the distribution of the graphite platelets within the single nodules.

Table 6
Bounds on the effective elastic moduli of a graphite polycrystalline aggregate. Entries are in GPa.

Bound order	Bulk modulus		Shear modulus	
	lower	upper	lower	upper
1st (Grimvall, 1997)	35.76	286.28	0.45	217.84
2nd (Grimvall, 1997)	36.20	204.20	0.80	146.20
3rd (Wawra et al., 1982)	36.56	163.48	1.41	111.35

3.2. Mesoscopic elastic constants of a 2-phase composite

This section presents the micromechanical techniques used to construct bounds and estimates for the overall response of GJS-400-15 considered as a composite material, given the properties of the single constituents.

3.2.1. Analytical bounds and estimates

Analytical results in relatively simple form are only available under the assumption of isotropic linear elastic behavior of both the nodules and the matrix and perfect interface bonding.

First order upper and lower bounds on the equivalent mesoscopic elastic moduli of the composite material are given by:

$$K_c^u = cK_n + (1-c)K_m; \quad G_c^u = cG_n + (1-c)G_m;$$
$$\frac{1}{K_c^l} = \frac{c}{K_n} + \frac{1-c}{K_m}; \quad \frac{1}{G_c^l} = \frac{c}{G_n} + \frac{1-c}{G_m} \tag{17}$$

where the subscripts "c", "n" and "m" refer to composite, nodules and matrix respectively and c denotes the graphite nodules' volume fraction. Relations (17) require as input the effective isotropic elastic moduli of the nodules, which are only known within the domains defined by the bounds discussed in the previous section. Nevertheless, by using expressions (13), it is possible to demonstrate that for a

prescribed value of the nodules' effective Young's modulus E_n lying in the interval (15), the maximum upper bounds and minimum lower bounds obtained by varying the nodule Poisson's ratio ν_n within the range (16) are given by:

$$K_c^{u,max} = \frac{cE_n}{3(1-2\nu_n^u)} + (1-c)K_m;$$
$$G_c^{u,max} = \frac{cE_n}{2\left(1+\nu_n^l\right)} + (1-c)G_m;$$
$$\frac{1}{K_c^{l,min}} = \frac{3c\left(1-2\nu_n^l\right)}{E_n} + \frac{1-c}{K_m};$$
$$\frac{1}{G_c^{l,min}} = \frac{2c(1+\nu_n^u)}{E_n} + \frac{1-c}{G_m} \tag{18}$$

Conversion to maximum upper bounds and minimum lower bounds in terms of Young's modulus and Poisson's ratio may then be easily performed on the basis of relations (12).

Often, second order Hashin–Shtrikman bounds are also employed in this kind of analyses. Unfortunately, they cannot be used here as they are strictly valid only if $K_n > K_m$ and $G_n > G_m$ (Hashin and Shtrikman, 1963), which is not always the case in the present investigations.

As the word says, bounds indicate the intervals where the composite equivalent mesoscopic moduli must lie. However, if there is a large difference in the elastic properties of the two constituents, the bounds may fall quite apart, becoming of little practical interest. In such a situation, it is important to have tools providing reasonable estimates (i.e. approximated unique values) for the mesoscopic moduli. A very widespread class of analytical estimates comprises the well-known "dilute methods", which work satisfactorily when the secondary phase volume fraction is limited to a few percent. For the problem at hand, however, the nodules' concentration is as high as 12%. Therefore, the Mori–Tanaka approach (Aboudi et al., 2012) is here preferred, which for spherical particles yields the following estimates for the mesoscopic bulk and shear moduli:

$$K_c = K_m + \frac{c(K_n - K_m)}{1 + (1-c)(K_n - K_m)/(K_m + 4G_m/3)}$$
$$G_c = G_m + \frac{15c(G_n - G_m)(1-\nu_m)}{(7-5\nu_m) + (8-10\nu_m)G_n/G_m - 2c(4-5\nu_m)(G_n/G_m - 1)} \tag{19}$$

Similarly to first order bounds, conversion to estimates in terms of Young's modulus and Poisson's ratio may be easily achieved by means of relations (12).

3.2.2. Numerical 3D unit cell predictions

In order to overcome the limitations affecting the analytical methods presented in the previous section and taking non-linearities into consideration, a numerical 3D periodic unit cell model is introduced. The GJS-400-15 microstructure is therefore schematized as a periodic cubic cell with a single central spherical nodule, as shown in Fig. 1. The ratio between nodule diameter and cell side is set to 0.61, hence satisfying the graphite volume fraction requirement. Due to geometrical considerations, only 1/8 of the unit cell is analyzed, as Fig. 2 shows. Symmetry boundary conditions are applied on the three faces of the cube intersecting the nodule, whereas periodic boundary

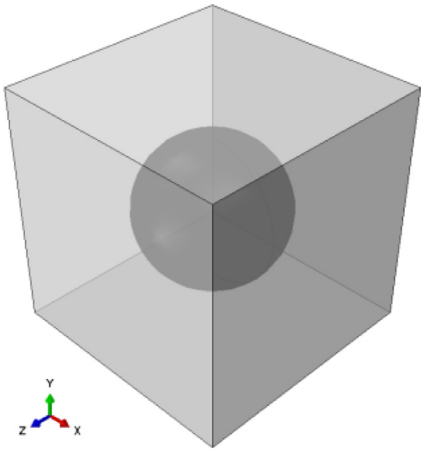

Fig. 1. Micromechanical 3D periodic unit cell representing the microstructure of GJS-400-15.

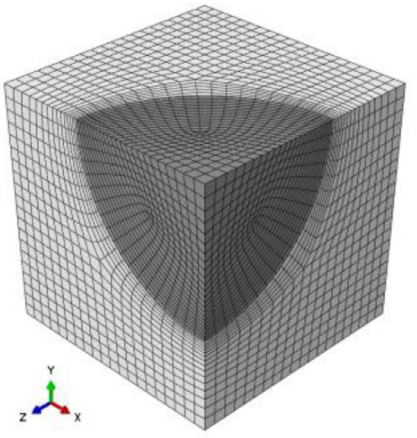

Fig. 2. Geometry and mesh used in the numerical simulations.

conditions are imposed on the other faces according to the procedure described in (Drago and Pindera, 2007), in order to fulfill continuity of displacements and surface tractions with the surrounding microstructure.

With the aim of investigating the effects of a weak nodule-matrix bonding on the unit cell mechanical response, the phase boundary is modeled as a frictionless contact interface with no tensile strength in the normal direction, as suggested in (Bonora and Ruggiero, 2005; Collini and Nicoletto, 2005). Moreover, local residual stresses arising due to the thermal expansion coefficient mismatch between graphite and ferrite during manufacturing are accounted for by applying a preliminary uniform cooling to the entire volume, from an initial stress-free temperature T_i down to 20 °C.

The composite mesoscopic moduli are calculated from simulations of "uniaxial" tensile tests along the x-axis on the basis of the following formulas:

$$E_c = \lim_{E_{11}\to 0}\left(\frac{\partial \Sigma_{11}}{\partial E_{11}}\right), \qquad \nu_c = \lim_{E_{11}\to 0}\left(-\frac{E_{22}}{E_{11}}\right) \tag{20}$$

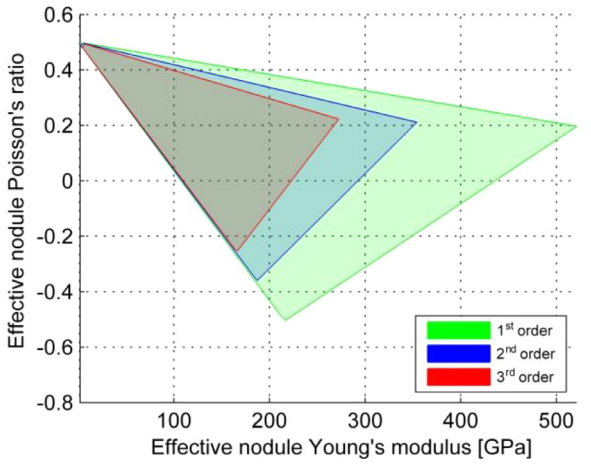

Fig. 3. Admissible domains for the nodules' effective isotropic elastic moduli.

where Σ_{11}, E_{11} and E_{22} denote normal components of the mesoscopic stress and strain tensors, given by the average over the unit cell volume V of the corresponding microscopic quantities:

$$\Sigma_{11} = \frac{1}{V}\int_V \sigma_{11} dV, \quad E_{11} = \frac{1}{V}\int_V \varepsilon_{11} dV,$$
$$E_{22} = \frac{1}{V}\int_V \varepsilon_{22} dV \tag{21}$$

In plain words, the limits appearing in expressions (20) simply indicate that it is the very initial slope of the uniaxial stress-strain curve which should be considered in the determination of the unit cell moduli. For practical implementation purposes, though, the secant modulus at a mesoscopic strain of 0.01% is used instead.

Finite element calculations are performed with the commercial software ABAQUS. The mesh adopted, visible in Fig. 2, is constituted by approximately 15,000 hexahedral 2nd order elements with reduced integration. A small-strain formulation in combination with a non-linear numerical solution procedure based on the full Newton–Raphson scheme is chosen, and the contact condition at the matrix-nodule interface is enforced via the augmented-Lagrange method. Integration of the Lemaitre's damage equations at the local level in the ferritic matrix is accomplished by a user-defined material subroutine, according to the implicit scheme proposed in (de Souza Neto, 2002), where a suitable expression for the consistent tangent modulus is also reported.

4. Results and discussion

4.1. Admissible domain for the nodules' elastic constants

The three different domains for the nodules' effective isotropic elastic moduli, which are admissible according to the three different levels of statistical order for the graphite platelets discussed in Section 3.1, are shown in Fig. 3. Not surprisingly, it is seen that an increase in the homogeneity requirement leads to a contraction of the corresponding admissible domain. At first glance, this is particularly evident for the maximum admissible value of the effective Young's modulus, which drops from the value of 521.3 GPa obtained by applying 1st order bounds to 272.2 GPa for 3rd order bounds; conversely, the minimum value increases from 1.3 GPa to 4.2 GPa. It is also interesting to observe that within each domain, intermediate Young's modulus values are characterized by a very large variation in Poisson's ratio, which may actually become negative. In principle, this possibility should not be excluded a priori, both theoretically and physically, as there is experimental evidence of polycrystalline materials whose cross-section expands when stretched under uniaxial tension (Lakes, 1993). Furthermore, it is known that pyrolytic graphite, which may be considered as transversely isotropic, shows negative Poisson's ratio in the isotropy plane (Bert, 1969).

From a practical viewpoint, an important conclusion may be drawn on the basis of the present results. As thoroughly discussed in Section 2.1, the isotropy assumption on the nodules' mechanical behavior holds only if the graphite platelets are arranged in a statistically homogeneous way throughout the nodules themselves. Consequently, their effective moduli must lie at least within the 1st order domain indicated in Fig. 3, henceforth simply denoted as admissible domain. This conclusion stems directly from the physical structure associated with the graphite nodules. It is worth remarking that most of the authors listed in Tables 1 and 2 have assumed values for Young's modulus and Poisson's ratio in the range 4–36 GPa and 0.2–0.3 respectively, which are outside the admissible domain. The reason for this discrepancy will be discussed in the remaining sections, where the implications of adopting nodules' effective moduli within the admissible domain are analyzed with respect to the effects they have on the mesoscopic elastic constants of GJS-400-15.

4.2. Perfect bonding assumption

Initially, the influence of nodules' effective moduli lying within the admissible domain is assessed by assuming linear elastic behavior of both material constituents and perfect interface bonding. In this way, the mechanical response of the composite GJS-400-15 may be studied using the analytical relations presented in Section 3.2.1.

Figs. 4 and 5 present the influence of the nodules' admissible moduli on the mesoscopic Young's modulus and Poisson's ratio respectively. It may be seen that several contours are plotted in addition to the reference literature values (American Foundrymen's Society, 1992; "Matbase: the free and independent online materials properties resource," 2015), which are quite standard for the SGI material at hand. The first contour indicates the extension of the 1st order Voigt-Reuss bounds: for each value of E_n, when ν_n is varied within the corresponding admissible range (16), the elastic response of GJS-400-15 is bounded by the green area. The second and third contours, instead, represent estimates produced by the analytical Mori-Tanaka approach and the numerical 3D unit cell model.

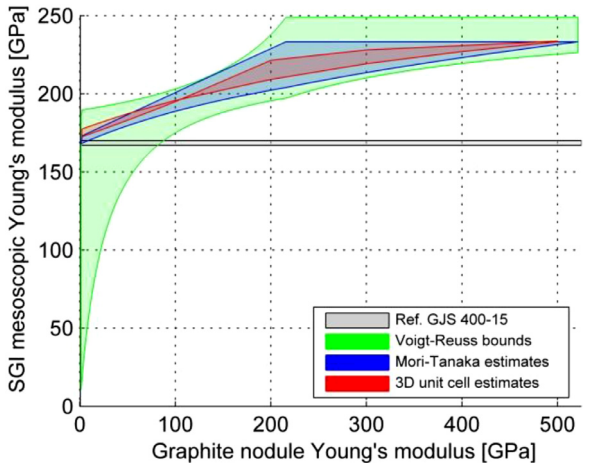

Fig. 4. Analytical bounds and estimates for the mesoscopic Young's modulus, compared to the numerical results from the 3D periodic unit cell.

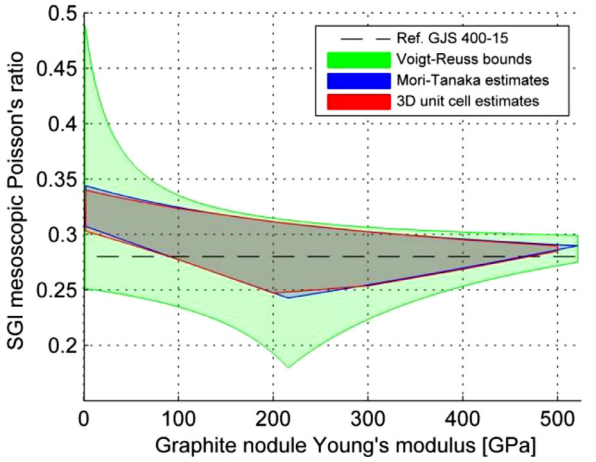

Fig. 5. Analytical bounds and estimates for the mesoscopic Poisson's ratio, compared to the numerical results from the 3D periodic unit cell.

As preliminary observation, it is seen that both analytical and numerical estimates are fully contained in the Voigt–Reuss bounds, indicating a good level of consistency of the former. The bounds tend to be very distant from each other at low E_n values, whereas they are quite close when E_n lies approximately in the interval 100–200 GPa. This is sensible, as it is well-known that the smaller the difference in the elastic properties of the composite constituents, the narrower the bounds. It is also worth noticing the very good agreement between analytical and numerical estimates, especially regarding predictions of the mesoscopic Poisson's ratio. This confirms the applicability of periodic unit cell models to the study of the mechanical response of composite materials.

By looking at Fig. 4, it may be concluded that values for the nodules' effective Young's modulus above approximately 100 GPa must be rejected, as the horizontal band indicating experimental measurements lies well outside the Voigt–Reuss bounds in that range. Conversely, with focus on the data of Fig. 5, no values can be excluded

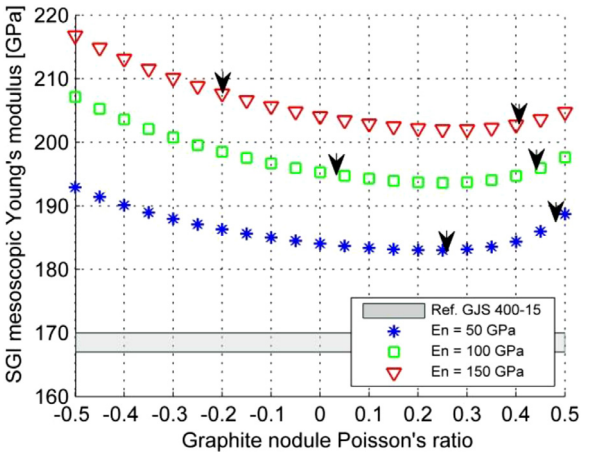

Fig. 6. 3D unit cell predictions of the mesoscopic Young's modulus as a function of the nodules' effective Poisson's ratio, for selected values of the nodules' effective Young's modulus. The black arrows indicate the extension of the admissible range.

on the basis of the same principle, because the reference Poisson's ratio always falls in between the bounds. Nevertheless, analytical and numerical estimates clearly indicate that the experimental value of GJS-400-15 can only be matched by assuming E_n to be above 100 GPa. Therefore, there is an evident contradiction between values which allow matching the mesoscopic Young's modulus and those which are necessary for matching the mesoscopic Poisson's ratio. However, it should be kept in mind that three critical aspects, like interface debonding, matrix plastification induced by residual stresses and inelastic deformation of the nodules are not considered here at all.

Before leaving this section, an important comment has to be made regarding the method used for the determination of the contours associated with the 3D unit cell predictions. In principle, for every admissible choice of E_n, many finite element simulations should be performed to cover all possible values of ν_n within the range (16). However, in order to keep the overall number of simulations at a reasonable level, only the two end-points of the interval are tested, i.e. $\nu_n = \nu_n^l$ and $\nu_n = \nu_n^u$. Obviously, this method works as long as the mesoscopic moduli vary monotonically with ν_n. Unfortunately, this is not always true. For instance, Fig. 6 shows that by increasing E_n progressively from 50 to 150 GPa, the dependence of the mesoscopic Young's modulus on ν_n in the admissible range changes from monotonically increasing to monotonically decreasing. This explains the intersection visible in Fig. 4 between the upper and lower limits of the numerical contour. On the contrary, the mesoscopic Poisson's ratio always varies monotonically with ν_n, as shown in Fig. 7, and in fact no intersection is present in Fig. 5. Nevertheless, it must be said that this phenomenon affects the present analyses only to a little extent. Indeed, simulations run using intermediate values of ν_n have shown that in almost all cases the obtained mesoscopic moduli lie within the range calculated using the extreme values ν_n^l and ν_n^u, and when this does not occur, the deviation is always small.

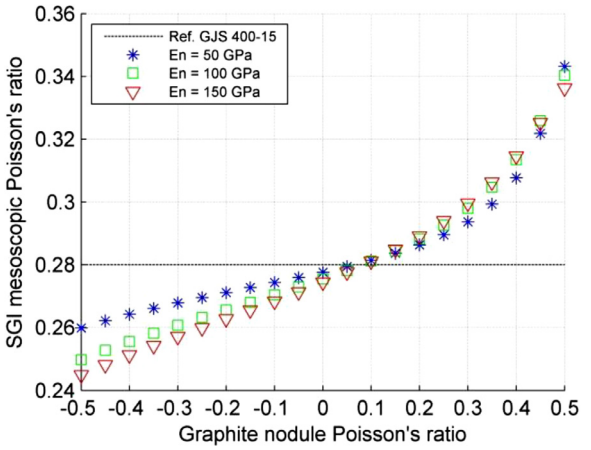

Fig. 7. 3D unit cell predictions of the mesoscopic Poisson's ratio as a function of the nodules' effective Poisson's ratio, for selected values of the nodules' effective Young's modulus.

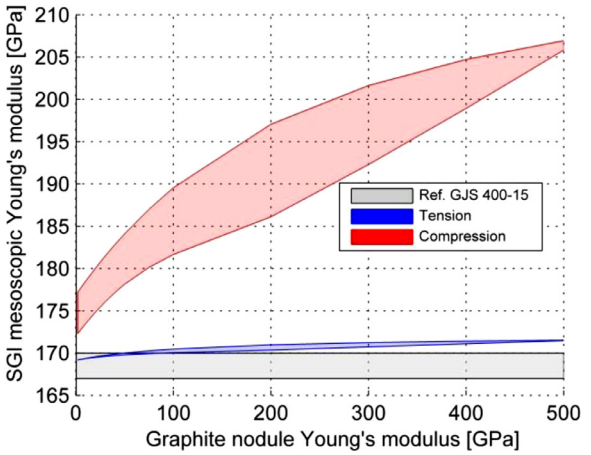

Fig. 8. 3D unit cell predictions of the mesoscopic Young's modulus in tension and compression. A frictionless nodule-matrix contact interface is assumed.

4.3. Effect of frictionless contact interface

Numerical estimates for the mesoscopic moduli of GJS-400-15 assuming a frictionless contact interface between the nodule and the matrix are reported in Figs. 8 and 9. As before, results have been obtained by varying the nodules' effective moduli within the admissible domain depicted in Fig. 3. The contact interface has two main consequences: it may open up, generating a non-linear effect, and it prevents transmission of shear stresses across the boundary. Both factors contribute to the reduction in the overall mesoscopic stiffness of the unit cell. However, while the second one plays the same role either in tension or in compression, contact opening occurs in tension only. This causes a strong dependence of the mesoscopic moduli on the loading condition type, which does not find confirmation in experimental findings (American Foundrymen's Society, 1992; Gilbert, 1964). In addition, although all investigations on nodule debonding mentioned in the introduction have detected early occurrence of the phenomenon, this was not recorded immediately. A retarded

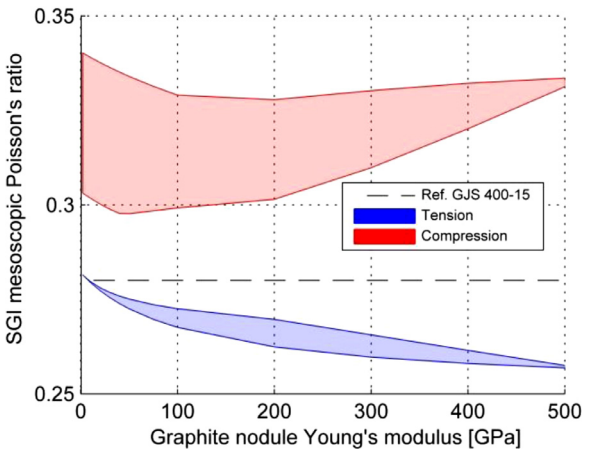

Fig. 9. 3D unit cell predictions of the mesoscopic Poisson's ratio in tension and compression. A frictionless nodule-matrix contact interface is assumed.

debonding mechanism may be physically justified by either some tensile interface strength or by the presence of residual stresses, induced by the lower thermal expansion coefficient of the nodules compared to that of the matrix. More precisely, the latter situation is expected to generate radial compressive stresses in the nodules during solid state cooling, hence delaying the debonding process upon subsequent loading. If elastic residual stresses are accounted for in the simulation by applying a preliminary uniform temperature decrease, it is found that the contours corresponding to tensile loading in Figs. 8 and 9 move upwards and overlap perfectly those calculated in compression. Unfortunately, even if the different tension-compression behavior is removed, a major problem remains: the predicted values for the mesoscopic moduli are overestimated, in terms of both Young's modulus and Poisson's ratio, and never match experimental findings.

4.4. Effect of local residual stresses

In this section, the effects of local microscopic residual stresses arising during solid state cooling are investigated for three different choices of the initial stress-free temperature T_i: 250, 500 and 750 °C. Higher temperatures are not considered for two reasons: time-dependent deformation mechanisms would become non-negligible and the eutectoid transformation would come into play, making the analysis much more complicated.

From a micromechanical viewpoint, the main consequence of introducing the initial cooling stage in the analysis is the formation of compressive radial stresses in the nodules and tensile tangential stresses in the matrix. Not surprisingly, their magnitude turns out to be proportional to three factors: the thermal expansion coefficient mismatch, the stiffness of both the nodules and the matrix, and the initial cooling temperature. Over the different simulations, only the choice of the initial temperature and the elastic properties of the nodules are varied. As intuition suggests, the spherical nodules are subjected to almost pure hydrostatic compression during cooling, meaning that the most important parameter controlling

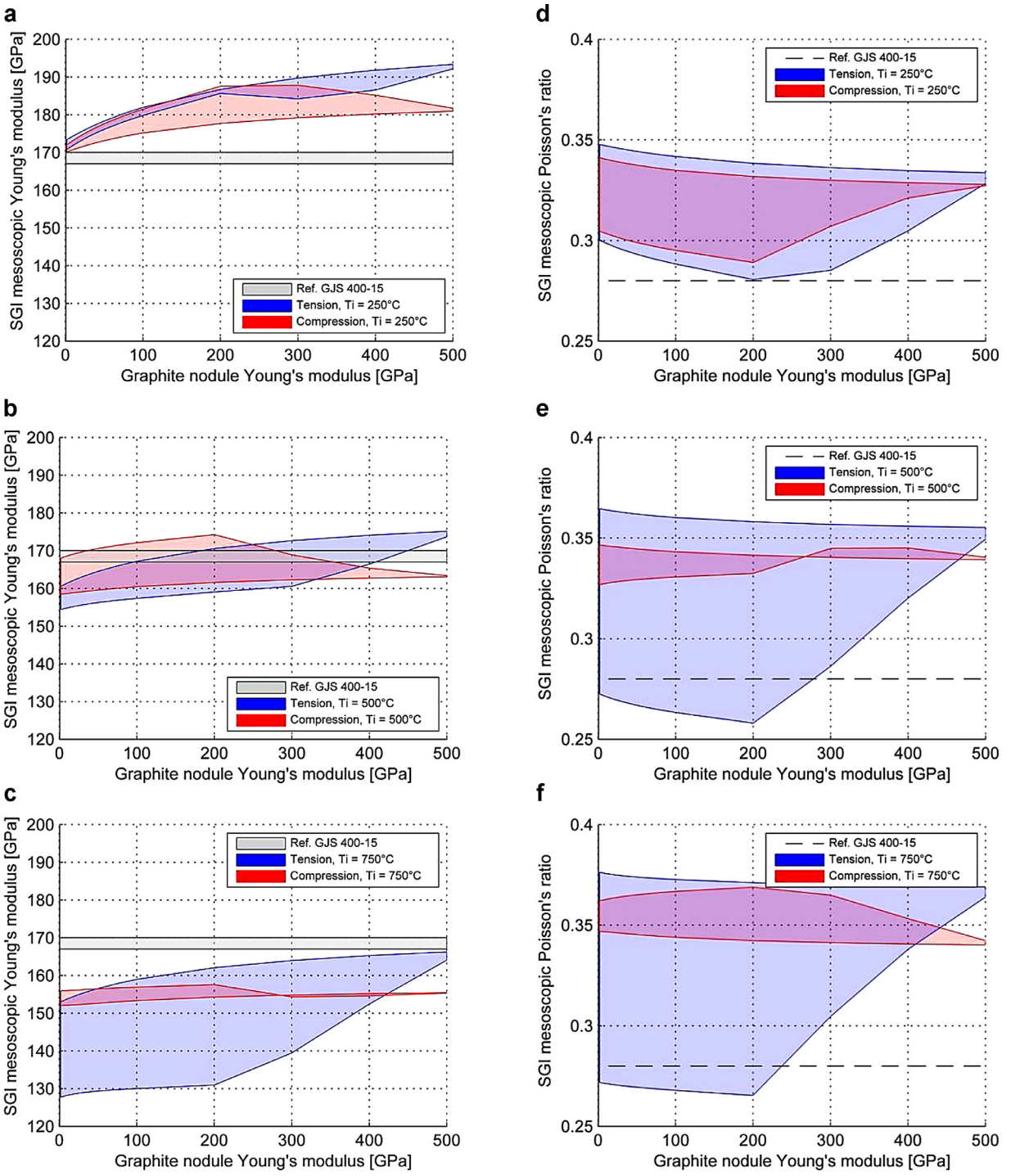

Fig. 10. 3D unit cell predictions of the mesoscopic moduli in tension and compression considering the influence of local residual stresses. a, b, c: predicted Young's modulus using T_i equal to 250, 500 and 750 °C, respectively. d, e, f: predicted Poisson's ratio using T_i equal to 250, 500 and 750 °C, respectively.

thermal deformation is their bulk modulus K_n. From the first of relations (13), it is seen that K_n increases monotonically with Young's modulus and Poisson's ratio; as a consequence, higher residual stresses are expected when either E_n, ν_n or T_i are increased. Clearly, if the stresses in the matrix become so large that the yield point is eventually reached, plasticity and ductile damage take place, according to Lemaitre's model described in Section 2.2.

Numerical predictions of the mesoscopic moduli taking local residual stresses into consideration are shown in Fig. 10. By increasing the initial cooling temperature, three main effects are recorded, all originating from the

progressive matrix plastification. First of all, the mesoscopic Young's modulus decreases, as the matrix becomes "softer", and, at the same time, the mesoscopic Poisson's ratio increases, due to plastic incompressibility. In addition, the influence of the effective Poisson's ratio ν_n becomes more pronounced, due to its direct impact on the compressibility of the nodules during the preliminary cooling stage. Finally, a different behavior in tension and compression becomes visible, due to the strong non-linearity of the underlying deformation mechanisms. In this respect, it is also worth saying that the contact condition does not have a major impact, as early interface separation upon uniaxial loading is always prevented by the presence of residual stresses.

From a comparison of the obtained numerical results with the reference data for GJS-400-15, it may be noticed that the predicted mesoscopic Young's modulus can actually match experimental values if initial cooling from a temperature of approximately 500 °C is accounted for in the simulations. However, for any choice of the initial stress-free temperature, the estimated mesoscopic Poisson's ratio is always above the reference data, independently of the selected admissible values for the nodules' effective moduli. This is particularly evident for compressive loading. Moreover, as already stated in the previous section, there is no experimental support for the observed dependence of the mesoscopic constants on the loading condition type.

4.5. Advanced constitutive models for the nodules

The results presented so far suggest that, despite adopted by a large number of authors, the isotropic linear elastic assumption is likely inadequate to represent the behavior of the nodules at the microstructural scale. Therefore, more advanced constitutive models are probably needed, capable of considering the influence of inelastic deformation and/or anisotropy.

Modeling the inelastic behavior of the graphite nodules is a very challenging task, mainly for the absolute absence of reliable experimental data concerning their non-linear mechanical response. In the present investigations, however, an attempt has been made, assuming a linear elastic-perfectly plastic behavior according to the J2-flow theory of plasticity, in order to set, in the simplest possible way, a maximum load carrying capacity for the nodules. As a consequence, all the simulations presented in the previous sections have been performed a second time, varying the nodule yield strength in the interval 25–100 MPa, which corresponds to the range of tensile strengths recorded for bulky reactor graphite (Taylor et al., 1967). However, it has been noticed that significant deviations in the results are not visible, except at very high values of the nodules' effective moduli. As explained in detail in (Andriollo et al., 2015b, a), the reason is that during the cooling stage the stress field developing in the nodules is mainly hydrostatic. Therefore, no yielding can occur according to the J2-flow theory of plasticity. During subsequent loading, deviatoric stress components build up, but they are not sufficient to cause appreciable amount of yielding, at least within the small deformation range investigated. Nevertheless, it must be kept in mind that there are no solid grounds to sustain that the J2-flow theory really reflects the physical behavior of the graphite nodules. This means that other inelastic formulations, perhaps allowing the possibility of having brittle fracture, might be more suitable.

Conversely, including a certain degree of anisotropy and inhomogeneity in the nodules, at the same time retaining the linear elastic structure of the constitutive equations, seems a more viable option. Dryden and Purdy (1989) proposed a radial symmetry model where the 5 elastic constants were directly taken from those characteristic of the graphite hexagonal unit cell. However, according to their findings, the SGI grade considered in the present work should have a Young's modulus of 190 GPa, which is 20 GPa larger than the experimental value. More recently, Di Cocco et al. (2015) assumed the nodules to be constituted by two isotropic concentric layers separated by a frictionless contact interface, both having Young's modulus and Poisson's ratio of 80 GPa and 0.3, respectively. Unfortunately, they did not perform any homogenization procedures to check the resulting elastic properties at the macroscale. A more detailed analysis of all advanced models for the nodules devised so far, along with some improvements proposed by the current authors, will be the subject of a future paper.

5. Conclusions

In the present work, an admissible domain for the effective Young's modulus and Poisson's ratio of the graphite particles in SGI has been determined by means of homogenization theory for polycrystalline materials. The result has been achieved on the basis of the nodules' real internal structure, composed of highly anisotropic graphite platelets, and by assuming an overall equivalent isotropic linear elastic behavior. Using both analytical and numerical micromechanical techniques, the implications of adopting nodules' effective moduli within such admissible domain have been investigated in relation to the mesoscopic elastic constants of GJS-400-15. However, it has been found that the predicted mesoscopic parameters never match the reference experimental values, no matter the choice of the admissible nodules' effective moduli. Furthermore, this important conclusion still holds when the influence of three relevant phenomena is taken into account: weak interface bonding, local microscopic residual stresses arising during solid state cooling and inelastic deformation of the nodules.

The reason for the present findings is probably that nodules cannot be assumed isotropic at a microscopic scale, at least from a micromechanical viewpoint. In other words, they cannot be considered as constituted of graphite platelets which are arranged in a statistically homogeneous way throughout the individual secondary-phase particles. This means that a satisfactory elastic constitutive description should take into consideration the intrinsic inhomogeneity and anisotropy of the nodules as well. It has to be remarked that it might still be possible to find values for the effective nodules' Young's modulus and Poisson's ratio which allow a good matching with the SGI

response recorded during uniaxial testing. In the end, this is what many of the authors listed in Table 1 have done. However, it is difficult to justify such isotropic parameters on the basis of physical grounds and, in addition, there is no guarantee that they will work for different loading conditions. Moreover, even if they provide good results at the mesoscopic level, the description they offer in terms of microscopic stress & strain fields in and around the nodules is quite disputable. This element has to be kept in mind especially if fatigue crack nucleation and propagation in SGI is to be analyzed.

References

47th Census of World Casting Production, 2013, Modern Casting - A publication of the American Foundry Society.

Aboudi, J., Arnold, S., Bednarcyk, B., 2012. Micromechanics of Composite Materials: A Generalized Multiscale Analysis Approach. Butterworth-Heinemann.

American Foundrymen's Society, 1992. Ductile Iron Handbook, American Foundrymen's Society.

Andriollo, T., Thorborg, J., Hattel, J., 2016. Analytical solution to the 1D Lemaitre's isotropic damage model and plane stress projected implicit integration procedure. Appl. Math. Model. doi:10.1016/j.apm.2016.01.024, in press.

Andriollo, T., Thorborg, J., Hattel, J., 2015a. The influence of the graphite mechanical properties on the constitutive response of a ferritic ductile cast iron – a micromechanical FE analysis. In: Proceedings of the XIII International Conference on Computational Plasticity, Fundamentals and Applications, pp. 632–641.

Andriollo, T., Thorborg, J., Tiedje, N., Hattel, J., 2015b. Modeling of damage in ductile cast iron – the effect of including plasticity in the graphite nodules. IOP Conf. Ser. Mater. Sci. Eng. 84 (1), 012027. doi:10.1088/1757-899X/84/1/012027.

Baer, W., Steglich, D., Brocks, W., Pusch, G., Petit, J., 1996. Experimental determination and micromechanical modelling of damage in nodular cast iron. In: Proceedings of the 11th European Conference on Fracture (ECF 11).

Berdin, C., Dong, M.J., Prioul, C., 2001. Local approach of damage and fracture toughness for nodular cast iron. Eng. Fract. Mech. 68, 1107–1117.

Bert, C.W., 1969. Unusual Poisson's ratios of pyrolytic graphite. AIAA J. 7, 1814–1815. doi:10.2514/3.5405.

Boccaccini, A.R., 1997. Young's modulus of cast-iron as a function of volume content, shape and orientation of graphite inclusions. Zeitschrift Fuer Met. Res. Adv. Tech. 88, 23–26.

Bonora, N., Ruggiero, A., 2005. Micromechanical modeling of ductile cast iron incorporating damage. Part I: Ferritic ductile cast iron. Int. J. Solids Struct. 42, 1401–1424. doi:10.1016/j.ijsolstr.2004.07.025.

Brocks, W., Hao, S., Steglich, D., 1996. Micromechanical modelling of the damage and toughness behaviour of nodular cast iron materials. J. Phys. IV 6, 43–52.

Carazo, F.D., Giusti, S.M., Boccardo, A.D., Godoy, L.A., 2014. Effective properties of nodular cast-iron: a multi-scale computational approach. Comput. Mater. Sci. 82, 378–390. doi:10.1016/j.commatsci.2013.09.044.

Collini, L., Nicoletto, G., 2005. Determination of the relationship between microstructure and constitutive behaviour of nodular cast iron with a unit cell model. J. Strain Anal. Eng. Des. 40, 107–116. doi:10.1243/030932405X7692.

Cooper, C.A., Elliott, R., Young, R.J., 2002. Investigation of elastic property relationships for flake and spheroidal cast irons using Raman spectroscopy. Acta Mater. 50, 4037–4046. doi:10.1016/S1359-6454(02)00202-1.

de Souza Neto, E, 2002. A fast, one-equation integration algorithm for the Lemaitre ductile damage model. Commun. Numer. Methods Eng. 18, 541–554. doi:10.1002/cnm.511.

Di Cocco, V., Iacoviello, D., Iacoviello, F., Rossi, A., 2015. Graphite nodules influence on DCIs mechanical properties: experimental and numerical investigation. Procedia Eng. 109, 135–143. doi:10.1016/j.proeng.2015.06.223.

Di Cocco, V, Iacoviello, F., Rossi, A., Cavallini, M., Natali, S., 2013. Graphite nodules and fatigue crack propagation micromechanisms in a ferritic ductile cast iron. Fatigue Fract. Eng. Mater. Struct. 36, 893–902. doi:10.1111/ffe.12056.

Dierickx, P., Verdu, C., Reynaud, A., Fougeres, R., 1996. A study of physico-chemical mechanisms responsible for damage of heat treated and as-cast ferritic spheroïdal graphite cast irons. Scr. Mater. 34, 261–268. doi:10.1016/1359-6462(95)00496-3.

Dong, M.J., Tie, B., Béranger, A.S., Prioul, C., François, D., 1997. Damage effect on the fracture toughness of nodular cast iron. Adv. Mater. Res. 4-5, 181–188. doi:10.4028/www.scientific.net/AMR.4-5.181.

Dorazil, E., 1991. High Strength Austempered Ductile Cast Iron. Horwood.

Drago, A., Pindera, M., 2007. Micro-macromechanical analysis of heterogeneous materials: macroscopically homogeneous vs periodic microstructures. Compos. Sci. Technol. 67, 1243–1263. doi:10.1016/j.compscitech.2006.02.031.

Dryden, J.R., Purdy, G.R., 1989. The effect of graphite on the mechanical properties of cast irons. Acta Metall. 37, 1999–2006. doi:10.1016/0001-6160(89), 90084-9.

Ductile Iron Society, 2013. Ductile Iron Data For Design Engineers, Ductile Iron Society [WWW Document]. URL http://www.ductile.org/ductile-iron-data/ (accessed 10.10.15).

Era, H., Kishitake, K., Nagai, K., Zhang, Z.Z., 1992. Elastic modulus and continuous yielding behaviour of ferritic spheroidal graphite cast iron. Mater. Sci. Technol. 8, 257–261.

Fernandino, D.O., Cisilino, A.P., Boeri, R.E., 2015. Determination of effective elastic properties of ferritic ductile cast iron by computational homogenization, micrographs and microindentation tests. Mech. Mater. 83, 110–121. doi:10.1016/j.mechmat.2015.01.002.

Gaudig, W., Mellert, R., Weber, U., Schmauder, S., 2003. Self-consistent one-particle 3D unit cell model for simulation of the effect of graphite aspect ratio on Young's modulus of cast-iron. Comput. Mater. Sci. 28, 654–662. doi:10.1016/j.commatsci.2003.08.021.

Gilbert, G.N.J., 1964. Stress/strain properties of nodular cast irons in tension and compression. BCIRA J. 12, 170–193.

Grimvall, G., 1997. Cast iron as a composite: conductivities and elastic properties. Adv. Mater. Res. 4-5, 31–46. doi:10.4028/www.scientific.net/AMR.4-5.31.

Hashin, Z., Shtrikman, S., 1963. A variational approach to the theory of the elastic behaviour of multiphase materials. J. Mech. Phys. Solids 11, 127–140.

Hervas, I., Bettaieb, M.B., Hug, E., 2013. Damage mechanisms evolution of ductile cast irons under thermomechanical loadings. Int. J. Mater. Prod. Technol. 47, 23. doi:10.1504/IJMPT.2013.058963.

Iron-foundry.com, n.d. Equivalent Grades of Ductile iron [WWW Document]. URL http://www.iron-foundry.com/grades-gray-ductile-sg-nodular-graphite-iron.html (accessed 6.8.15).

Kohout, J., 2001. A simple relation for deviation of grey and nodular cast irons from Hooke's law. Mater. Sci. Eng. A A313, 16–23.

Kosteski, L., Iturrioz, I., Galiano Batista, R., Cisilino, A.P., 2011. The truss-like discrete element method in fracture and damage mechanics. Eng. Comput. 28, 765–787. doi:10.1108/02644401111154664.

Kroner, E., 1977. Bounds for effective elastic moduli of disordered materials. J. Mech. Phys. Solids 25, 137–155.

Kuna, M., Sun, D.Z., 1996. Three-dimensional cell model analyses of void growth in ductile materials. Int. J. Fract. 81, 235–258. doi:10.1007/BF00039573.

Labrecque, C., Gagne, M., 1998. Review ductile iron: 50 years of continuous development. Can. Metall. Q. 37, 343–378.

Lakes, R., 1993. Advances in negative Poisson's ratio materials. Adv. Mater. 5, 293–296.

Lemaitre, J., 1985. A continuous damage mechanics model for ductile fracture. J. Eng. Mater. Technol. ASME 107, 83–89.

Liu, J.H., Hao, X.Y., Li, G.L., Liu, G.S., 2002. Microvoid evaluation of ferrite ductile iron under strain. Mater. Lett. 56, 748–755.

Matbase: The free and independent online materials properties resource [WWW Document], 2015. URL http://www.matbase.com/material-categories/metals/ferrous-metals/cast-iron/en-gjs-400-15-cen-en.html (accessed 6.3.15).

Miao, B., Fang, K., Bian, W., Liu, G., 1990. On the microstructure of graphite spherulites in cast irons by TEM and HREM. Acta Metall. Mater. 38, 2167–2174. doi:10.1016/0956-7151(90)90084-T.

Miao, B., North Wood, D.O., Bian, W., Fang, K., Fan, M.H., 1994. Structure and growth of platelets in graphite spherulites in cast iron. J. Mater. Sci. 29, 255–261. doi:10.1007/BF00356601.

Nicoletto, G., Collini, L., Konečná, R., Riva, E., 2006. Analysis of nodular cast iron microstructures for micromechanical model development. Strain 42, 89–96. doi:10.1111/j.1475-1305.2006.00259.x.

Oliver, W.C., Pharr, G.M., 1992. An improved technique for determining hardness and elastic modulus using load and displacement sensing indentation experiments. J. Mater. Res. 7, 1564–1580.

Pradhan, S.K., Nayak, B.B., Sahay, S.S., Mishra, B.K., 2009. Mechanical properties of graphite flakes and spherulites measured by nanoindentation. Carbon N. Y. 47, 2290–2292. doi:10.1016/j.carbon.2009.04.024.

Pundale, S.H., Rogers, R.J., Nadkarni, G.R., 1998. Finite element modeling of elastic modulus in ductile irons: effect of graphite morphology. Trans. Am. Foundrymen's Soc. 106, 99–105.

Rabold, F., Kuna, M., 2005. Cell model simulation of void growth in nodular cast iron under cyclic loading. Comput. Mater. Sci. 32, 489–497. doi:10.1016/j.commatsci.2004.09.016.

Savini, G., Dappe, Y.J., Öberg, S., Charlier, J.C., Katsnelson, M.I., Fasolino, A., 2011. Bending modes, elastic constants and mechanical stability of graphitic systems. Carbon N. Y. 49, 62–69. doi:10.1016/j.carbon.2010.08.042.

Sjögren, T., Svensson, I.L., 2004. Modelling the effect of graphite morphology on the modulus of elasticity in cast irons. Int. J. Cast Met. Res. 17, 271–279. doi:10.1179/136404604225022694.

Sjögren, T., Svensson, I.L., 2005. Studying elastic deformation behaviour of cast irons by acoustic emission. Int. J. Cast Met. Res. 18, 249–256. doi:10.1179/136404605225023117.

Speich, G.R., Schwoeble, A.J., Kapadia, B.M., 1980. Elastic moduli of gray and nodular cast iron. Trans. ASME. J. Appl. Mech. 47, 821–826.

Steglich, D., Brocks, W., 1998. Micromechanical modeling of damage and fracture of ductile materials. Fatigue Fract. Eng. Mater. Struct. 21, 1175–1188. doi:10.1046/j.1460-2695.1998.00078.x.

Taylor, R., Brown, R.G., Gilchrist, K., Hall, E., Hodds, A.T., Kelly, B.T., Morris, F., 1967. Mechanical properties of reactor graphite. Carbon N. Y. 5, 519–531.

Tiedje, N.S., 2010. Solidification, processing and properties of ductile cast iron. Mater. Sci. Technol 26, 505–514. doi:10.1179/026708310X12668415533649.

Watt, J.P., Peselnick, L., 1980. Clarification of the Hashin–Shtrikman bounds on the effective elastic moduli of polycrystals with hexagonal, trigonal, and tetragonal symmetries. J. Appl. Phys. 51, 1525. doi:10.1063/1.327804.

Wawra, H.H., Gairola, B.K.D., Kroner, E., 1982. Comparison between experimental values and theoretical bounds for the elastic constants E, G, K, and μ of aggregates of noncubic crystallites. Zeitschrift Fur Met. 73, 69–71.

Zhang, K.S., Bai, J.B., François, D., 1999. Ductile fracture of materials with high void volume fraction. Int. J. Solids Struct. 36, 3407–3425. doi:10.1016/S0020-7683(98) 00157-7.

Appendix C
PAPER III

International Journal of Solids and Structures 100–101 (2016) 523–535

Contents lists available at ScienceDirect

International Journal of Solids and Structures

journal homepage: www.elsevier.com/locate/ijsolstr

Modeling the elastic behavior of ductile cast iron including anisotropy in the graphite nodules

Tito Andriollo[a,c,*], Jesper Thorborg[a,b,d], Jesper Hattel[a,e]

[a] Department of Mechanical Engineering, Technical University of Denmark, DK-2800 Kgs. Lyngby, Denmark
[b] MAGMA GmbH, D-52072 Aachen, Germany
[c] Technical University of Denmark, Produktionstorvet, Building 425, room 125, 2800 Kgs. Lyngby, Denmark
[d] Technical University of Denmark, Produktionstorvet, Building 425, room 132, 2800 Kgs. Lyngby, Denmark
[e] Technical University of Denmark, Produktionstorvet, Building 425, room 128, 2800 Kgs. Lyngby, Denmark

ARTICLE INFO

Article history:
Received 15 December 2015
Revised 7 September 2016
Available online 21 September 2016

Keywords:
Micro-mechanics
Anisotropic
Elasticity
Ductile cast iron
Graphite nodules

ABSTRACT

This paper presents a micro-mechanical approach to model the intrinsic elastic anisotropy of the graphite particles in ductile iron. Contrary to most of the published works in the field, the constitutive behavior is directly derived on the basis of the nodule characteristic internal structure, composed of graphite platelets arranged into conical sectors. In this way, the large uncertainty traditionally associated with local mechanical measurements of micro-hardness is eliminated. The proposed anisotropic description is validated by simulating the macroscopic ductile iron elastic response by means of a 3D periodic unit cell model. In this respect, an explicit procedure to enforce both periodic displacement and periodic traction boundary conditions in ABAQUS is presented, and the importance of fulfilling the traction continuity conditions at the unit cell boundaries is discussed. It is shown that localized inelastic deformation is likely to develop for loading conditions which can still be considered as elastic at the macroscopic scale. The presence of a weak interface between the graphite and the matrix is also investigated, and it is found to affect the results to a limited extent only.

1. Introduction

Among the multitude of high-performance metallic materials available today, ductile cast iron, also known as spheroidal graphite iron (SGI), is probably one of the very few boasting a positive growth rate on the market since its commercial introduction in 1948 (Ductile Iron Society, 2013). According to recent estimates, as many as 25% of the castings produced worldwide are made of SGI (*47th Census of World Casting Production*, 2013) and represent mainly small and medium sized heavily loaded parts with high demands for consistent quality for the automotive sector and very large industrial components with extreme demands for mechanical properties, particularly fatigue strength and fracture toughness (Tiedje, 2010).

From a metallurgical perspective, SGI may be classified as a ternary Fe-C-Si alloy (Labrecque and Gagne, 1998) whose properties to a large extent are controlled by chemical composition, cooling rate and heat treatment. The final microstructure may be naturally considered as composite (Grimvall, 1997 and Sjögren and Svensson, 2004), consisting of graphite nodules embedded in a continuous matrix which, in most engineering applications, may be either ferritic, pearlitic or a mixture of the two.

Due to its high technological importance, a number of papers have addressed the problem of modeling the mechanical behavior of SGI, particularly ductile fracture and fatigue. Nevertheless, the intrinsic material complexity has always posed severe challenges, and as recently pointed out by (Hütter et al., 2015) in a review article, much work is still needed to bridge the gap between microstructural features and global properties. Particularly, according to the former authors, a deeper understanding of the mechanical response of the single constituents at the micro scale is highly necessary.

Concerning this point, an important element, which has probably received much less consideration than necessary in the past, is the mechanical nature of the graphite particles. Several numerical investigations on the non-linear behavior of SGI during tensile testing published in the late '90 s ((Kuna and Sun, 1996; Brocks et al., 1996 and Zhang et al., 1999) among others) were based on the concept of a voided material model, meaning that the nodules were simply neglected in the analyses. This was motivated by their presumed "soft" nature and the early debonding from the matrix,

* Corresponding author.
E-mail addresses: titoan@mek.dtu.dk (T. Andriollo), jest@mek.dtu.dk (J. Thorborg), jhat@mek.dtu.dk (J. Hattel).

http://dx.doi.org/10.1016/j.ijsolstr.2016.09.023
0020-7683/

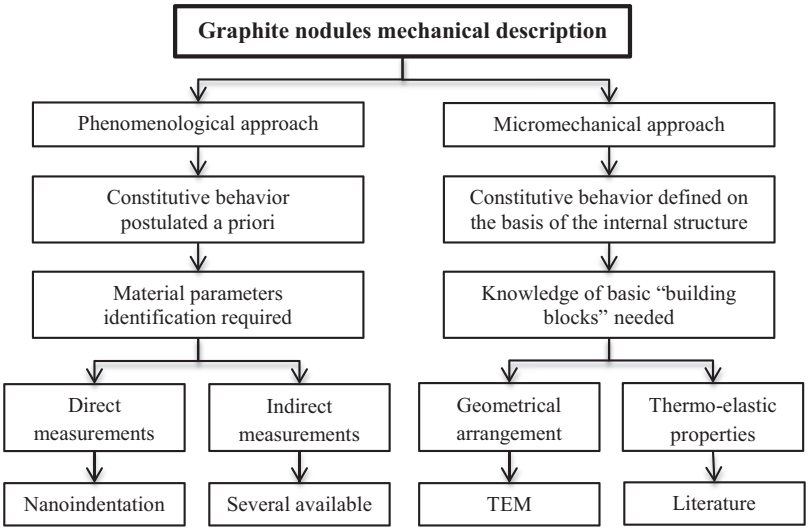

Fig. 1. Schematic of the two different approaches used to model the mechanical behavior of the graphite nodules.

often observed experimentally (Dong et al., 1997). It is quite clear, however, that this assumption may be reasonable at high values of the triaxiality ratio, but it cannot be justified under pure shear or in situations where the hydrostatic part of the stress tensor becomes negative. Several experimental facts point in this direction, as discussed in detail in (Andriollo et al., 2015a,b). Perhaps, the most striking evidence of this is that 1) at temperatures close to the eutectoid transformation, the nodules remain undeformed under heavy compressive deformation of SGI samples (Hervas et al., 2013) and 2) the low-cycle fatigue behavior with negative stress ratio is better reproduced by numerical models where nodules are treated as rigid spheres instead of voids (Rabold and Kuna, 2005). Hence, as loading scenarios for real SGI components usually involve complex combinations of tensile and compressive stresses (Shirani and Härkegård, 2011), the simplistic voided material assumption is likely inadequate.

On the other hand, including the graphite particles in the analysis is not trivial, primarily because of the lack of reliable data concerning their mechanical properties. The vast majority of authors who have tried to model the nodules' behavior have followed the phenomenological approach summarized in Fig. 1, assuming an isotropic linear elastic response. Unfortunately, the procedure suffers from two important shortcomings.

First of all, it is very hard, if not impossible, to perform a direct identification of the required material parameters. In fact, the only easy way to experimentally characterize the nodules is via nano-indentation (Oliver and Pharr, 1992). The method however, is quite disputable, as it relies on an exact isotropic elastic solution (Harding and Sneddon, 1945) whereas graphite is notoriously highly anisotropic at the local scale. Moreover, it was argued by (Bonora and Ruggiero, 2005) that the sharp indenter usually employed could simply separate the graphite layers without creating any elastic deformation at all. In light of these considerations, parameters identification based on indirect measurements, e.g. testing the stiffness of SGI at the macroscopic level, is sometimes preferred. In both cases, however, the phenomenological approach has proved to lead to large uncertainties, as confirmed by Table 1, which reports the nodules' isotropic elastic constants assumed by several researchers over the last 30 years.

The second important drawback is that the isotropy assumption cannot be justified using elastic bound theory analysis. In a recent work, (Andriollo and Hattel, 2016) determined an admissible domain for the Young's modulus and Poisson's ratio of the graphite particles by means of homogenization theory for polycrystalline materials. Using both analytical and numerical micromechanical techniques, the implications of adopting nodules' moduli within such admissible domain were investigated in relation to the effective elastic constants of a common grade of ductile iron. It was found that the predicted effective parameters never match the reference experimental values, no matter the choice of the admissible nodules' moduli. Furthermore, this important conclusion still holds when the influence of factors like weak interface bonding between the matrix and the graphite and local residual stresses arising during manufacturing is taken into account.

The limitations of the phenomenological approach discussed so far motivate the adoption of different strategies to model the nodules. As shown in Fig. 1, another possibility is to use a micromechanical approach, where the nodules' properties are obtained directly on the basis of their real internal structure. As previously mentioned, the latter is composed of graphite platelets arranged in a characteristic radial fashion (Theuwissen et al., 2012). As the moduli of the graphite hexagonal unit cell are known, the elastic response of the entire nodule can in principle be calculated without the need of any inverse analyses. To the authors' best knowledge, the only systematic work along this line was carried out by (Dryden and Purdy, 1989); in their analysis, however, a quite rough approximation of the platelets arrangement was made in order to solve the problem analytically, which was later found to generate unrealistic values for the macroscopic SGI elastic properties.

The aim of the present work is to extend the findings of the abovementioned authors by considering a more realistic description of the nodules' internal structure according to the most recent TEM investigations. More specifically, the observed subdivision of the graphite particles into conical sectors is taken into account. Validation of the proposed model is performed by calculating the effective elastic properties of a periodic SGI unit cell containing a single graphite nodule and comparing them with those of a well-known ferritic ductile iron grade. Due to the complexity of the underlying 3D geometry, the commercial software ABAQUS is used for the purpose. Within this context, a thorough discussion regarding the implementation of suitable boundary conditions is given, motivating the importance of prescribing both periodic displacements and tractions along the cell boundaries.

Table 1
Micromechanical modeling of the SGI elastic response: assumed values for the nodules' isotropic elastic moduli.

Year	Authors	Young's modulus (GPa)	Poisson's ratio
1980	(Speich et al., 1980)	8.5	0.29
1992	(Era et al., 1992)	303	Not specified
1997	(Boccaccini, 1997)	8.5	0.2
1998	(Pundale et al., 1998)	0 (void)	0 (void)
2002	(Cooper et al., 2002)	8.5	0.2
2003	(Gaudig et al., 2003)	4.17	0.2225
2004	(Sjögren and Svensson, 2004)	*	0.2
2005	(Bonora and Ruggiero, 2005)	300–375	Not specified
2005	(Collini and Nicoletto, 2005)	15	0.3
2006	(Nicoletto et al., 2006)	15	0.3
2014	(Carazo et al., 2014)	*	0.2225
2015	(T. Andriollo et al., 2015a, b)	0–20	0.15
2015	(Fernandino et al., 2015)	15	0.28

* $E_g = 0.173 \cdot Nodularity + 18.9 \rightarrow 36.2$ GPa for 100% nodularity.

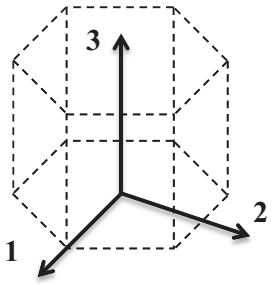

Fig. 2. Graphite platelet hexagonal unit cell.

Table 2
Elastic constants of a single graphite platelet. Entries are in GPa. (Savini et al., 2011).

C11	C44	C12	C13	C33
1107	4.4	175	−2.5	29

2. Micro-scale material models

2.1. Basic nodule structure according to TEM investigations

The characteristic spherical shape of the graphite particles in ductile cast iron is normally obtained by adding Mg and, in some cases, rare earth elements such as Ce and La to the base liquid metal, which combine with S and O to produce a melt of high purity. Formation of graphite nodules according to the stable Fe-C-Si phase diagram during subsequent solidification is achieved via addition of proper inoculants (Tiedje, 2010).

It seems to be well established now (Miao et al., 1990 and Theuwissen et al., 2012) that the basic building blocks forming the nodules in the solidified material are graphite platelets consisting of graphene layers piled up without any crystallographic defects. These structural units have thicknesses in the sub-micrometer range and appear to be elongated along the graphene planes. From a continuum point of view, they can be described on the basis of the hexagonal unit cell reported in Fig. 2 (Sjogren, 2007), where the 3-direction is orthogonal to the graphene layers. The elastic properties of such hexagonal symmetry may be fully defined in terms of 5 independent constants (Tromans, 2011), which are reported in Table 2. It can be noticed that the stiffness in the basal plane, expressed by C11, is extremely high, above 1 TPa, whereas that along the orthogonal direction, associated with C33, is more than one order of magnitude smaller.

The single graphite platelets are arranged into conical sectors, which radiate from the nodule center to the outer periphery as visible in Fig. 3(a). Within a sector, the platelets are stacked on each other, with the 3-direction constant and oriented approximately radially, as schematically shown in Fig. 3(b). Nevertheless, the stacking is not perfect, and rotations about the 3-axis occur on an almost regular basis, defining domains of similar orientation (Theuwissen et al., 2014).

2.2. Graphite nodule micromechanical models

2.2.1. Geometry

Assuming the nodule to have spherical shape, a natural problem is its subdivision into conical sectors of similar size. Moreover, their overall number must not exceed a few tens, according to the experimental data provided by the authors listed in the previous section. The simplest way to perform this task is to use orthogonal planes passing through the center of the sphere: this leads to the "Type6" and "Type8" nodule models visible in Fig. 4, where the name indicates the number of sectors generated. Models with more partitions may be obtained by subdividing each conical sector of "Type8" in a qualitatively symmetric fashion, hence creating nodules with 32, 48 and 80 sectors respectively. Except for "Type6", the basic features of each different model may be expressed in terms of parameters of the related spherical triangles, which are defined as the elements of the spherical surface identified by a given sector. This information is provided in Table 3, where the distortion index is defined as:

$$DI = \frac{|l_1 - \bar{l}| + |l_2 - \bar{l}| + |l_3 - \bar{l}|}{3\bar{l}}, \quad \bar{l} = \frac{l_1 + l_2 + l_3}{3} \tag{1}$$

l_i, i = 1,2,3 being the spherical triangle side lengths. It may be seen that DI is almost always close to zero, indicating a good level of symmetry of the underlying partitioning; furthermore, no large size differences exist among conical sectors of the same model type, in agreement with experimental observations.

2.2.2. Elastic properties

On the basis of the real nodule internal structure, each conical sector is assigned anisotropic elastic properties according to Table 2. The 3-direction is defined as the direction connecting the center of the nodule to the centroid of the related spherical triangle. As a body exhibiting hexagonal symmetry is transversely isotropic with respect to the basal plane (i.e. the graphene layers in this case), the other two material directions can be set arbitrarily without affecting the analysis.

In order to facilitate the comparison with (Dryden and Purdy, 1989) findings, an additional model is introduced, where the

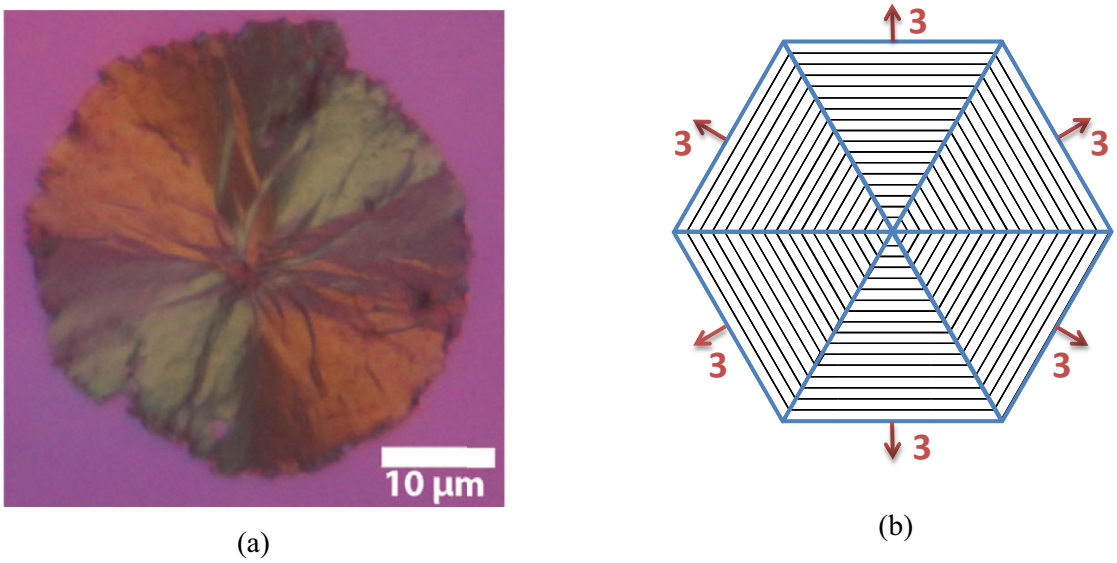

Fig. 3. (a) Optical micrograph (polarized light) of a graphite spheroid in cast iron showing sectors. Reprinted from (Theuwissen et al., 2012) with permission of Springer. (b) 2D schematic of the division of a nodule into sectors and orientation of the graphite platelets therein.

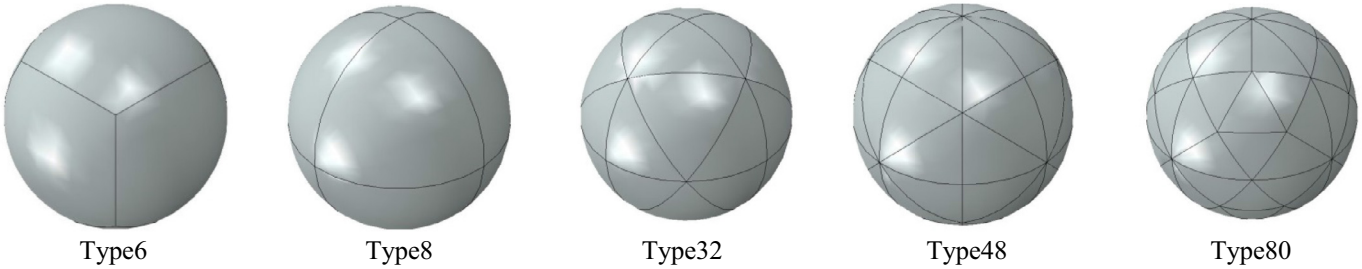

Fig. 4. Micromechanical models of a single spherical graphite nodule, with increasing number of conical sectors.

Table 3
Parameters of the spherical triangles related to the different nodule models.

Nodule model	Triangle subtype	Number	Angles (degrees)			Area / radius^2	Average side length / radius	Distortion index (%)
Type8	a	8	90.00	90.00	90.00	1.571	1.571	0.00
Type32	a	24	90.00	54.74	54.74	0.340	0.873	13.33
	b	8	70.53	70.53	70.53	0.551	1.047	0.00
Type48	a	48	90.00	45.00	60.00	0.262	0.873	13.33
Type80	a	48	45.00	54.74	90.00	0.170	0.641	14.96
	b	24	70.53	58.52	58.52	0.132	0.544	5.07
	c	8	62.96	62.96	62.96	0.155	0.586	0.00

3-direction is prescribed parallel to the radius pointwise throughout the nodule. The resulting spherically anisotropic model is denoted as "TypeInf", as it is essentially equivalent to assuming an infinite number of conical sectors.

2.3. Periodic unit cell for SGI

As pointed out in the introduction, it is generally not possible to validate micromechanical models for the nodules against measurements performed directly on the same graphite particles. Therefore, the only way to test the quality of the proposed model is to simulate the mechanical response of the overall "composite" SGI at the macroscale and compare the results with experimentally accessible quantities.

Today, homogenization methods extensively rely on the concept of representative volume element (Geers et al., 2010), which is intuitively defined as the minimum material element whose behavior is equivalent to that of a homogeneous fictitious material. Despite the recent application of this approach to SGI (Carazo et al., 2014), the main disadvantage for the case at hand is that a large number of nodules with complex internal geometry should be discretized at the same time, making any 3D computation cumbersome. In addition, replacement of the nodules with equivalent homogeneous isotropic particles to speed up the process is not admissible in the context of the present analysis, for the reasons discussed in (Andriollo and Hattel, 2016).

As a consequence, a periodic approach is adopted here, assuming the SGI microstructure to be periodic and generated by the spatial repetition of the cubic unit cell depicted in Fig. 5. The relative size of the single nodule is adjusted to give the 11.5% volumetric graphite concentration typical of GJS-400-15 ductile iron (Steglich and Brocks, 1998), which is taken as reference material throughout the analysis. The surrounding ferritic matrix is considered as isotropic linear elastic, with Young's modulus and Poisson's ratio equal to 205 GPa and 0.29 respectively. For later comparison,

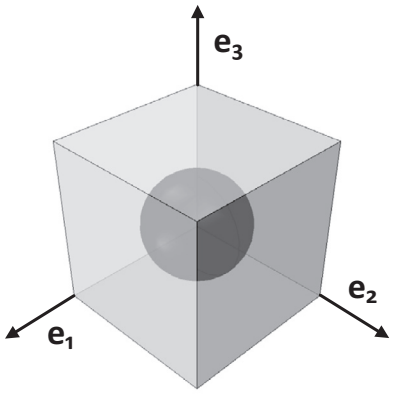

Fig. 5. Micromechanical periodic unit cell representing the microstructure of SGI.

it is useful mentioning here that these values correspond to a bulk modulus of 162.7 GPa and to a shear modulus of 79.5 GPa.

3. Homogenization technique

3.1. Periodic boundary conditions

Considering any two equivalent points $\boldsymbol{x}$ and $\boldsymbol{x}+\boldsymbol{d}$ lying on opposite faces of the unit cell and separated by the characteristic periodic length $\boldsymbol{d}$, boundary conditions can be applied as (Drago and Pindera, 2007):

$$\begin{aligned}\boldsymbol{u}(\boldsymbol{x}+\boldsymbol{d}) &= \boldsymbol{u}(\boldsymbol{x}) + \bar{\varepsilon}\cdot\boldsymbol{d}\\ \boldsymbol{t}(\boldsymbol{x}+\boldsymbol{d}) &= -\boldsymbol{t}(\boldsymbol{x})\end{aligned} \tag{2}$$

where $\boldsymbol{u}$ and $\boldsymbol{t}$ denote displacement and surface traction. The 2nd order tensor $\bar{\varepsilon}$ represents the average of the infinitesimal strain over the entire volume, and it is normally an externally imposed quantity. Application of the periodic conditions (2) is sufficient to guarantee continuity of the displacements and of the surface tractions across adjacent unit cells.

3.2. Averaging relations

A linear elastic relation between volume averages of the stress and strain fields over the unit cell is sought in the form:

$$\bar{\sigma} = \bar{\mathbb{C}} : \bar{\varepsilon} \tag{3}$$

where $\bar{\mathbb{C}}$ is the 4th order effective stiffness tensor. Its independent components are determined by prescribing in sequence six independent loadings in the form $\bar{\varepsilon}^{(1)},\ldots,\bar{\varepsilon}^{(6)}$ according to Eq. (2), and recording the resulting average stresses $\bar{\sigma}^{(1)},\ldots,\bar{\sigma}^{(6)}$. The resulting linear system of equations can then be solved for the effective elastic constants.

The calculated effective stiffness tensor can be decomposed into an isotropic and an anisotropic part as follows:

$$\bar{\mathbb{C}} = \bar{\mathbb{C}}^{\text{iso}} + \bar{\mathbb{C}}^{\text{ani}} \tag{4}$$

The former can be further written as:

$$\bar{\mathbb{C}}^{\text{iso}} = 3\bar{k}\mathbb{S} + 2\bar{\mu}\mathbb{D} \tag{5}$$

where $\mathbb{S}$ and $\mathbb{D}$ are the spherical and deviatoric projection tensors (Itskov, 2007) , which form an orthogonal basis for isotropic 4th order tensors. The quantities $\bar{k}$ and $\bar{\mu}$ represent the effective bulk and shear modulus respectively and may be calculated as:

$$\bar{k} = \frac{1}{3}\frac{\langle\bar{\mathbb{C}}|\mathbb{S}\rangle}{\langle\mathbb{S}|\mathbb{S}\rangle},\quad \bar{\mu} = \frac{1}{2}\frac{\langle\bar{\mathbb{C}}|\mathbb{D}\rangle}{\langle\mathbb{D}|\mathbb{D}\rangle} \tag{6}$$

where $\langle\cdot\,|\,\cdot\rangle$ indicates the scalar product between 4th order tensors. Conversion to effective Young's modulus and Poisson's ratio is performed via the basic relations:

$$\bar{E} = \frac{9\bar{k}\bar{\mu}}{3\bar{k}+\bar{\mu}},\quad \bar{\nu} = \frac{3\bar{k}-2\bar{\mu}}{2\left(3\bar{k}+\bar{\mu}\right)} \tag{7}$$

Finally, an anisotropy index may be obtained as (Fernandino et al., 2015):

$$I_a = \left(\frac{\left\langle\bar{\mathbb{C}}-\bar{\mathbb{C}}^{\text{iso}}\middle|\bar{\mathbb{C}}-\bar{\mathbb{C}}^{\text{iso}}\right\rangle}{\left\langle\bar{\mathbb{C}}\middle|\bar{\mathbb{C}}\right\rangle}\right)^{1/2} \tag{8}$$

The latter quantity provides an indication of the material degree of anisotropy and will be used in Section 5.4 to discuss the validity of the periodic unit cell assumption in the context of modeling the SGI behavior.

4. Numerical implementation

4.1. Setting up periodic boundary conditions in ABAQUS

In order to gain insight into the meaning of the periodic conditions (2), it is useful to write down the finite element system of equations for the entire unit cell, within the framework of small strain linear elasticity. For convenience, a symmetric mesh is assumed. All external boundary degrees of freedom (dofs) are grouped into the ordered vectors $\boldsymbol{u}_{\boldsymbol{b}}^{+}$ and $\boldsymbol{u}_{\boldsymbol{b}}^{-}$, such that the generic i-elements of such two vectors correspond to equivalent nodes lying on opposite faces of the unit cell, separated by the characteristic distance $\boldsymbol{d}$. The remaining internal dofs are denoted by the vector $\boldsymbol{u}_{\boldsymbol{i}}$. Under these assumptions, the finite element system of equations takes the form:

$$\begin{bmatrix}\mathbf{K}_{\mathbf{ii}} & \mathbf{K}_{\mathbf{ib}}^{+} & \mathbf{K}_{\mathbf{ib}}^{-}\\ \mathbf{K}_{\mathbf{bi}}^{+} & \mathbf{K}_{\mathbf{bb}}^{++} & \mathbf{K}_{\mathbf{bb}}^{+-}\\ \mathbf{K}_{\mathbf{bi}}^{-} & \mathbf{K}_{\mathbf{bb}}^{-+} & \mathbf{K}_{\mathbf{bb}}^{--}\end{bmatrix}\cdot\begin{Bmatrix}\boldsymbol{u}_{\boldsymbol{i}}\\ \boldsymbol{u}_{\boldsymbol{b}}^{+}\\ \boldsymbol{u}_{\boldsymbol{b}}^{-}\end{Bmatrix} = -\begin{Bmatrix}0\\ \boldsymbol{f}_{\boldsymbol{b}}^{+}\\ \boldsymbol{f}_{\boldsymbol{b}}^{-}\end{Bmatrix} \tag{9}$$

where the $\mathbf{K}$ elements represent submatrices of the global stiffness matrix and $\boldsymbol{f}_{\boldsymbol{b}}^{+}$ and $\boldsymbol{f}_{\boldsymbol{b}}^{-}$ denote the external nodal forces, which are initially unknown. The system (9) is complemented by the periodic boundary conditions (2), which promptly yield the following two additional sets of equations:

$$\begin{aligned}\left\{\boldsymbol{u}_{\boldsymbol{b}}^{+}\right\} &= \left\{\boldsymbol{u}_{\boldsymbol{b}}^{-}\right\} + [\bar{\varepsilon}]\cdot\{\boldsymbol{d}\}\\ \left\{\boldsymbol{f}_{\boldsymbol{b}}^{+}\right\} &= -\left\{\boldsymbol{f}_{\boldsymbol{b}}^{-}\right\}\end{aligned} \tag{10}$$

and if the stiffness matrix is non-singular, a unique solution may be found.

The natural method to impose linear constraints of the form (10) in ABAQUS is to use the "Linear constraint equations" command (Dassault Systèmes Simulia Corp., 2013a), which allows enforcing scalar linear relation among dofs of the type:

$$a_1u_1 + a_2u_2 + \ldots + a_ku_k = 0 \tag{11}$$

where u_j, $j=1{:}\ k$ are generic displacement dofs and a_j, $j=1{:}\ k$ are real coefficients. Nevertheless, this approach has two limitations:

1. the first dof appearing in an equation is always eliminated and cannot be used in subsequent relations;
2. equations can only be formulated in terms of displacement dofs, hence imposition of (10b) does not appear as trivial.

Recently, (Qi et al., 2015) have discussed the simplified ABAQUS implementation of only the displacement part of the periodic boundary conditions, claiming that (10a) alone was sufficient to obtain the desired periodic solution. However, as will be shown later in this work, this cannot ensure continuity of the surface tractions across adjacent unit cells.

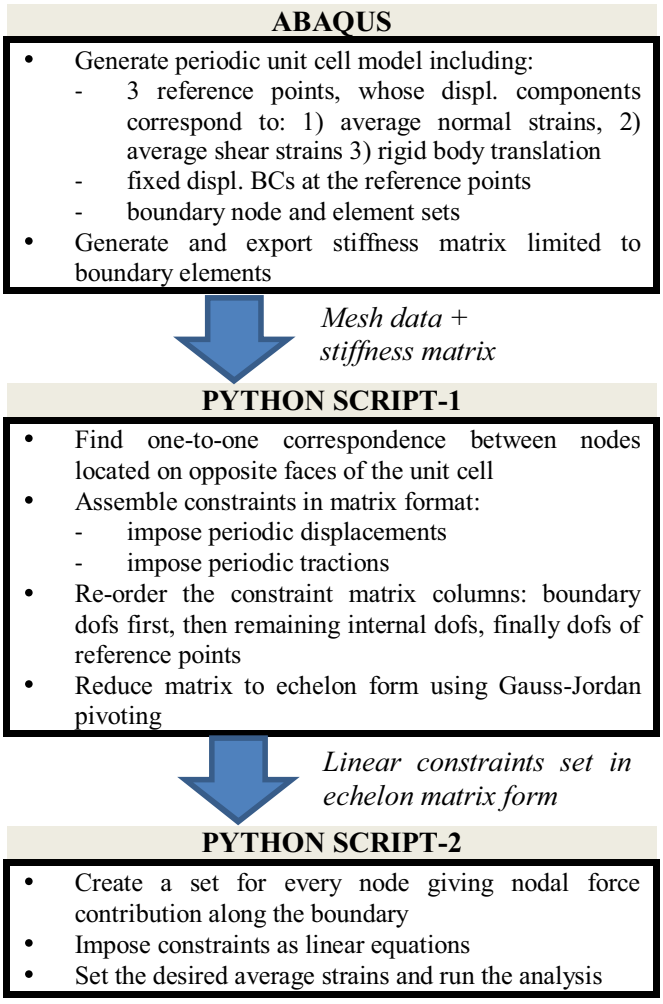

Fig. 6. Procedure for setting up periodic displacement and traction boundary conditions in ABAQUS.

In principle, within the ABAQUS environment, imposition of (10a) should imply that (10b) is satisfied a priori. The reason is that when an equation of the type (11) is prescribed, ABAQUS generates constraint forces (in addition to the internal nodal forces) at all dofs involved in the equation, which are proportional to their respective coefficients. Then, as the coefficients of the elements of $\boldsymbol{u}_b^+$ and $\boldsymbol{u}_b^-$ must be set as opposite in view of (10a), it means that the related constrained nodal forces are opposite too, which is exactly what (10b) specifies.

Nevertheless, in the context of the present work, a procedure which explicitly enforces both periodic displacement and periodic traction conditions is suggested. The reason is twofold. On the one hand, the proposed method is more general and can be used in other types of analyses where imposition of relations between tractions at the local level is required. On the other hand, a very simple way to cope with the first limitation of the "Linear constraint equations" command is given, which is relevant even in situations when only (10a) is to be imposed, especially when dealing with 3D unit cell geometries.

The procedure is illustrated in Fig. 6 and it is based on Python scripting. It can been seen that, in order to impose the periodic traction condition, entries of the global stiffness matrix related to the boundary nodal forces are extracted by means of the MATRIX GENERATE command (Dassault Systèmes Simulia Corp., 2013b). Moreover, repetition of dofs already set as first dof in previous equations is avoided by prior reduction to echelon form via Gauss-Jordan pivoting of the matrix associated with the set of linear constraints.

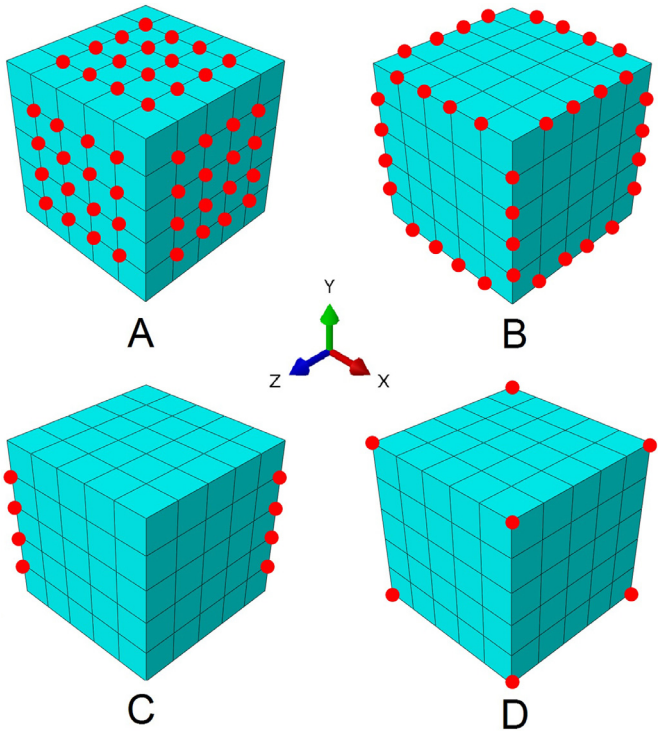

Fig. 7. Definition of useful node sets on the unit cell mesh: (a) face internal nodes, (b) edge internal nodes, (c) pair of opposite parallel edges along y-direction, (d) corner nodes.

4.2. Avoiding over-constraining

The choice of the boundaries over which periodic conditions have to be imposed deserves special attention. In fact, it is of utmost importance to avoid generating a number of linear independent constraints greater than the number of dofs associated with the boundary nodes: if that happens, spurious deformation will occur in the unit cell, adversely affecting the quality of the overall analysis.

A simple strategy to deal with the abovementioned issue is presented here. With reference to the 3D unit cell mesh of Fig. 7, the following quantities are introduced:

- n_f: number of face internal nodes
- n_e: number of edge internal nodes
- n_c: number of corner nodes
- $n_b = n_f + n_e + n_c$: number of total boundary nodes

Periodic displacement boundary conditions are applied considering all n_b nodes. Constraints are set between all possible pairs of equivalent nodes, meaning that a single corner node will be subjected to 3 linear constraints of the vector type (10)(a), an edge node to two, and a face node to one only. The total number of linear independent equations C_d generated in this way may be determined as:

$$C_d = 3\left(\frac{1}{2}n_f + \frac{3}{4}n_e + (n_c - 1)\right) \tag{12}$$

Conversely, periodic traction boundary conditions are imposed considering the face internal nodes only, plus the internal nodes lying on 3 pairs of opposite parallel edges as shown in Fig. 7(c), one pair for each Cartesian direction. Consequently, the number of

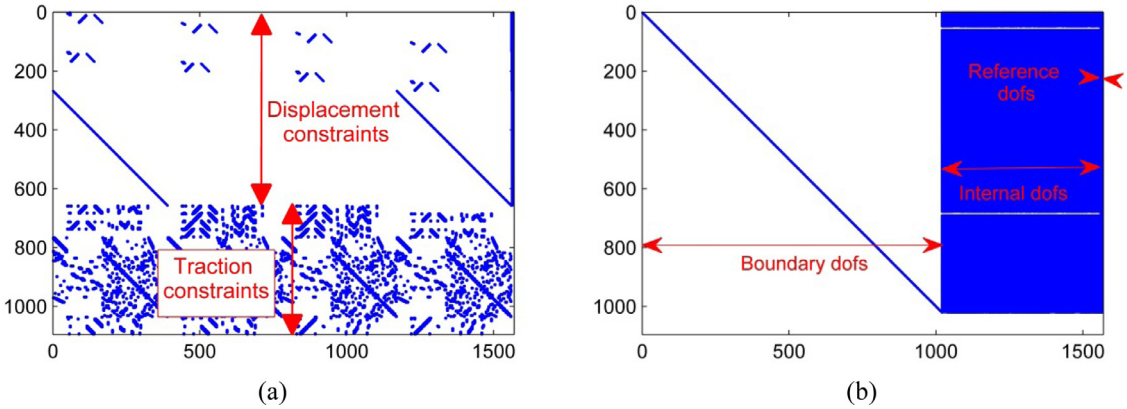

Fig. 8. Structure of the set of linear constraint equations associated with the periodic boundary conditions: (a) before and (b) after Gauss-Jordan pivoting.

independent traction constraints C_t created is given by:

$$C_t = 3\left(\frac{1}{2}n_f + \frac{1}{4}n_e\right) \tag{13}$$

The overall number of linear independent equations C_{tot} is then:

$$C_{tot} = C_d + C_t + 3 \tag{14}$$

where the last term relates to the prescribed motion of a single selected node, necessary to avoid rigid body translation. By inserting expressions (12 and 13) into (14), it can be easily verified that $C_{tot} = 3n_b$, i.e. the number of independent constraints is exactly equal to the number of boundary dofs.

5. Results and discussion

5.1. Periodic boundary conditions implementation verification

In order to verify the quality of the ABAQUS implementation procedure described in Sections 4.1 and 4.2, the full set of linear constraint equations for a test unit cell with 340 boundary nodes has been generated by imposition of the appropriate periodic conditions. The structure of the associated matrix is shown in Fig. 8(a), where the blue dots indicate the non-zero entries. Fig. 8(b) reports the structure of the same linear system, but after Gauss-Jordan pivoting: the number of pivots found is exactly $1020 = 3*340$. It may be noticed that each boundary dof is constrained to the internal dofs of the boundary elements and to the dofs of the reference points, which represent the average strains imposed to the unit cell. It has to be pointed out, however, that the blue area on the right-hand side of Fig. 8(b) is not as "numerically dense" as it might appear. Several entries are a few orders of magnitude smaller compared to the pivot coefficient, and some are non-zero only due to round-off errors; therefore, they can simply be neglected in order to speed up the analysis.

5.2. Necessity of the periodic boundary traction condition

The work of (Qi et al., 2015) previously mentioned offers an example of the application of the so-called "Unified displacement-difference periodic boundary conditions", proposed by (Xia et al., 2006) to model composites with periodical distribution of the reinforcing phase. According to the latter authors, within the framework of a displacement-based finite element analysis, the condition (10a) alone is sufficient to guarantee the uniqueness of the solution and the fulfillment of the traction continuity requirement along the unit cell boundaries.

However, it is the present authors' opinion that such statement may be misleading. In fact, if the traction condition (10b) is neglected, the associated system of equations (9) is underdetermined, unless further assumptions are made on the nature of the external nodal forces $\boldsymbol{f}_b^+$ and $\boldsymbol{f}_b^-$, which are of course unknown for the problem at hand. Such additional assumptions are to a large extent subjective and implementation-dependent, and therefore might lead to non-unique results.

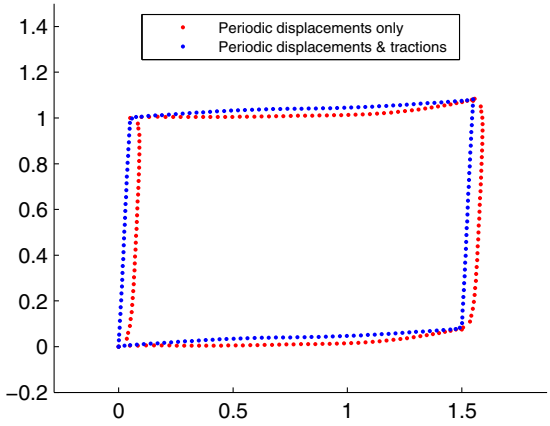

Fig. 9. Comparison between 2D plate deformed configurations obtained by either enforcing or not the periodic traction condition.

For instance, the constraints (10a) could be handled by introducing a corresponding number of Lagrange multipliers, which would essentially correspond to $\boldsymbol{f}_b^+$, while implicitly enforcing $\boldsymbol{f}_b^-$ to zero. To appreciate the implications of this particular choice on the finite element solution, a simple 100 by 150 μm rectangular plate subjected to plane strain conditions is analyzed. The plate has Young's modulus and Poisson's ratio equal to 205 GPa and 0.29 respectively. Moreover, a central circular graphite inclusion of radius 40 μm is present, with the graphene planes having the elastic properties listed in Table 2 and oriented at 45°. The solution to the finite element system of equations is calculated in Matlab, which offers a simpler interface to set up customized linear constraints. This can be achieved by generating the full stiffness matrix in ABAQUS first, by means of the MATRIX GENERATE command, and then exporting it to Matlab. Fig. 9 shows the deformed configuration of the plate subjected to an average shear strain of 0.1%, at a scaling factor of 50. On the same figure, the deformed configuration obtained by applying both constraints (10a and b) at the same time is plotted. It is seen that a large difference exists between the two solutions, despite both satisfy the displacement part of the periodic boundary conditions.

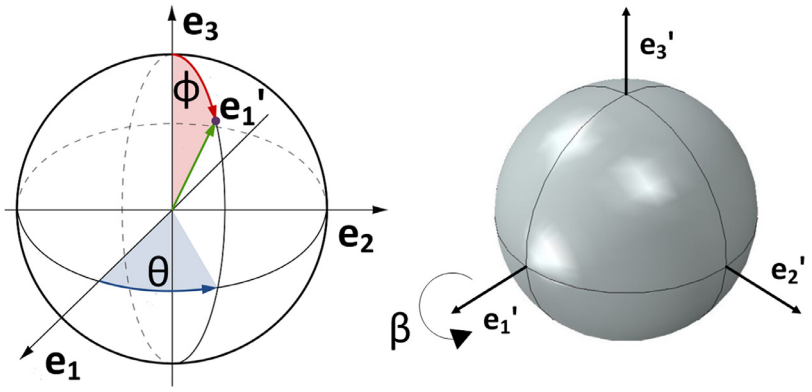

Fig. 10. Orientation of nodule model "Type8" with respect to the unit cell axes expressed in terms of the three angles θ, ϕ, β.

5.3. Effect of nodule orientation relative to the unit cell axes

After having verified the correct implementation of the periodic boundary conditions and before comparing numerical predictions to experiments, the focus is turned to the role played by the nodule orientation relative to the unit cell axes. In principle, this aspect should be discussed for all different models introduced in Section 2.2 except for "TypeInf", as conditions of spherical symmetry no longer exist due to nodule partitioning into a finite number of conical sectors. However, as the aim here is to find out whether or not the relative orientation has a significant impact on the effective elastic properties, the presentation can be restricted to "Type8" only, which will be shown later to be characterized by the largest value of the anisotropy index.

With reference to Fig. 10, the nodule orientation may be specified in terms of the three angles θ, ϕ, β. The first two give the direction of the nodule local Cartesian axis $\boldsymbol{e}_1'$ with respect to the unit cell axes $\boldsymbol{e}_1$, $\boldsymbol{e}_2$, $\boldsymbol{e}_3$, whereas the last one specifies the nodule rotation about $\boldsymbol{e}_1'$. When all θ, ϕ, β are set to zero the unit cell axes coincide with those defined locally on the nodule, i.e. $\boldsymbol{e}_1' = \boldsymbol{e}_1$, $\boldsymbol{e}_2' = \boldsymbol{e}_2$ and $\boldsymbol{e}_3' = \boldsymbol{e}_3$.

Due to symmetry considerations, the dependence of the effective isotropic elastic constants on the nodule relative orientation can be analyzed limiting θ and ϕ to the range$[0, \pi/2]$. In order to represent the results graphically, it is also useful to introduce the β-average of a generic quantity $q(\theta, \phi, \beta)$ as:

$$q_\beta(\theta, \phi) = \frac{1}{2\pi} \int_0^{2\pi} q(\theta, \phi, \beta) d\beta \tag{15}$$

and the β-range as:

$$\begin{aligned} \Delta q_\beta(\theta, \phi) = &\max\{q(\theta, \phi, \beta) |\ \beta \in [0, 2\pi]\} \\ &- \min\{q(\theta, \phi, \beta) |\ \beta \in [0, 2\pi]\} \end{aligned} \tag{16}$$

The β-average of the effective isotropic Young's modulus $\bar{E}_\beta(\theta, \phi)$ and the corresponding β-range $\Delta\bar{E}_\beta(\theta, \phi)$ for nodule model "Type8" are plotted in Fig. 11(a and b) respectively. It is seen that by changing the nodule orientation with respect to the unit cell axes only variations within less than 1 GPa are recorded. Changes in the effective Poisson's ratio are even less pronounced and bounded by the interval 0.278–0.279. Therefore, it is concluded that nodule orientation is perfectly negligible within the context of the present work and henceforth, zero value of the θ, ϕ, β angles is always assumed.

5.4. Effective isotropic elastic constants for SGI

Numerical calculations of the elastic properties of the 3D unit cell reported in Fig. 5 have been carried out using trilinear hexahedral elements and approximately 2000 boundary nodes. Local mesh refinement has been performed in both the nodule and the matrix nearby the material discontinuity interface, in order to capture strong gradients arising in this region. Results in terms of all four effective isotropic elastic constants and anisotropy index are reported in Table 4. Besides the nodule models with increasing number of sectors introduced previously, the case of graphite replaced by a spherical void is also considered; in addition, reference elastic values for GJS-400-15 ductile iron are given to allow comparison with experimental findings.

In general, it is immediately clear that all models largely overestimate the overall material stiffness. If Young's modulus and Poisson's ratio are chosen to describe the elastic properties of SGI, the latter quantity is in quite good agreement with experimental measurements, but the former is constantly 20 to 30 GPa above the admissible range, no matter the number of sectors considered. The discrepancy with the reference values is so large that even the voided material model provides a better approximation as regards macroscopic elastic properties of SGI at room temperature, despite being inadmissible from a physical point of view because in contrast with some experimental observations, as mentioned in the introduction.

Fig. 12(a and b) offer a more direct interpretation of the dependence of the isotropic constants on the number of partitions the nodule is divided into. The higher this number, the greater Poisson's ratio and the lower Young's modulus, despite a sort of plateau seems to be present for this last quantity when the number of sectors is increased beyond 32. Conversely, the effective shear modulus steadily decreases, indicating a progressive reduction in shear resistance of the unit cell with increasing number of partitions. The only non-monotonic behavior is shown by the bulk modulus, which achieves a minimum value in correspondence of the "Type48" nodule model.

From a physical perspective, the reason for the very high stiffness exhibited by the unit cell is the particular spatial arrangement of the graphite platelets in the nodule. Fig. 13 shows stress contours taken over the x-y mid-section of the unit cell for an externally imposed average volumetric strain of $\bar{\varepsilon}_{11} = 0.05\%$, with the other average strain components set to zero. It can be noticed that, independently of the number of conical sectors, the normal stress component perpendicular to the graphite platelets, reported in Fig. 13(c and d), is more than five times smaller than the maximum principal stress, visible in Fig. 13(e and f), which lies in the plane of the graphenes. In addition, only the more external layers of the nodule are mechanically loaded, whereas the central region is almost stress-free. This suggests that the nodule behaves similar to a rigid shell: the very high hoop stiffness, which is more than 30 times larger than the radial one according to Table 2, prevents any stress transmission from the surface to the bulk of the graphite particle. Not surprisingly, this phenomenon is more pronounced in

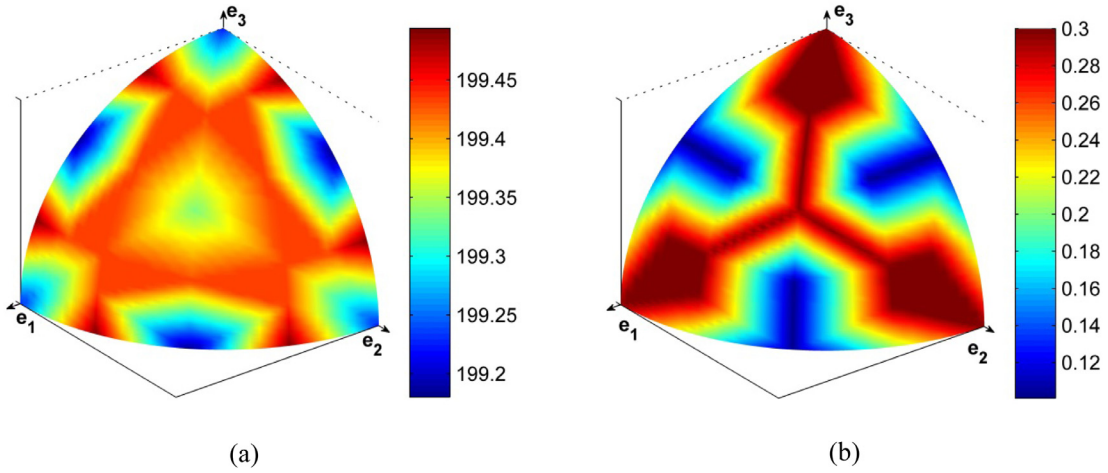

Fig. 11. Calculated effective Young's modulus as a function of the nodule orientation with respect to the unit cell axes, for "Type8" model. (a) Average value for a given $\boldsymbol{e}_1$' direction. (b) Variation range due to nodule rotation around local $\boldsymbol{e}_1$' axis. Values are in GPa.

Table 4
Effective isotropic elastic constants and anisotropy index calculated for different nodule models. Values for the case of graphite replaced by a spherical void are also given, as well as the reference experimental values for GJS-400-15 ductile iron.

Nodule model	Bulk modulus (GPa)	Shear modulus (GPa)	Young's modulus (GPa)	Poisson's ratio	Anisotropy index (%)
Void	122.9	63.7	163.1	0.279	1.32
Type6	150.1	79.1	201.8	0.276	3.12
Type8	149.3	77.8	198.9	0.278	3.31
Type32	148.7	75.9	194.7	0.282	0.05
Type48	148.6	75.8	194.3	0.282	0.31
Type80	148.8	75.7	194.1	0.283	0.09
TypeInf	150.8	75.6	194.3	0.285	0.04
Exp. GJS–400–15	126.5 ÷ 128.7	65.2 ÷ 66.4	167.0 ÷ 170.0	0.280	–

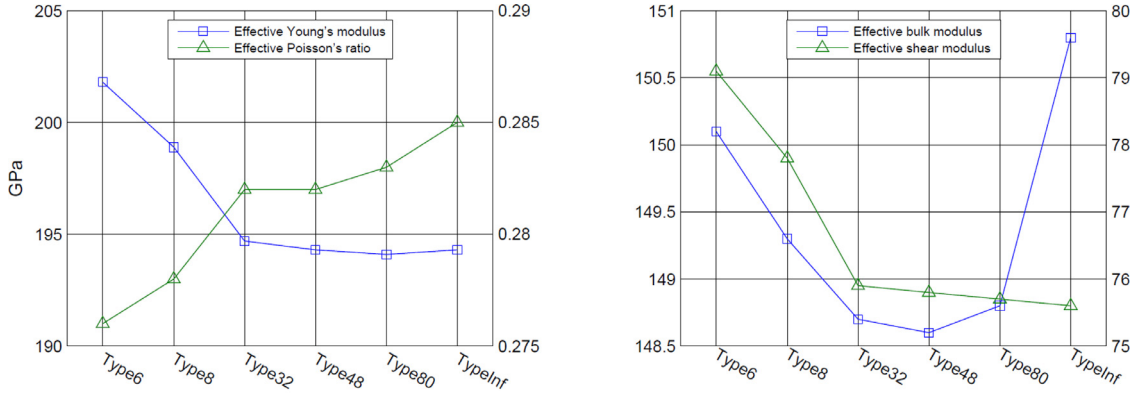

Fig. 12. Effective elastic constants for nodule models with increasing number of conical sectors, expressed as (a) Young's modulus and Poisson's ratio, (b) bulk modulus and shear modulus.

"TypeInf" rather than in "Type8', the former being characterized by a higher level of spherical symmetry.

Fig. 13(e and f) also indicate that unrealistic stress values, in the order of several hundred MPa, are generated in the nodule external layers for effective strain levels which are not sufficient to promote yielding of the material at the macroscale. Indeed, if the experimental isotropic constants for SGI are used to calculate the effective stress tensor for the loading configuration under examination, an equivalent von Mises stress of only 75 MPa is obtained, which is approximately 1/3 the macroscopic yield strength. This suggests that localized inelastic deformation either in the matrix or in the graphite probably occurs while ductile iron is still "macroscopically" in the elastic regime. The incapability of the present model to take into account the inelastic behavior of the SGI constituents might explain its excessively high effective stiffness compared to the measured one.

Concerning analogies with previous works in the field, the only partial comparison can be done with the analytical findings of (Dryden and Purdy, 1989). Considering a graphite platelets arrangement equivalent to the "TypeInf" model discussed in the present analysis, the previous authors came up with the following simple mathematical expressions for the dependence of the effective bulk and shear moduli on the graphite volume fraction c_g:.

$$\begin{aligned} \bar{k} &= k_m(1 - 0.43c_g) \\ \bar{\mu} &= \mu_m(1 - 0.83c_g) \end{aligned} \tag{17}$$

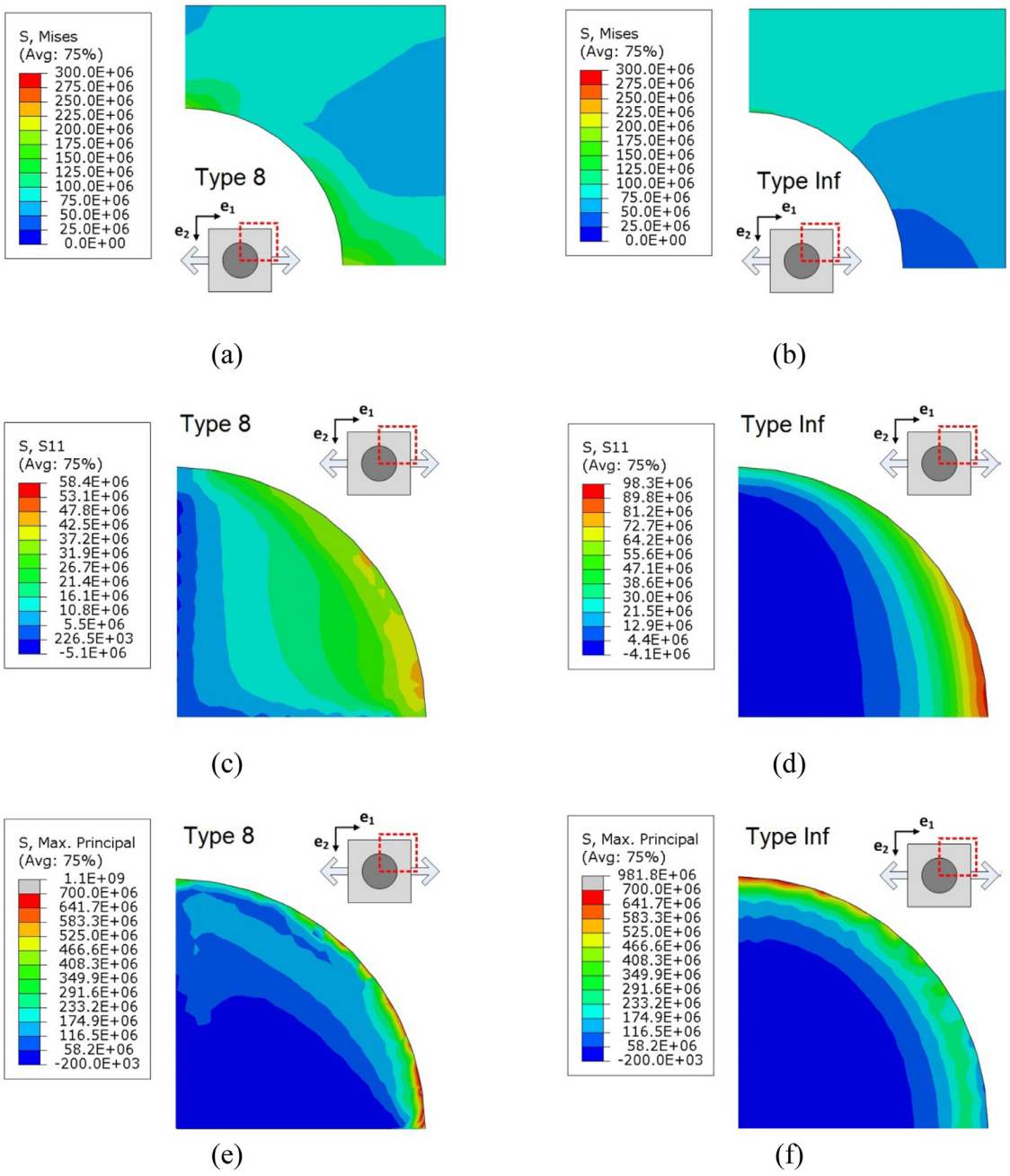

Fig. 13. Stress contours over the x-y mid-section of the periodic unit cell, for an imposed average volumetric strain of $\bar{\varepsilon}_{11} = 0.05\%$, with the other $\bar{\varepsilon}_{ij}$ components set to zero. (a)(b) Von Mises stress in the matrix. (c)(d) Normal stress component perpendicular to the graphite platelets. (e)(f) Maximum principal stress recorded in the graphite.

where k_m and μ_m denote the bulk and shear moduli for the matrix. By inserting in the last formulas the values reported in Section 2.3 for the specific SGI grade under consideration, effective elastic properties corresponding to a Young's modulus of 186.8 GPa and to a Poisson's ratio of 0.299 are obtained. They are respectively 3.9% lower and 4.9% greater than what predicted with the present unit cell approach. The difference might be due to the "dilute" assumption made by (Dryden and Purdy, 1989), which, as stated by the same authors, is inaccurate if the graphite phase occupies a volume fraction greater than or equal to 10%.

Before concluding this section, a few remarks regarding the intrinsic anisotropy degree exhibited by the unit cell have to be made.

Table 4 shows that the calculated anisotropy index spans the range 0.04% to 3.31%, with the lower limit corresponding to the "TypeInf" nodule model and the upper one to the "Type8" model. These low anisotropy levels fully justify the initial assumption of modeling the macroscopically isotropic SGI microstructure with a simplified 3D periodic unit cell model.

In order to get more insight into the meaning of the actual anisotropy index values, it is useful to look at the dependence of the apparent effective Young's modulus on the θ, ϕ angles, which is graphically represented in Fig. 14. The apparent Young's modulus is here defined as the ratio between the normal stress applied in a certain direction (the other stress components being zero) and the corresponding induced longitudinal strain. It is seen that with an anisotropy index of 0.04% ("TypeInf" model) only variations within 0.4 GPa are observed. On the other hand, when the anisotropy is increased to 3.31% ("Type8" model), a difference of almost 20 GPa between the most stiff and the most compliant

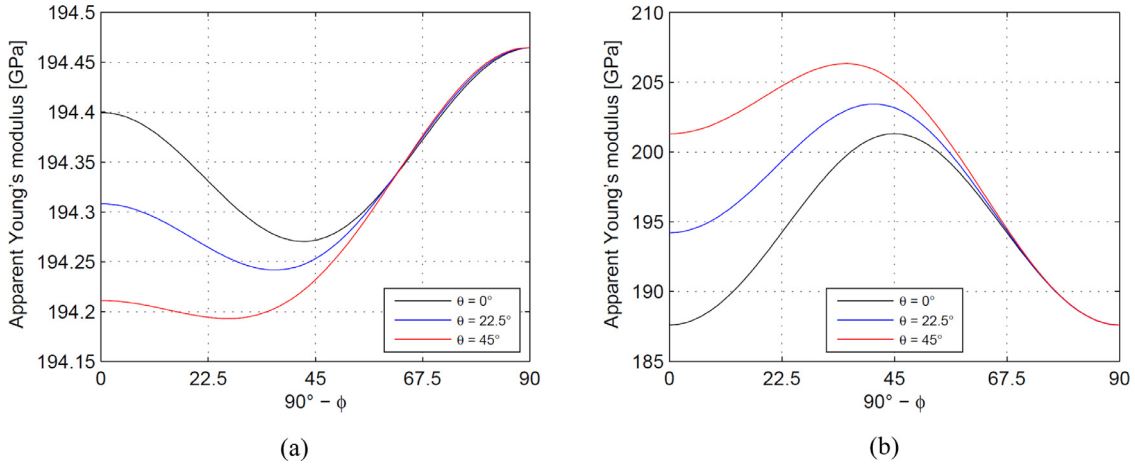

Fig. 14. Apparent Young's modulus as a function of the ϕ angle, for selected values of the θ angle. (a) Nodule model "TypeInf" and (b) nodule model "Type8".

direction is recorded. For the sake of comparison, it is worth remarking here that a common ferrite single crystal shows a variation from 130 to 280 GPa. The considerably larger spatial variation observed for the "Type8" model is associated with its lower degree of spherical symmetry compared to the "TypeInf" model. Indeed, in the former case the nodule contributes to the overall unit cell stiffness in different amount according to the particular spatial direction considered. Conversely, when the number of conical sectors grows and eventually tends to infinite, the nodule mechanical response becomes less and less dependent on the choice of the θ and ϕ angles.

5.5. Weak nodule-matrix interface

According to a number of experimental observations (Dong et al., 1997; Cooper et al., 2002 and Di Cocco et al., 2014), debonding between the nodules and the matrix is often observed during tensile testing of SGI, indicating a weak bonding between the two phases. In order to investigate the influence of this aspect on the elastic properties of the unit cell, a frictionless contact interface is introduced between the graphite and the surrounding ferrite. However, as contact opening could add a substantial amount of nonlinearity to the model, the nodule is initially "pre-compressed" by simulating part of the cooling process occurring during manufacturing. The reason behind this is that, as pointed out by (Bonora and Ruggiero, 2005), the average thermal expansion coefficient of graphite is much lower compared to ferrite, meaning that the nodules are subjected to a sort of hydrostatic compression during solid state cooling. If the arising residual stresses are sufficient to keep the interface closed during subsequent loading, the linear structure of relation (3) between volume averages of the applied strains and volume averages of the induced stresses can be retained. Moreover, linearity of the equations governing thermo-elasticity implies that the calculated effective stiffness tensor (4) is independent of the residual stress magnitude. As a consequence, the choice of the initial cooling temperature is somehow arbitrary, provided that it suffices to avoid any contact opening.

The variation in the effective Young's modulus and Poisson's ratio calculated using the frictionless contact condition in place of the perfect bonding assumption is shown in Fig. 15. For the sake of clarity, it is worth mentioning that the employed values for the thermal expansion coefficient were $12x10^{-6}\,°C^{-1}$ for the ferrite (Touloukian and Lafayette, 1975) and $25x10^{-6}\,°C^{-1}$ and $-1x10^{-6}\,°C^{-1}$ for the graphite platelets along the 3- and 1-, 2-direction respectively (Steward et al., 1960). A generalized decrease in Young's modulus and an increase in Poisson's ratio compared to the data presented in Table 4 may be observed, except for the "TypeInf" model, which exhibits the opposite behavior. Nevertheless, the recorded variations in the elastic properties are by far quite limited, meaning that a weak nodule-matrix interface is not enough to explain the existing discrepancy with the experimental results.

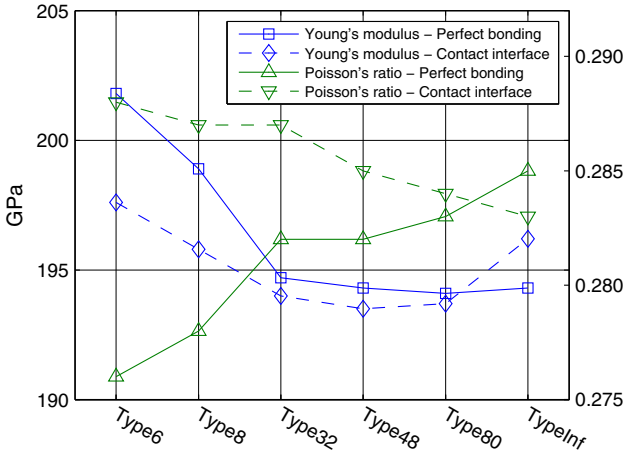

Fig. 15. Variation in the effective elastic constants due to introduction of a frictionless contact interface between the nodule and the matrix.

6. Conclusions

In the present work, a micromechanical approach to model the intrinsic elastic anisotropy of the graphite particles in ductile iron has been described. The constitutive behavior is directly derived from the nodule characteristic internal structure, composed of graphite platelets arranged into conical sectors. In this way, the large uncertainty traditionally associated with local mechanical measurements is eliminated.

In order to validate the proposed anisotropic description, a unit cell model has been introduced to simulate the overall SGI elastic behavior. An explicit procedure to enforce both periodic displacement and periodic traction boundary conditions in ABAQUS has been presented, and the importance of fulfilling the traction continuity conditions at the unit cell boundaries has been discussed.

The effective isotropic elastic stiffness of the unit cell turns out to be 20–30 GPa larger compared to reference experimental values for SGI, no matter the number of sectors the nodule is divided into. Introduction of a weak interface between the graphite

particle and the ferritic matrix does not change the results significantly. The mismatch between numerical predictions and experiments is probably due to the incapability of the present model to account for localized inelastic deformation of the SGI constituents.

References

47th Census of World Casting Production, 2013., MODERN CASTING - A publication of the American Foundry Society.

Andriollo, T., Hattel, J., 2016. On the isotropic elastic constants of graphite nodules in ductile cast iron: analytical and numerical micromechanical investigations. Mech. Mater. 96, 138–150. doi:10.1016/j.mechmat.2016.02.007.

Andriollo, T., Thorborg, J., Hattel, J., 2015. The influence of the graphite mechanical properties on the constitutive response of a ferritic ductile cast iron – a micromechanical FE analysis. In: Proceedings of the XIII International Conference on Computational Plasticity, Fundamentals and Applications, pp. 632–641.

Andriollo, T., Thorborg, J., Tiedje, N., Hattel, J., 2015. Modeling of damage in ductile cast iron - the effect of including plasticity in the graphite nodules. 14th International Conference on Modeling of Casting. Welding and Advanced Solidification Processes (MCWASP).

Boccaccini, A.R., 1997. Young's modulus of cast-iron as a function of volume content, shape and orientation of graphite inclusions. Zeitschrift Fuer Met. Res. Adv. Tech. 88, 23–26.

Bonora, N., Ruggiero, A., 2005. Micromechanical modeling of ductile cast iron incorporating damage. Part I: ferritic ductile cast iron. Int. J. Solids Struct. 42, 1401–1424. doi:10.1016/j.ijsolstr.2004.07.025.

Brocks, W., Hao, S., Steglich, D., 1996. Micromechanical modelling of the damage and toughness behaviour of nodular cast iron materials. J. Phys. IV 6, 43–52.

Carazo, F.D., Giusti, S.M., Boccardo, A.D., Godoy, L.A., 2014. Effective properties of nodular cast-iron: a multi-scale computational approach. Comput. Mater. Sci. 82, 378–390. doi:10.1016/j.commatsci.2013.09.044.

Collini, L., Nicoletto, G., 2005. Determination of the relationship between microstructure and constitutive behaviour of nodular cast iron with a unit cell model. J. Strain Anal. Eng. Des. 40, 107–116. doi:10.1243/030932405X7692.

Cooper, C.A., Elliott, R., Young, R.J., 2002. Investigation of elastic property relationships for flake and spheroidal cast irons using Raman spectroscopy. Acta Mater. 50, 4037–4046. doi:10.1016/S1359-6454(02)00202-1.

Dassault Systèmes Simulia Corp., 2013a. Abaqus 6.13, Abaqus Analysis User's Guide section 35.2.1.

Dassault Systèmes Simulia Corp., 2013b. Abaqus 6.13, Abaqus Analysis User's Guide section 10.3.1.

Di Cocco, V., Iacoviello, F., Rossi, A., Iacoviello, D., 2014. Macro and microscopical approach to the damaging micromechanisms analysis in a ferritic ductile cast iron. Theor. Appl. Fract. Mech. 69, 26–33. doi:10.1016/j.tafmec.2013.11.003.

Dong, M.J., Tie, B., Béranger, A.S., Prioul, C., François, D., 1997. Damage effect on the fracture toughness of nodular cast iron. Adv. Mater. Res. 4-5, 181–188. doi:10.4028/www.scientific.net/AMR.4-5.181.

Drago, A., Pindera, M., 2007. Micro-macromechanical analysis of heterogeneous materials: macroscopically homogeneous vs periodic microstructures. Compos. Sci. Technol. 67, 1243–1263. doi:10.1016/j.compscitech.2006.02.031.

Dryden, J.R., Purdy, G.R., 1989. The effect of graphite on the mechanical properties of cast irons. Acta Metall. 37, 1999–2006. doi:10.1016/0001-6160(89)90084-9.

Ductile Iron Society. Ductile Iron data for design engineers [WWW Document] URL (accessed 10.10.15).

Era, H., Kishitake, K., Nagai, K., Zhang, Z.Z., 1992. Elastic modulus and continuous yielding behaviour of ferritic spheroidal graphite cast iron. Mater. Sci. Technol. 8, 257–261.

Fernandino, D.O., Cisilino, A.P., Boeri, R.E., 2015. Determination of effective elastic properties of ferritic ductile cast iron by computational homogenization, micrographs and microindentation tests. Mech. Mater. 83, 110–121. doi:10.1016/j.mechmat.2015.01.002.

Gaudig, W., Mellert, R., Weber, U., Schmauder, S., 2003. Self-consistent one-particle 3D unit cell model for simulation of the effect of graphite aspect ratio on Young's modulus of cast-iron. Comput. Mater. Sci. 28, 654–662. doi:10.1016/j.commatsci.2003.08.021.

Geers, M.G.D., Kouznetsova, V.G., Brekelmans, W.A.M., 2010. Multi-scale computational homogenization: trends and challenges. J. Comput. Appl. Math. 234, 2175–2182. doi:10.1016/j.cam.2009.08.077.

Grimvall, G., 1997. Cast iron as a composite: conductivities and elastic properties. Adv. Mater. Res. 4-5, 31–46. doi:10.4028/www.scientific.net/AMR.4-5.31.

Harding, J.W., Sneddon, I.N., 1945. The elastic stresses produced by the indentation of the plane surface of a semi-infinite elastic solid by a rigid punch. Proc. Camb. Philol. Soc. 41, 16–26.

Hervas, I., Bettaieb, M.B., Hug, E., 2013. Damage mechanisms evolution of ductile cast irons under thermomechanical loadings. Int. J. Mater. Prod. Technol. 47, 23. doi:10.1504/IJMPT.2013.058963.

Hütter, G., Zybell, L., Kuna, M., 2015. Micromechanisms of fracture in nodular cast iron: From experimental findings towards modeling strategies – A review. Eng. Fract. Mech. 144, 118–141. doi:10.1016/j.engfracmech.2015.06.042.

Itskov, M., 2007. Tensor Algebra and Tensor Analysis for Engineers. Springer Berlin Heidelberg, Berlin, Heidelberg doi:10.1007/978-3-540-36047-6.

Kuna, M., Sun, D.Z., 1996. Three-dimensional cell model analyses of void growth in ductile materials. Int. J. Fract. 81, 235–258. doi:10.1007/BF00039573.

Labrecque, C., Gagne, M., 1998. Review ductile iron: 50 years of continuous development. Can. Metall. Q. 37, 343–378.

Miao, B., Fang, K., Bian, W., Liu, G., 1990. On the microstructure of graphite spherulites in cast irons by TEM and HREM. Acta Metall. Mater. 38, 2167–2174. doi:10.1016/0956-7151(90)90084-T.

Nicoletto, G., Collini, L., Konečná, R., Riva, E., 2006. Analysis of nodular cast iron microstructures for micromechanical model development. Strain 42, 89–96. doi:10.1111/j.1475-1305.2006.00259.x.

Oliver, W.C., Pharr, G.M., 1992. An improved technique for determining hardness and elastic modulus using load and displacement sensing indentation experiments. J. Mater. Res. 7, 1564–1580.

Pundale, S.H., Rogers, R.J., Nadkarni, G.R., 1998. Finite element modeling of elastic modulus in ductile irons: effect of graphite morphology. Trans. Am. Foundrymen's Soc. 106, 99–105.

Qi, L., Tian, W., Zhou, J., 2015. Numerical evaluation of effective elastic properties of composites reinforced by spatially randomly distributed short fibers with certain aspect ratio. Compos. Struct. 131, 843–851. doi:10.1016/j.compstruct.2015.06.045.

Rabold, F., Kuna, M., 2005. Cell model simulation of void growth in nodular cast iron under cyclic loading. Comput. Mater. Sci. 32, 489–497. doi:10.1016/j.commatsci.2004.09.016.

Savini, G., Dappe, Y.J., Öberg, S., Charlier, J.C., Katsnelson, M.I., Fasolino, A., 2011. Bending modes, elastic constants and mechanical stability of graphitic systems. Carbon 49, 62–69. doi:10.1016/j.carbon.2010.08.042, N.Y.

Shirani, M., Härkegård, G., 2011. Casting defects and fatigue behaviour of ductile cast iron for wind turbine components: a comprehensive study. Materwiss. Werkstsch. 42, 1059–1074. doi:10.1002/mawe.201100911.

Sjogren, T., 2007. Influences of the Graphite Phase on Elastic and Plastic Deformation Behaviour of Cast Irons PhD Thesis. Linköping University.

Sjögren, T., Svensson, I.L., 2004. Modelling the effect of graphite morphology on the modulus of elasticity in cast irons. Int. J. Cast Met. Res. 17, 271–279. doi:10.1179/136404604225022694.

Speich, G.R., Schwoeble, A.J., Kapadia, B.M., 1980. Elastic moduli of gray and nodular cast iron. Trans. ASME. J. Appl. Mech. 47, 821–826.

Steglich, D., Brocks, W., 1998. Micromechanical modeling of damage and fracture of ductile materials. Fatigue Fract. Eng. Mater. Struct. 21, 1175–1188. doi:10.1046/j.1460-2695.1998.00078.x.

Steward, E.G., Cook, B.P., Kellet, E.A., 1960. Dependence on temperature of the interlayer spacing in carbons of different graphitic perfection. Nature 187, 1015–1016.

Theuwissen, K., Lacaze, J., Véron, M., Laffont, L., 2014. Nano-scale orientation mapping of graphite in cast irons. Mater. Charact. 95, 187–191. doi:10.1016/j.matchar.2014.06.021.

Theuwissen, K., Lafont, M.-C., Laffont, L., Viguier, B., Lacaze, J., 2012. Microstructural characterization of graphite spheroids in ductile iron. Trans. Indian Inst. Met. 65, 627–631. doi:10.1007/s12666-012-0162-5.

Tiedje, N.S., 2010. Solidification, processing and properties of ductile cast iron. Mater. Sci. Technol. 26, 505–514. doi:10.1179/026708310X12668415533649.

Touloukian, Y.S., Lafayette, I., 1975. Thermophysical properties of matter. The TPRC data series. A comprehensive compilation of data by the Thermophysical Properties Research Center (TPRC). 12: thermal expansion. Metallic Elements and Alloys. IFI/Plenum. Purdue university.

Tromans, D., 2011. Elastic anisotropy of hcp metal crystals and polycrystals. Int. J. Res. Rev. Appl. Sci. 6.

Xia, Z., Zhou, C., Yong, Q., Wang, X., 2006. On selection of repeated unit cell model and application of unified periodic boundary conditions in micro-mechanical analysis of composites. Int. J. Solids Struct. 43, 266–278. doi:10.1016/j.ijsolstr.2005.03.055.

Zhang, K.S., Bai, J.B., François, D., 1999. Ductile fracture of materials with high void volume fraction. Int. J. Solids Struct. 36, 3407–3425. doi:10.1016/S0020-7683(98)00157-7.

Tito Andriollo is a third year Ph.D. student at the Technical University of Denmark. He holds a master degree in Materials Engineering from the University of Padova and a master degree in Manufacturing Engineering from the Technical University of Denmark. He is currently working on modeling the effects of the manufacturing process on the final mechanical properties of ductile iron components.

Jesper Thorborg studied at the Technical University of Denmark, where here got a master degree in mechanical engineering. During his subsequent Ph.D. project he worked in the field of solid mechanics and constitutive modeling of high temperature processes. He joined the development group at MAGMA GmbH in 2004 and today he is working as a developer on the MAGMAstress module.

Jesper H. Hattel, born in Copenhagen, Denmark 1965, obtained his M.*Sc*. in structural engineering in 1989 and his Ph.D. in mechanical engineering in 1993 both from the Technical University of Denmark (DTU). He currently holds a full professorship in modeling of manufacturing processes at the Department of Mechanical Engineering, DTU. His research interests are modeling of processes like casting, joining, composites manufacturing and additive manufacturing in materials such as metals and polymers. Applications range from microelectronics over automotive industry to large structures like wind turbines.

Appendix D
PAPER IV

IOP Publishing Modelling and Simulation in Materials Science and Engineering

Modelling Simul. Mater. Sci. Eng. **24** (2016) 055012 (19pp) doi:10.1088/0965-0393/24/5/055012

A micro-mechanical analysis of thermo-elastic properties and local residual stresses in ductile iron based on a new anisotropic model for the graphite nodules

Tito Andriollo[1,3], Jesper Thorborg[1,2], Niels Tiedje[1] and Jesper Hattel[1]

[1] Department of Mechanical Engineering, Technical University of Denmark, DK-2800 Kgs. Lyngby, Denmark
[2] MAGMA GmbH, D-52072 Aachen, Germany

E-mail: titoan@mek.dtu.dk

Received 2 March 2016, revised 27 April 2016
Accepted for publication 9 May 2016
Published 6 June 2016

Abstract

In this paper, the thermo-elastic behavior of the graphite nodules contained in ductile iron is derived on the basis of recent transmission electron microscopy investigations of their real internal structure. The proposed model is initially validated by performing a finite element homogenization analysis to verify its consistency with the room-temperature elastic properties of ductile iron measured at the macro scale. Subsequently, it is used to investigate the formation of local residual stresses around the graphite particles by simulating the manufacturing process of a typical ferritic ductile iron grade, and the results are compared with preliminary measurements using synchrotron x-rays. Finally, the obtained accurate description of the stress & strain field at the micro scale is used to shed light on common failure modes reported for the nodules and on some peculiar properties observed in ductile iron at both micro and macro scale.

Keywords: micromechanics, synchrotron x-ray diffraction, ductile iron, anisotropic elasticity, residual stresses, graphite nodules

(Some figures may appear in colour only in the online journal)

[3] Technical University of Denmark, Produktionstorvet, Building 425, room 125, 2800 Kgs. Lyngby, Denmark.

1. Introduction

Ductile iron represents today a modern engineering material offering a unique combination of castability, high ductility and strength at lower prices compared to traditional low carbon steels [1, 2]. Its high technological importance is confirmed by recent market growth analyses [3], indicating that as many as 25% of the castings currently produced worldwide are made of ductile iron. Typical applications include small and medium sized heavily loaded parts with high demands for consistent quality for the automotive sector and very large industrial components with extreme demands for mechanical properties, particularly fatigue strength and fracture toughness [4].

From a metallurgical standpoint, ductile iron is a ternary Fe–C–Si alloy with 'composite' microstructure [5, 6], consisting of graphite nodules embedded in a metallic matrix which, in most engineering applications, may be either ferritic, pearlitic or a mixture of the two. The very high degree of nodularity of the secondary phase particles has justified the alternative designation of spheroidal graphite iron (SGI), to emphasize the difference with other members of the cast iron family where the graphite is present in more irregular forms.

Despite a large number of investigations carried out in the past decades, a complete description of the mechanical behavior of the individual SGI constituents at the micro scale is still missing in the published literature [7]. This represents a major obstacle towards obtaining a thorough understanding of those properties which are intimately related to the local thermo-mechanical interactions arising among the different microstructural elements. For instance, fatigue crack propagation in the ferritic matrix has been experimentally shown to be strongly affected by the presence of the graphite particles [8], and cannot be explained on the basis of classical theoretical models which consider the material as homogeneous [9].

As discussed in [10], the lack of reliable constitutive data is more critical for the nodules rather than for the matrix, probably because their reduced size has always challenged mechanical characterization based on direct techniques. A detailed literature survey has shown that all micromechanical models for ductile iron proposed so far may be roughly listed under three different categories, according to the assumption made for the nodules' mechanical properties.

A first possibility is to simply consider the graphite particles as voids, indeed reducing SGI to a metallic material with high degree of porosity. Several researchers have followed this approach to investigate damage and ductile fracture occurring during uniaxial tensile testing, e.g. [9, 11, 12]. The main justification for completely neglecting the nodules in the analysis is the early debonding between the matrix and such graphitic morphologies observed already at early deformation stages on the lateral surface of a tensile test specimen. Needless to say, this assumption is not justifiable under different loading conditions, as experimental evidence exists for the capability of the nodules to oppose compressive stresses [13].

A second option, adopted by the major part of the authors, is to assume an isotropic linear elastic description of the nodules. The main problem in this case is the choice of suitable values for the elastic constants, especially Young's modulus, which is usually taken in the range 4–25 GPa [6]. These values are macroscopically consistent in the sense that they allow recovering the global elastic properties of ductile iron according to common micromechanical homogenization procedures [14]. Furthermore, they are also in fairly good agreement with nano-indentation tests [15, 16] performed according to the Oliver–Pharr method [17]. Nevertheless, the validity of such measurements is quite disputable as graphite is highly anisotropic at the nanoscale, meaning that the concept of nano-indentation based Young's modulus loses its significance. In addition, it has been argued by Bonora and Ruggiero [18] that the sharp indenter usually employed could simply separate the graphite layers without creating any elastic deformation at all. In contrast, the latter authors have proposed much higher values,

in the order of 300–375 GPa, on the basis of an inverse analysis in which the influence of the manufacturing process was taken into account for one of the very first times in literature. On the other hand, it was subsequently shown that values greater than approximately 100 GPa are inadmissible, as the elastic properties of common grades of ductile iron cannot be retrieved due to excessive plastification of the matrix during the initial cooling stage [19, 20]. Whatever the 'correct' Young's modulus, the main drawback of the isotropy assumption is that it cannot be justified using elastic bound theory analysis, assuming a statistically homogeneous distribution of the graphite platelets throughout the individual nodules [10]. This means that even if the macroscopic properties may be retrieved under particular loading conditions, there is no guarantee that the predicted stress and strain fields be accurate at the micro scale.

Finally, a third group of authors have considered an elastic anisotropic description of the nodules [21, 22], in an attempt to take their internal structure into account. However, the latter one was reproduced with a low fidelity level, due to the scarce experimental knowledge available at that time and the intrinsic limitations of the analytical approach adopted. As a result, the macroscopic ductile iron stiffness turned out to be over predicted.

In conclusion, a reliable theoretical model for predicting the graphite particles' mechanical behavior does not seem to be currently available. Hence, it is the aim of the present paper to propose a new thermo-elastic anisotropic formulation on the basis of the most recent transmission electron microscopy investigations of the nodules' internal structure, able to provide a realistic description of the stress & strain field existing at the microstructural level. The model is initially validated by performing a homogenization analysis to verify its consistency with the room-temperature elastic behavior of SGI at the macro scale. Subsequently, it is used to investigate the formation of local residual stresses in the ductile iron matrix by simulating the manufacturing process of a typical ferritic SGI grade, and the results are compared with preliminary measurements using synchrotron x-rays [23]. Last but not least, thermomechanical arguments stemming from the analysis are put forth to cast light on common failure modes reported for the nodules and on some peculiar properties observed at both the micro and macro scale.

2. Theory

Figure 1(a) shows the microstructure of a typical grade of ferritic ductile iron, constituted by graphite nodules of high nodularity dispersed in a matrix of Si-rich ferrite. From a chemical perspective, each nodule is made of a small nucleus containing complex oxides and sulfides, which served as nucleation site during solidification [24], and a much thicker outer shell of graphitic nature, which represents the major part of the nodule by volume. As shown by electron microscopy investigations [25], the latter one, which will be the focus of the present analysis, may be schematically subdivided into two parts (figure 1(b)): a bulk region, constituted by oriented graphite crystals arranged into conical sectors radiating from the nodule center to the outer periphery, and a superficial graphite layer, characterized by smaller grains with high misorientation.

It seems to be well established now that the basic building blocks forming the conical sectors in the internal region are graphite platelets consisting of graphene layers piled up with only few crystallographic defects [26, 27]. These structural units have thicknesses in the sub-micrometer range and appear to be elongated along the graphene planes. From a continuum point of view, they can be described on the basis of the hexagonal unit cell reported in figure 1(c) [28], where the c-direction is orthogonal to the graphene layers. Within a sector, the platelets are stacked on each other, with the c-direction constant and oriented approximately

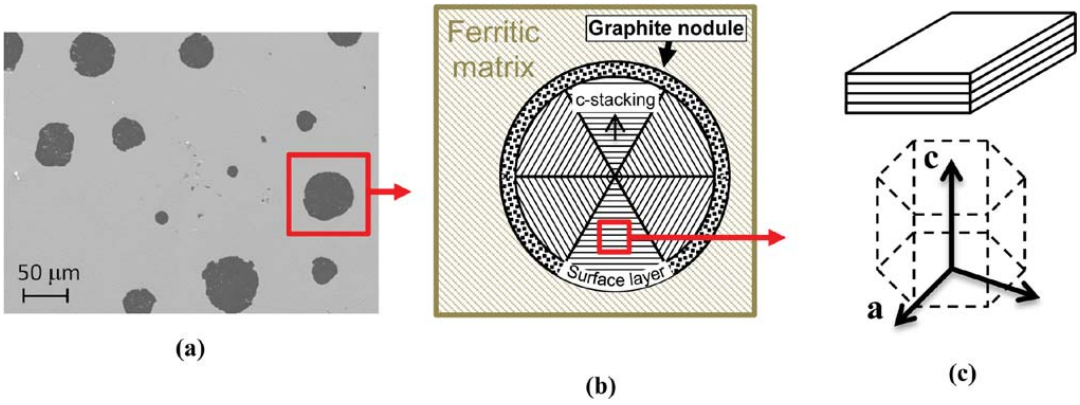

Figure 1. Nodules' structure at different scales. (a) Micrograph of ferritic ductile iron. (b) Schematic of the division of a nodule into an oriented internal bulk region and an external surface layer. (c) Platelets arrangement within a single sector and hexagonal graphite unit cell.

radially. Nevertheless, the stacking is not perfect, and rotations about the *c*-axis occur on an almost regular basis, defining domains of similar orientation [29].

In contrast, only a few investigations have been reported in literature so far regarding the nature of the superficial structure of the nodules. Monchoux *et al* [25] described a microcrystalline, highly disorientated layer approximately 1.5 μm thick over an overall diameter of approximately 30–40 μ, giving a powder-like diffraction diagram; later, the presence of microcrystalline areas at the extreme outer periphery of the nodules was also observed by Theuwissen *et al* [30]. According to the former authors, the existence of this surface layer would be connected to the amount of graphite which precipitates during solid state cooling, due to the reduced carbon solubility in the metallic matrix. This hypothesis is also supported by the extensive work of Di Cocco *et al* [31–33], who, in order to justify some experimental results, speculated on the existence of a gradient of mechanical properties within the nodules connected to the different stages of growth during solidification. On the basis of thermodynamic calculations, they suggested a value for the thickness of the layer associated with solid state cooling of 10% the final nodule radius, which is in very good agreement with Monchoux *et al* findings. However, the reason for the different structure of the graphite crystals in this region compared to the bulk of the nodule remains unclear.

3. Modeling and simulation

3.1. Nodules

On the basis of the experimental studies presented in the previous section, a new anisotropic micromechanical model for the nodules is proposed here, which is physically consistent with their intrinsic structure. Each graphite particle is assimilated to a sphere composed of two concentric regions: an internal core and an external shell with thickness equal to 10% the radius. The former is additionally subdivided into a progressive number of conical sectors by means of sectioning with orthogonal planes passing through the sphere center. In this way, internal regions with 8, 48 and 80 partitions are obtained, as shown in figure 2(a), which qualitatively cover the range of values suggested by the experimental investigations. The sectors are assigned the elastic properties characteristic of rhombohedral graphite reported in table 1, as this was the graphene layer arrangement primarily observed inside the single platelets [27].

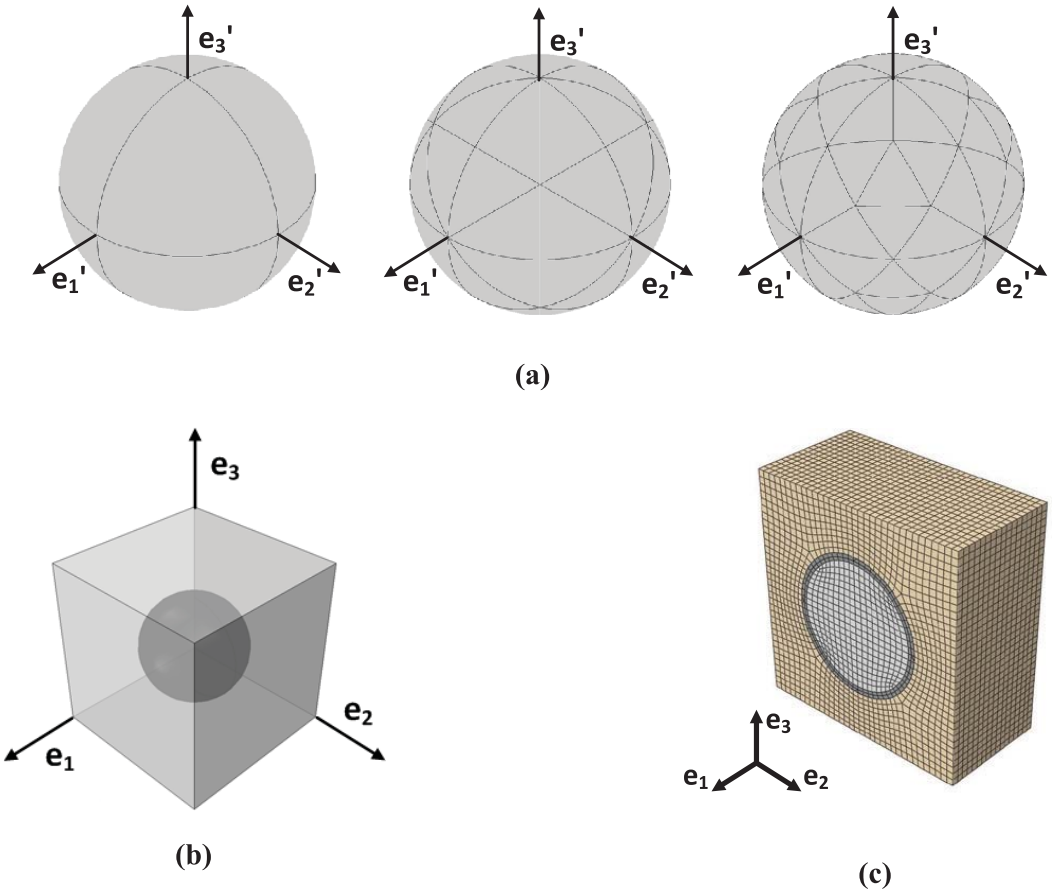

Figure 2. Micromechanical modeling. (a) Subdivision of the internal spherical nodule core region into 8, 48 and 80 sectors respectively. (b) Nodule model embedded in the 3D periodic unit cell representing the SGI microstructure. (c) Middle cross-section of a meshed unit cell in ABAQUS, assuming 8 conical sectors. The different colors of the elements represent the matrix, the nodule surface layer and the nodule core.

Table 1. Elastic constants of rhombohedral graphite [34].

C11	C44	C12	C13	C33
1107	4.4	175	−2.5	29

Note: Entries are in GPa.

Within each conical partition, the *c*-direction is associated with the axis connecting the center of the sphere to the centroid of the related spherical triangle, which is formally defined as the element of the spherical surface identified by a given sector. As a body exhibiting hexagonal symmetry is transversely isotropic with respect to the basal plane (i.e. the graphene layers in this case), the other two principal material directions can be set arbitrarily without affecting the analysis. It has to be remarked that if the *c*-direction is prescribed parallel to the radius pointwise throughout the entire nodule core, a spherically anisotropic description is obtained, which is essentially equivalent to assuming an infinite number of conical sectors. For the external shell instead, which is supposed to be representative of the superficial layer of the nodule, a linear elastic isotropic behavior is assumed. This is motivated by the much smaller size of the crystallites in that region and their high degree of misorientation. As a consequence,

Table 2. Physical properties of commercial grades of fine grain isotropic graphite produced by Asbury Carbons [35].

Type	Fine grain	Super fine grain	Ultra fine grain
Grade	IPG	IPG15	IPG19
Average grain size (micron)	25	8	4
Young's modulus (GPa)	9.7	10.1	10.9
Compressive strength (MPa)	79	106	135

the elastic properties are assumed to be equal to those of commercial grades of fine grain isotropic graphite, reported in table 2. In particular, a variation of Young's modulus between 9.7 and 10.9 GPa is considered, associated with the uncertainty on the real size of the crystallites. Regarding Poisson's ratio, a sharp value of 0.2 is chosen instead, as preliminary investigations showed a limited influence of this quantity on the numerical results.

3.2. Ductile iron microstructure

In order to assess the impact of the proposed model for the graphite nodules on the macroscopic elastic properties and simulate the formation of local residual stresses in the matrix, the microstructure of ductile iron is modeled using a periodic unit cell approach [36]. Therefore, a single nodule embedded in a cubic cell of ferrite is considered, as shown in figure 2(b), whose relative size is adjusted to provide the 11.5% graphite volume fraction typical of GJS-400-15 ferritic SGI, which is taken as reference material throughout the analysis. A study similar to the one presented in [37] has shown a very limited influence of the nodule core orientation on the results (less than 1% on the calculated effective properties). As a consequence, the nodule core main axes $\boldsymbol{e}'_1, \boldsymbol{e}'_2, \boldsymbol{e}'_3$ visible in figure 2(a) can be assumed to be aligned with the principal unit cell axes e_1, e_2, e_3 without significant loss of generality.

Concerning the ferritic matrix, it is assumed to be isotropic, with Young's modulus and Poisson's ratio equal to 205 GPa and 0.29 respectively [38]. The former value is slightly lower than that of a traditional low carbon steel, and it is due to the presence of silicon, which exerts a non-negligible effect at concentrations of a few points percent in mass [39].

An example of unit cell discretization in ABAQUS is given in figure 2(c). It has to be pointed out that more advanced methods are currently available to simulate the macroscopic behavior of materials with composite internal structure, which are primarily based on the concept of representative volume element (RVE) [40]. Nevertheless, the main disadvantage for the case at hand is that a large number of nodules with complex internal geometry should be discretized at the same time to produce a realistic RVE, making any 3D computation cumbersome.

3.3. Manufacturing process

The accurate thermomechanical analysis of all different stages involved in the manufacturing process is simplified by the fact that the particular SGI grade considered is normally used in the as-cast state, without any additional heat treatment.

Figure 3 shows a schematic of the Fe–C–Si phase diagram corresponding to a silicon concentration of 2.4 wt.%. Under the assumption of thermodynamic equilibrium, which suffices for the present purposes, it may be assumed that solidification of a hypereutectic melt proceeds as dictated by the red dashed arrow. The nodules form first; soon after, the eutectic

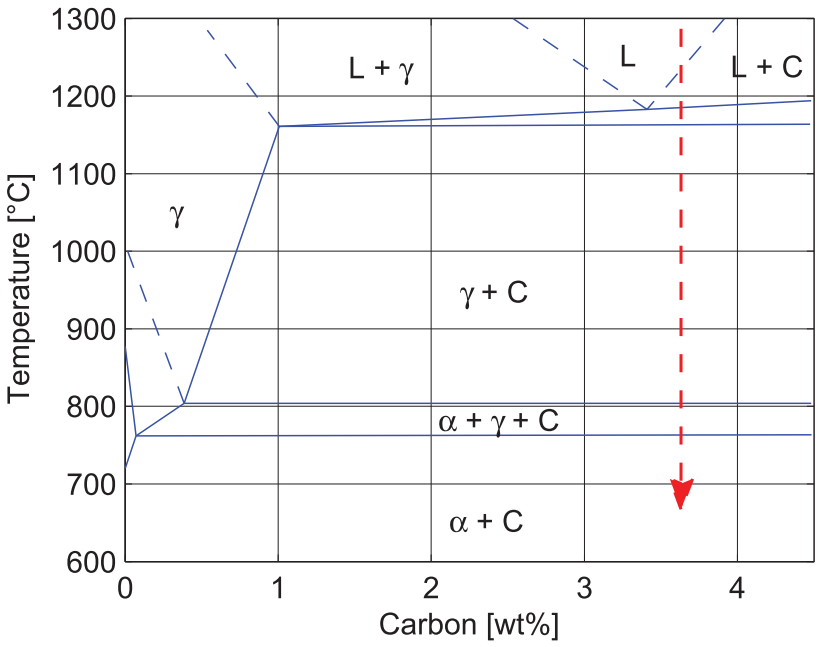

Figure 3. Schematic slice of the ternary Fe–C–Si phase diagram for a silicon concentration of 2.4 wt%. Data taken from [42].

reaction occurs, which leads to the formation of the austenite grains. At this point, the radius of the nodules is already equal to approximately 90% of its final value [32]. As cooling continues in the austenitic field, the nodules expand another 5%, while the surrounding metallic phase undergoes thermal contraction. Nevertheless, it seems reasonable to assume that during this stage the volume mismatch is compensated by plastic flow of the soft austenitic matrix, and any tension is released almost instantaneously due to its very low flow stress, probably in the order of a few MPa [41].

The situation becomes more complicated when the eutectoid interval is reached, as on the one hand the matrix transforms into ferrite, hence increasing in volume and creating more space for the graphite particles, but on the other hand the nodules expand too, due to carbon migration from the metallic phase. It is clear that modeling the complex thermo-mechanical interactions between all phases involved would in principle require simulating the nucleation and growth of the single ferritic grains. As the interest here is only in capturing the global effect, a simplified analysis is performed, as schematically shown in figure 4(a). It is assumed that the eutectoid reaction takes place simultaneously throughout the matrix at a fixed point, which may correspond to either the upper T_U or the lower T_L eutectoid temperature.

In the first case, the austenite containing 0.5 wt% carbon transforms into supersaturated ferrite at T_U, with a resulting volume expansion ΔV. Subsequently, the ferrite gradually releases the excess of carbon until the equilibrium concentration of 0.02% is achieved at T_L. Meanwhile, the nodule radius increases of approximately 5%, which is far more than the ΔV associated with the austenite–ferrite transformation. Therefore, no 'clearance' between the nodule and the matrix remains at the end of the process.

Conversely, in the second case the austenite cools down without transforming from T_U to T_L, gradually loosing carbon. During this stage, the nodule expands to almost its final size, promoting plastic flow in the matrix. This should not look unrealistic, as Hervas *et al* [13] have

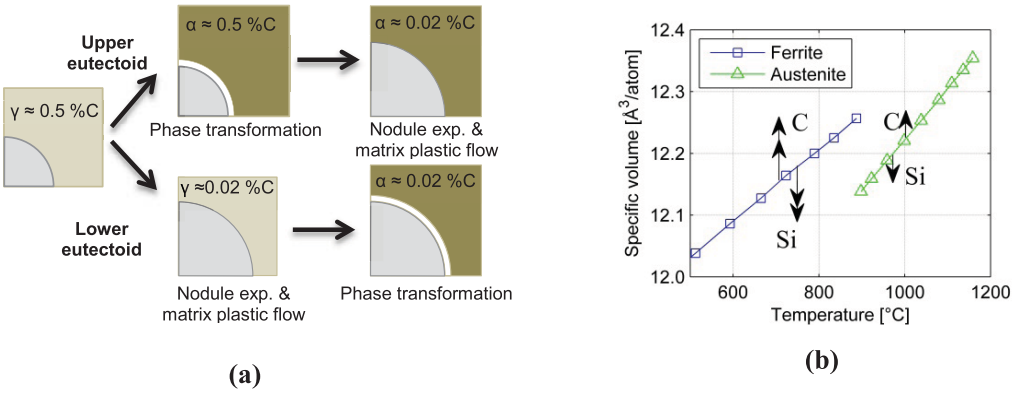

Figure 4. (a) Schematic of the volume variations occurring during the eutectoid transformation. (b) Specific volume as a function of temperature for pure iron [44], with indication of the effects of C and Si. Double arrows indicate a stronger effect compared to single arrows.

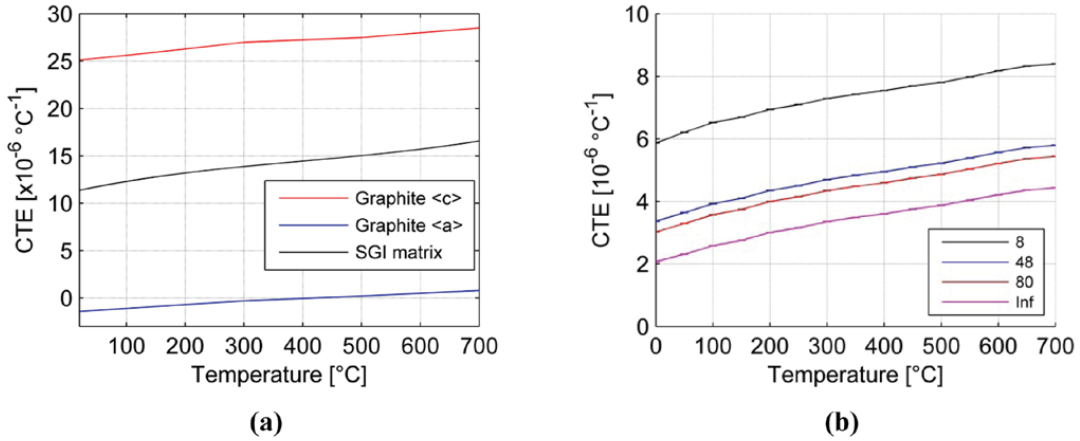

Figure 5. (a) CTE for graphite [47] and SGI matrix [48]. (b) Equivalent CTE calculated for the nodule model with different number of internal conical sectors subjected to free cooling without external matrix constraints. The error bars indicate the spread due the variation in the surface layer Young's modulus between 9.7 and 10.9 GPa. The fact that they almost collapse to a point indicates the reduced influence of the former quantity on the results.

shown that at temperatures close to the eutectoid transformation the compressive strength of the graphite particles is much larger compared to that of the matrix. Subsequently, the low-carbon austenite transforms into ferrite at T_L with an associated ΔV.

The main difference between the two scenarios just described is that in the first one no differential expansion between the nodules and the matrix remains, whereas in the second one a differential volume change is produced. This is equal to the ΔV of the austenite–ferrite transformation, which, for pure iron, is of approximately 1% at 910 °C [43]. The main ductile iron allying elements, namely C and Si, affect this volume variation in two ways: by increasing/decreasing the transformation temperature and by changing the lattice parameter to a different extent in the ferrite and in the austenite. As explained by Cockett and Davis [44], silicon increases the transformation temperature, therefore reducing the associated 'jump'

between the specific volume curves shown in figure 4(b). At the same time, it also promotes a larger lattice contraction in ferrite than in austenite: both factors contribute to reduce ΔV. Carbon instead generates exactly the opposite effect. Cockett and Davis measured ΔV for an iron alloy with 0.005 wt% C and increasing Si content, concluding that the primary variable controlling ΔV was the transformation temperature. For instance, with 1.45 wt% Si, the phase change occurred at 1020 °C with a ΔV of 0.79%, which is exactly the value that may be calculated from the curves for pure iron of figure 4(b) assuming the transformation to take place at the same temperature. Hence, assuming T_{L} to be equal to 700 °C for the case at hand, ΔV may be estimated as 1.4%.

In conclusion, according to the first hypothesis no differential expansion would take place during the eutectoid transformation, whereas according to the second one the matrix would expand locally 1.4% more than the nodules in volume. As what happens in reality is probably something in between the two extremes, an average value of 0.7% is considered in the calculations.

Finally, from 700 °C down to room temperature the carbon mass contained in the nodules is assumed to remain constant. On the other hand, thermomechanical interactions with the matrix still arise from the mismatch in the values of the thermal expansion coefficient (CTE), reported in figure 5(a). Regarding this point, the data for the matrix are taken equal to those of a commercial grade of electrical steel, due to close similarities in the chemical composition [45]. As no information is available for the CTE of the nodules' surface layer, an average value among the three principal graphite directions is considered.

3.4. Mechanical loading: elastic homogenization

In the following, a suitable elastic homogenization procedure is described in order to verify the consistency of the proposed micromechanical model with the room-temperature behavior of ductile iron at the macro scale. Between any two equivalent points $\boldsymbol{x}$ and $\boldsymbol{x}+\boldsymbol{d}$ lying on opposite faces of the unit cell of figure 2(b) and separated by the characteristic periodic length $\boldsymbol{d}$, the following periodic boundary conditions are applied:

$$\begin{aligned} \boldsymbol{u}(\boldsymbol{x}+\boldsymbol{d}) &= \boldsymbol{u}(\boldsymbol{x}) + \overline{\boldsymbol{\varepsilon}} \cdot \boldsymbol{d} \\ \boldsymbol{t}(\boldsymbol{x}+\boldsymbol{d}) &= -\boldsymbol{t}(\boldsymbol{x}) \end{aligned} \tag{1}$$

where $\boldsymbol{u}$ and $\boldsymbol{t}$ denote displacement and surface traction and the 2nd order tensor $\overline{\boldsymbol{\varepsilon}}$ represents the average of the infinitesimal strain over the entire cell volume. A detailed discussion of the implementation of the conditions (1) in the software ABAQUS is given by the authors in [37].

A linear elastic anisotropic relation between volume averages of the stress and strain fields over the unit cell is sought in the form:

$$\overline{\boldsymbol{\sigma}} = \overline{\mathbb{C}} : \overline{\boldsymbol{\varepsilon}} \tag{2}$$

where $\overline{\mathbb{C}}$ is the 4th order effective stiffness tensor. Its components are determined by prescribing in sequence six independent loadings in the form $\overline{\boldsymbol{\varepsilon}}^{(1)}, \ldots, \overline{\boldsymbol{\varepsilon}}^{(6)}$ according to expression (1), and recording the resulting average stresses $\overline{\boldsymbol{\sigma}}^{(1)}, \ldots, \overline{\boldsymbol{\sigma}}^{(6)}$. The linear system of equations generated in this way can then be solved for the effective elastic constants. Once $\overline{\mathbb{C}}$ is determined, values for the effective bulk $\overline{k}$ and shear $\overline{\mu}$ moduli are obtained as:

$$\overline{k} = \frac{1}{3}\frac{\left\langle \overline{\mathbb{C}} | \mathbb{S} \right\rangle}{\left\langle \mathbb{S} | \mathbb{S} \right\rangle}, \quad \overline{\mu} = \frac{1}{2}\frac{\left\langle \overline{\mathbb{C}} | \mathbb{D} \right\rangle}{\left\langle \mathbb{D} | \mathbb{D} \right\rangle} \tag{3}$$

where $\mathbb{S}$ and $\mathbb{D}$ are the spherical and deviatoric projection tensors [46], which form an orthogonal basis for isotropic 4th order tensors, and $\langle \cdot | \cdot \rangle$ indicates the associated scalar product. Conversion to effective Young's modulus $\overline{E}$ and Poisson's ratio $\overline{\nu}$ is performed via the basic relations:

$$\overline{E} = \frac{9\overline{k}\,\overline{\mu}}{3\overline{k} + \overline{\mu}}, \overline{\nu} = \frac{3\overline{k} - 2\overline{\mu}}{2(3\overline{k} + \overline{\mu})} \tag{4}$$

Values calculated from the latter expressions can be directly compared with those determined experimentally by means of e.g. uniaxial tensile tests, provided that the anisotropy index [14]:

$$I_{\mathrm{a}} = \left(\frac{\left\langle \overline{\mathbb{C}} - \overline{\mathbb{C}}^{\mathrm{iso}} | \overline{\mathbb{C}} - \overline{\mathbb{C}}^{\mathrm{iso}} \right\rangle}{\left\langle \overline{\mathbb{C}} | \overline{\mathbb{C}} \right\rangle} \right)^{1/2}, \ \overline{\mathbb{C}}^{\mathrm{iso}} = 3\overline{k}\mathbb{S} + 2\overline{\mu}\mathbb{D} \tag{5}$$

is $\ll 1$. Among all simulations performed, the maximum recorded value of I_{a} was only 1.5 %. This indicates that the unit cell model is suitable to represent the well-known isotropic elastic behavior of ductile iron at the macro-scale to a sufficient degree of approximation.

An important observation is to be made regarding the experimental values to be compared with those delivered by equation (4). As shown by Sjögren and Svensson [6], the graphite morphology strongly affects the macroscopic Young's modulus of SGI, meaning that a correction for the non-perfect spherical nodule shape of the material under investigation is necessary. Löhe *et al* [38] thoroughly investigated this issue for grades of composition similar to the SGI considered in the present work and same graphite volume fraction, 11.5%. From their findings, it seems that a limit value of approximately 175 ± 2 GPa is attained for SGI with perfect spherical nodules. As this is also the value suggested in [2], it will be taken as reference value through the rest of the analysis.

4. Results

4.1. Equivalent CTE for the nodules

A preliminary set of finite element simulations have been performed considering one nodule alone, without the presence of the surrounding matrix. Figure 5(b) shows numerical values for an equivalent CTE calculated on the basis of the average volume contraction during cooling according to the formula:

$$\mathrm{CTE}_{\mathrm{eq}} = \frac{1}{3V}\frac{\mathrm{d}V}{\mathrm{d}T} \tag{6}$$

By comparing with figure 5(a), it may be noticed that the average thermal contraction of the nodule is always smaller than that of the ferritic matrix over the entire temperature range examined, independently of the number of sectors. From a physical point of view, this indicates the existence of a driving force for the formation of local residual stresses during the manufacturing process, as the free shrinkage of the ferrite is hindered by the presence of the embedded graphite particles.

In addition, it can also be observed in figure 5(b), that the larger the number of conical sectors, the smaller the corresponding equivalent CTE. This is because the graphite in the core region contracts almost only in the *c*-direction, which is oriented approximately radially. However, the contraction towards the nodule center is opposed by the high in-plane stiffness of the graphite platelets with different orientation located in the neighboring sectors. Obviously, this effect becomes more pronounced when the distance between adjacent partitions is decreased, or, equivalently, the number of sectors is increased. When this number

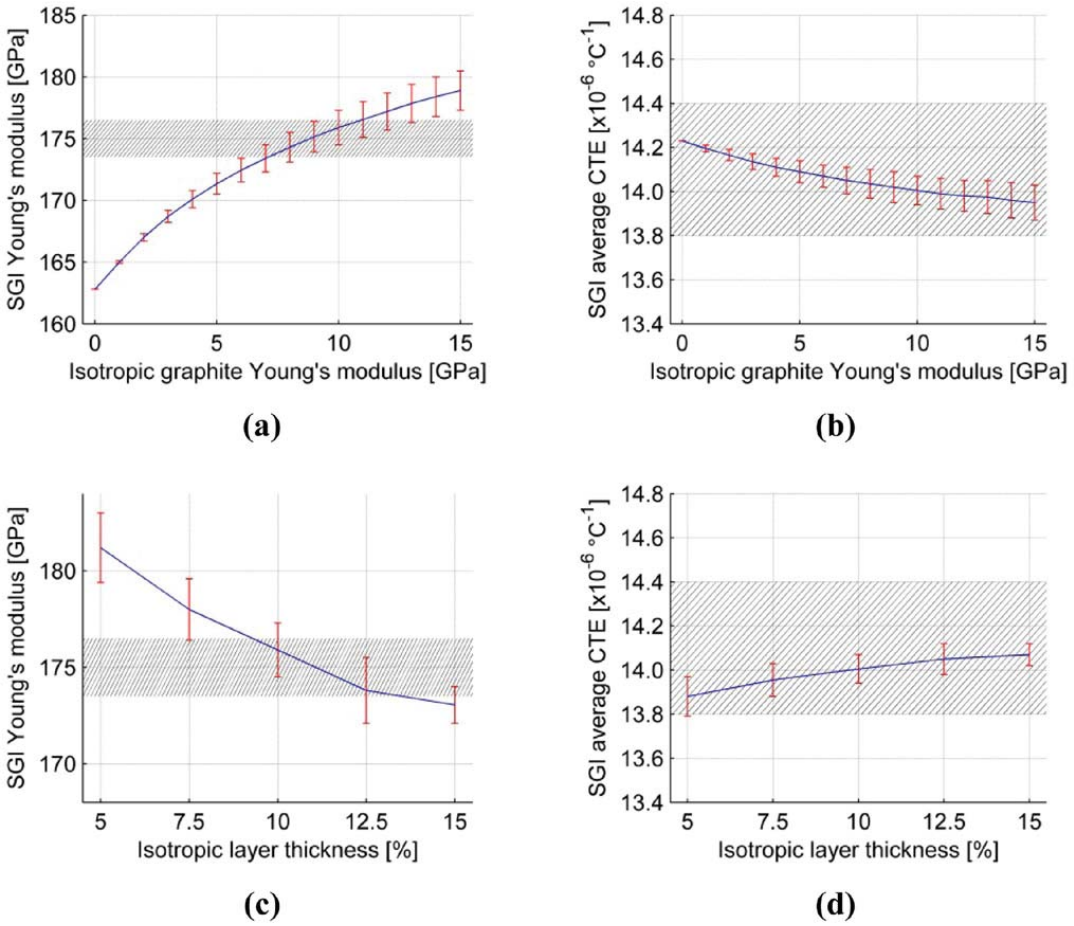

Figure 6. Effective SGI thermo-elastic properties predicted by the model, as a function of the superficial nodule layer Young's modulus ((a) and (b)) and thickness ((c) and (d)). In ((a) and (b)) the thickness is fixed at 10% of the nodule radius, whereas in ((c) and (d)) the Young's modulus is set at 10 GPa. In all plots the error bars denote the spread due the variation in the number of conical sectors contained in the nodule core region. The hatched intervals indicate reference exp. values for the SGI grade considered; the avg. CTE interval is defined by the values given in [2] and [49].

tends to infinity, the nodule core behaves as a sort of shell with high tangential stiffness, subjected to a negative internal pressure which builds up progressively as the temperature diminishes. In section 5, the consequence of this particular loading configuration will be discussed more thoroughly in relation to some experimental findings.

4.2. Thermo-elastic properties at the macro scale

A fundamental requirement for the nodules model is the capability of providing properties at the macro scale which are in agreement with experimental measurements for ductile iron. As visible in figures 6(a) and (b), the elastic homogenization procedure of the 3D unit cell provides effective values for Young's modulus at room temperature and average CTE in the interval 700 ÷ 20 °C which are in excellent agreement with experiments, according to the assumed range 9.7–10.9 GPa for the nodule surface layer stiffness. Within this range, it may also be seen from the error bars that a variation in the number of conical sectors from a minimum of 8 up to plus infinite produces a change in the effective Young's modulus of 2–3 GPa.

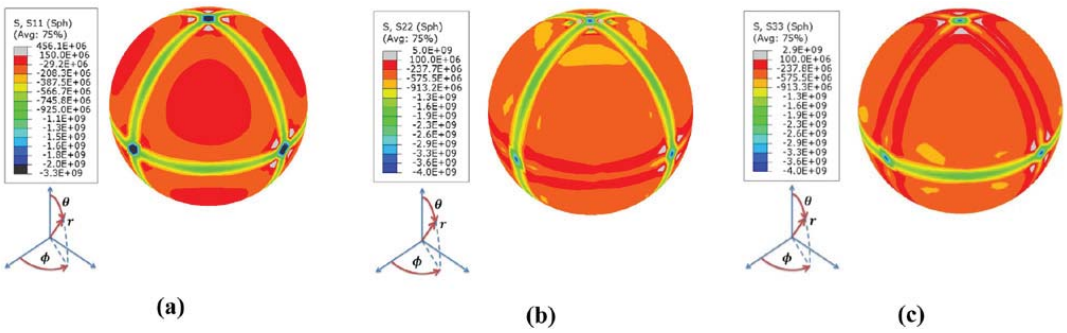

Figure 7. (a) Radial, (b) circumferential and (c) meridional residual stress components on the outer part of a nodule core with 8 internal sectors, for a surface layer Young's modulus of 10 GPa and thickness of 10% the nodule radius. The spherical coordinate system used has the origin in the nodule center and the zenith direction points upward. Units are Pa. The upper contour limits have been artificially reduced to avoid the spurious influence of a few elements close to the contact points between 4 sectors.

This is related to the increment in the nodule core stiffness associated with the tendency of the graphite platelets to form a rigid shell as the number of sectors increases, as explained previously. Regarding the third and last effective isotropic thermo-elastic quantity, namely Poisson's ratio, calculated values turn out to be always in the range 0.278–0.280. Again, there is a very good match with experimental measurements, which have been reported between 0.275 and 0.280 according to different sources [2, 49]. Finally, figures 6(c) and (d) provide an indication of the sensitivity of the predicted effective elastic properties to variations of the surface layer thickness, for the particular choice made of the other model parameters. It is seen that in order to match the experimental Young's modulus, the former quantity has to have a value of approximately 10% the nodule radius, which is in agreement with the TEM observations and thermodynamic calculations discussed in section 2.

4.3. Residual stresses

Having verified the consistency of the proposed model with the macroscopic thermo-elastic properties of ductile iron, the attention is now turned to the residual stress prediction at the microscopic scale. In general, it is observed that very large hoop stresses are generated during cooling at the extreme outer periphery of the nodule core, as visible in figure 7, due to the high in-plane stiffness of the graphite platelets in that region, which strongly opposes the compressive action generated by the matrix. In particular, extremely high compressive stresses, above 1 GPa, are recorded at the points of contact between two or more conical sectors. These values are probably unrealistic, as local buckling and/or fracture of the single platelets are likely to occur. Nevertheless, as inelastic deformation is not considered in the present model, the stresses arising at these concentration points propagate through the nodule surface layer into the matrix. In order to diminish their unphysical impact on the overall analysis, results for the residual stresses in the matrix are presented not in terms of the maximum stress recorded, but by using an average criterion. More specifically, two average values are considered: one related to a fictitious shell enveloping the nodule and another one associated with the unit cell external boundary layer, both having a thickness of 10% the nodule radius. They are assumed to be representative of the overall stress state in the matrix regions closest to and most distant from the nodule respectively. In this way, a global indication of the residual stress gradient existing in the metallic phase of ductile iron can be obtained.

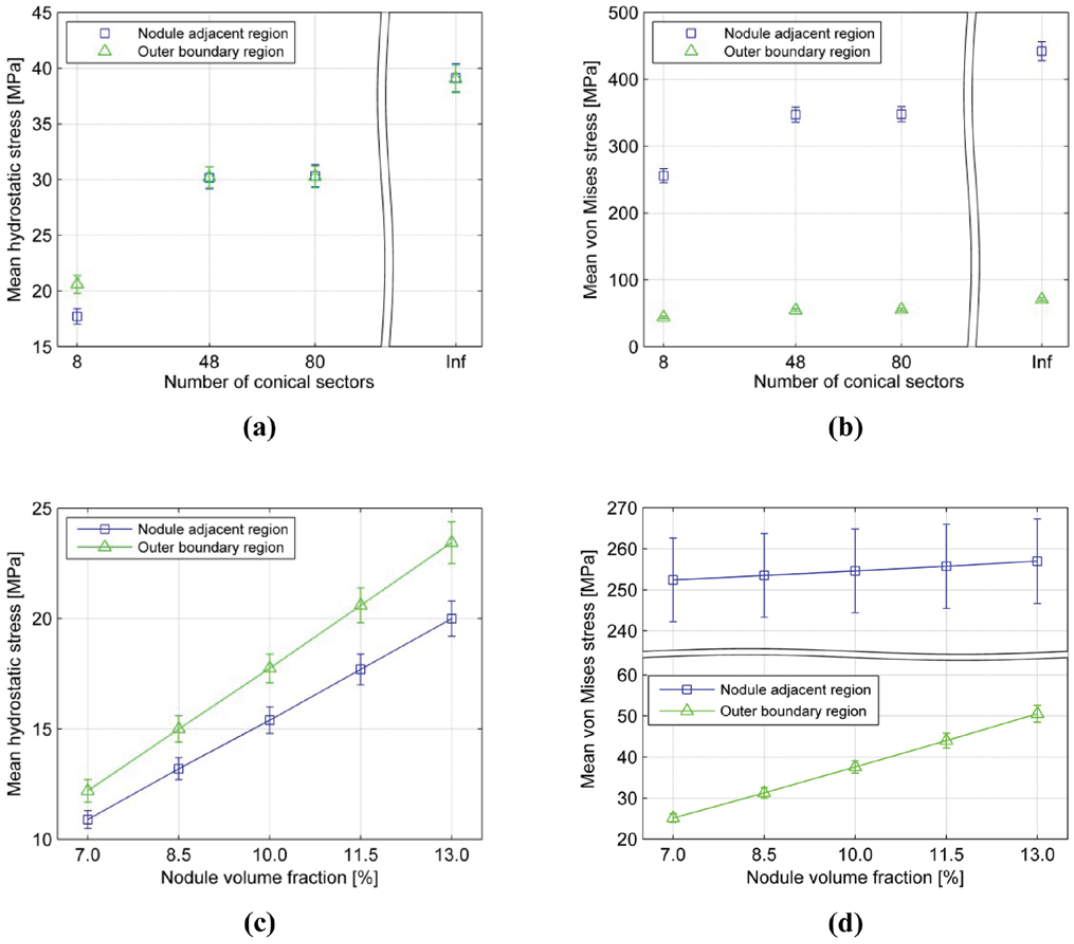

Figure 8. Mean hydrostatic and von Mises residual stresses in the matrix as a function of the number of conical sectors in the nodule core ((a) and (b)) and the graphite particles volume fraction ((c) and (d)). In ((a) and (b)) the volume fraction is 11.5%, whereas in ((c) and (d)) the number of sectors is 8. The nodule-adjacent region is identified as the matrix shell enveloping the nodule with a thickness of 10% its radius. Similarly, the outer boundary region corresponds to the 10% thick unit cell boundary layer. In all plots the error bars indicate the spread due the variation in the surface layer Young's modulus between 9.7 and 10.9 GPa.

From an analysis of the related data reported in figures 8(a) and (b), two major observations can be made. First of all, the mean von Mises stress is approximately one order of magnitude larger close to the nodule than at the unit cell boundary, but, at the same time, the mean hydrostatic stress shows almost negligible variations between these two different regions. The reason is that near the interface the matrix is compressed along the nodule radial direction, while it is stretched tangentially, hence generating stress components which are primarily deviatoric. Accordingly, a steep gradient in the von Mises stress is recorded. In addition, a strong influence of the nodule core partitioning is observed: it appears that by varying the number of conical sectors from 8 to 48, a 50% increment in the values of both deviatoric and hydrostatic mean stresses is obtained, followed by another 50% increase when their number tends to infinite. This effect is simply due to the increased CTE mismatch between the matrix and the nodule which arises from the reduced thermal contraction of the latter one, already pointed out in connection with figure 5.

Finally, figures 8(c) and (d) show how the mean residual stresses in the matrix are affected by a variation of the graphite volume fraction within the range 7.0–13.0%. This interval is representative of values found in typical grades of ductile iron, obtained by minor changes in the composition, solidification parameters, etc. Not surprisingly, it is seen that by increasing the nodule relative volume, the surrounding stress field increases accordingly. Nevertheless, while the other mean stress quantities almost double throughout the considered interval, the mean von Mises stress around the nodule, which is by far the most critical in terms of absolute values, exhibits only a modest 3% variation.

5. Discussion

5.1. Local residual elastic strains: predictions versus experiments

The results presented in figure 8 suggest that local residual stresses of magnitudes close to the matrix yield strength might develop around the nodules during manufacturing. To verify this, experimental investigations are currently being carried out to determine the lattice parameter of the neighboring ferritic grains using the synchrotron x-rays technique described in [23], and will be presented in detail in a future work [50]. In the context of the present paper, it is important to say that a preliminary measurement of the radial residual elastic strain component in the matrix showed a continuous decrease in its compressive magnitude with increasing distance from the nodule, as predicted by the numerical model, even though the simulated gradients and absolute values seemed somewhat overestimated by a factor 2.

Considering the thermo-elastic nature of the proposed anisotropic model for the nodules and the limited mechanical data available, which makes any inelastic description out of reach, the good agreement between theoretical predictions and measurements is surprisingly good. A possible explanation is that inelastic deformation does take place in the outer part of the nodule core during solid-state cooling, but it somehow remains localized to a region of limited thickness, without propagating to the entire graphite particle. In this way, the pressure exerted by the surrounding matrix is partially relieved, and the residual gradients smoothed out, but at the same time the overall material elastic stiffness remains almost unaffected. This hypothesis could justify the over prediction of the residual elastic strains, while at the same time explaining the excellent agreement obtained in terms of SGI macroscopic elastic properties (see figure 6). In addition, one should keep in mind that other important sources of error are present. In fact, a quite rough approximation of the eutectoid transformation is considered in the analysis, and any kind of high-temperature creep mechanism in the matrix, which could partly relieve the elastic strains, is ignored. Moreover, the anisotropy of the single ferritic grains is also neglected. Given the microscopic scale considered, including in the simulation some crystallographic information of the region around the nodule would probably improve the results. Finally, the periodic unit cell approach also constitutes a limitation, especially in relation to the accuracy of the calculated local stress and strain fields.

5.2. Link with nodules failure modes

As just mentioned, at the outer periphery of the nodules' core the predicted stress state is likely inaccurate, due to the probable occurrence of inelastic deformation. Nevertheless, outside that region the global pattern might still be quite trustworthy, at least from a qualitative point of view. Therefore, it makes sense to try to use such information to shed light on some typical failure modes observed experimentally for the graphite particles.

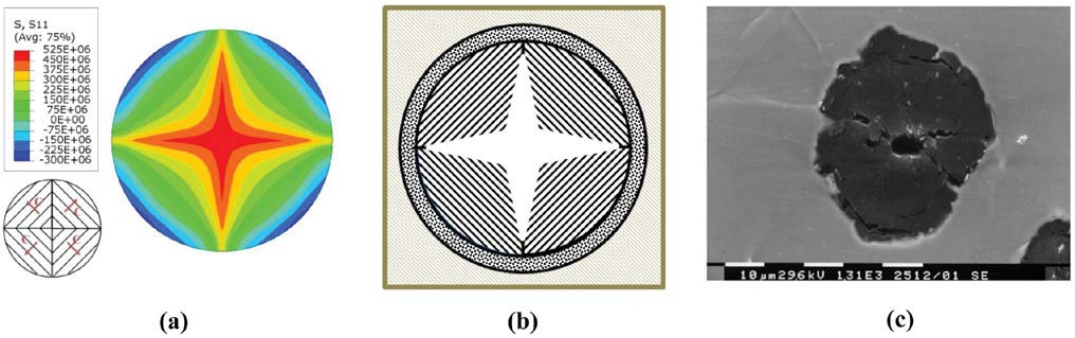

Figure 9. 'Disgregation' mechanism in the bulk of a nodule. (a) Stress component locally orthogonal to the graphite platelets, over the middle section of a nodule core with 8 sectors, in Pa, after cooling neglecting the presence of the SGI matrix. (b) Schematic of the expected failure mode. (c) Radial cracks propagating from the nodule center after tensile loading in a partially debonded nodule, reprinted from [33] with permission from Elsevier.

In the series of works cited in section 2, Di Cocco *et al* described the presence of an internal form of damage in the nodules, which was referred to as 'disgregation' [33]. It was characterized by the formation of cracks originating from the center of the particles and propagating radially. The fact that this type of failure was detected during both tensile and fatigue testing suggests that it is, to a certain extent, independent of the specific loading condition applied. Rather, it could be related to the presence of a specific residual stress state in the nodules, representing the main driving force for fracture.

More specifically, it was observed during tensile testing of SGI that the nodules tend to separate from the matrix [9], hence becoming mechanically 'isolated'. Nevertheless, a non-negligible stress field probably still exists inside them, associated with the anisotropic thermal deformation of the graphite occurring during manufacturing. As explained in section 4.1, the free contraction in the *c*-direction of the platelets located in a given sector is hindered by the presence of the adjacent partitions with different orientations. This implies that during cooling tensile stresses locally develop perpendicularly to the graphite platelets, as shown in figure 9(a). The predicted stresses are particularly high in the center of the nodule and along the interfaces between different sectors, where, additionally, a weaker mechanical bonding probably exists. It is not difficult to realize that the local change in orientation of these tensile forces could have a 'tearing' action in the latter regions, at the same time promoting the formation of a 'void' in the center of the particle. As long as a nodule remains fully embedded in the ferrite, the superposed compressive action of the matrix probably prevents any crack opening, but when debonding begins, the probability of having this 'disgregation' mechanism increases. By comparing figure 9(b), which schematically shows the expected failure mode for a debonded particle, with figure 9(c), taken from the work of Di Cocco *et al* support for the argument is found.

Another peculiar form of damage seems to be revealed by Cooper *et al* [51], associated with radial cracks located on the surface of nodules which had debonded from the matrix during tensile testing. The depth of these cracks, visible in figure 10(a), was approximately of 10% the nodule radius, suggesting that they were fully localized in the microcrystalline surface layer. Figures 10(b) and (c) present the distribution of the circumferential and meridional residual stress components on the surface of a nodule with 48 internal sectors, subjected to cooling without the presence of the surrounding matrix, to simulate the elastic deformation existing in a debonded particle at room temperature. It is seen that the stress pattern is highly affected by the partitioning of the inner core, and high tensile stresses are predicted along the continuation of the junctions between the conical sectors. Clearly, these

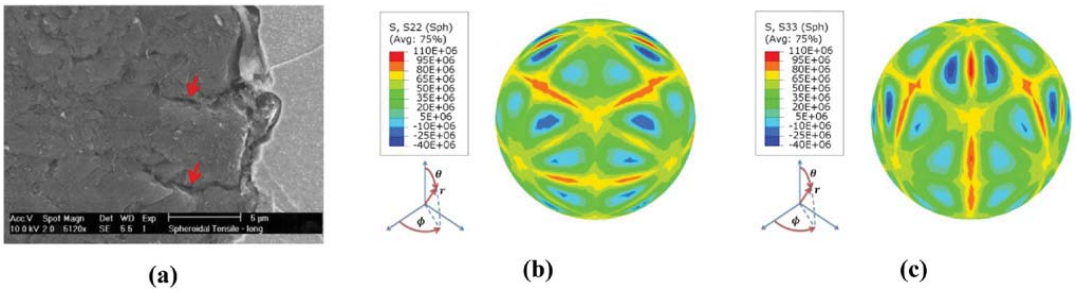

Figure 10. (a) Micrograph of the surface layer of a debonded nodule, reprinted from [51] with permission from Elsevier. The red arrows mark radial cracks. (b) Circumferential and (c) meridional normal residual stress components on the surface of a nodule with 48 internal sectors, after cooling neglecting the surrounding matrix. In ((b) and (c)) a spherical coordinate system is used, where the origin is the nodule center and the zenith direction points upward. Units are Pa.

could play an important role in the formation of the type of cracks observed in the work of the previous authors.

Finally, it should also be remarked that while performing heat treatment, Monchoux *et al* [25] detected preferential radial diffusion paths in the nodule surface layer, coinciding with the continuation of the boundary between sectors. This is also in agreement with the discussion above, as areas subjected to high tensile stresses are known to favor atom diffusion.

5.3. Potential consequences of the nodule-matrix interaction

In this last section, the thermo-mechanical interaction arising between the nodules and the ferritic matrix during manufacturing is discussed in relation to potential changes in the material properties at both the macro and micro scale.

5.3.1. Ductile iron mechanical performance. The present results indicate that the graphite particles drive the formation of high deviatoric residual stresses in the surrounding matrix which strongly increase in magnitude as the number of conical sectors grows. Considering the model overestimation, discussed in section 5.1, a variation of at least 50 MPa in their magnitude close to the nodule is expected when the number of core partitions is varied from 8 to 48. This is approximately 1/3 of the maximum stress amplitude that can be applied to the SGI grade under investigation in order to achieve a target fatigue life of 2.5 million cycles under axial loading [52]. An obvious question then arises with regard to the factors controlling such number. Intuitively, one would expect that larger nodules contain a higher number of partitions. This seems to find confirmation in several experimental works on the subject [27, 29, 30, 53], where some sectors appear to branch at a certain distance from the nodule center, even though this could be an artificial effect due to sectioning of a 3D geometry with a plane. However, if confirmed, it would suggest the presence of a material size-effect, i.e. a non-scaling relation between particle size and magnitude of the surrounding residual stresses, which could provide additional justification for the observed link between SGI fatigue resistance and dimensions of the graphite spheroids [54, 55]. Further experimental investigations would be useful to verify this potential connection and its relative importance compared to other factors.

5.3.2. Nodules' internal structure. During solid-state cooling the matrix exerts compressive stresses on the nodules, which can realistically be of up to 100–200 MPa. These values are

not too far from the compressive strength of the isotropic graphite which the nodules' surface layer is assumed to be made of, reported in table 2. Moreover, the actual strength is probably higher, because compression tests are usually performed without lateral confining pressure, whereas in ductile iron the nodules are confined in all directions by the presence of the matrix. From this point of view, it might be that the variation in the graphite crystal structure between the surface and the bulk of the nodules be related to the increasing pressure exerted by the matrix during cooling. Oku *et al* [56] investigated the effects of compressive pre-stresses on fine-grain isotropic graphite, and found that upon subsequent compression the material Young's modulus was reduced, whereas its strength was increased. The changes were more pronounced at high temperatures and were connected to rotation and cracking of the single crystallites, which tended to assume a low-energy configuration with the stiff basal planes oriented perpendicularly to the applied stress. These findings suggest that something similar could happen during the manufacturing process of ductile iron. As long as the nodules are not subjected to significant external pressure, i.e. until the end of solidification, graphite keeps growing in conical sectors. However, when tangential stresses start building up in the outer nodule layers due to contraction of the surrounding solid matrix, this growing condition is no longer energetically favorable. As a consequence, smaller crystallites with different orientation form, hence generating the surface layer observed by the authors cited in section 2.

6. Conclusions

The present paper proposes a new thermo-elastic anisotropic micro-mechanical model for the spheroidal graphite particles contained in ductile iron. Its main features are:

- it is consistent with the most recent TEM investigations of the nodules' internal structure;
- it yields homogenized values for the ductile iron elastic properties at the macro scale in agreement with experiments;
- it describes correctly the overall local residual elastic strain pattern existing in the ferritic matrix after manufacturing, whereas absolute values seem to be somewhat over predicted, but within a factor 2 only. A reason for such overestimate is probably the inelastic deformation which is likely to occur in the outer part of the nodule internal core, due to the formation of high hoop stresses during solid-state cooling.

In addition, the proposed model seems to provide theoretical explanation for several experimental facts. First of all, it gives reason for some typical failure modes reported in literature for the graphite particles. Secondly, it predicts higher stresses in the matrix for nodules with a larger number of internal partitions. If the latter quantity were found proportional to the particles' dimension, as experiments seem to suggest, then a material size-effect would arise, which could provide additional justification for the observed link between SGI fatigue resistance and nodules' dimensions. Finally, the different graphitic structure of the superficial layer of the nodules might be explained by the observed tendency of the graphite crystallites to rotate and fragment under compressive forces, which are demonstrated to be present during solid-state cooling.

Acknowledgments

Part of this work has been supported by the Strategic Research Center 'REWIND-Knowledge based engineering for improved reliability of critical wind turbine components', Danish Research Council for Strategic Research, grant no. 10-093966. The authors gratefully acknowledge Y Zhang and S Fæster (Technical University of Denmark, Department of Wind Energy) for scientific support during preparation of the manuscript.

References

[1] Labrecque C and Gagne M 1998 Review ductile iron: 50 years of continuous development *Can. Metall. Q.* **37** 343–78

[2] Ductile Iron Society 2013 Ductile Iron data for design engineers www.ductile.org/ductile-iron-data/ (accessed 10 October 2015)

[3] 47th Census of World Casting Production 2013

[4] Tiedje N S 2010 Solidification, processing and properties of ductile cast iron *Mater. Sci. Technol.* **26** 505–14

[5] Grimvall G 1997 Cast iron as a composite: conductivities and elastic properties *Adv. Mater. Res.* **4–5** 31–46

[6] Sjögren T and Svensson I L 2004 Modelling the effect of graphite morphology on the modulus of elasticity in cast irons *Int. J. Cast Met. Res.* **17** 271–9

[7] Hütter G, Zybell L and Kuna M 2015 Micromechanisms of fracture in nodular cast iron: from experimental findings towards modeling strategies—a review *Eng. Fract. Mech.* **144** 118–41

[8] Fernandino D O and Boeri R 2015 Study of the fracture of ferritic ductile cast iron under different loading conditions *Fatigue Fract. Eng. Mater. Struct.* **38** 610–20

[9] Dong M J, Tie B, Béranger A S, Prioul C and François D 1997 Damage effect on the fracture toughness of nodular cast iron *Adv. Mater. Res.* **4–5** 181–8

[10] Andriollo T and Hattel J 2016 On the isotropic elastic constants of graphite nodules in ductile cast iron: analytical and numerical micromechanical investigations *Mech. Mater.* **96** 138–50

[11] Berdin C, Dong M J and Prioul C 2001 Local approach of damage and fracture toughness for nodular cast iron *Eng. Fract. Mech.* **68** 1107–17

[12] Steglich D and Brocks W 1998 Micromechanical modeling of damage and fracture of ductile materials *Fatigue Fract. Eng. Mater. Struct.* **21** 1175–88

[13] Hervas I, Bettaieb M B and Hug E 2013 Damage mechanisms evolution of ductile cast irons under thermomechanical loadings *Int. J. Mater. Prod. Technol.* **47** 23

[14] Fernandino D O, Cisilino A P and Boeri R E 2015 Determination of effective elastic properties of ferritic ductile cast iron by computational homogenization, micrographs and microindentation tests *Mech. Mater.* **83** 110–21

[15] Dierickx P, Verdu C, Reynaud A and Fougeres R 1996 A study of physico-chemical mechanisms responsible for damage of heat treated and as-cast ferritic spheroïdal graphite cast irons *Scr. Mater.* **34** 261–8

[16] Pradhan S K, Nayak B B, Sahay S S and Mishra B K 2009 Mechanical properties of graphite flakes and spherulites measured by nanoindentation *Carbon* **47** 2290–2

[17] Oliver W C and Pharr G M 1992 An improved technique for determining hardness and elastic modulus using load and displacement sensing indentation experiments *J. Mater. Res.* **7** 1564–80

[18] Bonora N and Ruggiero A 2005 Micromechanical modeling of ductile cast iron incorporating damage. Part I: ferritic ductile cast iron *Int. J. Solids Struct.* **42** 1401–24

[19] Andriollo T, Thorborg J, Tiedje N and Hattel J 2015 Modeling of damage in ductile cast iron—the effect of including plasticity in the graphite nodules *IOP Conf. Ser.: Mater. Sci. Eng.* **84** 012027

[20] Andriollo T, Thorborg J and Hattel J 2015 The influence of the graphite mechanical properties on the constitutive response of a ferritic ductile cast iron—a micromechanical FE analysis *Proc. XIII Int. Conf. on Computational Plasticity* pp 632–41

[21] Dryden J R and Purdy G R 1989 The effect of graphite on the mechanical properties of cast irons *Acta Metall.* **37** 1999–2006

[22] Era H, Kishitake K, Nagai K and Zhang Z Z 1992 Elastic modulus and continuous yielding behaviour of ferritic spheroidal graphite cast iron *Mater. Sci. Technol.* **8** 257–61 (www.maneyonline.com/doi/abs/10.1179/mst.1992.8.3.257 (accessed 12 May 2015))

[23] Yang W, Ice G E, Budai J D, Tischler J Z and Larson B C 2002 Three-dimensional x-ray structural microscopy with submicrometre resolution *Nature* **415** 887–90

[24] Stefanescu D M 1989 Cast iron *Metals Handbook* 9th edn (Materials Park, OH : ASM International) pp 168–81

[25] Monchoux J P, Verdu C, Thollet G, Fougères R and Reynaud A 2001 Morphological changes of graphite spheroids during heat treatment of ductile cast irons *Acta Mater.* **49** 4355–62

[26] Miao B, Fang K, Bian W and Liu G 1990 On the microstructure of graphite spherulites in cast irons by TEM and HREM *Acta Metall. Mater.* **38** 2167–74

[27] Miao B, North Wood D O, Bian W, Fang K and Fan M H 1994 Structure and growth of platelets in graphite spherulites in cast iron *J. Mater. Sci.* **29** 255–61
[28] Sjogren T 2007 Influences of the graphite phase on elastic and plastic deformation behaviour of cast irons *PhD Thesis* Linköping University
[29] Theuwissen K, Lacaze J, Véron M and Laffont L 2014 Nano-scale orientation mapping of graphite in cast irons *Mater. Charact.* **95** 187–91
[30] Theuwissen K, Lafont M-C, Laffont L, Viguier B and Lacaze J 2012 Microstructural characterization of graphite spheroids in ductile iron *Trans. Indian Inst. Met.* **65** 627–31
[31] Di Cocco V, Iacoviello F and Cavallini M 2010 Damaging micromechanisms characterization of a ferritic ductile cast iron *Eng. Fract. Mech.* **77** 2016–23
[32] Di Cocco V, Iacoviello F, Rossi A, Cavallini M and Natali S 2013 Graphite nodules and fatigue crack propagation micromechanisms in a ferritic ductile cast iron *Fatigue Fract. Eng. Mater. Struct.* **36** 893–902
[33] Di Cocco V, Iacoviello F, Rossi A and Iacoviello D 2014 Macro and microscopical approach to the damaging micromechanisms analysis in a ferritic ductile cast iron *Theor. Appl. Fract. Mech.* **69** 26–33
[34] Savini G, Dappe Y J, Öberg S, Charlier J C, Katsnelson M I and Fasolino A 2011 Bending modes, elastic constants and mechanical stability of graphitic systems *Carbon* **49** 62–9
[35] Asbury Carbons 2015 Isotropic graphite for high strength applications http://asbury.com (accessed 6 December 2015)
[36] Drago A and Pindera M 2007 Micro-macromechanical analysis of heterogeneous materials: macroscopically homogeneous versus periodic microstructures *Compos. Sci. Technol.* **67** 1243–63
[37] Andriollo T, Thorborg J and Hattel J 2016 Modeling the elastic behavior of ductile cast iron including anisotropy in the graphite nodules *Int. J. Solids Struct.* submitted
[38] Löhe D, Vohringer O and Macherauch E 1983 On Young's modulus of ferritic cast iron *Z. Met.* **74** 265–73
[39] Münstermann S, Feng Y and Bleck W 2014 Influencing parameters on elastic modulus of steels *Can. Metall. Q.* **53** 264–73
[40] Geers M G D, Kouznetsova V G and Brekelmans W A M 2010 Multi-scale computational homogenization: trends and challenges *J. Comput. Appl. Math.* **234** 2175–82
[41] Kaibyshev R and Kazakulov I 2000 Deformation behavior of Fe–3%Si steel at high temperatures *Key Eng. Mater.* **171–4** 213–8
[42] Vogel C, Juhl C and Maahn E 2001 *Metallurgi for Ingeniører* 9th edn (København : Polyteknisk Forlag)
[43] Lyman T, Boyer H E, Unterweiser P M, Foster J E, Hontas J P and Lawton H (ed) 1961 *Metals Handbook* (*Properties and Selection of Metals*) vol 1, 8th edn (Materials Park, OH : ASM International)
[44] Cockett G H and Davis C D 1963 The lattice expansion of Fe–Si alloys and the volume change at the A3 point *J. Iron Steel Inst.* **201** 110–5
[45] Moses X 1990 Electrical steels: past, present and future developments *IEE Proc.* A **137** 233–45
[46] Itskov M 2007 *Tensor Algebra and Tensor Analysis for Engineers* (Berlin: Springer)
[47] Steward E G, Cook B P and Kellet E A 1960 Dependence on temperature of the interlayer spacing in carbons of different graphitic perfection *Nature* **187** 1015–6
[48] Grain-oriented electrical steel 2015 Technical data sheet www.atimetals.com (accessed 7 December 2015)
[49] American Foundrymen's Society 1992 *Ductile Iron Handbook* (Schaumburg, Il : American Foundrymen's Society)
[50] Zhang Y *et al* 2016 Local residual stresses around individual graphite nodules in a ductile cast iron: experimental characterization and comparison with theoretical models in preparation
[51] Cooper C A, Elliott R and Young R J 2002 Investigation of elastic property relationships for flake and spheroidal cast irons using Raman spectroscopy *Acta Mater.* **50** 4037–46
[52] Shirani M and Härkegård G 2011 Large scale axial fatigue testing of ductile cast iron for heavy section wind turbine components *Eng. Fail. Anal.* **18** 1496–510
[53] Hara T *et al* 2014 Morphologies of some graphites in ductile cast irons *Mater. Trans.* **55** 1500–5
[54] Caldera M, Chapetti M, Massone J M and Sikora J A 2007 Influence of nodule count on fatigue properties of ferritic thin wall ductile iron *Mater. Sci. Technol.* **23** 1000–4
[55] Vaško A 2014 Fatigue properties of synthetic nodular cast irons *Key Eng. Mater.* **635** 5–8
[56] Oku T, Kurumada A, Imamura Y, Kawamata K and Shiraishi M 1998 Effects of prestresses on mechanical properties of isotropic graphite materials *J. Nucl. Mater.* **258–63** 814–20

Appendix E
PAPER V

Analysis of the equivalent indenter concept used to extract Young's modulus from a nano-indentation test: Some new insights into the Oliver-Pharr method.

Tito Andriollo[1,3], **Jesper Thorborg**[1,2,4] **and Jesper Hattel**[1,5]

[1]Department of Mechanical Engineering, Technical University of Denmark, DK-2800 Kgs. Lyngby, Denmark

[2]MAGMA GmbH, D-52072 Aachen, Germany

[3]Corresponding author. Address: Technical University of Denmark, Produktionstorvet, Building 425, room 125, 2800 Kgs. Lyngby, Denmark. Phone: +45 45 25 47 22. E-mail: titoan@mek.dtu.dk

[4]Address: Technical University of Denmark, Produktionstorvet, Building 425, room 132, 2800 Kgs. Lyngby, Denmark. E-mail: jest@mek.dtu.dk

[5]Address: Technical University of Denmark, Produktionstorvet, Building 425, room 128, 2800 Kgs. Lyngby, Denmark. E-mail: jhat@mek.dtu.dk

Abstract

In this paper a thorough analysis of the equivalent indenter concept applied to nano-indentation is carried out, motivated by the fact that previous works in the field have not considered the requirement of a consistent relation between contact depth and projected contact area. Dimensional analysis is initially used to prove that the shape of the axisymmetric equivalent indenter can be regarded as a material property, provided that size-effects are negligible. Subsequently, it is shown that such shape can effectively be employed to describe the nano-indentation unloading stage by means of Sneddon's elastic solution which is formally valid only for indentation into a flat surface. This allows for formulating the problem of extracting Young's modulus from the unloading curve as an optimization problem. However, it is proved that the latter does not have a unique solution, due to the particular mathematical structure of the underlying equations; hence, additional constraints are needed to set restrictions on the admissible equivalent indenter shapes. An example of such constraint is hidden in some apparent inconsistencies of the well-known Oliver-Pharr method, which is demonstrated to be based on an equivalent conical indenter whose semi-apical angle depends on the ratio between residual and total penetration. Specifically, this angle tends to 90 degrees when the material exhibits extensive inelastic deformation, whereas it reduces to the one characteristic of the real indenter for a perfectly elastic material. This provides a new physical explanation for the relatively good accuracy of the method even in presence of a non-negligible residual contact impression on the sample.

Keywords

Indentation; Analytical solutions; Young's modulus; Elastic modulus; Oliver-Pharr method; Equivalent indenter

Article structure

1. Introduction

Instrumented nano-indentation is a well-established technique which is widely used for probing mechanical properties of materials at length scales in the sub-micrometer range. Its high scientific relevance combined with a relatively simple experimental setup have attracted the attention of many researchers in the last decades, and several dedicated review papers exist which offer extensive accounts of the subject, e.g. (Fischer-Cripps, 2006)(Oliver and Pharr, 2004)(Cheng and Cheng, 2004).

In essence, a nano-indentation test consists in pressing a 3-sided pyramidal Berkovich indenter onto the surface of the sample under investigation and recording the resulting applied force vs penetration curve (figure 1-a). The main difference compared to traditional indentation techniques performed at the micron or millimeter scale is that the area of the residual impression left on the material is normally not measured, due to its much reduced size. For this reason, mechanical properties are usually estimated on the basis of the loading and unloading characteristics alone. Concerning this, a number of methods have been proposed so far which allow deriving parameters related to elastic and plastic material behavior, fracture toughness, creep, impact resistance, etc., a full list of which has recently been given in a comprehensive monograph (Fischer-Cripps, 2011).

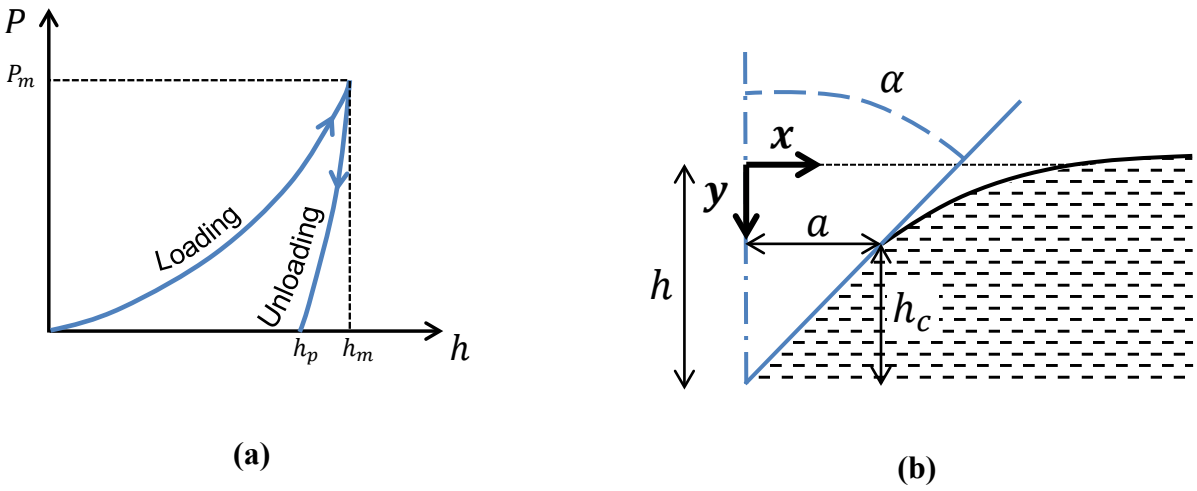

Figure 1: Nano-indentation test. (a) Recorded load vs penetration curve. (b) Definition of the main geometrical quantities for axisymmetric conical indentation: α is the indenter semi-apical angle, h is the total indenter penetration, h_c is the contact depth and a is the contact radius.

Focusing in particular on the determination of the isotropic elastic constants from nano-indentation data, the main analysis procedures available at the present time can be roughly classified into three distinct categories. The first one comprises methods which make use of additional experimental quantities, for instance measurements of the residual surface profile using the atomic force microscope (Li et al., 2002)(Mata and Alcala, 2003) or of the contact area at maximum load using electrical resistance techniques (Poon et al., 2008a). Despite delivering very precise results, the application of these procedures has been limited somehow by the much higher degree of experimental complexity they involve, which seems in contrast to the conceptual simplicity of a nano-indentation test. In order to keep the experimental burden to a minimum, a second group of methods has been devised which only require knowledge of the force-penetration curve. The latter is analyzed on the basis of a set of dimensionless functions which are constructed from a large number of finite element simulations of the indentation process, as done in e.g. (Dao et al., 2001)(Cheng and Cheng, 1998)(Cheng et al., 2002). An intrinsic limitation in this case is the range of validity of the derived dimensionless relations, which are typically obtained under specific assumptions for the material inelastic behavior during loading. As a consequence, they should be used with caution for materials whose constitutive response is either completely unknown or remarkably different from the one employed in the numerical simulations. Finally, the third category refers to methodologies which rely on exact analytical solutions to the so-called Boussinesq's problem of indentation into an elastic half-space (Boussinesq, 1885). The well-known technique proposed by (Doerner and Nix, 1986) and later extended and improved by (Oliver and Pharr, 1992) belongs to this group, and it is still widely adopted in the scientific community for its simplicity combined with relatively good accuracy.

How purely elastic solutions developed for axisymmetric indenters (Love, 1939)(Harding and Sneddon, 1945)(Sneddon, 1948)(Segedin, 1957)(Sneddon, 1965) can effectively be used to analyze nano-indentation data, which is normally affected by an appreciable amount of inelastic deformation, is a matter which indeed deserves a special comment. The very first point to note is that the Oliver-Pharr method considers only the unloading part of a nano-indentation test, which is assumed to be an entirely elastic process. Furthermore, the force-penetration curve produced by the pyramidal Berkovich indenter is supposed to be the same as that generated by a conical indenter with the same area-to-depth ratio. Extensive finite element calculations and experimental investigations have confirmed that these two assumptions are either fully satisfied, or lead to negligible errors in almost all practical cases (Dao et al., 2001)(Pharr and Bolshakov, 2002)(Poon et al., 2008a)(Sakharova et al., 2009).

Besides the points just discussed, another critical aspect exists which relates to the applicability of solutions obtained for indentation into a perfectly flat half-plane to the description of the unloading stage, which involves contact with a surface containing a residual impression. In principle, this particular contact condition can be described by the equivalent indenter concept (Bolshakov et al., 1995), whose profile is determined pointwise by

the vertical distance between the real indenter and the profile of the sample surface after unloading, as schematically shown in figure 2. That is, the elastic solutions previously mentioned can be effectively used to model the unloading stage provided that the equivalent indenter geometry is entered into the equations.

According to (Woirgard and Dargenton, 1997)(Woirgard et al., 1998a)(Pharr and Bolshakov, 2002), the Oliver-Pharr method is intrinsically based on the equivalent indenter concept. This justifies the relative good accuracy of the method, achieved even when the residual impression left on the sample is actually not negligible. In particular, the dependency on the equivalent geometry is reflected in the value of the parameter ϵ appearing in the formula

$$h_c = h - \epsilon \frac{P}{P'} \tag{1}$$

which allows calculating the contact depth h_c from knowledge of the applied load P, the total downward displacement h of the indenter tip relative to the undeformed sample surface and the slope P' of the unloading curve. Figure 1-b provides the geometrical definition of these quantities.

It is the present authors' opinion, however, that there are two aspects of the Oliver-Pharr method which do not appear to be fully consistent with the equivalent indenter concept, at least apparently. The first one is the way the projected contact area A (equal to πa^2 in figure 1-b) is estimated after h_c has been calculated from equation (1). Indeed, an expression based on the *real* indenter geometry is assumed to hold, which, neglecting tip rounding effects, has the form

$$A = A_r(h_c) = \pi(\tan(\alpha)\, h_c)^2 \tag{2}$$

where $\alpha = 70.3^0$ is the semi-apical angle of the conical punch with the same area-to-depth ratio of the Berkovich indenter. Within the equivalent indenter framework, one would expect the contact area to be

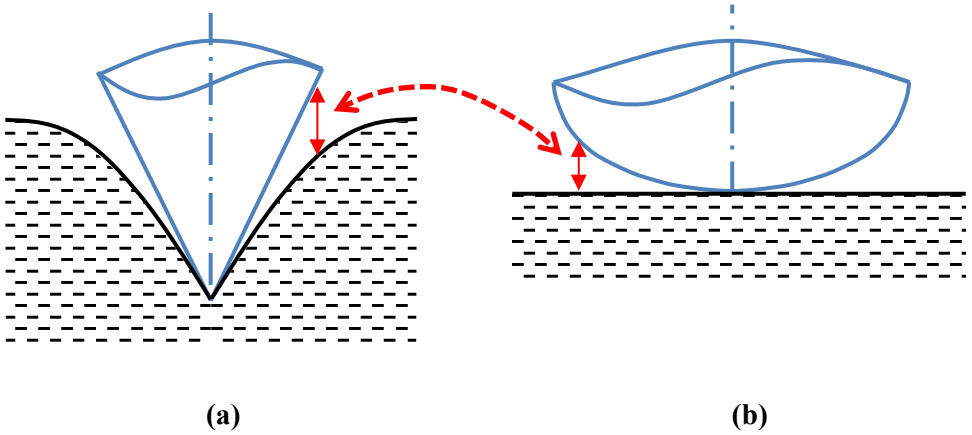

(a) **(b)**

Figure 2: Definition of the equivalent indenter concept. (a) Real conical indenter after unloading. (b) Equivalent indenter geometry.

determined by means of the relation $A = A_{eq}(h_c)$ proper to the *equivalent* indenter instead. Clearly, it should be recognized that the relation $A = A_{eq}(h_c)$ is generally unknown, as can be realized easily from figure 2. In fact, it depends on the shape of the residual impression left on the sample, which in turn is determined by the mechanical properties of the material under investigation.

The second aspect of the Oliver-Pharr method which is seemingly in contrast to the equivalent indenter concept is the particular value of h used in equation (1). In fact, as previously said, h is assumed to represent the *total* downward displacement of the indenter tip. At first glance, according to the geometrical construction of figure 2 it would appear more logical to assume h to represent only the *recoverable* part of the penetration, i.e. the total minus the residual. In the standard Oliver-Pharr procedure, equation (1) is evaluated only at maximum load. Nevertheless, by assuming the equivalent indenter concept to hold, the elastic relations describing the unloading stage should be satisfied for any value of the load, and so should equation (1). However, it is easily seen that when the indenter separates from the sample at the end of the unloading stage, meaning that $h_c = 0$, h is equal to the residual penetration h_p indicated in figure 1-a. But then, to satisfy the equation, some load $P \neq 0$ should still be transmitted across the contact surface, which is non-physical.

For the sake of clarity, it is useful to say at this point that with a value for the projected contact area at hand, the reduced Young's modulus E^* can be found via the well-known relation between A, E^* and P' as

$$E^* = \frac{\sqrt{\pi}}{2\beta}\frac{P'}{\sqrt{\mathrm{A}}} \tag{3}$$

where β is a correction factor which normally takes the value of ≈ 1.05 (Oliver and Pharr, 2004). Subsequently, the standard Young's modulus E can be eventually calculated on the basis of the relation

$$E^* = \frac{E}{1-\nu^2} \tag{4}$$

assuming that the Poisson's ratio ν of the material being indented is known.

In light of the arguments put forth so far, it appears that the Oliver-Pharr method does not seem to be fully consistent with the equivalent indenter concept. This raises two questions. First of all, what would happen if a fully consistent method were used? Would it provide better results? Secondly, how to explain the relatively good accuracy of the Oliver-Pharr method then, since it does not satisfy the equivalent indenter assumptions? In other words, why does this method work anyway?

In order to clarify these points, it is the aim of the present paper to re-examine the application of the equivalent indenter concept to the Young's modulus estimation from nano-indentation unloading curves by means of classic analytical solutions to the Bousinnesq' problem. Initially, the latter will be reviewed and re-formulated at the same time in a more convenient dimensionless form. Subsequently, the validity of the equivalent indenter

concept for the description of the contact condition with a deformed surface will be tested, emphasizing the level of accuracy which can be possibly obtained. After that, the inverse problem (Dao et al., 2001) will be defined and critically analyzed within a rigorous and consistent framework. Finally, solution strategies will be discussed, eventually establishing a link with the traditional Oliver-Pharr method and showing that its apparent inconsistencies are in reality associated with a concealed, convenient choice of the equivalent indenter profile.

2. Theory

In this section, the most common solutions available in the literature for axisymmetric indentation into an isotropic elastic half-space are presented and reformulated for convenience in a dimensionless format. The main geometrical parameters considered are shown in figure 1-b.

2.1 General solution by Sneddon

Let us assume that the axisymmetric profile of a rigid indenter is given by a smooth monotonic function

$$y = f(x) \Rightarrow y = f(a\tilde{x}) \tag{5}$$

where a is the contact radius and $\tilde{x} = x/a$ is a normalized x-coordinate. According to (Sneddon, 1965), the load P and penetration h corresponding to a certain value of a are given by

$$h = \int_0^1 \frac{f'_{\tilde{x}}(a\tilde{x})}{\sqrt{1-\tilde{x}^2}} d\tilde{x}, \qquad P = 2E^* a \int_0^1 \frac{\tilde{x}^2 f'_{\tilde{x}}(a\tilde{x})}{\sqrt{1-\tilde{x}^2}} d\tilde{x} \tag{6}$$

where the symbol $f'_{\tilde{x}}$ indicates the derivative of f with respect to $\tilde{x}$

$$f'_{\tilde{x}} = \frac{df}{d\tilde{x}} = \frac{df}{dx}\frac{dx}{d\tilde{x}} = f'a \tag{7}$$

and E^* is the reduced Young's modulus defined in equation (4). It is worth mentioning that if the indenter were not perfectly rigid, equation (4) could be easily modified to include an additional dependency on the elastic constants of the latter, as discussed in (Fischer-Cripps, 2006).

The normalization with respect to the contact radius is somewhat inconvenient, as this quantity is usually an unknown for the problem. Therefore, it is useful to introduce a normalization based on a length scale which is directly available from an indentation test, for instance the maximum penetration h_m, which will be indicated with the symbol ($\bar{}$). Accordingly, relations (6) take the form

$$\bar{h} = \int_0^{\bar{a}} \frac{f'(h_m\bar{x})}{\sqrt{1-(\bar{x}/\bar{a})^2}} d\bar{x}, \qquad P = 2E^* h_m^2 \int_0^{\bar{a}} \frac{\bar{x}^2 f'(h_m\bar{x})}{\sqrt{\bar{a}^2-\bar{x}^2}} d\bar{x} \tag{8}$$

Note that as f' is dimensionless, with this formulation the integrals appearing in the last two equations turn out to be dimensionless as well.

2.2 Segedin's formulas and extensions

Let us assume that the function f in equation (5) is given by the following expression

$$y = \sum_{n=1}^{N} b_n x^n \tag{9}$$

Normalization provides

$$\bar{y} = \sum_{n=1}^{N} \bar{b}_n \bar{x}^n, \qquad \bar{b}_n = b_n h_m^{n-1} \tag{10}$$

By introducing the coefficients

$$\bar{c}_n = \sqrt{\pi} \frac{\Gamma\left(\frac{n}{2}+1\right)}{\Gamma\left(\frac{n}{2}+\frac{1}{2}\right)} \bar{b}_n \tag{11}$$

where Γ denotes the gamma-function, it is possible to demonstrate that the relation between normalized penetration depth $\bar{h}$ and contact radius $\bar{a}$ can be written in closed-form as

$$\bar{h} = \sum_{n=1}^{N} \bar{c}_n \bar{a}^n \tag{12}$$

Similarly, the expression for the load P becomes

$$P = 2E^* h_m^2 \sum_{n=1}^{N} \frac{n}{n+1} \bar{c}_n \bar{a}^{n+1} \tag{13}$$

The last two equations are commonly attributed to Segedin (Segedin, 1957).

Expressions (12) and (13) allow for deriving other useful relations. The load derivative with respect to normalized penetration is given by

$$P' = \frac{dP}{d\bar{h}} = \frac{dP}{d\bar{a}} \left(\frac{d\bar{h}}{d\bar{a}}\right)^{-1} = 2E^* h_m^2 \left(\sum_{n=1}^{N} n \bar{c}_n \bar{a}^n\right) \cdot \left(\sum_{n=1}^{N} n \bar{c}_n \bar{a}^{n-1}\right)^{-1} = 2E^* h_m^2 \bar{a} \tag{14}$$

It is important to point out that the last relation, which justifies equation (3), can be obtained directly from the general relations (6), as demonstrated in (Pharr et al., 1992).

Finally, the elastic work W done during indentation can be calculated as

$$W = \int_0^h P\, dh = \int_0^{\bar{a}} P \frac{dh}{d\bar{a}} d\bar{a} =$$

$$= 2E^* h_m^2 \int_0^{\bar{a}} \left(\sum_{n=1}^{N} \frac{n}{n+1} \bar{c}_n \bar{a}^{n+1} \right) \left(h_m \sum_{n=1}^{N} n \bar{c}_n \bar{a}^{n-1} \right) d\bar{a} =$$

$$= 2E^* h_m^3 \int_0^{\bar{a}} \left(\sum_{n,s=1}^{N} \frac{ns}{n+1} \bar{c}_n \bar{c}_s \bar{a}^{n+s} \right) d\bar{a} =$$

$$= 2E^* h_m^3 \sum_{n,s=1}^{N} \frac{ns}{(s+n)(n+1)} \bar{c}_n \bar{c}_s \bar{a}^{n+s+1} \tag{15}$$

The last expression will come useful to formulate experimentally accessible dimensionless functions which are independent of E^*.

2.3 Special case

If only one term is retained in the expansion (9), the following direct relation between load and penetration may be obtained by combining equations (12) and (13) together:

$$P = 2E^* h_m^2 \frac{n}{(n+1)\bar{c}_n{}^{1/n}} \bar{h}^{1+1/n} \tag{16}$$

Furthermore, for a conical indenter $n = 1$ and the last expression reduces to

$$P = \frac{E^* h_m^2}{\bar{c}_1} \bar{h}^2 \tag{17}$$

Equation (11) then yields

$$\bar{c}_1 = \sqrt{\pi} \frac{\Gamma\left(\frac{1}{2}+1\right)}{\Gamma\left(\frac{1}{2}+\frac{1}{2}\right)} \bar{b}_1 = \sqrt{\pi} \frac{\sqrt{\pi}/2}{1} \bar{b}_1 = \frac{\pi}{2} \bar{b}_1 \tag{18}$$

By inserting the latter result with $\bar{b}_1 = \cot(\alpha)$ into equation (17) one obtains

$$P = E^* h_m^2 \frac{2}{\pi \cot(\alpha)} \bar{h}^2 \tag{19}$$

which represents the traditional load-penetration formula for a conical indenter of semi-apical angle α, originally derived by Love (Love, 1939).

3. Material and methods

3.1 Numerical simulations

It seems logical to test the validity of the equivalent indenter concept for indented surfaces with realistic geometries. To avoid direct experimental measurements, which would require a huge investment of time and resources, nano-indentation tests are simulated via the finite element software ABAQUS. In this way, a large

number of residual impression profiles can be generated without resorting to atomic force microscope profilometry.

As already explained in the introduction, previous investigations have demonstrated that the Berkovich indentation process can be analyzed by means of the simplified axisymmetric geometry depicted in figure 3-a, where the semi-apical angle of the conical indenter is set to $\alpha = 70.3°$ (Oliver and Pharr, 2004). The latter is represented in ABAQUS by an analytic rigid surface, whereas the sample is assumed to be made of a generic metallic material whose behavior is considered to be isotropic elasto-plastic. A standard large-strain J2-flow plasticity formulation is adopted and the material parameters are chosen as follows: Poisson's ratio is set to $\nu = 0.3$, Young's modulus to $E = 100\ GPa$ and the yield stress σ_y is varied in the range $1x10^{-4}E \div 2x10^{-2}E$, which should be sufficiently wide to cover values for all common metals (Ashby et al., 2010). Concerning hardening, following (Larsson et al., 1996) and (Bolshakov and Pharr, 1998) an isotropic linear law is used, with three different values for the hardening modulus K: $0.05E$, $0.01E$ and $0.002E$.

The interaction between the cone and the sample surface is realized via a finite sliding, surface-to-surface contact discretization with zero friction, as previous studies have reported a minor influence of this last parameter on the results (Larsson et al., 1996)(Sakharova et al., 2009). In addition, in all simulations a maximum indentation depth of 1 micron is used, which is sufficiently deep to ensure that indenter tip rounding effects, often observed during real nano-indentation tests, do not need to be taken into account (Oliver and Pharr, 2004). Accordingly, the height and radius of the cylindrical sample are both set to 100 microns following the criterion proposed by (Poon et al., 2008b), which guarantees fulfillment of the "infinite" half-space assumption, common to all analytical solutions presented in the previous section.

The adopted mesh, visible in figure 3-b, consists of approximately 2000 axisymmetric quadrilateral hybrid elements CAX4H. To avoid excessive distortion close to the indenter tip during loading, an Arbitrary Lagrangean-Eulerian (ALE) adaptive technique is employed (Dassault Systèmes Simulia Corp., 2013). The quality of the mesh is sufficient to ensure a precision of 1 % on the slope of the recorded P vs h curves.

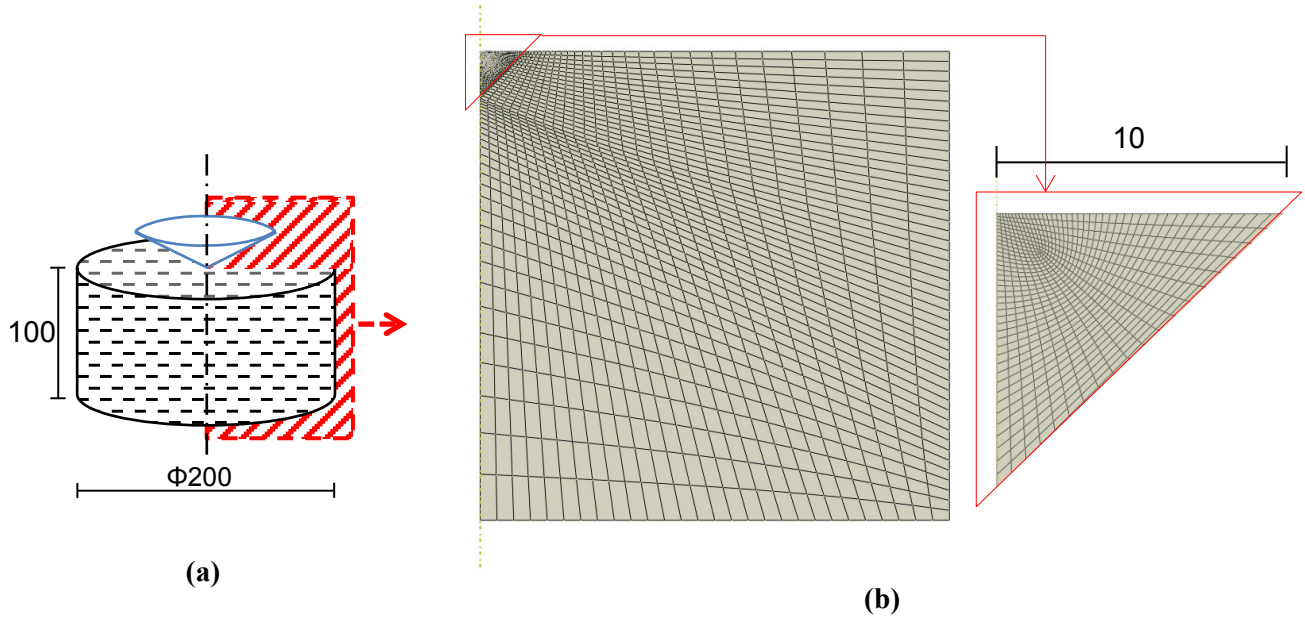

Figure 3: Finite element model for nano-indentation. (a) Geometry of the indenter and of the sample. (b) Mesh adopted. Dimensions are in microns.

3.2 Determination of the equivalent indenter profile

From each ABAQUS simulation, the shape of the residual impression after unloading is extracted in the form of a function $u_r(x)$, which describes the permanent downward displacement of the sample surface relative to the Cartesian coordinate system (x, y) shown in figure 1-b.

The shape of the equivalent indenter profile turns out to be naturally defined by the function

$$f_{eq}(x) = u_r(x) - \left(h_p - x\cot(\alpha)\right) \tag{20}$$

where h_p is the recorded residual plastic penetration, visible in figure 1-a, and α is the semi-apical angle of the conical indenter. For convenience, the last expression can be re-cast in dimensionless form as follows:

$$\bar{f}_{eq}(\bar{x}) = \bar{u}_r(\bar{x}) - \left(\bar{h}_p - \bar{x}\cot(\alpha)\right) \tag{21}$$

In order to obtain a representation for the function $\bar{f}_{eq}(\bar{x})$ which can easily be used in combination with the analytical solutions presented in section 2, the following polynomial approximation is introduced:

$$\bar{f}_{eq}(\bar{x}) \approx \sum_{n=1}^{N} \bar{b}_n \bar{x}^n \tag{22}$$

The optimal choice of the coefficients appearing at the right-hand-side of the last expression depends on the extension of the domain considered for $\bar{f}_{eq}(\bar{x})$. In the present work, two possible options are investigated:

- The "contact" domain, suggested by (Pharr and Bolshakov, 2002): $\bar{x} \in [0, \bar{a}_m]$, where $\bar{a}_m$ is the normalized value of the contact radius at maximum load.
- The "extended" domain: $\bar{x} \in [0,5]$, which is approximately double the size of the previous one.

Figure 4 shows an example of the function $\bar{u}_r(\bar{x})$ extracted from ABAQUS, with indication of the two different domains mentioned above.

3.3 Young's modulus calculation

The $\bar{b}_n$ coefficients determined according to equation (22) can be employed to find analytical estimates for the sample Young's modulus using the simulated force-penetration curves as starting point. In fact, the two functions $P(t)$ and $\bar{h}(t)$ recorded during the elastic unloading stage can be extracted from ABAQUS and used together with the $\bar{b}_n$ to solve the system of equations (11)-(12)-(13) for the function $E^*(t)$, where t indicates the relative time-coordinate with respect to the entire unloading process. Subsequently, conversion to the standard Young's modulus $E(t)$ may be easily performed by means of equation (4), assuming that Poisson's ratio is known.

The function $E(t)$ determined in this way turns out to be defined over 100 points, which simply correspond to the ABAQUS increments the unloading step is subdivided into. An average value of $E(t)$ may then be calculated on the basis of the upper 50 % of the unloading data. The lower 50 % is discarded for three main reasons. Firstly, it is affected by an artificial lack of smoothness due to the fact that the number of mesh elements in contact with the indenter reduces quickly, eventually becoming zero at 100 % unloading. Secondly, as will be explained in the next section, it is sometimes necessary to correct the equivalent indenter profile close to the indenter tip. While this does not sort any significant effect on the top part of the unloading curve, it might adversely affect the results when the contact area becomes very small. Thirdly, in this way the analysis becomes more similar to a real nano-indentation test, in which it is common practice to consider only the upper part of the unloading curve for the calculation of the Young's modulus.

For the sake of clarity, it is important to remark that only the elastic part of the indenter tip penetration is entered in the analytical expressions presented in section 2, i.e. the difference between the absolute penetration relative to the original undeformed sample surface and the residual plastic penetration $\bar{h}_p$. Unless stated otherwise, $\bar{h}(t)$ and $\bar{h}$ will always denote this elastic part of the indenter penetration throughout the rest of the analysis.

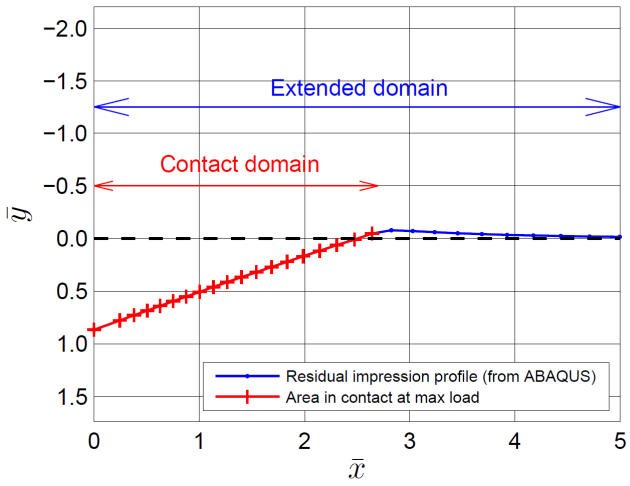

Figure 4: Example of residual impression profile extracted from ABAQUS, with indication of the two different domains considered to approximate the function $\bar{f}_{eq}(\bar{x})$. The data refer to a simulation run using $\sigma_y/E = K/E = 1\%$.

4. Results and Discussion

4.1 Functional dependence of the equivalent indenter shape

Before attempting any description of the relation between force and penetration during unloading using the equivalent indenter concept, it is essential to examine whether or not the analytical form of the function $\bar{f}_{eq}(\bar{x})$ defined in (21) can be considered as a material property.

The first step to clarify this point is to write down explicitly the functional dependence of the function u_r appearing in (20), which gives the shape of the residual impression. It is not difficult to realize that the variables influencing u_r are the maximum penetration achieved during loading, the elastic and plastic material parameters and obviously the coordinate x:

$$u_r = u_r(h_m, E, \nu, \sigma_y, K, x) \tag{23}$$

The dimension matrix associated with the latter expression has a rank equal to 2. As there are 7 physical quantities involved, Buckingham's Pi Theorem (Barenblatt, 1996) indicates that it can be rewritten in terms of $7 - 2 = 5$ dimensionless variables. For the sake of convenience, the following dimensionless groups are chosen:

$$\bar{u}_r = \frac{u_r}{h_m}, \qquad \bar{x} = \frac{x}{h_m}, \qquad \nu, \qquad \frac{\sigma_y}{E}, \qquad \frac{K}{E} \tag{24}$$

so that (23) becomes

$$\bar{u}_r = \Pi_1(\nu, \sigma_y/E, K/E, \bar{x}) \tag{25}$$

Similar arguments may be used to show that the normalized residual penetration $\bar{h}_p$ has to be function of the last three dimensionless groups appearing in (24) (Dao et al., 2001):

$$\bar{h}_p = \Pi_2(\nu, \sigma_y/E, K/E) \tag{26}$$

By inserting relations (25) and (26) into (21) one obtains

$$\bar{f}_{eq}(\bar{x}) = \Pi_1\left(\nu, \frac{\sigma_y}{E}, \frac{K}{E}, \bar{x}\right) - \Pi_2\left(\nu, \frac{\sigma_y}{E}, \frac{K}{E}\right) + \bar{x}\tan(\alpha) \tag{27}$$

The latter relation proves that the shape of the equivalent indenter, i.e. the analytical form of the function $\bar{f}_{eq}(\bar{x})$, depends only on dimensionless combinations of the material parameters and it is hence unaffected by the particular choice of the maximum indentation depth. This guarantees that the results are insensitive to the arbitrary values of h_m and E employed in the present numerical simulations.

Another important observation can be made regarding the $\bar{b}_n$ coefficients defined in (22), which are used to approximate $\bar{f}_{eq}(\bar{x})$. From a mathematical point of view, they can be seen as provided by an operator which accepts $\bar{f}_{eq}(\bar{x})$ and its domain size as input. In the context of the present analysis, the latter is either fixed or defined by the upper limit $\bar{a}_m$ as explained in section 3.2. However, straightforward application of Buckingham's Pi Theorem can show that the normalized value $\bar{a}_m$ of the contact radius at maximum load is also uniquely determined in terms of material properties (Cheng and Cheng, 1999). As a consequence, the $\bar{b}_n$ coefficients turn out to be material parameters as well.

4.2 Shape of the equivalent indenter profile from finite element simulations

Figure 5 shows the equivalent indenter profiles calculated for selected values of the plastic material parameters according to the procedure described in section 3.2. As the "contact" domain assumption is considered, all curves are interrupted in correspondence to the point where $\bar{x} = \bar{a}_m$. As already pointed out by (Pharr and Bolshakov, 2002), it can be seen that the function $\bar{f}_{eq}(\bar{x})$ is not linear, and the deviation from linearity is larger for higher values of the σ_y/E ratio. On the other hand, in contrast to the observations of the previous authors, the function $\bar{f}_{eq}(\bar{x})$ determined from the present simulations is not always monotonic. For large σ_y/E values a small initial decrease is visible, where $\bar{f}_{eq}(\bar{x})$ becomes negative. The reason is that during the final part of the unloading stage, the area of the sample in contact with the indenter gradually shrinks to a point which does not coincide with the indenter tip. As this local lack of monotonicity in $\bar{f}_{eq}(\bar{x})$ near $\bar{x} = 0$ would preclude the application of the general Sneddon's equations (8), the equivalent profiles featuring this characteristic are modified by "flattening" their tips as shown in figure 6-a. It must be emphasized that since the maximum negative value of $\bar{f}_{eq}(\bar{x})$ is always small in comparison to the equivalent indenter size, less than 1% of the

contact radius at maximum load, this shape modification does not sort any significant effects on how the upper part of the unloading curve is described by the equivalent indenter.

The varying curvature of the profiles shown in figure 5 suggests seeking an approximation to $\bar{f}_{eq}(\bar{x})$ based on a 3rd order polynomial. This means that only the first three terms are retained in equation (22). Moreover, preliminary analyses showed that the quadratic term did not play a major role, so that it can be neglected in order to keep the number of fitting parameters as low as possible. Consequently, the following expression is used to approximate $\bar{f}_{eq}(\bar{x})$:

$$\bar{f}_{eq}(\bar{x}) \approx \bar{b}_1\bar{x} + \bar{b}_3\bar{x}^3 \tag{28}$$

Figure 6-b shows an example of equivalent indenter profile fitted using the formula above.

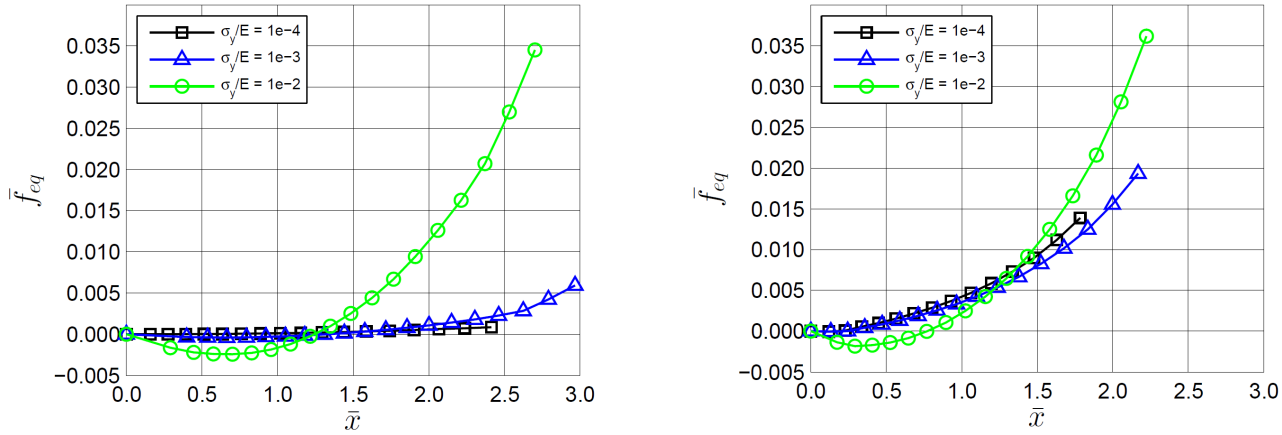

(a) **(b)**

Figure 5: Calculated equivalent indenter profiles for selected values of the ratio σ_y/E, considering the "contact" domain. In (a) the ratio K/E is 0.2 %, whereas in (b) it is 5.0 %.

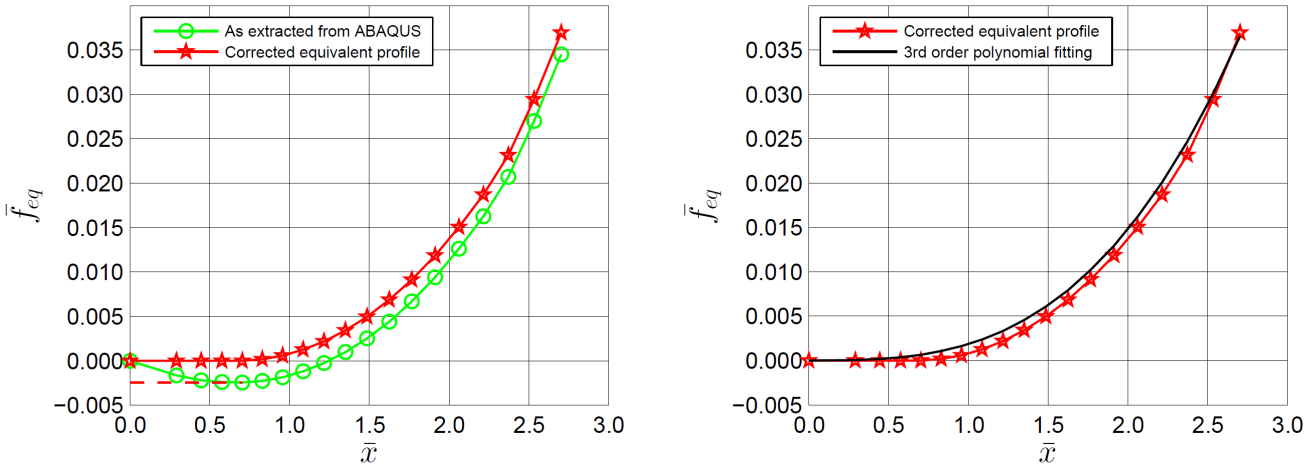

Figure 6: Analysis of the equivalent indenter profile corresponding to $\sigma_y/E = 1\%$ and $K/E = 0.2\%$. (a) Correction for local lack of monotonicity close to the indenter tip. (b) Third-order polynomial fitting of the equivalent indenter profile.

4.3 Validity of the equivalent indenter concept

On the basis of the $\bar{b}_n$ coefficients determined using equation (28), the procedure described in section 3.3 can be carried out to obtain estimates for the sample Young's modulus, which can then be compared with the reference value given as input to the finite element simulations. The agreement between the two provides a quantitative indication of the capability of the equivalent indenter geometry to describe the contact condition with a surface containing a residual impression.

Results obtained in this way are reported in figure 7-a. It can be noticed that a consistent overestimation of the Young's modulus (calculated on the basis of the upper 50 % of the unloading data) seems to be present. Nevertheless, the maximum relative deviations from the reference value are limited to 10 ÷ 15 % for all combinations of material parameters tested. In addition, the associated standard deviation, shown in figure 7-b, is always below 1.5 %. This is important, as in principle the same value of Young's modulus should be obtained independently of the particular point along the force-penetration curve considered for the calculation, i.e. the particular pair of (P, h) values.

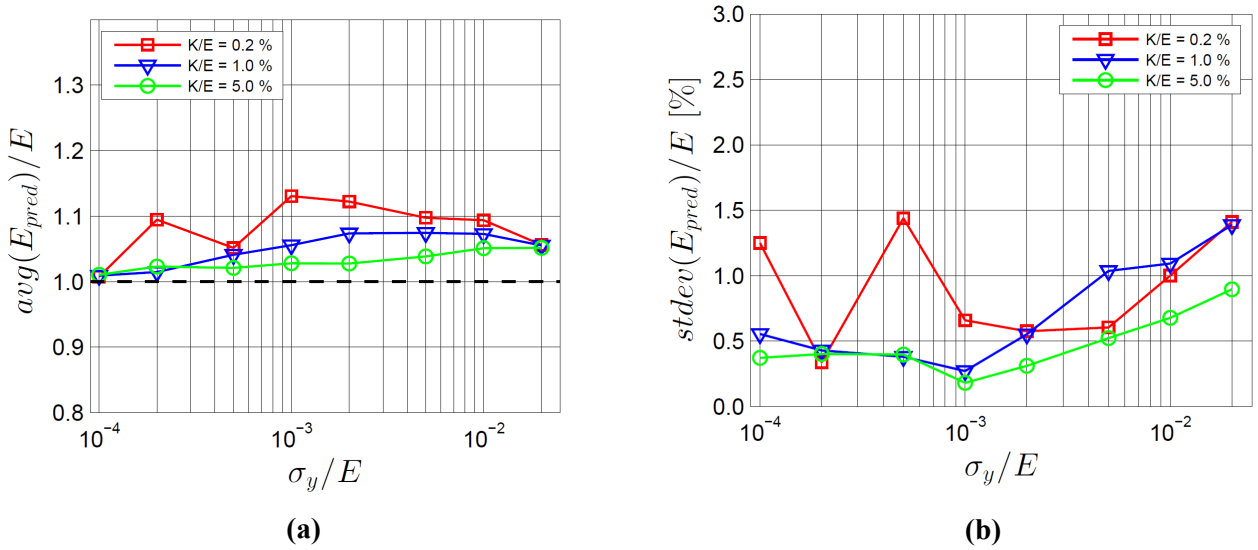

Figure 7: Results for third-order polynomial fitting of the equivalent indenter profile over the "contact" domain. (a) Mean value of the Young's modulus and (b) associated standard deviation.

The consistent Young's modulus overestimation can be explained, at least partly, by the fact that all analytical solutions presented previously neglect the radial displacement of the material points in contact with the axisymmetric indenter. This issue was thoroughly addressed in the work of (Hay et al., 1999), where it was shown that Sneddon's equations are formally correct only for Poisson's ratio equal to 0.5. Conversely, when a certain amount of material compressibility is introduced, a progressive error builds up, which leads to a Young's modulus overestimation of about 8 % for a Poisson's ratio of 0.25. The relevance of this aspect for the present analysis is made clear in figure 8, which shows results obtained for different values of the latter parameter. It can be noticed that the deviation from the reference value of Young's modulus decreases as ν tends to 0.5, in agreement with the considerations of the former authors. As a consequence, by implementing correction factors in the analytical solutions which take into account the influence of Poisson's ratio, such as the ones proposed in (Hay et al., 1999), the 10 ÷ 15 % error bound could probably be reduced by a considerable amount. This means that the equivalent indenter concept is actually very suitable to model the particular contact problem arising during the unloading part of a nano-indentation test, provided that a sufficiently good approximation to the function $\bar{f}_{eq}(\bar{x})$ is available.

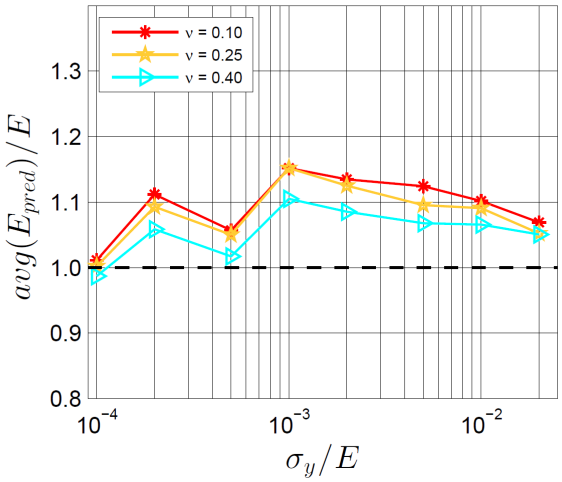

Figure 8: Effect of the Poisson's ratio on the calculated mean value of the Young's modulus using third-order polynomial fitting over the "contact" domain. A value of $K/E = 0.2$ % is assumed.

Regarding this last point, previous works in the field have adopted almost exclusively power-law approximations to the equivalent indenter profile, of the type $\bar{f}_{eq}(\bar{x}) = \bar{b}_n \bar{x}^n$ (Pharr and Bolshakov, 2002; Woirgard and Dargenton, 1997). The main advantage compared to a polynomial approximation is that the elastic analytical relation between load and penetration assumes the simple form of equation (16), implying that the following connection should exist between the exponent n, which describes the shape of the equivalent indenter, and the exponent m, which describes the power-law relation between load and penetration:

$$m = 1 + 1/n \tag{29}$$

The results reported in figure 9-a, based on the present simulations, indicate that this relation is to some extent satisfied, even though deviations as large as 50 % are seen for some combinations of the material parameters. In addition, figure 9-b suggests that the accuracy of the power-law approximation is lower compared to the one associated with expression (28), despite both mathematical formulations possess the same number of fitting parameters. Therefore, low-order polynomials seem to be a better option for describing the shape of the equivalent indenter.

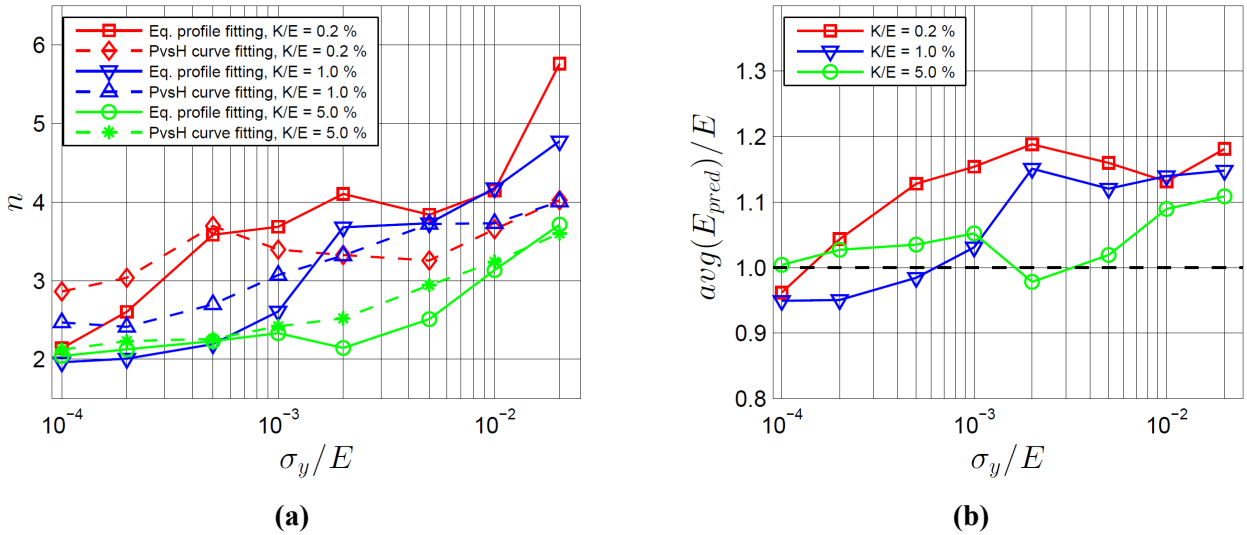

Figure 9: Results for power-law fitting of the equivalent indenter profile over the "contact" domain. (a) Comparison between the power-law exponents derived from fitting either the equivalent indenter profile or the load-penetration curve during the unloading stage. (b) Mean value of the Young's modulus.

Before leaving this section, a few considerations on the choice of the domain over which $\bar{f}_{eq}(\bar{x})$ is approximated need to be made as well. When the "contact" domain is replaced by the "extended" domain visualized in figure 4, the number of terms considered in equation (22) has to be increased, in order to follow the more complex shape of the residual impression beyond the point of contact at maximum load. However, it was observed that the accuracy of the Young's modulus calculation does not improve significantly compared to figure 7, for all combinations of material parameters tested. This indicates that, concerning the description of the elastic contact between the real indenter and the surface containing a residual impression, the information contained in the shape of the $\bar{u}_r$ function beyond $\bar{a}_m$ does not probably play a major role.

4.4 Definition of the inverse problem

The previous section indicates that the equivalent indenter concept does indeed provide a way to describe the elastic unloading stage by means of analytical solutions which are formally valid only for indentation into a flat surface. The following paragraphs discuss how to use this result to extract information about the sample elastic constants from a real nano-indentation test.

Let us assume that the curves $P(t)$ and $\bar{h}(t)$ have been recorded during unloading, with t denoting the time variable. The inverse problem consists in finding an equivalent indenter profile $\bar{f}_{eq}(\bar{x})$ and a value for the reduced Young's modulus E^* such that relations (8) can be satisfied at any instant t for a smooth monotonic function $\bar{a}(t)$.

On the basis of the previous findings, an expression of the type (28) is sufficient to approximate $\bar{f}_{eq}(\bar{x})$. Therefore, only 2 coefficients are needed to characterize the equivalent indenter profile. This means that the inverse problem could in principle be formulated as an optimization problem where suitable values for the 3 scalar unknowns $\bar{b}_1,\ \bar{b}_3$ and E^* have to be determined, which provide values for $P(t)$ and $\bar{h}(t)$ according to Segedin's equations (11) – (13) which are as close as possible to those recorded experimentally. This formulation looks particularly attractive because any deviation of the real indenter from the ideal conical geometry could be naturally taken into account without the need for any area-function calibration.

The number of unknowns can be reduced by one if the following dimensionless function:

$$\Phi(t) = \frac{W(t)}{P(t)h_m} \tag{30}$$

is employed. It should be noted that experimental values for Φ are easily calculated, as the work $W(t)$ can be obtained from a nano-indentation curve via integration. By inserting (15) and (13) into the latter expression, one obtains

$$\Phi\left(\bar{c}_1, \bar{c}_3, \bar{a}(t)\right) = \left(\sum_{n,s=1,3} \frac{ns}{(s+n)(n+1)} \bar{c}_n \bar{c}_s \bar{a}^{n+s+1}\right) \times \left(\sum_{n=1,3} \frac{n}{n+1} \bar{c}_n \bar{a}^{n+1}\right)^{-1} \tag{31}$$

where the $\bar{c}_n$ coefficients are uniquely related to the $\bar{b}_n$ via equation (11). Furthermore, relation (12) can be inverted by means of common formulas for the roots of third-order polynomials. If the obtained expression $\bar{a} = r(\bar{h}, \bar{c}_1, \bar{c}_3)$ is inserted into (31), the original system reduces to the single equation

$$\begin{aligned} \Phi\left(\bar{c}_1, \bar{c}_3, \bar{h}(t)\right) = &\left(\sum_{n,s=1,3} \frac{ns}{(s+n)(n+1)} \bar{c}_n \bar{c}_s r\left(\bar{h}, \bar{c}_1, \bar{c}_3\right)^{n+s+1}\right) \times \\ &\left(\sum_{n=1,3} \frac{n}{n+1} \bar{c}_n r(\bar{h}, \bar{c}_1, \bar{c}_3)^{n+1}\right)^{-1} \end{aligned} \tag{32}$$

A standard optimization algorithm could then be used to determine values for $\bar{c}_1, \bar{c}_3$ which minimize the deviation with the experimental values of Φ over the range of $\bar{h}$ considered. After that, the reduced Young's modulus E^*could be easily calculated from either (13) or (15) just replacing $\bar{a}$ with $r(\bar{h}, \bar{c}_1,\ \bar{c}_3)$.

4.5 Non-uniqueness of the solution

Unfortunately, the particular structure of the general equations (8) implies that the inverse problem previously formulated is not well-posed, in the sense that it does not have a unique solution. In fact, let us assume that a solution $f_{eq,1}(x)$, $E_1^*,\ \bar{a}_1(t)$ has been found, where normalization of the first quantity is ignored momentarily for convenience. An infinite set of solutions can then be constructed as:

$$f_{eq,k}(x) = f_{eq,1}(kx), \quad E_k^* = kE_1^*, \quad \bar{a}_k(t) = \bar{a}_1(t)/k \tag{33}$$

with k being a real number. To prove this, let us write Sneddon's equations (8) corresponding to the 1-solution:

$$\bar{h} = \int_0^{\bar{a}_1} \frac{f'_{eq,1}(h_m\bar{x})}{\sqrt{1-(\bar{x}/\bar{a}_1)^2}}\,d\bar{x}\,, \qquad P = 2E_1^* h_m^2 \int_0^{\bar{a}_1} \frac{\bar{x}^2 f'_{eq,1}(h_m\bar{x})}{\sqrt{\bar{a}_1^2 - \bar{x}^2}}\,d\bar{x} \tag{34}$$

By inserting the relations (33) for E_1^* and $\bar{a}_1$ into (34) one obtains

$$\bar{h} = \int_0^{k\bar{a}_k} \frac{f'_{eq,1}(h_m\bar{x})}{\sqrt{1-\bar{x}^2/(k\bar{a}_k)^2}}\,d\bar{x}\,, \qquad P = 2\frac{E_k^*}{k} h_m^2 \int_0^{k\bar{a}_k} \frac{\bar{x}^2 f'_{eq,1}(h_m\bar{x})}{\sqrt{k^2\bar{a}_k^2 - \bar{x}^2}}\,d\bar{x} \tag{35}$$

Noticing that

$$f'_{eq,1}(x) = \frac{df_{eq,1}(x)}{dx} = \frac{df_{eq,k}(x/k)}{dx} = \frac{df_{eq,k}}{d(x/k)}\frac{d(x/k)}{dx} = \frac{1}{k} f'_{eq,k}(x/k) \tag{36}$$

Substituting into (35) gives

$$\bar{h} = \int_0^{k\bar{a}_k} \frac{f'_{eq,k}(h_m\bar{x}/k)}{k\sqrt{1-\bar{x}^2/(k\bar{a}_k)^2}}\,d\bar{x}\,, \qquad P = 2\frac{E_k^*}{k} h_m^2 \int_0^{k\bar{a}_k} \frac{\bar{x}^2 f'_{eq,k}(h_m\bar{x}/k)}{k\sqrt{k^2\bar{a}_k^2 - \bar{x}^2}}\,d\bar{x} \tag{37}$$

Finally, by making the dummy variable substitution $\bar{x}/k = \bar{z}$ in the integrals appearing in the last formulas one obtains

$$\bar{h} = \int_0^{\bar{a}_k} \frac{f'_{eq,k}(h_m\bar{z})}{\sqrt{1-(\bar{z}/\bar{a}_k)^2}}\,d\bar{z}\,, \qquad P = 2E_k^* h_m^2 \int_0^{\bar{a}_k} \frac{\bar{z}^2 f'_{eq,k}(h_m\bar{z})}{\sqrt{\bar{a}_k^2 - z^2}}\,d\bar{z} \tag{38}$$

which confirms that the k-solution is also a solution.

From a physical point of view, equation (33) states that if the indenter profile is made shallower (resp. steeper) by a scaling transformation, the elastic force-penetration relation does not change if the reduced Young's modulus is increased (resp. decreased) correspondingly by the same scaling factor. What is interesting to note, however, is that the contact depth is the same for all k-solutions:

$$h_{c,k} = f_{eq,k}(h_m\bar{a}_k) = f_{eq,1}(kh_m\bar{a}_k) = f_{eq,1}(h_m\bar{a}_1) = h_{c,1} \tag{39}$$

independently of the specific value of k.

4.5.1 Application to polynomial expansion

To demonstrate an application of the previous theorem, we consider the case of $f_{eq}(x)$ given by the polynomial expansion (9). If we have a solution to the inverse problem, i.e. a set $E_1^*, \bar{b}_{1n}$ such that Segedin's equations (12)-(13) are satisfied

$$\bar{h} = \sum_{n=1}^{+\infty} \bar{c}_{1n} \bar{a}_1^n \,, \qquad P = 2E_1^* h_m^2 \sum_{n=1}^{+\infty} \frac{n}{n+1} \bar{c}_{1n} \bar{a}_1^{n+1} \tag{40}$$

with the $\bar{c}_{1n}$ given by (11), then another solution can be found by setting

$$E_2^* = kE_1^*, \qquad \bar{c}_{2n} = \bar{c}_{1n}(k)^n \tag{41}$$

with k arbitrary. In fact, by inverting the last relations and inserting them into (40), simple algebra provides

$$\bar{h} = \sum_{n=1}^{+\infty} \bar{c}_{2n}(1/k)^n \bar{a}_1^n \,, \qquad P = 2\frac{E_2^*}{k} h_m^2 \sum_{n=1}^{+\infty} \frac{n}{n+1} \bar{c}_{2n}(1/k)^n \bar{a}_1^{n+1}$$

$$\bar{h} = \sum_{n=1}^{+\infty} \bar{c}_{2n} \bar{a}_2^n \,, \qquad P = 2E_2^* h_m^2 \sum_{n=1}^{+\infty} \frac{n}{n+1} \bar{c}_{2n} \bar{a}_2^{n+1} \tag{42}$$

were we have set $\bar{a}_2 = \bar{a}_1/k$ in the last passage.

4.6 Additional constraints

In order to remove the non-uniqueness affecting the inverse problem identified by equation (32), additional assumptions have to be introduced, which somehow pose limitations on the equivalent indenter shape. It is worth noticing that the addition of only one scalar condition of the type

$$g(\bar{b}_1, \bar{b}_3) = 0 \tag{43}$$

would be sufficient to single out a particular solution in equation (41). In principle, the function g should be universal, i.e. independent of the material parameters. However, it seems more realistic to be able to construct one such function which depends on one or more experimentally accessible quantities which are related to the material properties. On the other hand, if the chosen g turned out to be dependent on more than one parameter, the overall idea of using an analytical solution combined with the equivalent indenter concept would break down, as Dao et al. (Dao et al., 2001) showed that the reduced Young's modulus itself can be expressed as a function of two indentation parameters:

$$E^* = \frac{P_m}{h_m^2} \Pi_3 \left(\frac{P_m' h_m}{P_m}, \bar{h}_p \right) \tag{44}$$

where the subscript "m" denotes evaluation of the physical quantity at maximum load. Fortunately, it seems to be actually possible to find g functions which depend on less than two parameters and, at the same time, allow solving the inverse problem to a sufficient level of accuracy in most practical cases. An example of this is given in the next section.

4.7 The Oliver-Pharr method

In the following, it will be shown that the classic Oliver-Pharr method can be considered as an example of an inverse problem in the sense discussed in section 4.4, where very specific assumptions are made for the analytical form of the function $\bar{f}_{eq}(\bar{x})$ and the constraint (43). Remarkably, it turns out that these assumptions are intrinsically embedded in the apparent inconsistencies of the method which were pointed out in connection with expressions (1) and (2).

To begin with, it has to be noted that the latter of these relations can be rewritten in dimensionless form as

$$\bar{a} = \bar{h}_c \tan(\alpha) \tag{45}$$

due to the fact that $\bar{A} = \pi \bar{a}^2$. It is also useful to re-cast equation (1) in the following form

$$\bar{h}_{c,OP} = \bar{h} + \bar{h}_p - \epsilon \frac{P}{P'} \tag{46}$$

We emphasize that now the symbol $\bar{h}$ appearing in the last expression denotes only the elastic part of the penetration, i.e. the difference between the total penetration recorded and the plastic residual penetration $\bar{h}_p$, both normalized by the total maximum penetration h_m. Hence, $\bar{h} + \bar{h}_p$ corresponds to the total penetration.

The first step to unveil the underlying assumptions of the method is to note that the factor P/P' appearing at the right-hand-side of equation (46) was derived in (Oliver and Pharr, 1992) from the original Sneddon's solution for a conical indenter, equation (19). By differentiating that expression, one can easily see that $P/P' = \bar{h}/2$. This result holds also for indenters with power-law profiles, as can be easily checked by taking the derivative of equation (16). By inserting it into (46) one obtains

$$\bar{h}_{c,OP} = \bar{h}_p + (1 - \epsilon/2)\bar{h} \tag{47}$$

As mentioned in the introduction, in the Oliver-Pharr method this formula is used only at maximum load. Consequently, it is possible to use the identity $\bar{h} + \bar{h}_p = 1$ to rewrite it as

$$\bar{h}_{c,OP} = \left(\frac{\bar{h}_p}{1 - \bar{h}_p} + \frac{2 - \epsilon}{2} \right) \bar{h} \tag{48}$$

Finally, equations (45) and (48) can be combined together to obtain

$$\bar{h} = \cot(\alpha) \left(\frac{\bar{h}_p}{1 - \bar{h}_p} + \frac{2 - \epsilon}{2} \right)^{-1} \bar{a} \tag{49}$$

The last expression represents a linear relation between contact radius and elastic penetration. By comparing it with equation (12), it is immediately realized that the constant multiplying $\bar{a}$ at the right-hand-side corresponds to the $\bar{c}_1$ coefficient for an equivalent indenter with linear profile, whose slope is delivered by equation (18) as

$$\bar{b}_{OP} = \frac{2}{\pi}\bar{c}_1 = \frac{2\cot(\alpha)}{\pi}\left(\frac{\bar{h}_p}{1-\bar{h}_p} + \frac{2-\epsilon}{2}\right)^{-1} \tag{50}$$

and whose semi-apical angle α_{OP} turns out to be

$$\alpha_{OP} = \pi/2 - \mathrm{atan}\left(\bar{b}_{OP}\right) \tag{51}$$

A few crucial observations can be made at this point. First of all, the Oliver-Pharr method can be considered as entirely based on the equivalent indenter concept, without any inconsistencies. Secondly, such equivalent indenter is assumed to be conical a priori. Thirdly, the associated semi-apical angle turns out to be given by equations (50)-(51), where the former simply represents the particularization of the g constraint (43).

Concerning this last aspect, figure 10-a shows the dependence of α_{OP} on $\bar{h}_p$. Two different values for the constant ϵ are considered: 0.72, which is typical of a conical indenter, and 0.75, which relates to a paraboloid but is often used in practice as it seems to provide better results (Oliver and Pharr, 2004). It can be noted that when the material is perfectly elastic, i.e. $\bar{h}_p = 0$, α_{OP} reduces to $\alpha = 70.3^0$, the semi-apical angle of the real indenter. This happens exactly for $\epsilon = 0.72$, whereas a small deviation is seen for $\epsilon = 0.75$. Conversely, when the material exhibits extensive plastic deformation and $\bar{h}_p$ tends to one, α_{OP} approaches 90 degrees, independently of the ϵ value. This is sensible, as during loading the material conforms perfectly to the real indenter shape, which is retained during subsequent unloading due to negligible elastic recovery. A reason for the big success of the Oliver-Pharr method could be this concealed convenient choice of the equivalent indenter profile, which explains why the underlying elastic equations describe the unloading stage relatively well even in the presence of a non-negligible residual impression on the sample.

The present analysis is also useful to re-examine the predictive capabilities of the Oliver-Pharr method under a different perspective. As extensively discussed in the literature (Bolshakov and Pharr, 1998)(Hay et al., 1999)(Poon et al., 2008a) errors above 10 % are likely when $\bar{h}_p$ grows beyond 0.7, due to extensive plastic flow with associated pile-up, and these are usually larger for materials showing little amount of work-hardening. This seems to be the case also for the present findings, reported in figure 10-b. The visible strong influence of the hardening parameter indicates that, for a given value of $\bar{h}_p$, multiple values of the equivalent indenter angle α_{OP} would be required to match the theoretical value of Young's modulus. As a consequence, to further improve the accuracy of the method, equation (50), which represents the g constraint (43), should be modified somehow to include a dependency on some other experimentally accessible quantities related to work-hardening. Nevertheless, this would make the method less attractive compared to other procedures suggested in the literature, for the reason explained in the last paragraph of section 4.6.

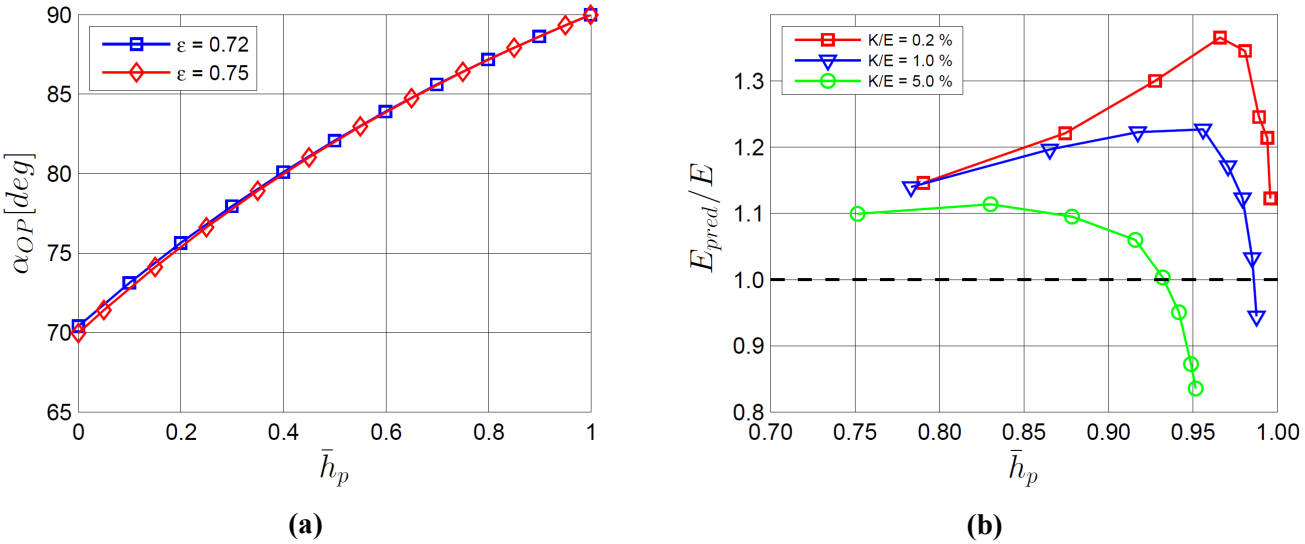

Figure 10: The Oliver-Pharr method. (a) Semi-apical angle of the implicitly assumed equivalent conical indenter as a function of the ratio between residual and maximum penetration. (b) Young's modulus predictions using the data of the present simulations.

5. Conclusions

In this paper, a thorough analysis of the equivalent indenter concept applied to nano-indentation was carried out, motivated by the fact that previous works in the field were apparently incomplete, having neglected the requirement of a consistent relation between contact depth and projected contact area. Dimensional analysis was initially used to prove that the shape of the axisymmetric equivalent indenter can be considered as a material property, provided that size-effects are negligible. Subsequently, it was shown that such shape can effectively be employed to describe the nano-indentation unloading stage by means of elastic analytical solutions which are formally valid only for indentation into a flat surface. This intermediate result was then used to formulate the problem of extracting Young's modulus from the unloading curve as an optimization problem. However, it was also proved that the latter does not have a unique solution, due to the particular mathematical structure of Sneddon's equations, and additional constraints are needed to set limitations on the admissible equivalent indenter shapes. An example of such constraint is hidden in the apparent inconsistencies of the Oliver-Pharr method, which was demonstrated to be based on an equivalent conical indenter whose semi-apical angle depends on the ratio between residual and total penetration. Specifically, this angle tends to 90 degrees when the material exhibits extensive inelastic deformation, whereas it reduces to the one characteristic of the real indenter for a perfectly elastic material. This offers a new physical explanation for why the elastic equations on which the

method is based on, which are formally valid for contact with a perfectly flat surface only, describe the unloading stage relatively well even in the presence of a non-negligible residual impression on the sample.

Acknowledgements

This research did not receive any specific grant from funding agencies in the public, commercial, or not-for-profit sectors.

References

Ashby, M., Shercliff, H., Cebon, D., 2010. Materials : engineering, science, processing and design. Elsevier Butterworth-Heinemann.

Barenblatt, G.I., 1996. Scaling, Self-similarity, and Intermediate Asymptotics. Cambridge University Press, Cambridge.

Bolshakov, A., Oliver, W.C., Pharr, G.M., 1995. An explanation for the shape of nanoindentation unloading curves based on finite element simulation. Mater. Res. Soc. Symp. Proc. 356, 675–680.

Bolshakov, A., Pharr, G.M., 1998. Influences of pileup on the measurement of mechanical properties by load and depth sensing indentation techniques. J. Mater. Res. 13, 1049–1058.

Boussinesq, J., 1885. Applications des potentiels a l'etude de equilibre et du mouvement des solides elastiques, Gauthier-Villars. Paris.

Cheng, Y.-T., Cheng, C.-M., 1998. Relationships between hardness, elastic modulus, and the work of indentation. Appl. Phys. Lett. 73, 614. doi:10.1063/1.121873

Cheng, Y.-T., Cheng, C.-M., 1999. Scaling relationships in conical indentation of elastic-perfectly plastic solids. Int. J. Solids Struct. 36, 1231–1243. doi:10.1016/S0020-7683(97)00349-1

Cheng, Y.-T., Cheng, C.-M., 2004. Scaling, dimensional analysis, and indentation measurements. Mater. Sci. Eng. R Reports 44, 91–149. doi:10.1016/j.mser.2004.05.001

Cheng, Y.-T., Li, Z., Cheng, C.-M., 2002. Scaling relationships for indentation measurements. Philos. Mag. A 82, 1821–1829. doi:10.1080/01418610210135043

Dao, M., Chollacoop, N., Van Vliet, K.J., Venkatesh, T.A., Suresh, S., 2001. Computational modeling of the forward and reverse problems in instrumented sharp indentation. Acta Mater. 49, 3899–3918. doi:10.1016/S1359-6454(01)00295-6

Dassault Systèmes Simulia Corp., 2013. Abaqus 6.13, Abaqus Analysis User's Guide section 12.2.7.

Doerner, M.F., Nix, W.D., 1986. A method for interpreting the data from depth-sensing indentation instruments. J. Mater. Res. 1, 601–609. doi:10.1557/JMR.1986.0601

Fischer-Cripps, A.C., 2006. Critical review of analysis and interpretation of nanoindentation test data. Surf. Coatings Technol. 200, 4153–4165. doi:10.1016/j.surfcoat.2005.03.018

Fischer-Cripps, A.C., 2011. Nanoindentation. Springer.

Harding, J.W., Sneddon, I.N., 1945. The elastic stresses produced by the indentation of the plane surface of a semi-infinite elastic solid by a rigid punch. Proc. Camb. Philol. Soc. 41, 16–26.

Hay, J.C., Bolshakov, A., Pharr, G.M., 1999. A critical examination of the fundamental relations used in the analysis of nanoindentation data. J. Mater. Res. 14, 2296–2305.

Larsson, P.-L., Giannakopoulos, A.E., SÖderlund, E., Rowcliffe, D.J., Vestergaard, R., 1996. Analysis of Berkovich indentation. Int. J. Solids Struct. 33, 221–248. doi:10.1016/0020-7683(95)00033-7

Li, Z., Cheng, Y.-T., Yang, H.T., Chandrasekar, S., 2002. On two indentation hardness definitions. Surf. Coatings Technol. 154, 124–130. doi:10.1016/S0257-8972(02)00021-X

Love, A.E.H., 1939. Bousinnesq's problem for a rigid cone. Q. J. Math. os-10, 161–175. doi:10.1093/qmath/os-

10.1.161
Mata, M., Alcala, J., 2003. Mechanical property evaluation through sharp indentations in elastoplastic and fully plastic contact regimes. J. Mater. Res. 18, 1705–1709.
Oliver, W.C., Pharr, G.M., 1992. An improved technique for determining hardness and elastic modulus using load and displacement sensing indentation experiments. J. Mater. Res. 7, 1564–1580.
Oliver, W.C., Pharr, G.M., 2004. Measurement of hardness and elastic modulus by instrumented indentation: Advances in understanding and refinements to methodology. J. Mater. Res. 19, 3–20.
Pharr, G.M., Bolshakov, A., 2002. Understanding nanoindentation unloading curves. J. Mater. Res. 17, 2660–2671.
Pharr, G.M., Oliver, W.C., Brotzen, F.R., 1992. On the generality of the relationship among contact stiffness, contact area, and elastic modulus during indentation. J. Mater. Res. 7, 613–617.
Poon, B., Rittel, D., Ravichandran, G., 2008a. An analysis of nanoindentation in elasto-plastic solids. Int. J. Solids Struct. 45, 6399–6415. doi:10.1016/j.ijsolstr.2008.08.016
Poon, B., Rittel, D., Ravichandran, G., 2008b. An analysis of nanoindentation in linearly elastic solids. Int. J. Solids Struct. 45, 6018–6033.
Sakharova, N.A., Fernandes, J.V., Antunes, J.M., Oliveira, M.C., 2009. Comparison between Berkovich, Vickers and conical indentation tests: A three-dimensional numerical simulation study. Int. J. Solids Struct. 46, 1095–1104. doi:10.1016/j.ijsolstr.2008.10.032
Segedin, C.M., 1957. The relation between load and penetration for a spherical punch. Mathematika 4, 156. doi:10.1112/S0025579300001236
Sneddon, 1948. Boussinesq's problem for a rigid cone. Proc. Camb. Philol. Soc. 44, 492–507.
Sneddon, I.N., 1965. The relation between load and penetration in the axisymmetric boussinesq problem for a punch of arbitrary profile. Int. J. Eng. Sci. 3, 47–57. doi:10.1016/0020-7225(65)90019-4
Woirgard, J., Dargenton, J.C., 1997. An alternative method for penetration depth determination in nanoindentation measurements. J. Mater. Res. 12, 2455–2458.
Woirgard, J., Dargenton, J.-C., Tromas, C., Audurier, V., 1998a. A new technology for nanohardness measurements: principle and applications. Surf. Coatings Technol. 100–101, 103–109. doi:10.1016/S0257-8972(97)00597-5
Woirgard, J., Tromas, C., Girard, J.C., Audurier, V., 1998b. Study of the mechanical properties of ceramic materials by the nanoindentation technique. J. Eur. Ceram. Soc. 18, 2297–2305. doi:10.1016/S0955-2219(98)00083-1

Appendix F
PAPER VI

Acta Materialia 121 (2016) 173–180

Contents lists available at ScienceDirect

Acta Materialia

journal homepage: www.elsevier.com/locate/actamat

Full length article

Three-dimensional local residual stress and orientation gradients near graphite nodules in ductile cast iron

Y.B. Zhang [a, *], T. Andriollo [b], S. Fæster [a], W. Liu [c], J. Hattel [b], R.I. Barabash [d]

[a] Section for Materials Science and Advanced Characterization, Department of Wind Energy, Technical University of Denmark, Risø Campus, Roskilde, DK-4000, Denmark
[b] Department of Mechanical Engineering, Technical University of Denmark, DK-2800, Kgs. Lyngby, Denmark
[c] Advanced Photon Source, Argonne National Laboratory, Argonne, IL, 60439-4800, USA
[d] Materials Science & Technology Division, Oak Ridge National Laboratory, P.O. Box 2008, Oak Ridge, TN, 37831-6118, USA

ARTICLE INFO

Article history:
Received 14 August 2016
Received in revised form
4 September 2016
Accepted 6 September 2016

Keywords:
Cast iron
Residual strain/stress
Plastic deformation
Differential aperture X-ray microscopy (DAXM)
Finite element modeling

ABSTRACT

A synchrotron technique, differential aperture X-ray microscopy (DAXM), has been applied to characterize the microstructure and analyze the local mesoscale residual elastic strain fields around graphite nodules embedded in ferrite matrix grains in ductile cast iron. Compressive residual elastic strains are measured with a maximum strain of ~$6.5–8 \times 10^{-4}$ near the graphite nodules extending into the matrix about 20 μm, where the elastic strain is near zero. The experimental data are compared with a strain gradient calculated by a finite element model, and good accord has been found but with a significant overprediction of the maximum strain. This is discussed in terms of stress relaxation during cooling or during storage by plastic deformation of the nodule, the matrix or both. Relaxation by plastic deformation of the ferrite is demonstrated by the formation of low energy dislocation cell structure also quantified by the DAXM technique.

1. Introduction

Ductile cast iron (DCI) is an attractive engineering material, as it has strength and toughness very similar to steel, and the machinability advantages make it very cost effective [1]. An example of industrial applications is the heavy components for wind turbine, e.g. the main shaft. One design requirement for such components is good fatigue resistance, as the fatigue failure is a main failure mode during their service life [2].

From a microscopic point of view, DCI is a composite material, consisting of graphite nodules embedded in a metal matrix which, in most engineering applications, can be either ferrite, or pearlite or a mixture of the two [1]. The differences in the thermal expansion coefficients between the metal matrix and the graphite nodules can lead to local thermal residual stresses in the composites during cooling from the processing temperature to room temperature [3,4]. Due to the presence of the local residual elastic stresses, fatigue cracks may be initiated at the nodules because of overstrain, as the local residual stresses may be larger than the flow stress of the metal matrix. But they may also be lower as they may relax by plastic deformation of the nodules or the surrounding volume [5]. In the past many studies have been conducted to quantify and model the residual stresses in metal matrix composites containing particles that are harder than the metal matrix, e.g. SiC or Al_2O_3 reinforced aluminum matrix composite [6,7] and Al/W metal matrix composite [8]. For a system like DCI, where the particles (graphite nodules) are considerably softer than the metal matrix, there has however not been much knowledge about the local residual stress. Many researchers believed the local residual stresses to be minor, considering the fact that graphite is soft; and the local residual stresses were neglected in most micromechanical models [9]. However, recently the formation of residual stress comparable to the material yield stress has been predicted by finite element models in DCI [10]. To optimize design and processing of DCI components, the magnitude of the local mesoscale residual stresses must therefore be known.

It is however a challenging task to quantify local residual stresses experimentally. Recently, the development of new experimental characterization techniques has given promising possibilities. For example, a novel synchrotron X-ray technique, the so-

* Corresponding author.
E-mail address: yubz@dtu.dk (Y.B. Zhang).

http://dx.doi.org/10.1016/j.actamat.2016.09.009
1359-6454/

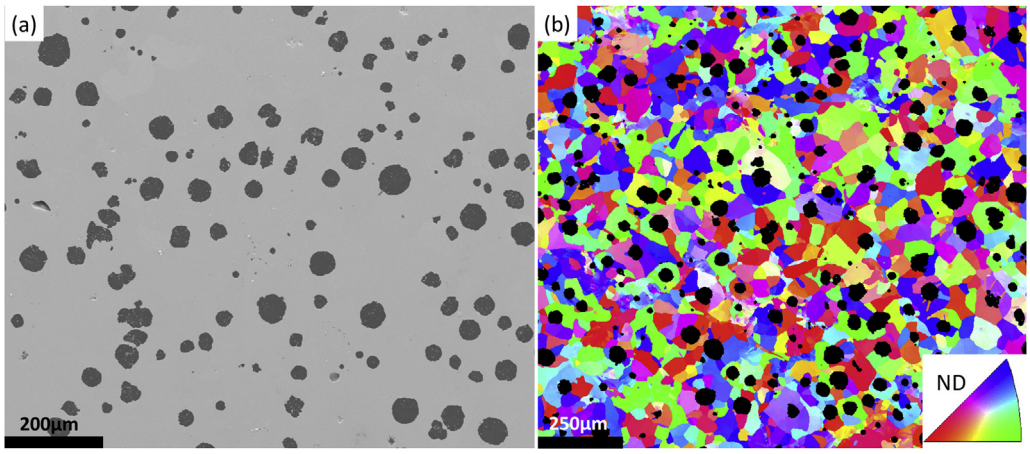

Fig. 1. Microstructures of the DCI showing the graphite nodules and metal matrix. (a) Scanning electron microcopy image and (b) EBSD map. In (a) dark regions are graphite nodules and the rest is metal matrix, while in (b) the black particles are graphite nodules and the colored grains are the metal matrix. The colors of the matrix grains correspond to the crystallographic orientation along the specimen surface normal direction (ND) (see the insert).

Table 1
Chemical composition of the sample (mass%).

C	Si	Mn	P	S	Cr	Ni	Co	Cu	Ti	V	Mg	Ce	Se
3.68	2.30	0.22	0.015	0.011	0.027	0.048	0.024	0.016	0.017	0.014	0.11	0.042	0.043

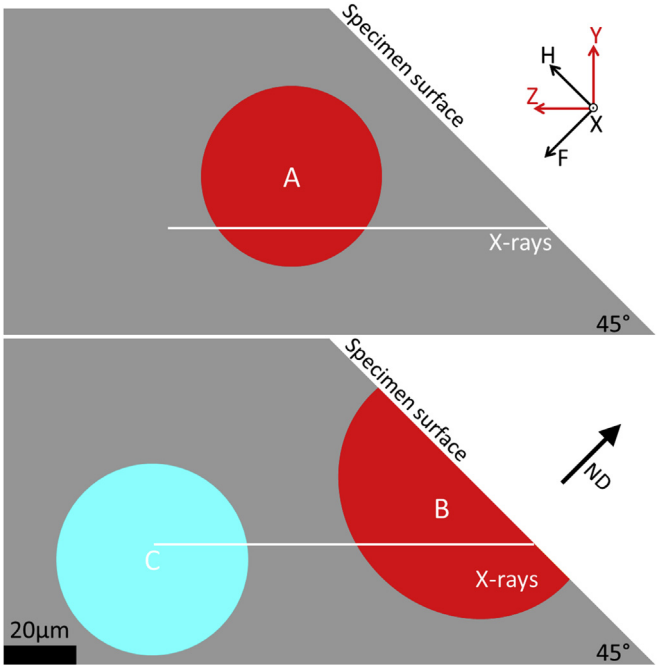

Fig. 2. Sketches showing a side view of the detailed scanning positions relative to the selected nodules. The selected nodules are marked by A, B and C. Specimen surface normal direction (ND) is marked by the black arrow. The white lines represent the projections of the mapping planes illuminated by the incoming X-rays, which are along the Z direction.

called differential aperture X-ray microscopy (DAXM), has been developed during the last 15–20 years for non-destructive 3D characterization of microstructure and local elastic strains [11,12]. With DAXM, local elastic strain distribution inside individual grains has been measured in e.g. deformed bicrystal Ni [13] and NiAl-Cr(Mo) composite [14]. The use of focused microbeam offers spatial resolutions of sub-micrometers [15].

Table 2
Sizes and positions of the selected three nodules.

Graphite nodule	Diameter (μm)	Depth (μm)[a]
A	50	40
B	72	10
C	63	78

[a] Depth means the perpendicular distance from the center-of-mass of the nodules to the sample surface.

In this study, we use DAXM to characterize the microstructures and local residual strains/stresses in matrix grains surrounding graphite nodules in a DCI sample. The objective of the study is to answer the following questions: i) are the matrix grains plastically deformed? ii) what is the magnitude of the residual elastic stress and is it comparable with the flow stresses of the cast iron? iii) how the residual elastic stress distributes? and iv) how residual stress relaxes? A DCI sample is chosen based on a previous study, where the fatigue properties of the sample are already available in a large data base. The results on the local residual stresses will provide a new aspect to evaluate the obtained fatigue properties.

2. Material and methods

2.1. Materials

Metal mold DCI was chosen for the study. A specimen was extracted from the head of a sample that has been fatigue tested to failure after ~5 million cycles under stress level 5.5 as described in Ref. [16]. It therefore was considered as not affected by the fatigue test. The sample consists of almost spherical graphite nodules and a metal matrix with a relatively homogeneous structure, being mainly ferrite with a small fraction of perlite (~5%). The graphite nodules were distributed relatively homogeneously in the metal matrix (see Fig. 1a). The mean size (equivalent circle diameter) and volume fraction of the graphite nodules were ~30 μm and 11.5%, respectively. The mean distance between nodules and the

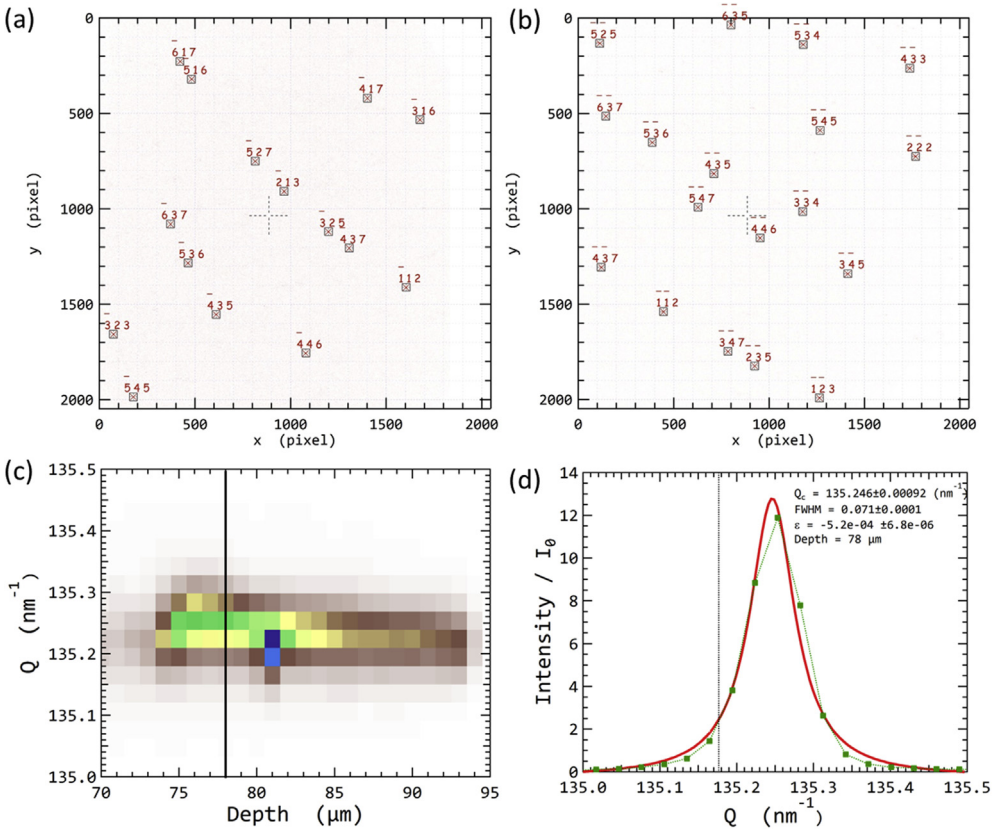

Fig. 3. Illustration of orientation indexing based on white beam Laue diffraction patterns and determination of crystallographic plane spacing. (a) and (b) show two examples of indexed depth-resolved Laue diffraction patterns. (a) and (b) are from the grains marked by white boxes in Fig. 4a and b, respectively. The crosses in dashed lines in (a) and (b) mark the diffraction center. (c) The diffraction vector, Q, as a function of depth for one wire energy scan corresponding to the (−3 2 5) Laue spot in (a). (d) Fitted intensity distribution for the (−3 2 5) Laue spot for the depth marked by the black vertical line at the frame in (c). The center of the fitted Q-distribution, Q_C, is used for determination of the crystallographic plane spacing. The dashed line in (d) marks the Q value for d_0 of the (−3 2 5) crystallographic plane determined based on the lattice parameter in Section 2.2.

maximum nodule size are both ~70 μm. The ferrite matrix has an average grain size of ~30 μm (Fig. lb), measured by electron backscattered diffraction in a Zeiss Supra 35 scanning electron microscope using a Channel 5 software from HKL Technology. The chemical composition of the sample is listed in Table 1.

2.2. Lattice parameter

It is known that the ferrite lattice parameter depends on the amount of solute elements [17]. For the present material, the main alloying elements, i.e. C, Si, and Mn, were considered for the calculation of the lattice parameter. The resulting ferrite lattice parameter was calculated using a function that was deduced based on various publications [17]:

$$a_0 = a_{Fe} + \left(3a_{Fe}^2\right)^{-1} \times \left[(a_{Fe} - 0.001297w_C)^2(a_{Fe} + 0.011606w_C) - a_{Fe}^3\right] - 0.0006w_{Si} + 0.0006w_{Mn} \quad (1)$$

where $a_{Fe} = 2.8664$ Å is the lattice parameter of pure ferrite, and w_x is the weight percentage of x element (x = C, Si and Mn). For the present sample, the Si and Mn contents listed in Table 1 and a maximum solubility of 0.005 wt% of C in ferrite at room temperature were used as w_{Si}, w_{Mn} and w_C, respectively. The lattice parameter for the current ferrite was calculated to be $a_0 = 2.8653$ Å using Eq. (1).

2.3. X-ray tomography

To assist the synchrotron measurements, the 3D distribution of the graphite nodules was characterized by X-ray tomography using a Zeiss Xradia 520 Versa micro-CT system. For the CT scan, a polychromatic conical beam with X-ray energies up to 140 keV and 1401 image projections over a rotation of 360° were used. For the present study, two nodules with size ≥50 μm were selected for residual stress measurements: one nodule beneath the specimen surface, defined as nodule A, and one nodule exposed to the specimen surface, defined as nodule B, see Fig. 2. Nodule A represents a bulk nodule, while nodule B represents a surface nodule. Part of another nodule, defined as nodule C, which was neighboring to nodule B, has also been illuminated. Some of the results around this nodule are included in the analysis. The distance of center-of-mass between nodules B and C is about 95 μm. Nodule A is about 400 μm away from nodule B/C. The sizes and distances between the center-of-mass of the selected nodules and the specimen surface are given in Table 2.

2.4. DAXM experiment

The differential aperture X-ray microscopy (DAXM) was performed at beam line 34-ID-E at the Advanced Photon Source (APS), Argonne National Laboratory [18]. In the DAXM experiment, the X-rays were focused at the specimen using two non-dispersive

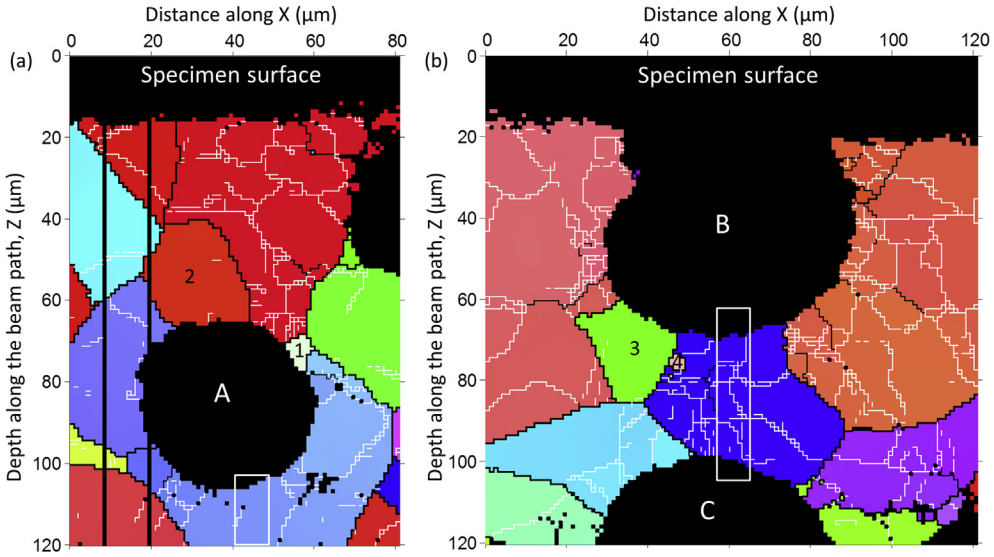

Fig. 4. Microstructures of the DCI near selected nodules characterized using white beam DAXM. (a) and (b) showing microstructures around the selected graphite nodules A and B/C, respectively. In the maps, dislocation boundaries with misorientation angles in the range of 0.1–1°, 1–3°, and >3° are shown in thin white, thin black and thick black lines, respectively. The colors of the matrix grains correspond to the crystallographic orientation along the specimen surface normal direction in the specimen coordinate system (XHF system in Fig. 2). The color code is the same as that in the insert in Fig. 1b. The two white boxes mark regions where monochromatic energy scans were conducted. The numbers mark grains, which are nearly deformation-free. The two black lines in (a) were caused by a technical fault during the Pt-wire scans, and the data were not recorded for that two positions. The black individual pixels in the matrix away from the nodules are non-indexed.

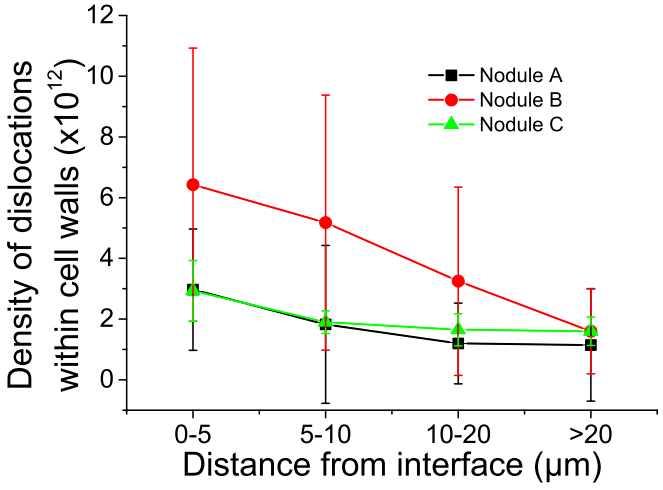

Fig. 5. Average dislocation density as a function of distance from interface. The dislocation densities are calculated from the dislocation boundaries with misorientation angles in the range 0.1–3° [21]. The error bars were estimated based on the variations in the distances between the dislocation boundaries, reflecting the differences between matrix grains.

Kirkpatrick-Baez (K-B) focusing mirrors. The resulting microbeam has a Lorentzian profile and a full-width half maximum of ~0.5 μm. The specimen was mounted on an inclined holder at a 45° incidence angle to the incoming X-ray beam, and was scanned horizontally by moving the specimen stage with a step size of 1 μm. Two sections through the selected nodules were scanned. The detailed scanning position relative to the selected nodules is sketched in Fig. 2. The Laue diffraction patterns from the whole volume within the incident microbeam were recorded on a flat panel detector (409.6 × 409.6 mm^2, 2048 × 2048 pixels) mounted in 90° reflection geometry 510.3 mm above the specimen. The detector's geometry with respect to the incident beam was calibrated using a standard strain-free silicon single crystal. To resolve the diffraction pattern from each volume element at different depths, a Pt-wire of 50 μm diameter was used as a differential aperture and scanned at a distance of ~200 μm from the specimen surface. The Laue patterns at each depth were reconstructed by ray-tracing algorithm using the LaueGo software available at APS beamline 34-ID-E [19]. The reconstructions were conducted to a depth of about 100 μm into the specimen with a step size of 1 μm.

Two beam modes were used in the present study: first a polychromatic beam was used to determine the orientations of the matrix grains; then a monochromatic beam was used for determining absolute lattice parameters of selected grains in the mapped sections. Two examples of depth-resolved Laue diffraction patterns for two probed grains from polychromatic scans are shown in Fig. 3a and b. The patterns were indexed, from which the hkl indices of individual spots as well as their corresponding X-ray energies were determined [19]. Based on the energies and spot positions, a Laue spot with high intensity and diffraction vector approximately parallel to the specimen surface normal direction, was chosen for the monochromatic energy scan for each selected grain. From this energy scan, the intensity distributions as a function of the diffraction vector $Q = 2\pi/d$ (Q-distribution) were determined for the selected diffraction Laue spot at all depths, see for example Fig. 3c, which was obtained from the Laue spot (−3 2 5) shown in Fig. 3a. At each depth, the Q-distribution was fitted using a Gaussian function and the center of the distribution, Q_C, was used to determine the absolute diffraction plane spacing, d (see Fig. 3d).

3. Results

3.1. Depth-dependent grain orientation distribution from polychromatic scans

The depth-dependent 3D grain orientation distributions obtained from DAXM around the selected nodules are shown in Fig. 4. Here the ferrite matrix around the selected nodules is shown in color and the graphite nodules are shown as black sphere-like blocks. The three selected nodules are marked by A, B and C. Two

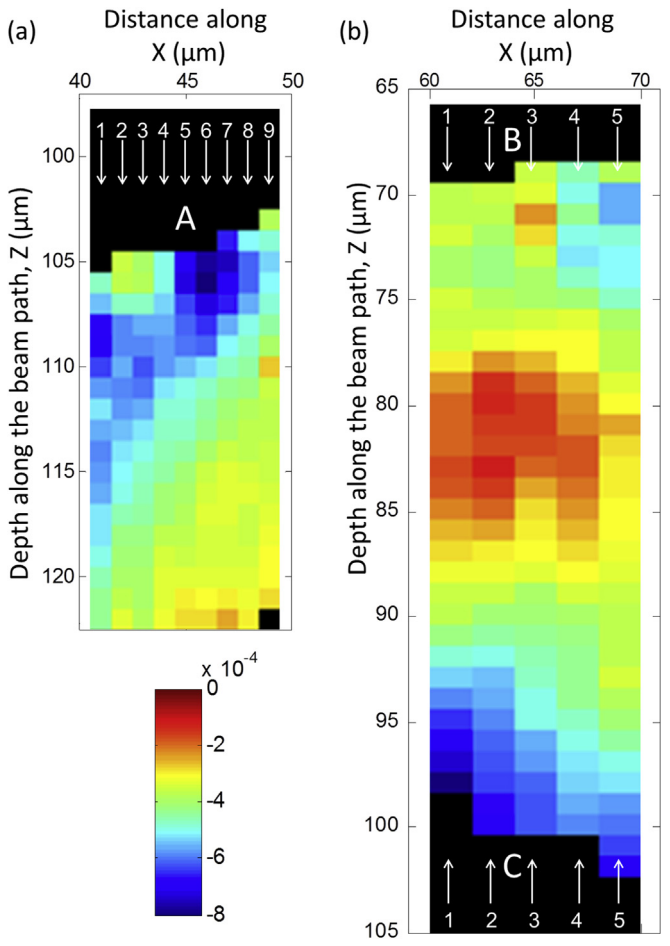

Fig. 6. Maps colored according to the strains determined based on the monochromatic energy scans. The strains in (a) and (b) are calculated along the [-3 2 5] and [-3 -3 4] directions for the grains marked by the white boxes in Fig. 4a and b, respectively.

neighboring graphite nodules are also partly seen. In the matrix grains, a critical angle of ~0.1° is used for revealing the detailed boundary structure, and a critical angle of 3° is used for defining individual grains in the matrix. It is evident that most of the grains are deformed containing dislocation boundaries with misorientation angles below 1°, and the dislocation boundaries are organized in a cell structure. Only a few grains with relatively small sizes (<25 μm) are nearly deformation-free (see the numbered grains in Fig. 4). This may be related to an effect of grain orientations [20].

The grains around nodule B contain evidently more dislocation boundaries as well as more boundaries with misorientation between 1 and 3° (seen as thin black lines) than those around nodules A and C. To quantify the local plastic strains in the matrix grains around the nodules, the average dislocation densities grouped within cell-wall dislocation boundaries at different distances from the nodule/matrix interface are calculated based on the microstructure using the following equation [21],

$$\rho = K/D_c \cdot \theta_c/b, \tag{2}$$

where K is a number typically equal to 3, D_c is the average spacing between dislocation boundaries, θ_c is the average misorientation angle across the dislocation boundaries, and b is Burgers vector. All dislocation boundaries with misorientation angles in the range 0.1–3° are included for the calculation, i.e. the grain boundaries are not included. The results are shown in Fig. 5. It is found that the average cell-wall dislocation densities are large at places close to the nodules, and decrease with increasing distance from the nodule/matrix interface. The maximum cell-wall dislocation density around nodule B is ~6.4 × 10^{12} m^{-2}, which is about twice of those around nodules A and C. The cell-wall dislocation density in the matrix away (>20 μm) from nodule is in the range 1.2–1.6 × 10^{12} m^{-2}.

3.2. Monochromatic energy scans

Two grains marked by the white boxes in Fig. 4 were chosen for the monochromatic energy scans to determine the absolute crystallographic lattice plane spacings. Diffraction from the (−3 2 5) and (-3 -3 4) planes was used for the grains around nodules A and B/C, respectively, as their normals are nearly parallel to the specimen normal direction (see Fig. 3a and b), with deviation angles of ~3.5° and ~3°, respectively. Based on the measured absolute crystallographic plane spacings and the lattice parameter specified in Section 2.2, the strains along the selected crystallographic directions (roughly perpendicular to the nodule/matrix interface) were determined. For the areas around nodules A and B/C, a step size of 1 μm and 2 μm, respectively, was used.

The results are shown in Fig. 6. For the grain around nodule A, compressive strains are observed for most part of the grain, and they are higher at regions close to the interface than in the interior volume. For the grain in-between nodules B and C, compressive

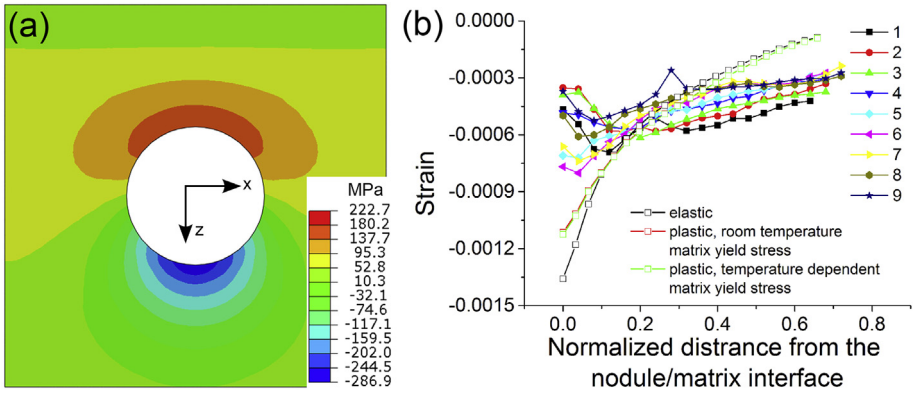

Fig. 7. Comparison between the experimental and modeling results. (a) distribution of σ_{33} component at a X-Z section equivalent to that marked by white line in Fig. 2 for nodule A, calculated assuming linear elastic behavior of the matrix. (b) The ε_{33} profiles from experiments and modeling. The experimental profiles are converted from the data in Fig. 6a, each curve corresponds to each vertical line. The modeling profiles are averaged over 9 lines geometrically equivalent to those in Fig. 6a.

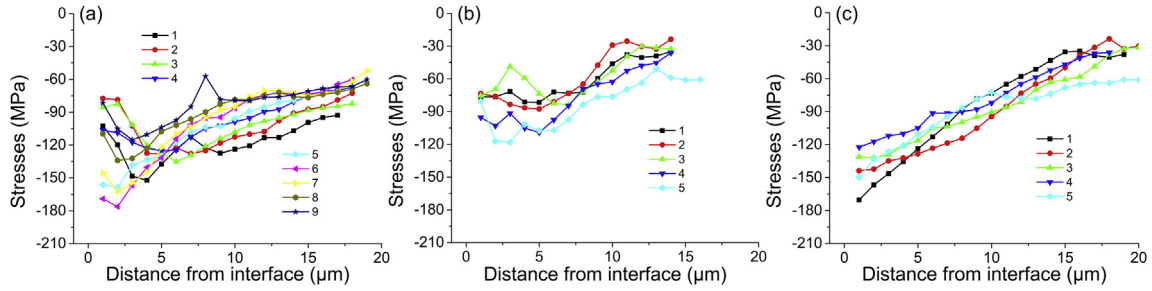

Fig. 8. Residual stresses calculated based on the measured strains from the monochromatic energy scans as a function of distance from interface for nodules. (a)–(c) are for the strains measured in the matrix grains near nodules A–C. The line profiles are calculated based on the strain data shown in Fig. 6, each curve corresponds to each vertical line.

strains are observed at regions close to the nodule/matrix interface, while nearly zero strains are seen in the middle of the characterized area of the grain. The compressive strains at the interface around nodule C are generally larger than those around nodule B. The maximal compressive strain is -8×10^{-4} and -6.3×10^{-4} for the grains around nodules A and B/C, respectively. It should be noted that the maximal compressive strain is found at the interface for nodule C but about 2–5 μm away from the interface for nodule A. Within the grains, strains change rather smoothly, and no abrupt change is seen at the dislocation boundaries (see the microstructure within the white boxes in Fig. 4).

4. Discussion

The present study demonstrates that DAXM is a powerful and unique technique for non-destructive 3D characterization of both microstructure and local residual strain at the mesoscale for the ferrite matrix grains within a 3D volume in the present DCI. By using focused microbeam with size of 0.5 × 0.5 μm^2, a spatial resolution of 1 μm in all directions is obtained. With the polychromatic beam mode of DAXM, the local dislocation cell structures around the nodules are revealed with an angular resolution of ~0.1°. With the monochromatic energy scan of DAXM, the local elastic strains are measured for the two selected grains with a resolution of 1×10^{-4}. To the best knowledge of the authors, no other techniques can provide such good combination of depth-dependent spatial, angular and strain resolutions within a local volume of 1 μm^3.

With these techniques, the results have shown evidently that ferrite matrix grains at the nodules are plastically deformed, most at large nodules. The plastic deformation is reflected in the formation of a dislocation structure at or near the nodules. The dislocations are stored in cell wall boundaries with low misorientation angles, showing that the plastic strain has not been high. The plastic strains are different between matrix grains around the same nodule. This difference may be due to the fact that the grains have different crystallographic orientations, and their plastic properties and deformation microstructure will therefore depend on their orientations [20]. It may also be due to the complex stress pattern around the nodule (see for example Fig. 7a in Section 4.2). To investigate the details of this nodule/matrix interaction may be possible by a local crystal plasticity analysis also encompassing the strain gradient in the matrix, which will be performed in the future.

Both plastic and elastic strain gradients are seen in the matrix grains at the nodules. In the following, the existence of the residual elastic strain gradients and their formation mechanism will be discussed. For the latter, a finite element model of residual elastic strain developed in a previous publication [10] is used to calculate the residual stress/strain distribution. The last three questions raised in the Introduction will be addresses based on the discussion. The effects of nodule sizes as well as specimen surface on the residual strains/stresses, and their roles in the material fatigue properties are discussed in the end.

4.1. Residual elastic strain gradients in the matrix grains surrounding nodules

The measured elastic strains depend on the lattice parameter, which according to Eq. (1) varies with variations in local chemical contents. The present monochromatic energy scan shows that there are significant compressive strains along directions nearly perpendicular to the nodule/matrix interface, with maximum of 6.5–8 × 10^{-4} and a gradient of 5–6 × 10^{-4} over a distance of ~20 μm (see Fig. 6). Although the strain resolution is 1×10^{-4}, one may speculate that the measured strain gradients are just a reflection of gradients of chemical contents in the matrix. This speculation is not inurbane, as it is well known that during solidification process of DCI, certain alloying elements segregate, including the main alloying elements C, Si and Mn in the present DCI [22]. This possibility can however be ruled out by the following analysis.

During solidification Si is generally segregated at the first solidification region around graphite nodules, leading to a high Si content there, and a low Si content at the last solidification region, i.e. at the joints of eutectic cells. Mn segregates in a reverse way, i.e. low Mn content close to the nodules and high content within the eutectic zones [22]. Our measurements were conducted within matrix grains that neighbor the graphite nodules directly. Therefore it is very likely that the characterized region is within the first solidification region, especially for the grain in-between nodules B and C. The Si/Mn contents there should be higher/lower than the average Si/Mn contents in the material. If we assume that the Si/Mn contents were ~20% higher/lower within the characterized region than the average percentage of the sample, i.e. 2.76% and 0.18% for Si and Mn, respectively, the measured compressive strain will reduce only about 1×10^{-4}, which is much smaller than the observed strains. Moreover, it has to be noted that the chemical difference considered here is between the first solidification region and the last solidification regions. The chemical variation within the first solidification region should be even less than that [23]. According to Eq. (1), a strain difference of 5–6 × 10^{-4} requires Si + Mn variation of 2.5–3%, which is almost more than the total average chemical contents of Si + Mn in the material. It is therefore almost impossible that such large chemical variations can exist within the two characterized matrix grains.

Additionally, C is another main element in DCI that can affect the lattice parameter. In the present paper, we assumed the C content to be the maximum C solubility (0.005%) in ferrite at room temperature. From Eq. (1), it can be seen that in order to reduce the lattice parameter, and thus reduce the observed compressive strain,

the C content should be even less. However, in total the 0.005% C content changes only the strain about 5×10^{-5}.

Last but not least, a similar magnitude of compressive strains and a slightly larger strain gradient are also seen in the deviatoric ε_{33} map for the marked grain around nodule A (see Fig. S3a in the supplementary materials). As the determination of the deviatoric strains does not depend on the input lattice parameter, the measured strain gradient therefore must be real. Based on this evidence and the analysis of chemical contents, it can be concluded that the observed compressive strains and strain gradients over the 20 μm distance from the interface are not simply due to chemical variations. To further analyze the formation of the local residual strains, finite element modeling is conducted and described in the following section.

4.2. Finite element model

Several analytical models [3] are available in the literature to predict the formation of thermal residual stresses in materials containing secondary-phase particles, where Eshelby's equivalent inclusion method [24] is central, assuming homogeneity of the material constituents at the micrometer scale. In DCI, however, this assumption does not hold, due to the heterogeneous and anisotropic nature of the graphite nodules [25]. To overcome this limitation, Andriollo et al. [10] have recently proposed a new finite element model where the nodules' internal structure is explicitly taken into account. This model was applied to the present ductile iron assuming a graphite volume fraction of 11.5% and 48 conical partitions in the nodule. Time-independent plastic deformation in the matrix, neglected in the original version of the model, was here simulated via a standard J2-flow formulation, considering two sets of properties: strain-stress curve at room temperature [26], and temperature-dependent flow stress [27].

The patterns of the predicted residual elastic stresses/strains in the matrix around the graphite nodule are complex, having a cubic symmetry in the specimen coordinate system (XHF) and with each strain component varying along both the circumferential and radial directions. As an example, the predicted σ_{33} component at a section equivalent to that marked by the white line in Fig. 2 for nodule A is shown in Fig. 7a. The stress component is symmetrical with respect to the vertical Z axis but not to the horizontal X axis. This is mainly because the plane normal to the selected mapping section (see Fig. 2) is rotated about 45° from the specimen surface normal direction. For the comparison to the experimental elastic strain data, only profiles of the ε_{33} component (in the XHF system) within the region that is equivalent to the white box in Fig. 4a are considered. Comparison with the results based on the monochromatic energy scans around nodule A (Fig. 6a) is reported in Fig. 7b, where the measured strains are plotted as line profiles, with each curve corresponding to one vertical line marked in Fig. 6a. It can be seen that the general tendency of the measured compressive strains to decrease with increasing distance from the interface is captured by the model. However, the maximum compressive strain close to the nodule and the corresponding decreasing rate are over-predicted by a factor ~2.

There could be several reasons that the experimentally measured maximum compressive strains are smaller than those predicted by the model. Firstly, some plastic deformation in the matrix grains is seen for the selected nodules (see Figs. 4 and 5). The plastic strain predicted by the model is about 2.5×10^{-4} (Fig. 7b), which is relatively small compared to the differences between the measured and modeled strains. At the same time, when a material is plastically deformed and kept at a constant strain, stress relaxation occurs [28]. This mechanism can contribute also to the observed reduction in the measured residual strains. Secondly, it is assumed in the model that no plastic deformation occurs in the nodule. In reality, this assumption may not hold. Moreover, high-temperature creep could also reduce the elastic strain. And in the model, an isotropic matrix is used, while in reality the anisotropy of the individual ferrite grains may also induce some strain variations (see Figs. S1 and S2 in the supplementary materials).

Another inconsistency between the model and experimental results is that the peak positions of the measured maximum residual strains along each line are not as model predicted at the interface, but at a distance of 2–5 μm from the interface for nodule A. The compressive strains drop about $5 \times 10^{-5} - 3 \times 10^{-4}$ in this range for all lines. This strain drop is however not observed for nodule C (see Fig. 8c), i.e. it may not be a typical phenomenon. It could be due to some local microstructural variations in 3D that have not been captured by the present characterizations.

4.3. Size and surface effects on the residual stresses

By combining the DAXM with the X-ray μ-CT, it is possible to evaluate the effect of the nodule size on the residual stresses. To compare the results at different nodules, the residual stresses were estimated from the measured residual strains by means of the direction-dependent Young's moduli. The Young's moduli along the two crystal directions, [-3 2 5] and [-3 -3 4], are calculated to be 220 and 270 GPa, respectively, using the elastic constants for pure iron [29].

The calculated stresses as a function of distance from interface along vertical lines are shown in Fig. 8. A similar maximum compressive stresses are seen for the grains around nodules A and C, while relatively small compressive stresses are seen for the grain around nodule B. The 3D sizes of nodules A and C are similar (see Table 2). It is thus reasonable that the compressive stresses around nodules A and C are similar. Nodule B is bigger than the other two nodules. It is therefore interesting that the compressive stresses in the matrix grains are smaller around nodule B than around nodules A and C.

Two major possibilities should be considered. Firstly, as shown in Fig. 5, the average cell-wall dislocation density in the matrix grains around nodule B is higher than those around nodule A. The residual stresses are relaxed more by plastic deformation in the matrix grain around nodule B than those around nodule A. Secondly, nodule B is exposed at the specimen surface. The residual stresses at the interface around nodule B are compressive stresses along the specimen normal direction. When nodule B was completely inside the bulk material (i.e. before polishing), the compressive stresses at one side of the interface were counterbalanced by the compressive stresses at the opposite side, and the local compressive stresses could be maintained. However, when nodule B is exposed to free surface, the compressive stresses opposite to the side we measured were released. The compressive stresses at the inner interface are then pushing the nodule out of the surface, and are consequently reduced. The free surface releases not just the stresses at the interface. The stresses in the middle of the characterized grain between nodules B and C (~15–20 μm from the two interfaces) seem also to be affected, for a relatively small magnitude of compressive stresses are seen at that position compared to those away from nodule A (>15 μm from the interface).

Large nodules are selected for the present study, as they are the critical ones for the fatigue behavior [30]. The maximum residual stress at the selected nodules is about half of the yield stress of the matrix, which is about 297 MPa [27]. The residual stresses in the matrix grains therefore cannot be neglected for the material fatigue properties. The strength increase due to cell-wall dislocation structure in the matrix grains is maximum ~35 MPa for the largest nodule [21]. Altogether, the residual stresses are still not so critical for the fatigue properties, and that might be a reason for the high

fatigue cycles for this DCI [16]. For other DCI, where the largest nodule size can be > 200 μm, the resulting residual stresses may be critical for the fatigue life [16]. However, the large nodule size forms typically due to slow cooling rates, which at the other hand can reduce the residual stresses. How these two factors are balanced needs to be analyzed. At the same time, other factors as the nodule connectivity and shape as suggested in the previous study may also be critical for the material fatigue properties [16]. The effects of these factors on the residual stresses (thus on the fatigue properties) are planned to be examined in the future.

5. Conclusions

1. The DAXM technique is suitable for characterization of both local plastic and elastic residual strains in the present ductile cast iron. With this technique, an angular resolution of 0.1°, a spatial resolution of 1 μm, and an elastic strain resolution of 1×10^{-4} have been obtained.
2 The ferrite matrix grains at nodules have been plastically deformed as a result of the local stresses, which develop due to the interaction between the nodules and the matrix during cooling. The plastic deformation introduces dislocations which are stored as dislocation boundaries with low misorientations angles in the range 0.1–1°, and organized in a cell structure.
3 Compressive residual elastic strains along specimen surface normal direction are observed at interfaces that are approximately perpendicular to the specimen surface normal direction. The residual elastic strains have shown gradients with maximum of $6.5–8 \times 10^{-4}$ near the graphite nodules extending into the matrix about 20 μm, where the strains are near zero. These gradients are not caused by local chemical variations.
4 The finite element modeling captures the general trend that the elastic residual strain decreases as a function of the distance from the matrix/nodule interface. However, the maximum compressive strain close to the nodule and the corresponding decreasing rate are over-predicted by a factor ~2. These differences are mainly originated in relaxation processes reducing the strain at the nodules by plastic deformation of the matrix.
5 The free specimen surface releases some of the compressive residual elastic stresses along the surface normal direction. The maximum residual stresses in the matrix grains are about half of the yield stress of the matrix, which suggests that the local residual stresses cannot be neglected for the fatigue properties of ductile cast iron.

Acknowledgements

Part of this work has been supported by the Strategic Research Center "REWIND -Knowledge based engineering for improved reliability of critical wind turbine components," Danish Research Council for Strategic Research, grant no. 10-093966. The authors thank Profs. D Juul Jensen and N. Hansen for the helpful and stimulating discussions and for the useful comments during the preparation of the manuscript. Use of the Advanced Photon Source was supported by the U. S. Department of Energy, Office of Science, Office of Basic Energy Sciences, under Contract No. DE-AC02-06CH11357.

Appendix A. Supplementary data

Supplementary data related to this article can be found at http://dx.doi.org/10.1016/j.actamat.2016.09.009.

References

[1] C. Labrecque, M. Gagne, Review ductile iron: fifty years of continuous development, Can. Metall. Q. 37 (1998) 343–378.
[2] H. Mirzaei Rafsanjani, J. Dalsgaard Sørensen, Reliability analysis of fatigue failure of cast components for wind turbines, Energies 8 (2015) 2908–2923.
[3] S. Ho, E.J. Lavernia, Thermal residual stresses in metal matrix composites: a review, Appl. Compos. Mater 2 (1995) 1–30.
[4] P.J. Withers, H.K.D.H. Bhadeshia, Residual stress. Part 2 – nature and origins, Mater. Sci. Technol. 17 (2001) 366–375.
[5] C.Y. Barlow, N. Hansen, Deformation structures and flow stress in aluminium containing short whiskers, Acta Metall. Mater 39 (1991) 1971–1979.
[6] R.J. Arsenault, M. Taya, Thermal residual stress in metal matrix composite, Acta Metall. 35 (1987) 651–659.
[7] H. Ledbetter, M. Austin, Internal strain (stress) in an SiC-Al particle-reinforced composite: an X-ray diffraction study, Mater. Sci. Eng. 89 (1987) 53–61.
[8] H.F. Poulsen, T. Lorentzen, R. Feidenhans'L, Y.-L. Liu, A synchrotron x-ray diffraction study of the local residual strains around a single inclusion in an Al/W, Metal-Matrix Compos. 28 (1997) 237–243.
[9] G. Hütter, L. Zybell, M. Kuna, Micromechanisms of fracture in nodular cast iron: from experimental findings towards modeling strategies-A review, Eng. Fract. Mech. 144 (2015) 118–141.
[10] T. Andriollo, J. Thorborg, N. Tiedje, J. Hattel, A micro-mechanical analysis of thermo-elastic properties and local residual stresses in ductile iron based on a new anisotropic model for the graphite nodules. Model, Simulations Mater. Sci. Eng. 055012 (2016) 1–19.
[11] B.C. Larson, W. Yang, G.E. Ice, J.D. Budai, J.Z. Tischler, Three-dimensional X-ray structural microscopy with submicrometre resolution, Nature 415 (2002) 887–890.
[12] L.E. Levine, B.C. Larson, W. Yang, M.E. Kassner, J.Z. Tischler, M.A. Delos-Reyes, R.J. Fields, W. Liu, X-ray microbeam measurements of individual dislocation cell elastic strains in deformed single-crystal copper, Nat. Mater 5 (2006) 619–622.
[13] T. Ohashi, R.I. Barabash, J.W.L. Pang, G.E. Ice, O.M. Barabash, X-ray microdiffraction and strain gradient crystal plasticity studies of geometrically necessary dislocations near a Ni bicrystal grain boundary, Int. J. Plast. 25 (2009) 920–941.
[14] R.I. Barabash, W. Liu, J.Z. Tischler, H. Bei, J.D. Budai, Phase-specific elastic/plastic interface interactions in layered NiAl-Cr(Mo) structures, Acta Mater 60 (2012) 3279–3286.
[15] G.E. Ice, J.D. Budai, J.W.L. Pang, The race of X-ray microbeam and nanobeam science, Science 334 (2009) 1191–1201.
[16] K. Mukherjee, S. Fæster, N. Hansen, A. Bjorholm, C. Gundlach, A. Sturlason, Graphite Nodules in Fatigue-tested Cast Iron Characterized in 2D and 3D, (submitted for publication).
[17] H.K.D.H. Bhadeshia, S.A. David, J.M. Vitek, R.W. Reed, Stress induced transformation to bainite in pressure vessel steel, Mater. Sci. Technol. 7 (1991) 686–698.
[18] W. Liu, P. Zschack, J.Z. Tischler, G.E. Ice, B.C. Larson, X-ray laue diffraction microscopy in 3D at the advanced photon source, AIP Conf. Proc. 1365 (2010) 108–111.
[19] J.Z. Tishchler, Reconstructing 2D and 3D X-ray orientation map from white beam Laue, in: R. Barabash, G.E. Ice (Eds.), Strain and Dislocation Gradients from Diffraction Ch. 10, Imperial College Press, London, 2014.
[20] X. Huang, G. Winther, Dislocation structures. Part I. Grain orientation dependence, Philos. Mag. 87 (2007) 5189–5214.
[21] N. Hansen, Flow stress and microstructural parameters, 15th Risø International Symposium Mater. Sci. (1994) 325–334.
[22] A. Alhussein, M. Risbet, A. Bastien, J.P. Chobaut, D. Balloy, J. Favergeon, Influence of silicon and addition elements on the mechanical behavior of ferritic ductile cast iron, Mater. Sci. Eng. A 605 (2014) 222–228.
[23] M.J. Dong, B. Tie, A.S. Béranger, C. Prioul, D. François, Damage effect on the fracture toughness of nodular cast iron, Adv. Mater. Res. 4–5 (1997) 181–188.
[24] J.D. Eshelby, The determination of the elastic field of an ellipsoidal inclusion, and related problems, Proc. R. Soc. A Math. Phys. Eng. Sci. 241 (1957) 376–396.
[25] K. Theuwissen, J. Lacaze, M. Véron, L. Laffont, Nano-scale orientation mapping of graphite in cast irons, Mater. Charact. 95 (2014) 187–191.
[26] K.S. Zhang, J.B. Bai, D. François, Ductile fracture of materials with high void volumefraction, Int. J. Solids Struct. 36 (1999) 3407–3425.
[27] N. Bonora, A. Ruggiero, Micromechanical modeling of ductile cast iron incorporating damage. Part I: ferritic ductile cast iron, Int. J. Solids Struct. 42 (2005) 1401–1424.
[28] V.I. Dotsenko, Stress relaxation in crystals, Phys. Status Solidi 11 (1979) 11–43.
[29] Z. Hashin, S. Shtrikman, A Variational approach to the theory of the elastic behaviour of polycrystals, J. Mech. Phy. Solids 10 (1962) 343–352.
[30] C. Verdu, J. Adrien, J.Y. Buffière, Three-dimensional shape of the early stages of fatigue cracks nucleated in nodular cast iron, Mater. Sci. Eng. A 483–484 (2008) 402–405.

DTU Mechanical Engineering
Section of Manufacturing Engineering
Technical University of Denmark

Produktionstorvet, Bld. 427S
DK-2800 Kgs. Lyngby
Denmark
Phone (+45) 4525 4763
Fax (+45) 4593 0190
www.mek.dtu.dk
ISBN: 978-87-7475-476-3